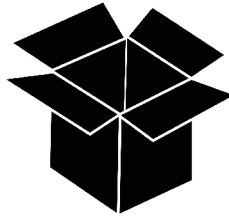


**PEEKING
INSIDE
THE
BLACK
BOX**



Héloïse Thouement

Peeking inside the black-box

**A model-based interpretation of multi-
elemental isotope data of chlorinated ethenes
in heterogeneous aquifer systems**

Héloïse Ana Amélie Thouement

This page was intentionally left blank

Peeking inside the black-box

A model-based interpretation of multi-elemental
isotope data of chlorinated ethenes in heterogeneous
aquifer systems

Dissertation

for the purpose of obtaining the degree of doctor
at Delft University of Technology
by the authority of the Rector Magnificus, Prof.dr.ir. T.H.J.J. van der Hagen,
chair of the Board for Doctorates
to be defended publicly on
Thursday 30 January 2020 at 12:30

By

Héloïse Ana Amélie THOUEMENT
Ingénieur chimiste, Ecole Nationale Supérieure de Chimie de Lille, France
Civilingeniør, cand. polyt., Danmarks Tekniske Universitet, Denmark
born in Vitré, France

This dissertation has been approved by the promotor.

Composition of the doctoral committee:

Rector Magnificus	chairperson
Prof.dr.ir. T. Heimovaara	Delft University of Technology, promotor
Dr. B.M. van Breukelen	Delft University of Technology, copromotor

Independent members:

Prof. dr. P.J. Stuyfzand	Delft University of Technology
Dr. T.A. Bogaard	Delft University of Technology
Dr. I. Nijenhuis	Helmholtz Centre for Environmental Research
Prof.dr. P. Höhener	Aix Marseille université
Prof.dr.ir. M. Bakker	Delft University of Technology

Cover : Sjoerd Houweling

Printed by Proefschrift All In One

ISBN : 978-94-93184-29-9

This book is available in PDF form on the TU Delft repository



This work was partially funded by the European Union under the 7th Framework Programme (project acronym CSI:ENVIRONMENT, contract number PITN-GA- 2010-264329, and by the Strategic Environmental Research and Development Program (SERDP) project ER-2623 “Identification of Abiotic Degradation Pathways of Chlorinated Ethenes by CSIA: A Proof-of-Concept Study”.

This page was intentionally left blank

This page was intentionally left blank

Table of contents

Samenvatting	1
Résumé	3

Chapter 1

General introduction	7
1.1 Background	7
1.1.1 Chloroethene contamination of aquifers.....	7
1.1.2 Compound-specific stable isotope analysis of chlorinated ethenes.....	9
1.1.3 Impact of subsurface heterogeneity on CSIA patterns.....	13
1.1.4 Modelling CSIA data: Opportunities and Challenges.....	15
1.2 Thesis objectives	17
1.3 Thesis outline.....	17

Chapter 2

Verifying a conceptual site model with triple element CSIA: assessment of biodegradation and physical attenuation of chlorinated ethenes	21
2.1 Introduction.....	23
2.2 Field site description	26
2.2.1 Site hydrogeology	26
2.2.2 Source zones and contaminant plumes	27
2.2.3 Redox conditions.....	30
2.2.4 Presence and activity of microorganisms	30
2.2.5 Potential for natural attenuation by degradation	31
2.2.6 Potential for natural attenuation by physical processes	32
2.3 Methods	33
2.3.1 Groundwater sampling.....	33
2.3.2 Groundwater analysis.....	33
2.3.3 CSIA calculations.....	34
2.4 Results and Discussion	36
2.4.1 Source characterization	36
2.4.2 PCE degradation	39
2.4.3 TCE transformation – Carbon isotopes.....	42
2.4.4 TCE transformation - Chlorine isotopes	46
2.4.5 TCE transformation - Hydrogen isotopes	49
2.4.6 Potential for DCE and VC transformation	49
2.4.7 Interaction of transport and physical attenuation with CSIA	56
2.4.8 CSIA-based refined interpretation of concentration decrease	62
2.4.9 Summary discussion on the impacts of CSIA on the CSM	63

2.5 Conclusion	66
Supporting information to chapter 2	69

Chapter 3

Dual C and Cl CSIA batch modeling for refinement of a conceptual site model on chlorinated ethene degradation 91

3.1 Introduction.....	93
3.2 Methodology.....	95
3.2.1 Field site description.....	95
3.2.2 Summary of the conceptual site model for CEs degradation and isotope fractionation.....	97
3.2.3 Groups of wells with similar isotope patterns.....	99
3.2.4 Rationale for batch modelling.....	100
3.2.5 Acquirement of enrichment factors for reductive dechlorination pathways.....	101
3.2.6 Reaction networks modelled.....	102
3.2.7 Simulation of TCE and DCEs degradation and isotope fractionation	104
3.3 Results and discussion.....	105
3.3.1 Field based assessment of TCE C and Cl isotope enrichment factors during reductive dechlorination	105
3.3.2 Modeling TCE degradation and DCE isomers production – C CSIA.....	108
3.3.3 Modeling TCE degradation and cis-DCE production - Cl CSIA.....	111
3.3.4 Modeling cis-DCE degradation.....	112
3.3.5 TCE cometabolic oxidation.....	118
3.4 Conclusion	121
Supporting information to chapter 3	123

Chapter 4

Do CSIA data from aquifers inform on natural degradation of chlorinated ethenes in aquitards?131

4.1 Introduction.....	133
4.2 Methods	135
4.2.1 General model concept.....	135
4.2.2 Modelling approach.....	137
4.2.3 General model settings.....	137
4.2.4 Pollutant source and degradation	138
4.2.5 Diffusion and diffusion-induced isotope fractionation.....	140
4.2.6 Sorption and sorption-induced isotope fractionation.....	141
4.3 Post-modelling calculations	143
4.3.1 Isotope ratio.....	143
4.3.2 Carbon isotope mass balance	143
4.3.3 Performance of the Rayleigh equation to estimate TCE degradation	144
4.4 Results and discussion.....	146
4.4.1 Complete model including CEs degradation: loading phase	146

4.4.2 Complete model including CEs degradation: release phase	150
4.4.3 Distinct CSIA patterns in the aquifer in presence of aquitard degradation	151
4.5 Performance of the Rayleigh equation in assessing the extent of degradation	153
4.5.1 Performance of the Rayleigh equation for local degradation assessment ..	154
4.5.2 Can mass destruction in the aquitard be estimated with CSIA data?	155
4.6 Sensitivity analysis of degradation assessment	157
4.7 Model limitations	157
4.8 Summary and implications	159
Supporting information to chapter 4	161

Chapter 5

Virtual experiments to assess opportunities and pitfalls of CSIA in physical-chemical heterogeneous aquifers.....185

5.1 Introduction.....	187
5.2 Methodology.....	189
5.2.1 General setup of model.....	189
5.2.2 Correlation between hydraulic conductivity and degradation rates.....	190
5.2.3 Simulation of isotope fractionation	192
5.2.4 Post-simulation calculations.....	194
5.3 Results and discussion.....	196
5.3.1 General patterns.....	196
5.3.2 Sampling effect.....	199
5.4 Conclusion and implications	204
Supporting information to chapter 5	207

Chapter 6

Synthesis.....211

6.1 Summary	211
6.2 Implications and outlook.....	215
6.2.1 Refining conceptual site models with CSIA data and modelling.....	215
6.2.2 Exploring subsurface heterogeneity	216
References.....	219
Acknowledgements.....	238
Curriculum Vitae.....	240

This page was intentionally left blank

Samenvatting

Gechloroerde ethenen worden gebruikt als industriële ontvetters voor mechanische onderdelen en als een van de werkzame stoffen binnen stomerijen. De verscheidenheid aan verschillende gebruiksmethoden heeft geleid tot tal van soorten bodemverontreiniging. Omdat deze verbindingen als puur product zwaarder zijn dan water, verspreiden ze zich snel diep in het grondwater, waar ze langdurige verontreiniging van waterbronnen kunnen veroorzaken. De noodzaak om onze bodem- en waterbronnen te herstellen of te beschermen en de inademing of inname van deze giftige of zelfs kankerverwekkende verbindingen te voorkomen, vereist dat de verspreiding van dergelijke vervuilingsspluimen in het grondwater wordt beperkt evenals inperking van de bodemvervuiling. Vanuit dit perspectief zijn veel min of meer invasieve methoden geprobeerd om de vervuiling actief te verwijderen en/of af te breken. De ontdekking van natuurlijke afbraakroutes voor gechloroerde ethenen tot niet-toxische verbindingen maakt het mogelijk om de natuurlijke capaciteit de ondergrond te gebruiken om het grondwater te zuiveren, waarmee het mogelijk is inspanningen, tijd en middelen te concentreren op locaties waar sanering dringend is of waar de ondergrond deze verbindingen niet natuurlijk kan afbreken. Deze methode (MNA) vereist dat kan worden aangetoond dat natuurlijke afbraak het mogelijk maakt om een bepaalde kwaliteit van water of bodem te verkrijgen en deze afbraak te volgen en te begrijpen. Voor dit doel is de studie van isotopen verhoudingen bijzonder interessant voor het schatten van de staat van afbraak van de vervuiling. Wanneer een verbinding afbreekt, leidt dit tot een meetbare verandering in de isotopensamenstelling van de verbinding. De stappen die leiden tot het breken van de bindingen vereisen een grotere energiebijdrage voor de bindingen die zware isotopen bevatten dan voor die welke lichtere isotopen bevatten, hetgeen leidt tot relatief lagere reactiesnelheden van de zware isotopen vergeleken met de meer overvloedige lichte isotopen. Bijgevolg zal een toenemende fractie van de overblijvende verbinding bestaan uit moleculen die zware isotopen in hun structuur omvatten naarmate de afbraak vordert. De verandering in isotopensamenstelling van de verbinding, genaamd isotopen fractionering, hangt af van de afbraakroute, de mate van afbraak, het element en de verbinding.

Aangezien goed gekarakteriseerde aquifers (watervoerende lagen) zeldzaam zijn, worden aquifers vaak beschouwd als "zwarte dozen" waarin de afbraak en het transport van gechloroerde ethenen moet worden bepaald met behulp van schaarse ruimtelijke en temporele gegevens. De voordelen van component-specifieke isotopenanalyse (CSIA) om het conceptuele locatie model (CSM) van een aquifer-systeem te verbeteren worden gepresenteerd in de hoofdstukken 2 en 3. Deze hoofdstukken presenteren de toepassing van de studie van meerdere elementen (koolstof (C), chloor (Cl) en zelfs waterstof (H)). Het bestaan van meerdere vervuilingbronnen, heterogene lithologieën en talloze afbraakroutes

maakte de interpretatie van isotopen gegevens van de luchtmachtbasis Hill, Utah, complex. Desondanks illustreert hoofdstuk 2 het potentieel van CSIA-gegevens voor gechloroerde ethenen om de bron van vervuiling en belangrijke afbraakroutes te karakteriseren, en om fysieke processen te detecteren die leiden tot natuurlijke afname van concentraties. Als vervolg op hoofdstuk 2 illustreert hoofdstuk 3 het potentieel van het modelleren van isotopen verhoudingen van koolstof en chloor voor de studie van afbraakpaden en hun verdeling op de Hill onderzoekslocatie. Hoofdstukken 2 en 3 tonen de invloed van de fysische en chemische heterogeniteit van de watervoerende laag op isotopengegevens. In reactie op deze observatie passen de hoofdstukken 4 en 5 virtuele experimenten toe om te verifiëren of een degradatiebeoordeling op basis van een punt meting betrouwbaar is wanneer degradatie optreedt in gebieden met een lage permeabiliteit van de watervoerende laag of in aquitards (d.w.z. slecht doorlatende lagen zoals bijvoorbeeld een klei laag) in de buurt. Hoofdstuk 4 bespreekt het potentieel van CSIA-gegevens verzameld in een watervoerende laag om de aanwezigheid en mate van TCE-afbraak in een reactieve kleilaag te beoordelen. Dit experiment leidt tot resultaten gevat en geïllustreerd in diagrammen die karakteristiek zijn voor de evolutie van isotopenconcentraties en -verhouding tijdens de diffusie van de verbindingen in de aquitard en hun diffusie in de aquifer. In hoofdstuk 5 worden fysicochemische heterogeniteiten binnen de aquifer gesimuleerd. Deze studie benadrukt de prestaties en limieten van dubbele C-Cl CSIA voor het bepalen van de afbraakroute(s) en voor het berekenen van de mate van afbraak. Tenslotte worden tijdens dit proefschrift interpretatie methoden die de studie van isotopen gegevens mogelijk maakten geëvalueerd op gegevens van een denkbeeldige locatie met fysisch-chemische heterogeniteiten verkregen door virtuele experimenten.

In de praktijk wordt isotopen analyse steeds vaker gebruikt op locaties waar de complexiteit van de diverse processen het lastig maakt om concentratie gegevens te interpreteren. Interpretatie van isotopen data van dergelijke locaties is dientengevolge ook een uitdaging. Dit onderzoek heeft geleid tot verschillende inzichten en adviezen om de herkomst van verontreinigende stoffen alsmede de afbraak processen vast te stellen bij locaties met een heterogene hydrogeologie. Isotopen gegevens kunnen uitkomst bieden om de aanwezigheid van meerdere bronnen, het voorkomen van meerdere afbraakroutes, en bepaalde fysische afname processen aan te tonen. Deze gevoeligheid van isotopen analyse voor al deze processen vraagt ook om methoden de isotopen gegevens te interpreteren. Dit proefschrift demonstreert de toepasbaarheid van CSIA-gegevens om afbraakprocessen en herkomst van vervuiling aan te tonen, ook in complexe situaties. En illustreert het voordeel van verschillende methoden, van basale gegevensinterpretatie tot computer simulatie modellen, om ons begrip van isotopen data te verbeteren en de waardevolle informatie die in isotopen data verborgen zit.

Résumé

Les éthènes chlorés ont été communément utilisés comme dégraissants industriels de pièces mécaniques et comme nettoyants à sec. La multiplicité des points d'usage a donné lieu à de nombreuses pollutions des sols. Ces composés étant denses, ils se propagent rapidement en profondeur dans les eaux souterraines où ils peuvent causer une pollution durable des ressources en eau. La nécessité de restaurer ou protéger nos ressources en sols et en eau et d'empêcher l'inhalation ou l'ingestion de ces composés toxiques voire carcinogènes requiert de limiter l'extension de tels panaches de pollution dans les eaux souterraines et de remédier à la pollution des sols. Dans cette optique, de nombreuses méthodes plus ou moins invasives ont été éprouvées. La découverte de voies de dégradation naturelles des éthènes chlorés en des composés non toxiques rend possible l'utilisation de la capacité naturelle des sols à se remédier, permettant de concentrer les efforts de temps et de moyens sur des sites où la remédiation est urgente ou les sols incapables de dégrader ces composés sans aide. Cette méthode requiert de pouvoir prouver que la dégradation naturelle permet d'obtenir une qualité de l'eau ou des sols donnée et de surveiller et comprendre cette dégradation. A cet effet, l'étude des ratios isotopiques est particulièrement intéressante pour estimer l'état de dégradation d'un composé. Lorsqu'un composé se dégrade, cela induit un changement mesurable dans la composition isotopique d'un composé en cours de dégradation par rapport à la composition isotopique initiale du composé. En effet, les étapes menant à la rupture des liaisons requièrent un apport énergétique plus important pour les liaisons contenant des isotopes lourds que pour celles contenant des isotopes plus légers, ce qui conduit à des vitesses de réaction relativement plus faibles des isotopes lourds par rapport aux isotopes légers plus abondants. En conséquence, une fraction croissante du composé restant sera constituée de molécules comprenant des isotopes lourds dans leur structure au fur et à mesure de la dégradation. Le changement de composition isotopique du composé, appelé fractionnement isotopique, dépend de la voie de dégradation, du degré de dégradation, de l'élément et du composé.

Les aquifères bien caractérisés étant rares, les aquifères sont souvent considérés comme des «boîtes noires» dans lesquelles la dégradation et de transport des éthènes chlorés (EC) doivent être déterminés à l'aide de données spatiales et temporelles clairsemées. Les avantages de l'analyse isotopique spécifique (compound specific isotope analysis ou CSIA) pour améliorer le modèle conceptuel (CSM) d'un système aquifère sont présentés dans les chapitres 2 et 3. Ces chapitres présentent l'application de l'étude d'éléments multiples (carbone (C), chlore (Cl) voire hydrogène (H)). L'existence de sources multiples, de lithologies hétérogènes et de nombreux chemins de dégradation ont rendu complexe l'interprétation des données isotopiques provenant de la base aérienne de Hill (Utah). Malgré cela, le chapitre 2 illustre le potentiel des données CSIA des éthènes chlorés pour caractériser la source de pollution et les voies de dégradation majeures, ainsi que pour

détecter des processus d'atténuation physique. Dans la continuité du chapitre 2, le chapitre 3 illustre le potentiel de la modélisation des ratios isotopiques du carbone et du chlore pour l'étude des voies de dégradation et de leur répartition sur le site de l'étude. Les chapitres 2 et 3 démontrent l'influence de l'hétérogénéité physique et chimique de l'aquifère sur les données isotopiques. En réponse à cette observation, les chapitres 4 et 5 utilisent des expériences virtuelles afin de vérifier si une évaluation de la dégradation basée sur des données isotopiques ponctuel est fiable lorsque la dégradation se produit dans des zones de faible perméabilité de l'aquifère ou dans des aquitards (par exemple un horizon argileux) à proximité. Le chapitre 4 porte sur le potentiel des données CSIA collectées dans un aquifère pour évaluer la présence et l'étendue de la dégradation du TCE dans un horizon argileux réactif. Cette expérience illustre des schémas caractéristiques des évolutions de concentrations et de ratio isotopiques lors de la diffusion des composés dans l'aquitard et leur rétro-diffusion dans l'aquifère. Lors du chapitre 5 des hétérogénéités physico-chimiques intra-aquifères sont simulées. Cette étude met en avant les performances et les limites de la CSIA double C-Cl pour la détermination de la voie de dégradation et pour le calcul du degré de dégradation. En conclusion, lors de cette thèse des outils permettant l'étude des données isotopiques ont été testés sur des données d'un site présentant des hétérogénéités physico-chimiques, puis des expériences virtuelles ont été appliquées permettant de caractériser l'impact de telles hétérogénéités sur interprétations de données ponctuelles, offrant plusieurs angles d'approche à l'étude isotopique des sites présentant des hétérogénéités physico-chimiques.

En pratique, l'analyse isotopique est de plus en plus utilisée lorsque la complexité des divers processus au droit de certains sites rend difficile l'interprétation des données de concentration. L'interprétation des données isotopiques à de tels sites est donc un défi. Cette recherche a conduit à divers éclaircissements et conseils dans l'optique de déterminer l'origine des polluants ainsi que les processus de dégradation au droit de sites présentant une hydrogéologie hétérogène. Les données isotopiques peuvent offrir des résultats lorsque plusieurs sources sont présentes, de multiples voies de dégradation ont effet de concert et lorsque des processus physique donnent lieu à la diminution des concentrations. Cette sensibilité de l'analyse isotopique à chacun de ces processus nécessite également des méthodes adaptées pour interpréter les données isotopiques. Cette thèse démontre l'applicabilité des données CSIA pour détailler les processus de dégradation et l'origine de la pollution, également dans des situations complexes, et illustre l'avantage de différentes méthodes, de l'interprétation des données de base aux modèles de simulation par ordinateur, pour améliorer notre compréhension des données isotopiques et des informations précieuses qui sont dissimulées au sein des données isotopiques.

This page was intentionally left blank

This page was intentionally left blank

Chapter 1

General introduction

1.1 Background

1.1.1 Chloroethene contamination of aquifers

Chloroethenes (CEs), which are employed as degreasing agents in multiple industries, are now ubiquitous in the environment due to spills or inadequate waste disposal. They pose a threat to the groundwater resources, as they are toxic and potentially carcinogenic (Chiu et al., 2013; Huang et al., 2014; IARC, 2008; Lash et al., 2014), and as concentrations in the microgram per litre range make water unsuitable for consumption. As dense non-aqueous phase liquids (DNAPLs), CEs propagate fast downwards (days to weeks) in permeable aquifers (sand or gravel) until settling on less permeable lithology (e.g. clay or silt layers) such as aquitards in which they diffuse. Such matrix diffusion might increase the longevity of the pollution by several decades after the DNAPL is entirely dissolved (Seyedabbasi et al., 2012). Being volatile, they can impact the air quality inside buildings located above shallow contamination plumes (see Fig. 1-1). The remediation of groundwater and soils might require the excavation of the most polluted zone and/or the use of less invasive methods such as thermal treatment, air sparging, and addition of reactive compounds promoting oxidation or reduction (Semprini et al., 1995; Stroo et al., 2012). Recent developments in the understanding of naturally occurring CEs degradation pathways encouraged the development of Monitored Natural Attenuation (MNA) for polluted site remediation (Bradley, 2003; Mulligan and Yong, 2004; Semprini et al., 1995; Vogel et al., 1987). Biotic reductive dechlorination, sequentially dechlorinates CEs to non-toxic ethene in the order perchloroethylene (PCE), trichloroethylene (TCE), dichloroethylene (DCE), vinylchloride (VC), and ethene, which can also degrade further to ethane (see Fig. 1-2). Of DCE isomers, *cis*-DCE is most commonly produced during biotic degradation of TCE, *trans*-DCE being also a potential product while 1,1-DCE is usually found as trace if present. Abiotic reductive dechlorination of CEs by naturally present minerals like pyrite or magnetite (Darlington et al., 2013; Dong et al., 2011; Han et al., 2012; Jeong and Kim, 2007; Lee and Batchelor, 2002; Liang et al., 2009) and oxidative degradation through metabolism or cometabolism (Fox et al., 1990; Fries et al., 1997; Gaza et al., 2019; Schmidt et al., 2010) also lead to non-toxic products such as acetylene or CO₂. In order to rely on the natural capacity of aquifers to degrade CEs as a remediation option, it is necessary to prove the occurrence of sustained degradation to non-toxic compounds based on sound monitoring.

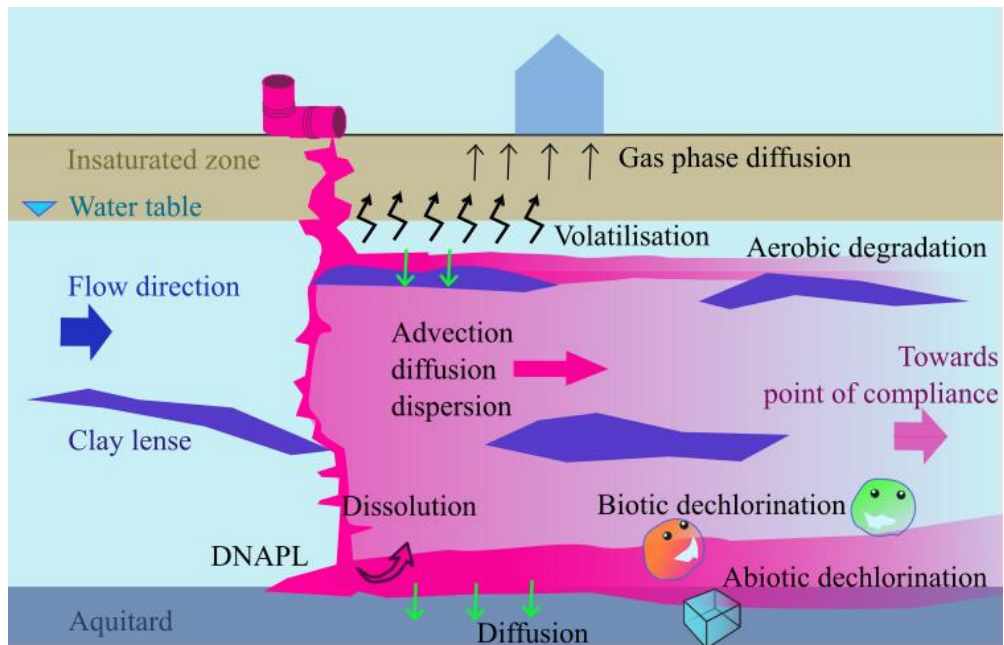


Fig. 1-1: Transport and fate of chlorinated ethenes in aquifers. The CEs quickly percolate in the permeable sediments (sand, gravel) before settling on less permeable sediments such as clay or silt inclusions in the aquifer or on a low permeability layer (clay, silt, or rock). Several processes govern the evolution of concentration in the aquifer, including degradative and non-degradative processes.

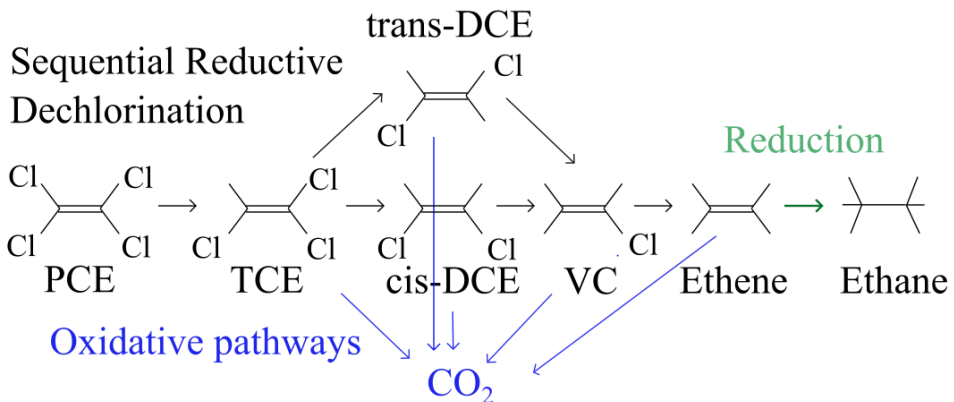


Fig. 1-2 : Reductive biotic dechlorination and aerobic degradation pathways for chlorinated ethenes and ethene. Abiotic reductive degradation leads to dechlorination similarly to biotic reductive dechlorination, with the co-production of acetylene (C₂H₂), ethene, ethane, and C₂-C₆ products. The relative amount of the compounds depends on the reactive mineral.

The success of MNA relies on a sound assessment of the performance of degradation, for example, through the development of a conceptual site model (CSM) (Wiedemeier et al., 1998). The MNA potential is evaluated in the CSM through the delineation of the source

zone(s), the determination of key transformation processes, and the assessment of attenuation through non-destructive physical processes, such as volatilization, sorption, or dilution. The lines of evidence for MNA potential rely on the geochemical conditions, hydrogeological setting, and spatial distribution and concentration trends of the contaminants (Wiedemeier et al., 1998). Microcosm degradation experiments and bacterial markers are also useful as complementary information on the aquifer potential for degradation (Abe et al., 2009a; Badin et al., 2016; Courbet et al., 2011; Lee et al., 2015; Nijenhuis et al., 2013; Wiedemeier et al., 1998). Ultimately, the estimation of degradation rate constants of the CEs at the site would shed light on the (future) spatial and temporal extent of CE plumes, which are crucial information when managing plumes in the vicinity of water resources or residential areas. Previous studies have shown that degradation rate constants measured in-situ are several orders of magnitude lower than found in the laboratory (Suarez and Rifai, 1999). This difference induces a large uncertainty on degradation assessment, hindering the application of MNA. MNA development requires in-situ field methods which more directly than concentration patterns provide specific information on pollutant degradation.

1.1.2 Compound-specific stable isotope analysis of chlorinated ethenes

With compound-specific stable isotope analysis (CSIA), direct in-situ information on degradation can be obtained. CSIA is therefore a promising tool for demonstrating the viability of MNA of CEs (US EPA 2008). CSIA is the measurement of the relative abundance of light and heavy stable isotopes (i.e., the isotopic composition) of an element in the compound. The isotopes of an element contain the same number of protons, but differ in their number of neutrons. In the case of CSIA, we focus on the stable isotopes, i.e., the isotopes that do not spontaneously undergo radioactive decay. For example, carbon occurs naturally as the two stable isotopes $^{12}_6\text{C}$ and $^{13}_6\text{C}$. The lighter isotope (i.e., $^{12}_6\text{C}$) has six neutrons and six protons, and is the main natural isotope of carbon as it accounts for 98.89% of carbon in nature (Table 1-1). The heavier isotope (i.e., $^{13}_6\text{C}$) comprises one additional neutron, and is less significant as it only accounts for 1.11% (Schmidt and Jochmann, 2012). CSIA is particularly of interest for degradation estimations, as degradation induces a measurable shift in the isotope composition of a compound undergoing degradation compared to the initial isotope composition of the compound. For instance, the steps towards bond breaking require a greater energetic input for bonds bearing heavy isotopes than for those bearing lighter isotopes, yielding relatively slower reaction rates of the heavy isotopes compared to the more abundant light isotopes. As a result, an increasing fraction of the remaining compound will consist of molecules including heavy isotopes in their structure as degradation proceeds (Fig. 1-3). The change in isotopic composition of the compound, called isotope fractionation, depends on the

degradation pathway, the degradation extent, the element, and the compound (Abe et al., 2009a; Chu et al., 2004; Fox et al., 1990). The ratio between the reaction rates of the lighter ${}^l k$ vs. the heavier ${}^h k$ isotope of an element is expressed as the enrichment factor $\varepsilon = 1 - {}^h k / {}^l k$ and can be measured through experiments. The isotope ratio of an element E in a sample, $R({}^h E / {}^l E)_{sample}$, represents the ratio of the amount of heavy isotope ${}^h E$ (for instance, carbon-13, chlorine-37, hydrogen-2) to light isotope ${}^l E$ (carbon-12, chlorine-35, hydrogen-1) of this element. For the sake of comparability, isotopic ratios are reported against international standards (see Table 1-1) and expressed using the delta notation

$$\delta^h E_{sample/std} = \frac{R({}^h E / {}^l E)_{sample}}{R({}^h E / {}^l E)_{std}} - 1$$

where $R({}^h E / {}^l E)_{std}$ is the standard ratio for an element

E .

The relation between the enrichment factor ε , the change in isotope ratio of a specific element E , and the residual fraction f of the substrate is described by the Rayleigh equation,

$$R({}^h E / {}^l E) = R({}^h E / {}^l E)_0 \times f^\varepsilon$$

where $R({}^h E / {}^l E)_0$ is the initial isotope ratio of the compound

allowing the quantification of the extent of transformation. Isotope effects also occur during equilibrium processes such as when CEs are in equilibrium between two phases. Enrichment factors for carbon isotope fractionation (and to a lesser extent, for chlorine) measured during a wide range of CEs degradation conditions offer the opportunity to attribute concentration changes to degradation at field sites (Fig. 1-3). The large carbon isotope fractionation of chlorinated ethenes detected during reductive dechlorination has also been used to quantify their degradation rates at field sites (Bloom et al., 2000; Clark et al., 2016; Palau et al., 2014; Sherwood Lollar et al., 1999). Additionally, the carbon isotope ratio of the daughter compound is initially depleted compared to its parent compound until its complete transformation. The carbon isotope composition of the daughter compound eventually equals the initial parent composition, to the condition the daughter compound does not degrade further (Fig. 1-3).

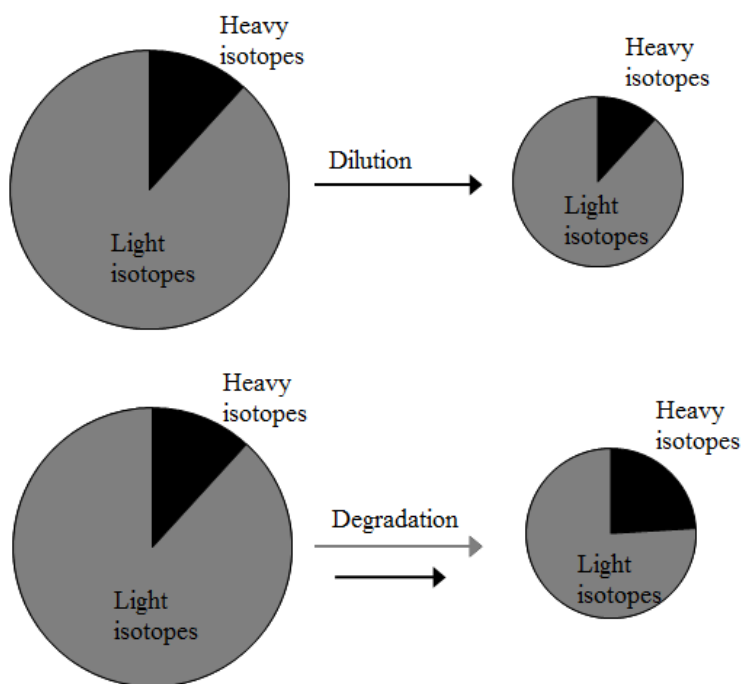


Fig. 1-3 : Illustration of the drive for the change of isotope composition, i.e. the proportion of the heavy (black) to light (grey) isotope. Dilution conserves the isotope composition (top) while degradation generally leads to enrichment in the isotopic composition (bottom).

In addition to the possibility of quantifying degradation, CSIA can also be used to close the mass balance, as the $^{13}\text{C}/^{12}\text{C}$ of all CEs combined plus ethene and ethane (carbon isotope mass balance, CIMB) is in principle constant provided there is no mineralisation (Bloom et al., 2000; Hunkeler et al., 1999). As such, the CIMB will detect whether CEs, ethene, and ethane constitute the only degradation products, in which case the CIMB will be similar to the source value; or that a significant amount was degraded to other carbon products not included in the CIMB such as CO_2 , in which case the CIMB will be enriched in ^{13}C (Fig. 1-4) (Hunkeler et al., 1999). Consequently, provided they do not degrade further, ethene and ethane are included in the CIMB to differentiate VC reductive dechlorination (\rightarrow ethene \rightarrow ethane) from VC oxidation ($\rightarrow \text{CO}_2$). A CIMB that does not include ethene will also show enrichment when VC degrades reductively to ethene (Fig. 1-4).

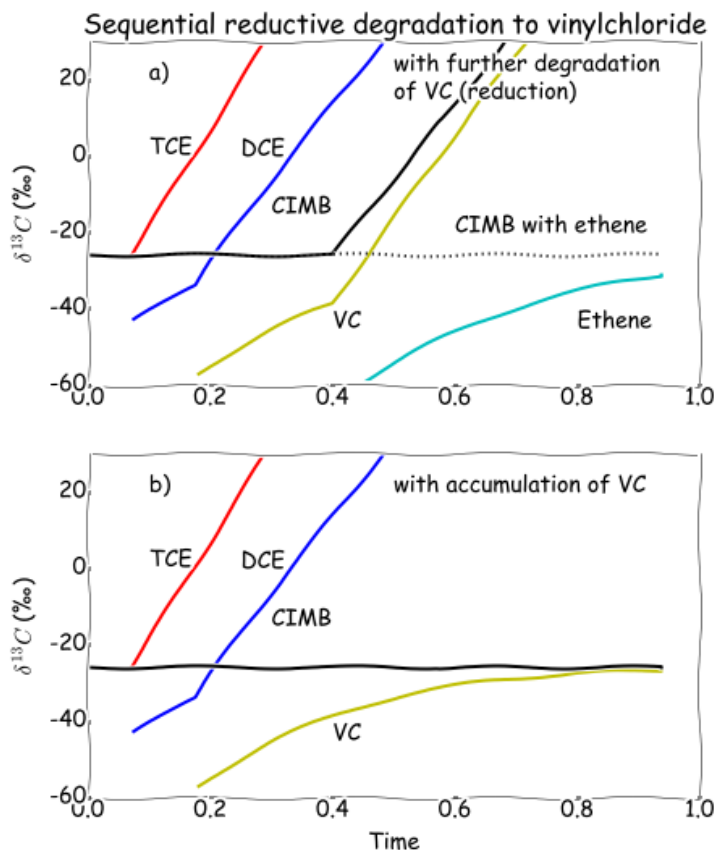


Fig. 1-4 : Hypothetical example of the pattern of the carbon isotope mass balance (CIMB, with and without including ethene) in the presence or absence of degradation beyond VC. In this simulation, DCE degradation started at $t=0.2$ and VC at $t=0.4$ (no unit).

The production of CEs by different manufacturers leads to variability in carbon (C), chlorine (Cl), and hydrogen (H) isotope ratios ($^{13}C/^{12}C$; $^{37}Cl/^{35}Cl$; and $^2H/^1H$, respectively). Both the origin of the raw material and the synthesis processes influence the isotopes ratios. The intrinsic variability of manufactured CEs has been used to discern the source of plumes of pollutants, the isotope composition being employed as a fingerprint of a pollutant source (Kuder and Philp, 2013; Lojkasek-Lima et al., 2012; Shouakar-Stash et al., 2003).

Adding the measurement of Cl and H isotope ratios to the regularly employed C isotope ratio studies looks to be a promising method to distinguish among different degradation pathways as these pathways do not lead to the same extent of isotope fractionation for each element (Abe et al., 2009b; Audí-Miró et al., 2013; van Breukelen et al., 2017). Despite the variability of isotope enrichment associated with CEs degradation during CEs reductive dechlorination (Badin et al., 2014; Cichocka et al., 2008; Jennings et al., 2009; Lihl et al.,

2019; Renpenning et al., 2014) or oxidation (Gafni et al., 2018; Jennings et al., 2009), CSIA has a strong potential for both source apportionment and degradation (Lutz et al., 2013).

Table 1-1 : Stable isotopes of the elements composing chlorinated ethenes: abundance, international standard, and international standard isotope ratio. The isotope ratio of one element is reported against the related international standard to allow inter-laboratories comparisons.

Element	Natural abundance of stable isotopes: Heavy : Light	International standard	International standard isotope ratio
Carbon $^{13}\text{C} : ^{12}\text{C}$	1.11 % : 98.89 %	Vienna Pee Dee Belemite (VPDB)	0.0111802
Chlorine $^{37}\text{Cl} : ^{35}\text{Cl}$	24.23 % : 75.77 %	Standard Mean Ocean Chlorine (SMOC)	0.319788
Hydrogen $^2\text{H} : ^1\text{H}$	0.015 % : 99.985 %	Vienna Standard Ocean Water (VSMOW)	$1.575 \cdot 10^{-4}$

In previous studies, CSIA has successfully facilitated refining of CSMs (Damgaard et al., 2013a; Hunkeler et al., 2011a; Pooley et al., 2009). The values of Carbon CSIA data and to lesser extent of Chlorine and Hydrogen CSIA data were employed for delineating both the source zone and the pollution plume (Audí-Miró et al., 2015; Kaown et al., 2014; Nijenhuis et al., 2013; Palau et al., 2014; Smith and Wang, 2015). The isotopic shifts of C and Cl CSIA data have provided supplementary information for the estimation of degradation extent or occurrence of specific degradation pathways (Aeppli et al., 2010; Amaral et al., 2011; Badin et al., 2016; Clark et al., 2016; Courbet et al., 2011; Hamonts et al., 2012; Hunkeler et al., 2011a, 1999; Puigserver et al., 2013). Dual element CSIA has also performed well in the study of combined degradation and source assessment of chlorinated ethenes and other organic compounds (Kaown et al., 2016; Lojkasek-Lima et al., 2012; Lutz and van Breukelen, 2014a, 2014b; Palau et al., 2014). Nonetheless, field data of multiple-element CSIA remain extremely scarce (Audí-Miró et al., 2015; Filippini et al., 2018), and isotope data of daughter products remain challenging to interpret as their isotope ratios are influenced by both production and degradation (Fig. 1-4) (Clark et al., 2016; Kaown et al., 2014). The development and testing of tools to improve the understanding of such multi-element and multi-compound CSIA datasets is therefore required as elaborated further in Section 1.1.4.

1.1.3 Impact of subsurface heterogeneity on CSIA patterns

Many field sites at which CSIA data were studied displayed complex spatial pollutant concentration and CSIA patterns in relation to the heterogeneous lithology (Clark et al., 2016; Kaown et al., 2016). As presented in Section 1.1.1, less permeable layers can act as long-term slow release reservoirs for such contaminants (Liu and Ball, 2002; Seyedabbasi

et al., 2012). Once concentrations in the aquifer decrease following remediation actions or natural attenuation the concentration gradient is reversed, and the pollutants are released from the silt or clay layers to more permeable aquifer, a process known as back-diffusion. Back-diffusion can maintain CEs concentrations above maximum concentration limits (MCLs) for decades after source removal from the high permeability zone (Chapman and Parker, 2005; Johnson and Pankow, 1992; Rivett et al., 2014; Seyedabbasi et al., 2012; Yang et al., 2015). In addition to back-diffusion, physical and chemical heterogeneities of aquifers have a direct impact on the reactive transport of pollutants.

Physical heterogeneities in aquifers, for instance interbedded clay layers, induce preferential flow and therefore mixing of reactants (Janot et al., 2015; Rivett et al., 2014). Transition zones between aquifer layers with preferential water flow and clay layers or bedrock with limited to no water flow (aquitards) can prove favourable for degradation of CEs (Puigserver et al., 2016). Such geochemical heterogeneity induces zones with abundant or limited occurrence of reactive components. It is likely that high permeability zones, where oxygen can be transported faster than it is consumed, will be more oxic, while zones of low permeability will be more reduced. Recent detailed studies of shallow subsurface sediments in the Netherlands show that clays present a generally higher potential reactivity than sands, because of the notably higher contents of reactive iron, pyrite, and organic matter compared with sands (Griffioen et al., 2016, 2012). This higher potential reactivity can promote both biotic (higher organic matter content) and abiotic degradation (higher Fe-S mineral content) of chlorinated ethenes. Natural attenuation through biotic or abiotic reductive dechlorination in the less-conductive layers may mitigate 'back-diffusion' concentrations and durations (Carey et al., 2015; Damgaard et al., 2013a; Sale et al., 2008; Schaefer et al., 2013; Wanner et al., 2018a, 2018b; West and Kueper, 2010). Less permeable zones and aquitards therefore play a key role in the spatial distribution of CEs and influence CEs fate in the subsurface.

High permeability zones are preferentially sampled when monitoring aquifer pollution, both because well screens are usually intentionally not set in low permeability zones and because of preferential flow from the more permeable zones to the well during sampling. MNA would benefit from tools able to detect and quantify the degradation potential of the low-permeability layers. However, the study of degradation in less-conductive layers requires sediment core samples, of which the cost is usually prohibitive in regular site assessment studies (Chapman and Parker, 2005; Filippini et al., 2016; Parker et al., 2004). CSIA of CEs, which is increasingly employed for MNA at field sites, could potentially help degradation assessment in the less-conductive layers and aquitards as monitored from the aquifer. Recently, Wanner et al. (2018b) demonstrated with a modelling study that TCE to cis-DCE degradation in shallow bioactive zones of aquitards can cause unique CSIA patterns in the above lying aquifers.

One potential complication in the use of CSIA is, however, that several non-destructive processes can also lead to isotope fractionation as shown in small-scale lab studies and aquifer-scale model simulations. Those processes include highly relevant processes in less-permeable layers, i.e., sorption (Höhener and Atteia, 2010; Kopinke et al., 2005; Qiu et al., 2013; van Breukelen and Prommer, 2008; Wanner et al., 2017) and diffusion (Jin et al., 2014; LaBolle et al., 2008; Rolle et al., 2010; Wanner and Hunkeler, 2015; Xu et al., 2017). Sorption-induced isotope fractionation for instance could lead to significant isotopic enrichment (i.e., accumulation of the heavy isotope) in the aquitard with depth (Wanner et al., 2017). While the effects are generally moderate for carbon isotope ratios compared to the enrichment resulting from reductive dechlorination, those physical processes can lead to significant isotope fractionation and need consideration in CSIA interpretation (Eckert et al., 2013; Hunkeler et al., 2004; Kuder et al., 2009; LaBolle et al., 2008; Smith and Wang, 2015; van Breukelen and Prommer, 2008; van Breukelen and Rolle, 2012; Wanner et al., 2016; Xu et al., 2017). Carbon isotope enrichment resulting from diffusion is likely attenuated during back-diffusion from a non-reactive aquitard to the aquifer (Xu et al., 2017). On the contrary, processes leading to stronger isotope fractionation in the aquitard such as degradation could potentially lead to detectable enrichment also when sampling is occurring only in the aquifer (Wanner et al., 2018b; Xu et al., 2017). Moreover, diffusion of daughter products from the less-permeable layers to the aquifer was shown to contribute to long term tailing of the plume (i.e. pollution remaining long after clean-up of the pollution source) (Rasa et al., 2011; Wanner et al., 2018b). It is therefore relevant to investigate whether CSIA data from the aquifer can be used for degradation assessment and degradation pathway identification when degradation occurs in less permeable zones or in an aquitard.

1.1.4 Modelling CSIA data: Opportunities and Challenges

Well-characterized aquifers are rare, and aquifers are often considered as ‘black boxes’ in which the degradation and transport patterns of CEs must be determined based on spatially and temporally sparse data sets. The various attenuation processes, destructive or not destructive, impact CEs concentration and potentially their isotope ratios (Atteia et al., 2008; Clement et al., 2000; Höhener et al., 2015; Höyng et al., 2015; van Breukelen et al., 2005). In practice, CSIA is employed as an additional tool for degradation assessment where concentration patterns are complex to interpret. This complexity can arise from the subsurface lithology, the presence of multiple sources, or the occurrence of multiple degradation pathways. A challenge, however, is that CSIA data also reflects this subsurface complexity.

Modeling of transport and degradation of organic compounds in aquifers is often used in complementarity with field data analysis. Combining isotope fractionation with analytical or numerical reactive transport models (IF-RTM) has shown to be highly beneficial for

degradation assessments at field sites, as it unravelled the complex isotope patterns resulting from combined production and degradation during reductive dechlorination (Höhener, 2016; Höhener et al., 2015; Höyng et al., 2015; Hunkeler et al., 2009, 1999; van Breukelen et al., 2005). However, the available modelling tools have mostly been beneficial at sites where degradation was homogeneous. Modelling tools and their application need to be extended in order to facilitate the interpretation of CSIA data at complex field sites. For example, recent reactive transport models have included sorption effects (Höhener, 2016; van Breukelen and Prommer, 2008) or heterogeneous degradation rate constants (Höhener et al., 2015). Similarly, multiple element isotope data have increasingly been modelled to predict the isotope composition of metabolites from biotic reductive dechlorination (Cretnik et al., 2014; Hunkeler et al., 1999; Kuder and Philp, 2013; Sherwood Lollar et al., 2001; van Breukelen et al., 2017).

Degradation assessment becomes increasingly intricate when sequential or parallel degradation occurs, as formation and degradation simultaneously impact the isotope ratios of the metabolites. The complexity of the modeling task often limits simulations to a single flow line with 1-D or 2-D simulations, resulting in the modeling of CSIA data from a limited number of wells (Atteia et al., 2008; D’Affonseca et al., 2011; Höhener, 2016; Höhener et al., 2015; Hunkeler et al., 1999; Pooley et al., 2009). A previous study bypassed limitations concerning aquifer complexity by employing a simpler modelling approach which does not include aquifer transport but only degradative pathways as in a batch reactor (van Breukelen et al., 2005). However, batch modeling has not been applied to the study of combined reductive dechlorination and oxidation of CEs or to multiple-element CSIA data. IF-RTMs exploiting all available data can assist to evaluate the requirements for improving the performance of IF-RTM under complex subsurface settings.

Another application of IF-RTM is the production of synthetic data sets for advising practitioners on the best sampling methods, monitoring networks, and rules for data interpretation (Höyng et al., 2015; Xu et al., 2017). For example, the recent inclusion of isotope fractionation induced by non-degradative processes in aquifers allows assessing their influence on measured isotope ratios and improve the interpretation of CSIA data from field sites (Eckert et al., 2013; Höhener et al., 2017; Rolle et al., 2010; van Breukelen et al., 2005; van Breukelen and Prommer, 2008; Wanner et al., 2018a, 2018b, 2017, 2016). The influence of diffusion, sorption, and/or degradation in low permeability zones or aquitards on the isotope signatures of CEs has been explored in a limited number of studies (Wanner et al., 2018b; Xu et al., 2017). Moreover, the modeling of Cl isotope fractionation has been relatively limited to date (Cretnik et al., 2014; Höhener, 2016; Kuder et al., 2016), and tools for degradation assessment in presence of multiple degradation pathways are rare (Aeppli et al., 2010).

1.2 Thesis objectives

This thesis aims to advance the understanding, the potential, and the limitations of CSIA studies in aquifers polluted with chlorinated ethenes in the presence of multiple degradation pathways and heterogeneous lithology. To this end, the interpretation of real field data is combined with modeling experiments carefully designed to reach the following objectives:

- i.** To illustrate the potential of multi-element C, Cl, H CSIA for refining and extending conceptual site models using as example a site with a heterogeneous lithology, multiple plumes, and multiple degradation pathways.
- ii.** To develop a Carbon and Chlorine CSIA batch model for reductive and oxidative degradation of CEs and test the applicability of the model for evaluating degradation hypotheses using the aforementioned site data.
- iii.** To perform modelling experiments on how the heterogeneity of aquifer systems can influence CSIA data and what the consequences are for interpretation. Specifically, further insight is needed concerning:
 - a.** The potential of aquifer CSIA data detecting degradation in underlying aquitards.
 - b.** The performance of dual C-Cl CSIA in assessing degradation in heterogeneous aquifers where oxidative transformation dominates in the high-permeability parts but reductive dechlorination dominates in the low-permeability parts.
 - c.** How sampling strategies (well location and screen length) affect CSIA-based degradation assessment.

1.3 Thesis outline

The thesis is structured as follows:

- Chapter 2 describes C, Cl, and H CSIA data of chlorinated ethenes at the Hill Air Force Base, Utah, where multiple plumes flow in a heterogeneous multiple sandy aquifer system containing interbedded clay layers and showing mixed (oxic/anoxic) redox conditions. Several methods for source apportionment and detection of degradation and physical attenuation pathways are presented with their applications to field CSIA data. Results are compared to the prior conceptual site model.
- Chapter 3 develops and applies C and Cl CSIA batch modeling to thoroughly exploit the available CSIA data presented in Chapter 2, for assessing the occurrence of degradation of CEs via reductive and oxidative pathways. This chapter illustrates how modeling improves degradation assessment and further

discusses the potential and limitations of employing batch modeling to assess degradation pathways of CEs.

- Chapter 4 illustrates through reactive transport modelling to what extent spatial and temporal carbon CSIA patterns in aquifers can indicate reductive degradation of CEs in aquitards despite the impacts of non-destructive processes on both concentration and isotope ratios. This is done using simulations where a TCE DNAPL settles on top of a reactive aquitard before being removed. This scenario was inspired by the field site studied in Chapters 2 and 3 where alternations of sand and clay layers occurred. The simulations include a sensitivity analysis and support the discussion about the potential for detecting and quantifying TCE reductive dechlorination in the aquitard based on CSIA data sampled in the aquifer. However, the simulation results did not agree with interpretation of the field data as further discussed in the synthesis of this thesis.
- Chapter 5 presents reactive transport model simulations of the hypothetical situation where two degradation processes are heterogeneously distributed in an aquifer. This concept was inspired by the suspected relation between the heterogeneity in lithology and the local degradation rate constant as described in Chapter 2. For these simulations, degradation rate constants were assumed to be correlated with the hydraulic conductivity: positively for oxidative transformation and negatively for chemical reduction of CEs. This chapter illustrates how spatially heterogeneous CSIA patterns evolve from physical-chemical heterogeneous conditions, in agreement with the results of Chapter 2. The simulations are discussed in the context of the capability of dual C-Cl CSIA for detecting the occurrence of both degradation pathways and calculating overall degradation under these conditions. The effect of groundwater sample collection (preferential pumping from the more permeable zones) on degradation assessment is also discussed.
- Finally, a summary of the key findings and recommendations for practitioners and further research is presented in Chapter 6.

This page was intentionally left blank

This page was intentionally left blank

Chapter 2

Verifying a conceptual site model with triple element CSIA: assessment of biodegradation and physical attenuation of chlorinated ethenes

Abstract

Triple element (carbon (C), chlorine (Cl), and hydrogen (H)) compound-specific stable isotope analysis (CSIA) was employed for source apportionment, degradation assessment, and physical attenuation characterization of chlorinated ethenes plumes for refinement of the conceptual site model (CSM) of the Operable Unit 10 of the Hill Air Force Base, Utah. The plumes spread through a heterogeneous multiple aquifer system containing interbedded clay and sand layers and showing mixed (oxic/anoxic) redox conditions. Based on C and Cl isotope enrichment of tetrachloroethene (PCE) and trichloroethene (TCE), the assumptions about spatial distribution of CEs reductive dechlorination in the prior CSM were confirmed. Limited cis- and trans-dichloroethene (cis-DCE and trans-DCE) C isotope enrichment confirmed that DCEs reductive dechlorination to VC was incomplete. TCE and PCE triple element CSIA is consistent with the prior hypothesis that TCE plumes originated from the same source, and that both TCE and PCE plumes barely mixed. H CSIA was notably of use for identifying a potential small TCE spill and rejecting large ethene concentrations as a result of TCE reductive dechlorination. H isotope enrichment of TCE contrasts with a prior microcosm experiment in which H isotope ratio decreased, possibly indicating two different degradation mechanisms. Analysis of DCEs C-Cl-H CSIA data supports that the variations of the trans-DCE to cis-DCE concentration ratio relate to the varying expression of at least two TCE pathways. CSIA pointed out that potential aerobic cometabolism of TCE and PCE, suggested in the prior CSM, either barely occurred in both the shallow and the deep aerobic zones, or occurred through processes leading to limited isotope enrichment, such as TCE degradation by methane-oxidizing microorganisms. C CSIA changes between two sampling events contradicted that TCE concentration changes over time necessary indicative of TCE degradation as suggested in the prior CSM. Simultaneously, significant enrichment of the carbon isotope mass balance (CIMB) simultaneous to cis-DCE C-Cl isotope slope decrease attested the presence of oxidative pathways degrading DCE and/or VC, but could not be conclusive on the presence of an oxidative degradation pathway for TCE.

In the absence of C isotope ratio enrichment, the overall variability of the dual C-Cl CSIA slope of TCE throughout both aquifers is assumed to point mostly to the faster diffusion of

light isotopologues to low-permeability layers, leading to noticeable chlorine isotope enrichment in the fraction remaining in the aquifer. The shallow PCE plume, above the TCE plume and away from the aquitard, does not present such variability. Interestingly, the depleted CIMB in the upgradient area of one of the plumes could also support the suggestion developed in the prior CSM that reductive dechlorination occurred mostly in the low-permeability layers (clay and silt layers). Diffusion of the daughter products from the low-permeability layers following the concentration gradient would lead to the detection of an excess of depleted daughter product in the nearby sand layers, depleting the CIMB. Some depleted CIMB in the downgradient area of the same plume might instead reflect the chromatographic separation of CEs induced by different degrees of sorption during transport.

This study illustrates the potential of CSIA to refine and extend CSMs, with the example of successful detection of oxidative transformation of lower chlorinated ethenes. The study also observes and interprets unusual impacts of physical processes which were suspected in the prior CSM.

2.1 Introduction

Chloroethenes (CEs) are toxic and potentially carcinogenic groundwater pollutants (Chiu et al., 2013; IARC, 2008; Lash et al., 2014). CEs, which are employed as degreasing agents in multiple industries, are now ubiquitous in the environment due to spills or inadequate waste disposal. Since CEs can be naturally degraded under specific conditions, the monitoring of natural attenuation processes (or monitored natural attenuation (MNA)) represents an alternative to otherwise invasive and energy intensive technologies for contaminated site remediation (Bradley, 2003; Mulligan and Yong, 2004). MNA success relies on a sound assessment of the performance of degradation, for example, through the development of a conceptual site model (CSM) (Wiedemeier et al., 1998). The MNA potential is evaluated in the CSM through the delineation of the source zone(s), the determination of key transformation processes, as well as the assessment of attenuation through non-destructive physical processes, such as volatilization, sorption, or dilution. The lines of evidence for MNA potential rely on the geochemical conditions, the hydrogeological setting, and the spatial distribution and concentration trends of the contaminants (Wiedemeier et al., 1998). Microcosm degradation experiments and bacterial markers are also useful as complementary information on the aquifer potential for degradation (Abe et al., 2009a; Badin et al., 2016; Courbet et al., 2011; Lee et al., 2015; Nijenhuis et al., 2013; Wiedemeier et al., 1998).

MNA of CEs is complex due to the number of processes influencing CEs concentrations. For instance, while sequential reductive dechlorination (in the order perchloroethylene (PCE), trichloroethylene (TCE), dichloroethylene (DCE), vinylchloride (VC), and ethene; Fig. 2-2) (Bradley, 2000) leads to detectable daughter products for each step, other degradative processes lead to the breakdown of the double C=C bond and form potentially less distinctive metabolites. Those latter processes include: reduction of ethene to ethane under anaerobic conditions (Mundle et al., 2012), VC and DCE mineralization to CH₄ and CO₂ under iron-reducing and methanogenic conditions (Bradley and Chapelle, 1997, 1996), and direct aerobic metabolism of lesser chlorinated compounds (VC, DCE) (Bradley and Chapelle, 2011; Coleman et al., 2002a, 2002b; Gossett, 2010). Furthermore, TCE, DCE, and VC can be cometabolised aerobically to CO₂ in the presence of other carbon sources such as methane or toluene (Fox et al., 1990; Fries et al., 1997). As reaction products of these latter pathways are not distinctive and their production is usually low with respect to relatively high background concentrations, those pathways are difficult to detect, which may result in the underestimation of the overall CEs degradation potential. Additionally, chemical reduction is potentially overlooked (He et al., 2009), as CEs resulting degradation products (such as acetylene, propane, and glycolate) are rarely analysed (Darlington et al., 2013, 2008; Dong et al., 2011; Han et al., 2012; Jeong and Kim, 2007; Lee and Batchelor, 2002; Liang et al., 2009). Lack of tools to detect these processes might hinder the use of

MNA and lead to implement unnecessary actions for remediation. Compound-specific stable isotope analysis (CSIA) is a promising tool to better assess the lines of evidence for MNA of CEs as explained below (US EPA 2008).

Source and degradation assessment, both necessary for the CSM, benefit from CSIA. For instance, CEs' carbon (C), chlorine (Cl), and hydrogen (H) isotope ratios ($^{13}\text{C}/^{12}\text{C}$; $^{37}\text{Cl}/^{35}\text{Cl}$; and $^2\text{H}/^1\text{H}$, respectively) depend on CEs manufacturing, and therefore fingerprint CEs' spills (Kuder and Philp, 2013; Shouakar-Stash et al., 2003). Hydrogen CSIA (H-CSIA) can distinguish industrial TCE (strongly enriched in ^2H) from TCE produced by PCE dechlorination (strongly depleted in ^2H) (Kuder and Philp, 2013). Furthermore, as isotope ratios are sensitive to CEs transformations, the change in isotope ratio (or isotope fractionation) may inform on the key degradative processes. Isotopic fractionation results from the usually relatively slower reaction rates of the heavy isotopes compared to the more abundant light isotopes. Carbon isotope fractionation of different intensity was observed during biotic reductive dechlorination (Badin et al., 2014; Bloom et al., 2000; Buchner et al., 2015; Hunkeler et al., 1999; Numata et al., 2002; Slater et al., 2001), aerobic transformation (Abe et al., 2009b; Barth et al., 2002; Clingenpeel et al., 2012; Gafni et al., 2018; Schmidt et al., 2014), and chemical reduction (Audí-Miró et al., 2013; Dayan et al., 1999; Liang et al., 2009; Liang and Dong, 2007; Slater et al., 2002). The large carbon isotope fractionation detected during reductive dechlorination has benefitted the quantification of CEs degradation (Bloom et al., 2000; Clark et al., 2016; Palau et al., 2014; Sherwood Lollar et al., 1999). Moreover, mass balance closure is eased by CSIA, as the $^{13}\text{C}/^{12}\text{C}$ of the source compound and the totality of its carbon-containing metabolites (carbon isotope mass balance, CIMB) is in principle constant (Bloom et al., 2000; Hunkeler et al., 1999). Finally, dual chlorine-carbon CSIA (Cl/C CSIA) looks promising for pathway distinction as the relative extent of C and Cl isotope fractionation depends on the reaction mechanism. For instance, DCE Cl/C CSIA slopes take different values for DCE aerobic cometabolism, biotic reductive dechlorination, and chemical reduction on zero-valent iron (Abe et al., 2009b; Audí-Miró et al., 2013). Unfortunately, TCE Cl/C CSIA slopes overlap in the middle range (about 0.2-0.3) for chemical reduction on zero-valent iron and biotic dechlorination (Audí-Miró et al., 2013; Buchner et al., 2015; Cretnik et al., 2014; Kuder et al., 2013). TCE oxidative degradation might provide a distinctively larger Cl/C CSIA slope of about 0.6 when degraded by a methane monooxygenase enzyme (sMMO or pMMO) (Abe et al., 2009b; Barth et al., 2002; Gafni et al., 2018), but also a positive slope near to 0 in presence of toluene dioxygenase (Gafni et al., 2018). Despite limitations (Badin et al., 2014; Cichocka et al., 2008; Jennings et al., 2009; Renpenning et al., 2014), CSIA has a strong potential for both source apportionment and degradation.

Although field conditions differ from the controlled conditions of the laboratory, CSIA has been successful for refining CSMs (Damgaard et al., 2013a; Hunkeler et al., 2011a; Pooley et al., 2009). For instance, CIMB could reconstruct the original source signatures of plumes

and therefore was employed for plumes delineation (Nijenhuis et al., 2013; Palau et al., 2014). More recently, H-CSIA was used specifically for discriminating between spilled industrial TCE and TCE as metabolite from PCE degradation with (Audí-Miró et al., 2015) and without (Smith and Wang, 2015) requiring additional C-Cl CSIA data. Multiple CE plumes in sandy aquifers were delineated using the information provided by C-Cl CSIA (Kaown et al., 2014). C-Cl CSIA performed similarly well for detecting mixing and degradation of different sources where source assessment was crucial for proper remediation (Kaown et al., 2016; Lojkasek-Lima et al., 2012; Palau et al., 2014), stressing the potential of dual isotope models as developed in (Lutz and van Breukelen, 2014a, 2014b) for assessing the extent of each processes. The study of C-Cl CSIA slopes helped identifying the key degradation pathway among several possible ones (Badin et al., 2016; Clark et al., 2016; Hunkeler et al., 2011a). Alternatively, the detection of several (two) C-Cl isotope slopes pointed out that degradation was performed through various pathways which could not be established with concentration data (Wiegert et al., 2013, 2012). C CSIA by itself acted as a supplementary line of evidence of the seasonal variations of reductive dechlorination and dilution at complex river-aquifer interfaces with mixed redox conditions (Courbet et al., 2011; Hamonts et al., 2012; Puigserver et al., 2013; Wiegert et al., 2012). Finally, CIMB as additional control of mass balance closure had beneficial implications for the monitoring of the last steps of CEs dechlorination (DCE and VC dechlorination), which often are limiting CEs complete dechlorination (Aeppli et al., 2010; Badin et al., 2016; Courbet et al., 2011; Hunkeler et al., 1999), and for the detection of daughter products' (DCE, VC) oxidation (Amaral et al., 2011). Due to its versatility, CIMB was recently successfully employed as model constraint for degradation assessment (Höhener et al., 2015). As a conclusion, CSIA potentially provides a clearer picture of degradative attenuation through improving both degradation and source assessment (US EPA 2008).

So, notwithstanding successful CSIA applications, CSIA interpretation is particularly complex when several processes simultaneously alter isotope and concentration patterns and when multiple CEs sources mix. CSIA performances might be limited for detecting processes leading to little isotope fractionation, such as some oxidative degradation pathways (Chu et al., 2004). Additionally, downgradient CIMB depletion is predicted in the presence of strong sorption due to CEs separation based on their different organic carbon – water partition coefficients (van Breukelen et al., 2005). Hence, CSIA may fail when applied to sites of increasing complexity and heterogeneity, where multiple degradation pathways, multiple sources, complex flow systems, or intense physical attenuation combine, therefore leaving unresolved patterns (Clark et al., 2016; Kaown et al., 2014). In addition, isotope fractionation linked to sorption, volatilization, and diffusion was detected in laboratory experiments (Jin and Rolle, 2014; Kopinke et al., 2005; Qiu et al., 2013; Wanner and Hunkeler, 2015), predicted based on computer models (Eckert et al., 2012; LaBolle et al., 2008; van Breukelen and Prommer, 2008; van Breukelen and Rolle, 2012), and

observed at field sites (Hunkeler et al., 2011b, 2004; Kuder et al., 2009; Smith and Wang, 2015; Wanner et al., 2016). Hence, under specific conditions and time windows, the additional isotope fractionation resulting from the impact of physical processes might affect CSIA-based degradation assessment. On the one hand, CSIA interpretation must be handled with care where these processes strongly contribute to isotope fractionation. On the other hand, CSIA alterations resulting from physical processes may also have the potential to support hypotheses of physical attenuation as part of the CSM.

The present study illustrates the benefits of C-Cl-H CSIA for refining the CSM of a site which had already been intensively sampled and studied, the Operable Unit 10 (OU10) at the Hill Air Force Base (Utah). The site was chosen for its complexity as it exhibits several CEs plumes and mixed redox conditions. An advantage of the study site is its comprehensive characterization by a number of conventional sampling campaigns, which allowed the development of a detailed CSM (CH2MHILL, 2009). At the OU10, two aquifers are divided by an aquitard. PCE and TCE are the main contaminants of the mostly aerobic shallow aquifer, whereas TCE and cis-DCE are of concern in the mostly anaerobic deep aquifer. The prior CSM has led to many hypotheses concerning potential degradation pathways of CEs at the site, including cometabolism of CEs in the aerobic zone, and partial reductive dechlorination of TCE selectively in the organic-rich low-permeability area of the anaerobic zone. Physical attenuation of the shallow plumes is potentially strong as water table fluctuations could trigger volatilizations of CEs, while the presence of organic matter in the deep aquifer impacts CEs transport. Furthermore, diffusion into and back-diffusion from clay lenses and the aquitard are suspected based on CEs concentrations patterns. Therefore, physical attenuation might be detectable from the isotope fractionation patterns. Consequently, our key objectives were (i) to evaluate the prevalent degradation pathways and physical attenuation mechanisms by means of CSIA, and (ii) to evaluate how our CSIA-based assessment compared to the prior concentration-based CSM.

2.2 Field site description

The field site description presented in this section summarizes the CSM of this site (CH2MHILL, 2009) at the onset of the current CSIA study.

2.2.1 Site hydrogeology

The subsurface consists of two aquifers separated by an aquitard (Fig. 2-1, Fig. 2-4, and Fig. 2-12). The shallow aquifer (depth 0 to 15 - 36 m b.g.s.) is unconfined, perched, and composed of fine to medium coarse sand and clay lenses. The deep aquifer (36 m b.g.s. and lower) is heterogeneous, with thin sand layers interbedded with clay layers near the recharge area in the East, and thicker sand packages in the West. At the bottom of the deep aquifer, a thick aquitard prevents further downwards migration of pollutants. The shallow

and deep aquifers are separated by an aquitard of varying thickness (< 36 m) composed of silt and clay with interbedded sand (details of the lithology are presented Fig. S2-5, S2-6, S2-7, and S2-8).

Groundwater velocities were calculated from hydraulic gradients and hydraulic conductivities obtained with slug and pump tests, or (tritium-helium) groundwater ages (CH2MHill, 2011). Average groundwater flow velocity in the shallow aquifer is of about $0.15 \text{ m}\cdot\text{d}^{-1}$ (Table A.1). In the deep aquifer, the groundwater velocity is overall higher and decreases from the most eastern part ($0.58 \text{ m}\cdot\text{d}^{-1}$) towards the west ($0.18 \text{ m}\cdot\text{d}^{-1}$) (Table S2-1 and Fig. S2-1). Groundwater flow directions are indicated with blue arrows in Fig. 2-1.

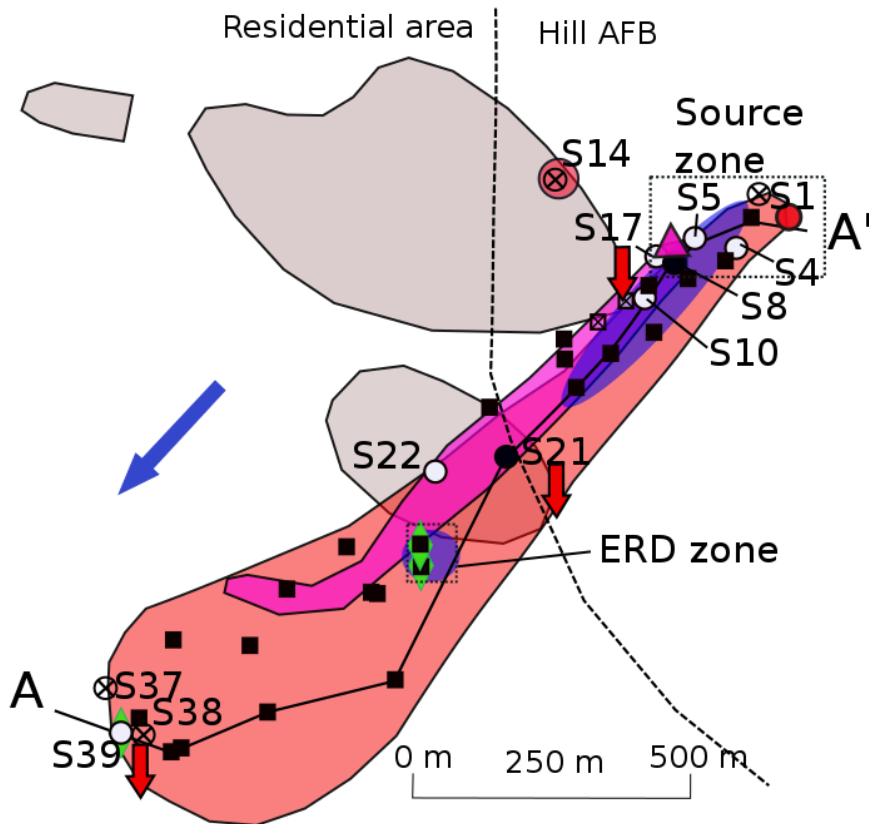
2.2.2 Source zones and contaminant plumes

The chlorinated solvents were released during the period 1940-1959. Site monitoring began in 1995 with semi-annual sampling since 2002. In total, approximately 300 sampling points were installed to monitor the CEs plumes. Whereas PCE was probably incidentally spilled at a parking lot, TCE originated from the continuous leakage of an oil/water separator. TCE probably initially sank as a DNAPL because it occurs near the spill location already at the basal portion of the shallow aquifer (Fig. 2-12). The volume of spilled PCE was estimated to be small (about 4 L (CH2MHILL, 2009)). TCE which represents a larger spilled volume, is mostly not related to the PCE spill, and originates from a unique source. The TCE source zone is likely to have been exhausted, as DNAPL was not detected during the period of the site investigation (1995-2013), and since CEs concentrations are low in the vicinity of the source zone compared to downgradient. Additionally, 3 m^3 of soil were excavated at the TCE spill zone in 2003.

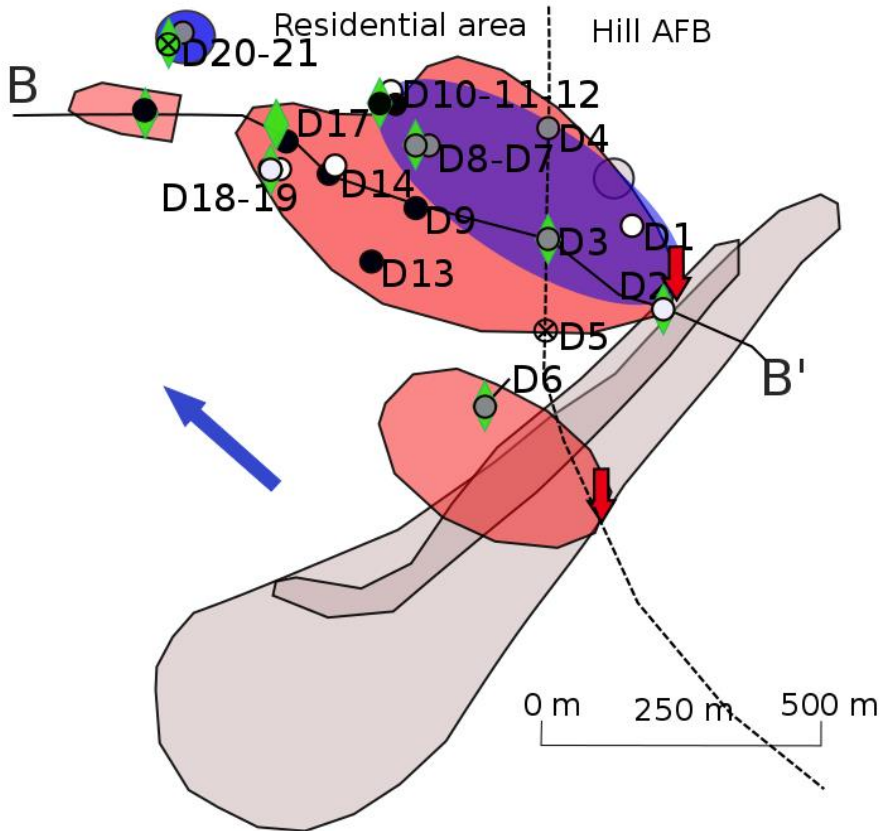
In the shallow aquifer, a relatively thin (6 - 12 m) and short (length of 950 m) PCE plume only partially mixes (only near well S23) with a TCE plume (later referred to as “shallow TCE plume”). The PCE plume, (maximum historical concentration of $0.82 \text{ }\mu\text{mol}\cdot\text{L}^{-1}$ – $136 \text{ }\mu\text{g}\cdot\text{L}^{-1}$) is mostly located a few meters below the water table between 2.5 and 7.5 m b.g.s. The shallow TCE plume (width of 90 - 425 m; thickness of 3 to 12 m, max. historical concentration of $1.07 \text{ }\mu\text{mol}\cdot\text{L}^{-1}$ – $140 \text{ }\mu\text{g}\cdot\text{L}^{-1}$) has travelled approximately 1500 m in southwestern direction, including 1000 m outside of the boundaries of the air force base and underneath a residential area. The aquitard, above which the shallow TCE plume is located, occurs at high depth beneath the source area (about 33 m b.g.s.), then is shallow for about 500 m (about 10 m to 15 m b.g.s.), and then is eroded in the western part (Fig. 2-12); consequently, the shallow TCE plume is detected between 7 and 30 m b.g.s. before dipping in the deep aquifer. In some areas, the aquitard is entirely eroded and leakage towards the lower aquifer occurs. Various lines of evidence (tracers, hydrochemistry, groundwater ages, and hydraulic gradients) show that the shallow TCE plume is leaking through the aquitard at three locations (red arrows Fig. 2-1, Fig. 2-12). The two main leakages form the two

lobes of the deep TCE plume (called northern and southern lobes). The deep TCE plumes flow towards the northwest; they are found between 53 m and 88 m b.g.s., and are up to 40 m thick. The northern lobe is max. 425 m wide and 800 m long and a maximum historical TCE concentration of $5.71 \mu\text{mol}\cdot\text{L}^{-1}$ ($750 \mu\text{g}\cdot\text{L}^{-1}$) was detected. The southern lobe is 245 m wide and 425 m long (max. historical concentration of $1.27 \mu\text{mol}\cdot\text{L}^{-1}$ – $167 \mu\text{g}\cdot\text{L}^{-1}$).

a) Shallow plume



b) Deep plume



Legend

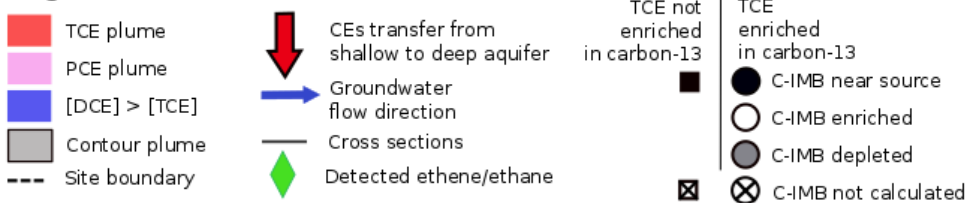


Fig. 2-1 : Map of the Operable Unit (OU) 10 at the Hill Air Force Base (Utah, USA). a) The shallow PCE and TCE shallow plumes flow in SW direction are shown in purple and red, respectively, the underlying deep plumes are in grey. b) The deep TCE plume (red) is flowing in NW direction. The overlying shallow plumes are depicted in grey. The markers represent the wells sampled during 2011, $\delta^{13}\text{C-TCE} < -24\text{‰}$: squares, $\delta^{13}\text{C-TCE} > -24\text{‰}$: circles, fill: $\text{CIMB} \approx \delta^{13}\text{C-TCE}_{\text{source}}$: black, $\text{CIMB} > -24\text{‰}$, white, and CIMB (including uncertainty) $< -26.5\text{‰}$: grey, where CIMB could not be calculated (incomplete CSIA data): a cross. For simplicity, wells at which TCE is not detected are not reported (S12, S24, D16, and D21, at which PCE, DCEs or ethene are detected). The green diamonds indicate wells where either ethene or ethane was detected at least once since 1996. The black dotted line represent the cross-sections A-A' and B-B' illustrated Fig. 2-12. The latest sampling period (2011-2014) employs results from 61 sampling points, S1 to S29 in the shallow aquifer and D1 to D22 in the deep aquifer.

The maximum historical concentrations of cis-DCE and trans-DCE are found in the deep aquifer, reaching $1.15 \mu\text{mol}\cdot\text{L}^{-1}$ ($111 \mu\text{g}\cdot\text{L}^{-1}$) and $1.6 \mu\text{mol}\cdot\text{L}^{-1}$ ($155 \mu\text{g}\cdot\text{L}^{-1}$), respectively (CH2MHILL, 2009). Historically, 1,1-DCE and VC are mostly present in trace amounts. The only potential source of DCEs and VC is their production through reductive dechlorination of TCE or PCE. Both ethene and ethane (investigated in 2007-2008) were found at trace concentrations at eight and seven wells in the deep aquifer, respectively, of which D2, D3, D6, D8, and D22 were sampled in 2011; and at three wells in the shallow aquifer (S23, S24, and S39) (CH2MHill, 2011). Ethene and ethane were not detected in pristine areas of the deep aquifer, and are therefore potential degradation products from CEs (CH2MHILL, 2009). While CEs degradation leads to chloride production, the large chloride concentrations in the shallow aquifer likely stemming from road salt dissolution prevent the use of chloride as a tracer for CEs degradation.

2.2.3 Redox conditions

Redox parameters were thoroughly investigated during summer 2007 (CH2MHILL, 2009). The assessment of the geochemical favourability for reductive dechlorination was supported by a scoring procedure developed by the U.S. EPA (Wiedemeier et al., 1998). The shallow aquifer was classified as overall oxic, while the aquitard and the deep aquifer were classified as mildly reducing (CH2MHILL, 2009). However, redox conditions are variable in both aquifers (Table S2-3). The redox variability of the shallow aquifer (dissolved oxygen (DO) $3.9\pm 2.1 \text{ mg}\cdot\text{L}^{-1}$; nitrate: $11.5\pm 10.0 \text{ mg}\cdot\text{L}^{-1}$; sulphate: $35.9\pm 20.1 \text{ mg}\cdot\text{L}^{-1}$; ferrous iron: $0.1\pm 0.1 \text{ mg}\cdot\text{L}^{-1}$; oxidation-reduction potential (ORP): $162\pm 137 \text{ mV}$) mainly reflects the difference between the upper aerobic part and the more reducing deeper part near the aquitard. The deep aquifer shows lower concentrations of oxidants (DO: $2.0\pm 1.2 \text{ mg}\cdot\text{L}^{-1}$; nitrate: $1.9\pm 6.3 \text{ mg}\cdot\text{L}^{-1}$; sulphate: $25.7\pm 26.5 \text{ mg}\cdot\text{L}^{-1}$) and higher concentrations of reduced species (ferrous iron: $0.9\pm 0.8 \text{ mg}\cdot\text{L}^{-1}$, methane up to $1 \text{ mg}\cdot\text{L}^{-1}$) as reflected in a lower ORP ($-91\pm 118 \text{ mV}$). Dual porosity was brought forward as explanation for the variability in redox conditions in the deep aquifer. The heterogeneous nature of the lithology of the deep aquifer (discontinuous lenses of clay and silt interbedded with sand layers, and presence of interbedded sand, silt, and clay) is favourable to the coexistence of methanogenic conditions in the clay or silt layers, and of more oxic conditions in the sand layers being recharged with aerobic water from the shallow aquifer. This system is analogous to the one described by (McMahon and Chapelle, 1991) where the oxidant sulphate in the anoxic aquifers was reduced by formate and acetate diffusing from the aquitards where they were formed from fermenting organic matter. Note that the relatively long well screens (0.15 to 0.9 m) sample and mix water from along the redox gradients from immobile to mobile zones causing water samples to contain both DO and methane.

2.2.4 Presence and activity of microorganisms

Bacteria were reported to degrade TCE while using another pollutant as growth-substrate, such as MTBE (Xie et al., 2016), toluene, methane, phenol, propene, glucose, ammonia, propane, butane, and benzene (see (Nzila, 2013) for recent overview). At the Hill site, the presence and activity of bacteria capable of TCE cometabolism in the TCE shallow plume were investigated through microcosms experiments, and functional genes and enzyme activity were measured in groundwater samples (results presented in Fig. S2-9). The combined functional genes and enzyme activity tests employed at the site targeted bacteria able of TCE cometabolism with toluene and methane as primary substrates. The combined results suggest that aerobic cometabolic activity may be contributing to TCE attenuation in the shallow aquifer (CH2MHILL, 2009). Additionally, the genes encoding the sMMO enzyme (indicative of methanotrophs) were detected in two of the three tested wells in the deep aquifer. Aerobic cometabolism of TCE and its degradation products is expected to be of potential relevance at the interfaces of low- and high-permeability zones in the deep aquifer where oxygenated water mixes with methane (CH2MHILL, 2009).

Bacteria capable of PCE and TCE reductive dechlorination to cis-DCE (*Desulfuromonas*, and *Dehalobacter*) were detected in the deep aquifer (CH2MHILL, 2009). However, their low counts relatively to methanogens, which compete for the electron donor hydrogen, suggest a limited activity (CH2MHILL, 2009). *Dehalococcoides* (*Dhc.*) bacteria, and the functional genes (*tceA* reductase, *bvcA* reductase, VC reductase) able to completely dechlorinate VC to ethene were below detection limit in the deep plume (4 sampled wells).

2.2.5 Potential for natural attenuation by degradation

The shallow aquifer might host both reductive and oxidative degradation pathway. PCE reductive dechlorination is expected in anaerobic zones of the shallow aquifer. Potential occurrence of PCE aerobic oxidation was not excluded. TCE in the shallow plume might degrade via aerobic cometabolism (Table 2-2). Supplementary to the proven cometabolic enzymes activity (see Section 2.2.4), TCE was estimated to degrade with a half-life to 27 ± 17 y using the Buscheck/Alcantar method between the two wells S28 and S33 (CH2MHILL, 2009). Moreover, TCE cometabolism would explain the decrease of the total dissolved mass of TCE as evaluated based on a Thiessen analysis (CH2MHILL, 2009). In addition to aerobic cometabolism, reductive dechlorination in the shallow TCE plume was reported to occur near the aquitard and at the plume front, where the plume enters the deep aquifer, as cis-DCE is detected.

In the deep aquifer, geochemical conditions likely range from highly anaerobic and reducing in impermeable clay/silt layers, conducive to reductive dechlorination, to aerobic in permeable sand layers, conducive to aerobic cometabolism and oxidative transformation (see Section 2.2.4). Reductive dechlorination within impermeable layers was postulated as the primary mechanism of TCE degradation. Its dechlorination products are supposed to

back-diffuse into the permeable and less reactive sand layers. This agrees with high cis-DCE concentrations at the transition of the shallow to deep aquifer where the heterogeneous lithology presents interbedded clay and silt layers as well as an aquitard. Low DCEs concentration in the sand packs at the front of the deep plume reflects the idea that the rate of reductive dechlorination in the aquifer itself is low. The lack of microorganisms from the *Dhc.* group agrees with the absence of clear reductive dechlorination beyond DCEs. Degradation of TCE and its daughter products is expected to potentially occur through cometabolic oxidation in the permeable layers of the aquifer.

2.2.6 Potential for natural attenuation by physical processes

Additionally to degradative processes, non-destructive attenuation mechanisms of the CEs plumes were expected to be relevant, namely volatilization to the unsaturated zone, sorption, and diffusion into low permeability layers (CH2MHILL, 2009). Volatilization is likely triggered by the groundwater level fluctuations in the shallow aquifer, which follow rain fall trends with a lag of 7 to 21 months (CH2MHILL, 2009). Shallow sampling wells can run dry after strong droughts (CH2MHILL, 2009). Both PCE and TCE were detected in 2008 with soil-gas probes in the unsaturated zone near the source area, but beneath the off-base residential area only PCE was found (CH2MHILL, 2009). PCE at some of these locations could not be clearly related to presence of the PCE plume. The lack of TCE in the soil-gas samples was rationalized by the larger depth of the TCE than of the PCE plume. Likely, any volatilization off-base is due to volatilization from groundwater.

With respect to sorption, it was calculated that organic matter adsorbs between 17 % and 59 % of the total CEs mass (17 %, 33 %, 17%, and 59 % for the shallow TCE, shallow PCE, deep cis-DCE, and deep TCE plumes, respectively). Sorbed fractions were estimated using the respective soil organic matter-water partition coefficient (K_{oc}) of the CEs, the soil bulk density, and the fraction of organic matter (CH2MHILL, 2009). Sorption is more intense in the deep aquifer because of its larger organic carbon content (0.2 %) than the shallow aquifer (sand, 0.03 % - silty sand, 0.07 %) (CH2MHILL, 2009).

With respect to diffusion, the preferential potential reductive dechlorination in low-permeability layers described before entails that strong CEs diffusion in and out of those layers impacts their transport in the aquifer. Since the source has been exhausted at time of investigation (1995-2014), and since concentrations in wells D1, D2, and D5 decline since the start of the deep aquifer investigation (2007) (results not shown; (CH2MHILL, 2009)), the water flowing through the deep aquifer is less polluted than it had been in the past, which can trigger back-diffusion from the low-permeability layers, and leads to prolonged tailing of the plume.

2.3 Methods

2.3.1 Groundwater sampling

Groundwater wells were selected for C-Cl-H CSIA based on contaminant concentrations as observed in 2009. Samples were taken during 2011 and 2014. The 2011 sampling campaign yielded samples from 59 sampling points: 36 in the shallow plume and 23 in the deep plume. During the 2014 sampling campaign, sampling was repeated at 8 shallow wells and 12 deep wells where TCE reductive dechlorination was expected. Samples aliquots of 1 L were collected for CSIA analysis by the base's sampling contractor (AEEC) and shipped on ice to the University of Oklahoma for analysis.

The following techniques were employed (see Supporting information (SI) for further details):

- Low-Flow Sampling (Puls and Barcelona, 1995): during sampling the drop in water level was kept limited and groundwater was led through flow-through cells until electrode measurements stabilized (employed for all shallow wells and two of the deep wells).
- Permeable Diffusion Bags (PDBs): four to nine PDB samplers (0.6 m) were applied at four deep wells (D1, D4, D5, D6) with exceptionally long screens (> 24 m) to enable point sampling.
- Barcad systems: Barcad pumps were buried within a well screen placed in sand layers of 1 meter thickness or less, and separated from each other with bentonite (employed for nine deep wells).

PDBs placed in long wells showed relatively constant concentrations and isotope ratios with depth and were, therefore, averaged as representative for the entire well and accounted for as a unique sampling point. The lack of depth gradients could be explained by the presence of strong vertical hydraulic gradients (0.14 – 0.30 m/m near the wells sampled with PDBs), which could lead to short-circuiting through the wells.

2.3.2 Groundwater analysis

For the 2011 and 2014 sampling campaign, groundwater samples were analysed for CEs concentrations and their carbon (C), chlorine (Cl), and hydrogen (H) isotopic composition following methods described by Kuder et al. (2013) (details presented in (Kuder et al., 2016)), i.e., gas chromatography-quadrupole mass spectrometry for Cl isotope ratios and concentrations, and gas chromatography-isotope ratio mass spectrometry for H and C isotope ratios. For quality insurance purposes, samples for isotopic analysis were duplicated to be analysed in two different laboratories (University of Oklahoma/contract laboratory

Hill AFB). Moreover, six of the samples were analysed twice, under different names, in the same laboratory as a control.

2.3.3 CSIA calculations

The isotope ratio of an element E in a sample, $R(^hE/^lE)_{sample}$, represents the ratio of the amount of heavy isotope hE (for instance, carbon-13, chlorine-37, hydrogen-2) to light isotope lE (carbon-12, chlorine-35, hydrogen-1) of this element. For the sake of comparability, isotopic ratios are reported using the delta notation (δ), which provides the relative difference from the respective standard ratio for an element E ($R(^hE/^lE)_{std}$) (eq. 2-1). The $^{13}C/^{12}C$, $^{37}Cl/^{35}Cl$ and $^2H/^1H$ standards are the Vienna Pee Dee Belemnite (VPDB), the Standard Mean Ocean Chloride (SMOC) and the Vienna Standard Mean Ocean Water (VSMOW), respectively. In the following the standards are implied in the delta notation.

$$\delta^hE_{sample/std} = \frac{R(^hE/^lE)_{sample} - R(^hE/^lE)_{std}}{R(^hE/^lE)_{std}} = \frac{R(^hE/^lE)_{sample}}{R(^hE/^lE)_{std}} - 1 \quad (2-1)$$

In order to evaluate whether all degradation products were detected, the carbon isotope mass balance (CIMB) is calculated by summing the products of each individual carbon isotope signature, $\delta^{13}C_i$, of all the detected CEs and daughter products ethene and ethane, with their respective molar concentrations, C_i , and dividing this sum by the total molar concentration (sum of C_i s) (Stelzer et al., 2009):

$$CIMB = \frac{\sum \delta^{13}C_i \times C_i}{\sum C_i} \quad (2-2)$$

During reductive dechlorination, the CIMB remains constant and equal to the $\delta^{13}C$ at the source as the carbon atoms are transferred to the daughter products through ethane (Fig. 2-2 reaction chain below). Such a CIMB will detect whether CEs, ethene and ethane constitute the only degradation products, in which case the CIMB will be similar to the source value; or a significant amount was degraded to products non included in the CIMB such as CO_2 , CH_4 etc., in which case the CIMB will be enriched in ^{13}C (Hunkeler et al., 1999). Here, ethene and ethane are included in the CIMB to differentiate VC reductive dechlorination (\rightarrow ethene) from VC oxidation ($\rightarrow CO_2$). Because of the limited mixing between the shallow PCE and TCE plumes, PCE is not included in the CIMB for degradation assessment.

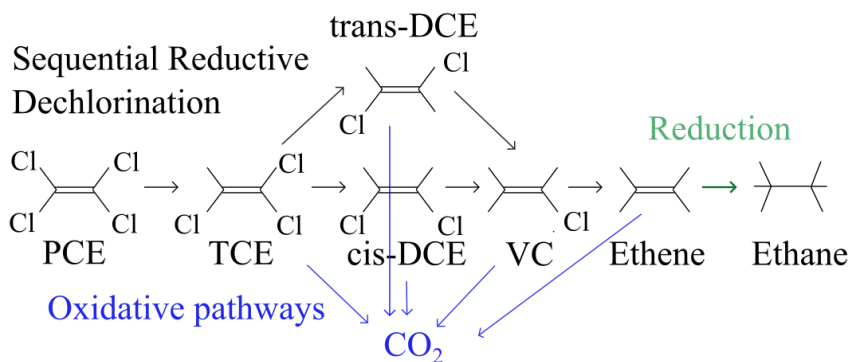


Fig. 2-2 : Reaction pathways for reductive dechlorination through sequential dechlorination (black); oxidative degradation pathways such as metabolic and cometabolic oxidation (blue); reduction of ethene to ethane (green).

In this study, CIMB was calculated only for wells where carbon isotope ratios were available for all species representing more than 5 % of the total CEs (85 % of the wells). An exception was made for seven wells at which trans-DCE molar fractions of less than 5-15 % were detected (S4, S8, S21, D1, D4, D6, for 2011 campaign and D9 for 2014 campaign), for which a conservative estimate of the missing $\delta^{13}\text{C}$ -tDCE was calculated using its relationship with $\delta^{13}\text{C}$ -cDCE (see Fig. S2-15). The uncertainty of the CIMB calculated following error propagation (see eq. S2-3) was in a similar range as the uncertainty of $\delta^{13}\text{C}$ signatures involved in the CIMB calculation (0.4 to 1.4 ‰ for CIMB uncertainty).

Parent CEs showing $\delta^{13}\text{C}$ enrichment compared to the source $\delta^{13}\text{C}$ (i.e., isotopic shift) usually indicate transformation. A $\delta^{13}\text{C}$ positive shift is generally considered to reflect degradation in a significant way when in the order of 2 ‰ or larger; this recommended minimum difference is set cautiously larger than the sum of the uncertainty of the samples to compare (~1 ‰) (Hunkeler et al., 2008). Even though the CIMB uncertainty could reach larger values than 0.5 ‰, a similar threshold of 2 ‰ seemed reasonable for identifying a significant enrichment of the CIMB.

The degree of bulk (molecularly averaged) isotopic fractionation induced by compound transformation or physical processes is expressed by the bulk kinetic isotope fractionation factor, α_k , which relates the isotope ratio of the instantaneous product $R(^hE/^lE)_{AP}$ to the isotope ratio of the substrate $R(^hE/^lE)_S$ through $R(^hE/^lE)_{AP} = \alpha_k \times R(^hE/^lE)_S$ (see (Elsner, 2010) and (Hofstetter and Berg, 2011) for review papers). In the literature the isotopic enrichment factor ε equal to $\alpha_k - 1$ is often employed instead of α_k . For a specific element E , the well-established Rayleigh equation describes the relationship between the observed isotope ratio of a degrading compound, the residual fraction f of this substrate, and the reaction specific isotope enrichment factor ε :

$$R(^hE/^lE) = R(^hE/^lE)_0 \times f^\epsilon \quad (2-3)$$

where $R(^hE/^lE)_0$ is the initial isotope ratio of the compound. A process inducing enrichment in the heavy isotope, called a “normal isotope effect”, leads to more enriched isotope values and is linked to a negative value of the enrichment factor, as opposed to an “inverse isotope effect”, which leads to depletion in the heavy isotope and is expressed by a positive enrichment factor. The simultaneous isotope fractionation of several elements can be characteristic of a reaction mechanism and therefore of a transformation process.

2.4 Results and Discussion

In the following, the prior CSM is verified and where needed improved through the study of the CSIA data. At first, the source isotope signature is retrieved from the site data. Secondly, the hypotheses developed on degradation pathways in the prior CSM are confronted with the CSIA isotope enrichment patterns. Finally, the relation between the physical attenuation patterns previously described in the CSM and specific isotope fractionation patterns is explained. The conclusions are summarized in Table 2-2.

2.4.1 Source characterization

CSIA-based degradation assessment relies on the isotopic shifts of samples compared to the source isotope signature. Therefore, it is crucial to determine the isotope signatures of the original solvent spills as precisely as possible. Due to the advanced age of the plume at this site, the highest concentrations and most depleted CSIA data were not located near the source area anymore (Fig. 2-4a, Fig. 2-4b). Consequently, the source signatures were determined indirectly by selecting conservative CSIA values observed at the site (Table S2-4, Fig. S2-11, Fig. S2-12) in the range of formerly analysed industrial compounds (Kuder and Philp, 2013; Shouakar-Stash et al., 2006).

The estimated source isotope signatures are plotted in Fig. 2-3, which displays dual plots of isotope ratios of all wells in the shallow and deep plumes for both sampling campaigns. No isotope data is available for VC which was only detected at trace levels (well D3) in the deep plume (2011 campaign); and few isotope data are available for ethene, which was detected in 4 different wells of the deep aquifer (D12, D16, D18, D21), at concentrations reaching up to $15 \mu\text{g}\cdot\text{L}^{-1}$. CSIA confirms that the deep TCE plume originates from leakages of the shallow TCE plume, since a unique TCE source signature is determined for both plumes ($\delta^{13}\text{C-TCE}_{\text{source}}$, -26.5 ‰ to -25.5 ‰, $\delta^{37}\text{Cl-TCE}_{\text{source}}$, 1.5 ‰ to 3.5 ‰; $\delta^2\text{H-TCE}_{\text{source}}$, -270 ‰ to -240 ‰; Table S2-4). PCE also reveals a unique source ($\delta^{13}\text{C-PCE}_{\text{source}}$, -32 ‰ to -31 ‰; $\delta^{37}\text{Cl-PCE}_{\text{source}}$, -2.5 ‰ to -0.5 ‰; Table S2-5). The depleted $\delta^2\text{H-TCE}_{\text{source}}$ is similar to a single previously analysed commercial product, albeit at the lower end of the

range for $\delta^2\text{H}$ of commercial TCE (-184 ‰ to +682 ‰) (Kuder and Philp, 2013). Uncertainty of CSIA was in general ± 0.5 ‰ for carbon, ± 1 ‰ for chlorine, and ± 15 ‰ for hydrogen.

Surprisingly, enriched $\delta^2\text{H}$ -TCE compared to the $\delta^2\text{H}$ -TCE_{source} (with ~ 50 ‰), is detected in wells S23, S25, S26, S29 and S31, while $\delta^{13}\text{C}$ -TCE and $\delta^{37}\text{Cl}$ -TCE remain near source values. In 2007, an enhanced reductive dechlorination (ERD) treatment was tested in this area, where the highest TCE concentrations were detected (near S23, S24; Fig. 2-1a, see Section S2.3 in supporting information). Little information is available concerning the ERD treatment, which might have influenced hydrogen isotopic ratios independently from carbon and chlorine isotopes; however, the impacts of the ERD zone are expected to be limited to S23 and S24 (see SI). Hence, enriched $\delta^2\text{H}$ -TCE might reveal a secondary source at the exact location where ERD was applied (a parking lot near an equipment rental company, off-base). The distance between the wells at which the enriched $\delta^2\text{H}$ -TCE is detected at year 2011 suggests that the pollutant would have travelled about 230 m, i.e. it could have been spilled in year 2005 based on TCE velocity (≈ 42 m/y based on groundwater velocity of $0.15 \text{ m}\cdot\text{d}^{-1}$ and retardation factor of 1.3). Modern $\delta^2\text{H}$ -TCE is of about +400 ‰ (Kuder and Philp, 2013). Therefore, this potential secondary spill probably only has a small contribution ($\sim 10\%$) to the plume mass in this area as $\delta^2\text{H}$ -TCE has only limitedly increased. As the mixing engages only a relatively small quantity of the modern spill, and as $\delta^{37}\text{Cl}$ and $\delta^{13}\text{C}$ of manufactured TCE vary within a small range (8 ‰ for each isotope, (Shouakar-Stash et al., 2003)), we assume that $\delta^{37}\text{Cl}$ and $\delta^{13}\text{C}$ have not been noteworthy affected.

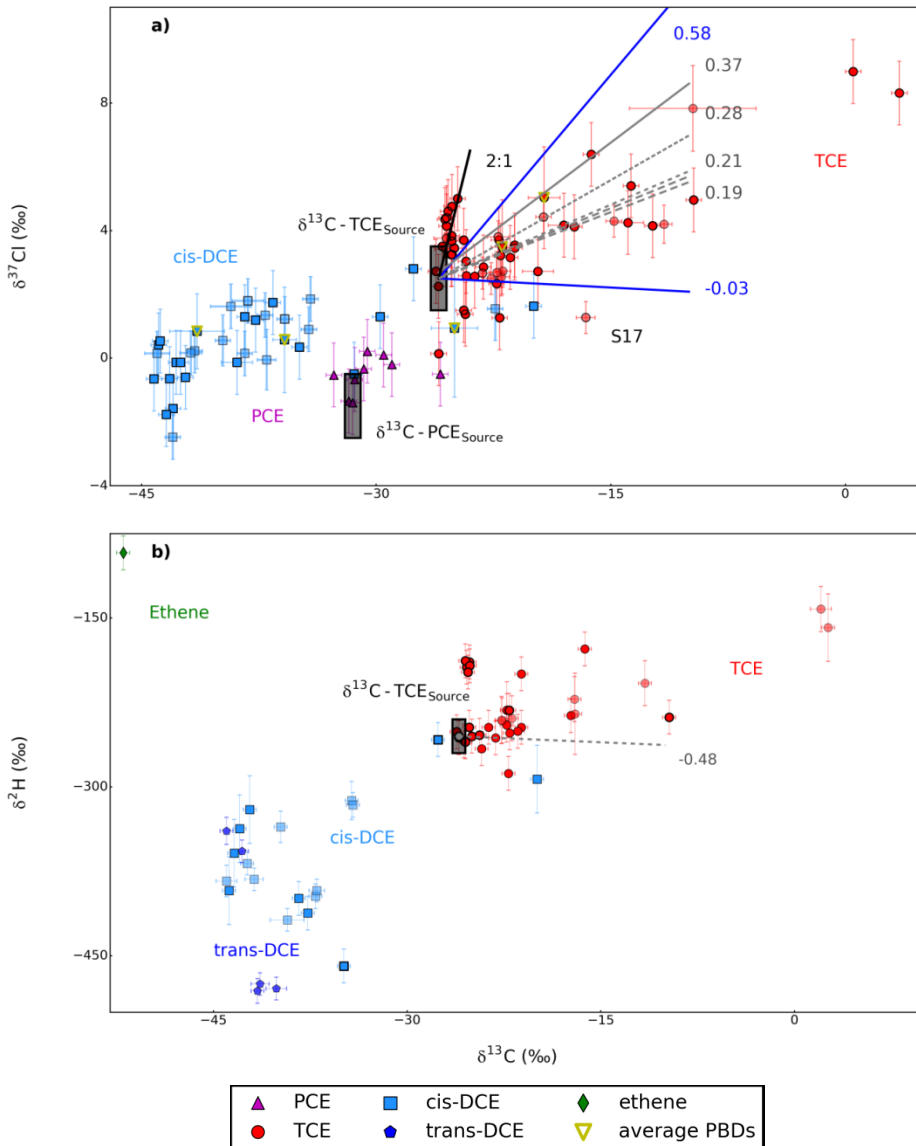


Fig. 2-3 : Dual isotope plots for all CEs, a) Cl/C and b) H/C, for both the deep and shallow plumes (thicker black edge for the shallow dataset). Data collected during the first sampling campaign (2011) are opaque; data collected in 2014 are transparent. The isotope ranges selected to represent the sources (Table S2-4 and S2-5) are indicated with dark rectangles. Data obtained from wells sampled with PDBs were averaged (yellow triangles). (a) Lines meeting radiating away from the TCE source signature represent literature values of $\epsilon_{\text{Cl}/\text{C}}$ for TCE reductive dechlorination in previous studies: plain grey lines: 0.37 (Wiegert et al., 2013); small grey stripes : 0.28, average from values displayed in (Cretnik et al., 2013); long grey stripes : 0.21 (Kuder et al., 2013), 0.19 (Renpenning et al., 2014). Blue lines radiating away from the TCE source signature represent the literature value of $\epsilon_{\text{Cl}/\text{C}}$ for TCE aerobic cometabolism: on methane (0.58), on toluene (-0.03) (Gafni et al., 2018). Black line indicates a 2:1 line similar to the dual Cl-C isotope trend observed for a group of shallow wells. (b) grey dashed line radiating away from the TCE source signature represents the literature value for $\epsilon_{\text{H}/\text{C}}$ for TCE reductive dechlorination, -0.48 (Kuder et al., 2013).

2.4.2 PCE degradation

The PCE plume is migrating near the water table where the geochemical conditions are largely oxic. While prior laboratory studies found both an enzyme and a fungus species capable of PCE oxidation under aerobic conditions, PCE has generally been found to be recalcitrant to aerobic oxidation (Marco-Urrea et al., 2008; Ryoo et al., 2000). However, $\delta^{13}\text{C}$ -PCE ranges between -32.7‰ and -20‰ , and PCE shows significantly enriched $\delta^{13}\text{C}$ values (i.e., $\delta^{13}\text{C}$ -PCE $> -29.5\text{‰}$) at 5 out of 14 wells in which PCE was detected (Fig. 2-4b). The largest $\delta^{13}\text{C}$ -PCE enrichments occur close to the aquitard (S5, S15), or in silty to clayish zones (S20, S23), zones which are potentially reductive and therefore where PCE reductive dechlorination could occur. As the least enriched of those 5 wells ($\delta^{13}\text{C}$ -PCE = -29‰), S27, was screened in a sand layer near the ERD, it might display enrichment due to degradation processes in the ERD zone (Fig. 2-1a). PCE concentrations were low and consequently the sample with the most enriched $\delta^{13}\text{C}$ -PCE could not be analysed for $\delta^{37}\text{Cl}$. However, for non-significant ($<2\text{‰}$) $\delta^{13}\text{C}$ enrichments, the $\delta^{37}\text{Cl}/\delta^{13}\text{C}$ slope through these samples is in the range of previously obtained slopes for $\epsilon_{\text{Cl}}/\epsilon_{\text{C}}$ of PCE reductive dechlorination (Badin et al., 2014; Wiegert et al., 2013)(Fig. 2-5). The enriched $\delta^{13}\text{C}$ -PCE values are therefore likely the result of reductive dechlorination under reduced conditions, instead of oxidative transformation.

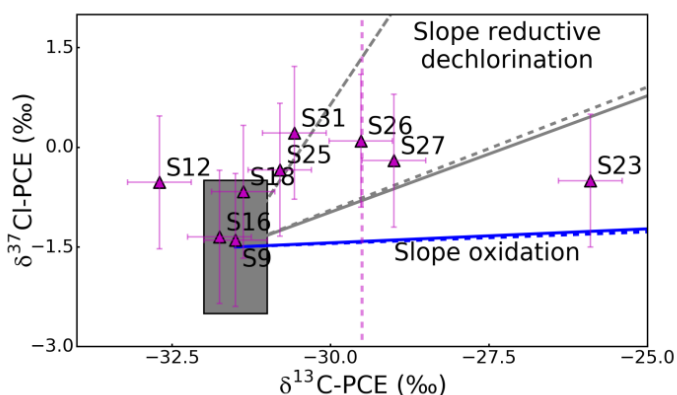
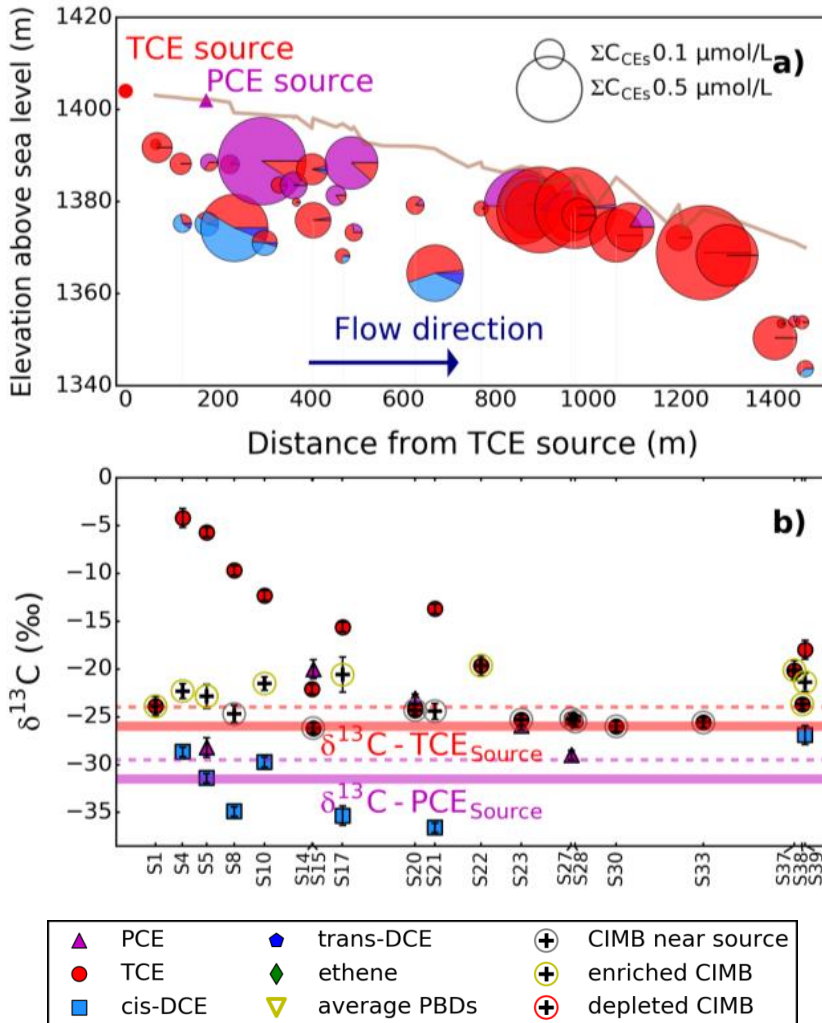


Fig. 2-5 : PCE dual C-Cl CSIA plot. Selected PCE source range (Table S2-5) is indicated with a dark rectangle. The dashed vertical magenta line corresponds to the minimum $\delta^{13}\text{C}$ signal indicative of degradation of 2‰ (Section 2.3.3). Lines radiating away from the PCE source signature represent literature values of $\epsilon_{\text{Cl}}/\epsilon_{\text{C}}$ for PCE reductive dechlorination: grey (short stripes): 1.42; grey (long stripes): 0.37 (Badin et al., 2014), grey plain: 0.35 (Wiegert et al., 2013). $\epsilon_{\text{Cl}}/\epsilon_{\text{C}}$ values for DCE and VC oxidation are also represented (dashed blue: DCE, 0.035; blue: VC, 0.042 (Abe et al., 2009b)). For location of wells, refer to Fig. 2-1 and Fig. 2-12.

The TCE plume is the dominant plume in the areas where $\delta^{13}\text{C}$ -PCE enrichment is observed; therefore the potentially produced TCE (with depleted isotope ratios) is likely mixed with

Shallow Plume



Deep plume

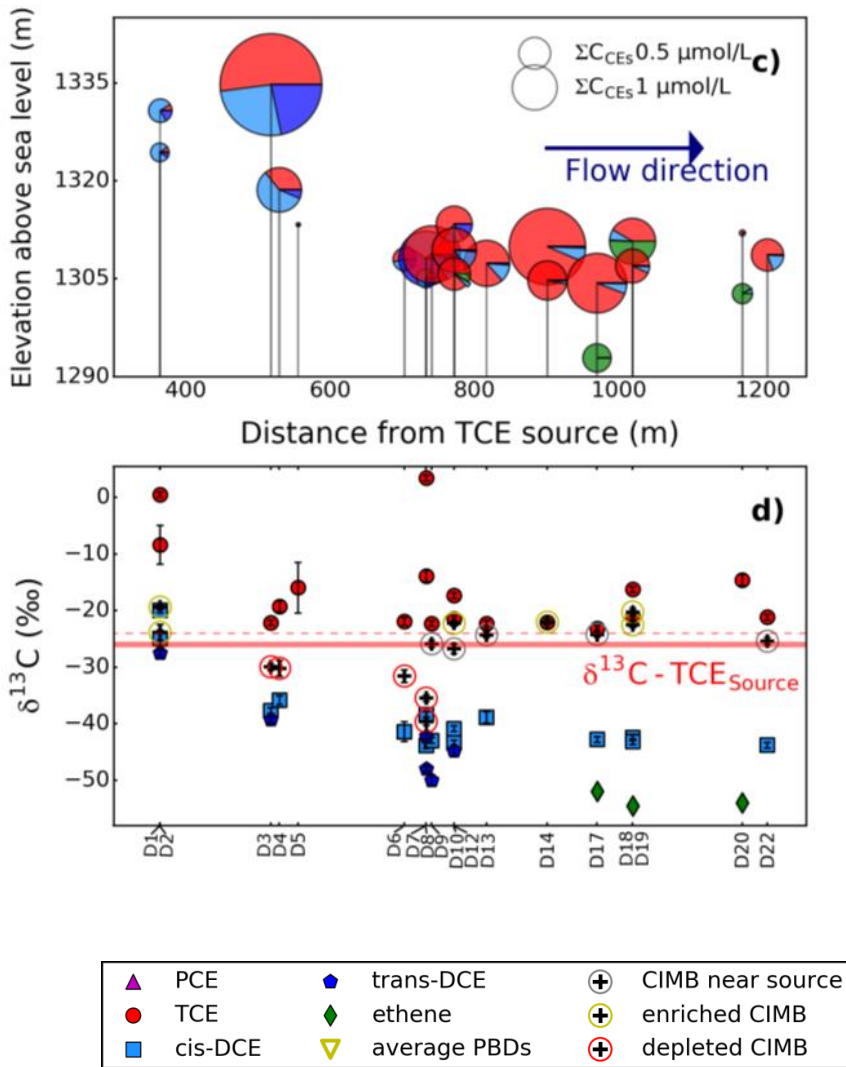


Fig. 2-4 a-d : Molar proportion of CEs and $\delta^{13}\text{C}$ of CEs at sampling locations approximately along the flow gradients (plotted against the distance from the TCE source). For readability, only 37 sampling points are presented, when relevant for discussion (for example presence of $\delta^{13}\text{C}$ enrichment). CIMB is presented with crosses, the circle indicates whether CIMB is significantly different from the source: CIMB $\approx \delta^{13}\text{C}-\text{TCE}_{\text{source}}$: grey, CIMB > -24 ‰, yellow, and CIMB including uncertainty < -26.5 ‰: red. (a, c) Cross-section, total CEs (incl. ethene) concentrations and their relative molar proportion for the shallow (a) and deep plume (c). The range for the carbon isotope source is indicated with a red (TCE) or magenta (PCE) thick line. The dashed vertical lines correspond to the minimum $\delta^{13}\text{C}$ enrichment indicative of degradation of 2 ‰ (Section 2.3.3). (b, d) $\delta^{13}\text{C}$ and CIMB for the shallow (b) and deep plume (d). CIMB excludes PCE and ethene. The uncertainty of concentration measurements was of 10 to 20 % (for location of wells, refer to Fig. 2-1 and Fig. 2-13).

large concentrations of industrial TCE (SI Section S2.8). However, CSIA could theoretically differentiate industrial TCE from PCE reductive dechlorination product (Kuder and Philp, 2013) if $\delta^2\text{H}$ of the produced TCE was strongly different from the depleted industrial $\delta^2\text{H-TCE}_{\text{source}}$ (-255 ‰). Kuder et al. (2013) showed that $\delta^2\text{H}$ of CE daughter products follow from $\delta^2\text{H-H}_2\text{O}$, since the hydrogen atom pool is influenced by the surrounding water, and by the additional fractionation effect associated with protonation ($\epsilon_{\text{protonation}}$). Since $\epsilon_{\text{protonation}}$ was observed to increase with the extent of dechlorination, $\epsilon_{\text{protonation}}$ during reductive dechlorination of PCE to TCE can be proposed to be similar to, or less than, the value reported for TCE dechlorination to DCEs ($\epsilon_{\text{protonation}} = -150$ ‰) (Kuder and Philp, 2013). In Utah, $\delta^2\text{H-rainfall}$ is of about -70 ‰ (IAEA/WMO, 2014), therefore, $\delta^2\text{H-TCE}$ from PCE is expected to be -70 ‰ + -150 ‰ = -220 ‰, or less depleted. Hence, industrial/source TCE and TCE from PCE dechlorination is probably indistinguishable at this site because the difference (-220 ‰ – -250‰ = 30 ‰) is small compared to the large H-CSIA uncertainty (± 15 ‰). Note that if $\delta^2\text{H-TCE}_{\text{source}}$ would have been in the higher range of reported $\delta^2\text{H-TCE}$ for commercial TCE (i.e., around 400 ‰), distinction would have been very well possible. In summary, PCE degrades locally through reductive dechlorination but its degradation products are not detectable. Provided PCE aerobic oxidation involves some degree of carbon isotopic fractionation, the general lack of $\delta^{13}\text{C-PCE}$ enrichment in the shallowest section of the PCE plume points out that the process likely does not occur.

2.4.3 TCE transformation – Carbon isotopes

2.4.3.1 TCE reductive dechlorination – Carbon isotopes

$\delta^{13}\text{C-TCE}$ fractionation is more intense in the deep aquifer than in the shallow aquifer. Significant $\delta^{13}\text{C-TCE}$ enrichment (> -24 ‰) occurs for 90 % of the deep wells vs. 25 % of the shallow wells, while the most enriched $\delta^{13}\text{C}$ values are detected in the deep aquifer (up to +3.4 ‰, vs. -4.2 ‰ for the shallow aquifer, Fig. 2-4b, Fig. 2-4d). Both the southern deep plume (D6) and the shallow bull eye plume (S14) show enriched $\delta^{13}\text{C-TCE}$.

As $\delta^{13}\text{C-TCE}$ enrichment is always detected in presence of cis-DCE, and as larger $\delta^{13}\text{C-TCE}$ enrichment corresponds to larger cis-DCE molar fractions (Fig. 2-4a, Fig. 2-4c), TCE reductive dechlorination is the most likely cause for $\delta^{13}\text{C-TCE}$ enrichment in both plumes. Moreover, the assumption developed in the prior CSM that DCEs molar fractions are proportional to the intensity of TCE reductive dechlorination is supported by the relation between $\delta^{13}\text{C-TCE}$ enrichment and large DCEs molar fractions (Fig. 2-4). Therefore, C CSIA confirms the spatial distribution for TCE reductive dechlorination intensity as described in the prior CSM (Section 2.2.5, Table 2-2).

The sporadic presence of relatively large trans-DCE concentrations (Fig. 2-4a and Fig. 2-4c) suggests spatial or temporal fluctuation of the microorganism population. Those variations

can impact both the preferential production (Cheng et al., 2010; Kittelmann and Friedrich, 2008; Marco-Urrea et al., 2011; Sung et al., 2003) or the favoured degradation (Cichocka et al., 2010; Maymo-Gatell et al., 1999; Song et al., 2002) of the one or the other DCE isomer. Specifically, the detection of a DCE isomer-specific degradation pathway, as opposed to multiple TCE degradation pathways, would suggest that some local CE degradation beyond DCEs occurs. As both isomers are frequently detected, (at 34 % and 15 % of the sites of the National Priority List of the US EPA for trans-DCE and cis-DCE, respectively (ATSDR, 2016)), the study of their respective production and degradation is relevant for site remediation.

The field data show both small (less than 0.12; $n = 25$) and large (0.12 to up to 3; $n = 13$) trans-DCE to cis-DCE ratios (tDCE/cDCE), the very large ratios (> 2) being limited to wells D8, D12, and D20. This large fraction of trans-DCE, comparable to observations made in a prior study (Griffin et al., 2004), reveals activity of microorganisms other than *Dehalobacter* or *Desulfuromonas*, as those bacteria mostly dechlorinate PCE or TCE to cis-DCE (Adrian and Löffler, 2016). Two strains were reported to yield large tDCE/cDCE concentration ratios, namely 1.2-1.7 for *Dehalobium chlorocoercia* DF-1 (Kittelmann and Friedrich, 2008; Miller et al., 2005) and 1.4-7.3 for *Dehalococcoides* sp. strain MB and strain CBDB1 (Cheng et al., 2010; Cheng and He, 2009; Marco-Urrea et al., 2011; Miller et al., 2005). Therefore, the largest trans-DCE to cis-DCE ratios (>2) detected at the OU10 could be due to presence and activity the *Dehalococcoides* sp. strains MB and strain CBDB1; unfortunately, those specific *Dhc.* strains are unable of TCE dechlorination beyond DCEs. Alternatively, preferred cis-DCE over trans-DCE reductive dechlorination could also result in high tDCE/cDCE concentration ratios. Additionally to concentration data, isotope ratios may help delineating zones where the one or the other process (preferential production or degradation) dominates. However both large and small $\delta^{13}\text{C}$ -TCE enrichment is detected for both large and small tDCE/cDCE concentration ratios (Fig. 2-4), therefore, the $\delta^{13}\text{C}$ -TCE fractionation extent is not indicative of the type of degradation pathway for TCE, which is further studied through DCEs isotope ratios (Section 2.4.6).

2.4.3.2 TCE aerobic oxidation – Carbon isotopes

Additionally to the reductive dechlorination processes, TCE cometabolism with toluene or methane as primary substrates might take place in the aerobic parts of the shallow TCE plume (Table 2-2, (CH2MHILL, 2009)). Microcosm experiments show the potential for TCE aerobic oxidation as TCE degradation after 32 days was almost complete when conducted with un-amended groundwater samples from two wells (S9, S36) and of about 70 % to 80 % for two other wells (S28, S21), while samples from S28 spiked with cell growth inhibitors or oxygenase inhibitors presented not TCE degradation (CH2MHILL, 2009). Although toluene and methane concentrations might be too small to fuel

cometabolism in the shallow aquifer ($< 20 \mu\text{g}\cdot\text{L}^{-1}$ and $< 30 \mu\text{g}\cdot\text{L}^{-1}$ for toluene and methane, respectively, except for S28, $112\text{-}216 \mu\text{g}\cdot\text{L}^{-1}$ of toluene reported in 2006 (but again much lower later), the very long contact time between reactants could enhance cometabolism in the aquifer. Consequently, TCE cometabolism could be a relevant process even in presence of low toluene and methane concentrations.

CSIA is an appropriate tool for assessing TCE aerobic degradation at field sites, since cometabolic oxidation leads to $\delta^{13}\text{C}$ -TCE enrichment (ϵC from -1.1‰ to -20.7‰ , values are only available for methane and toluene substrates) (Barth et al., 2002; Chu et al., 2004; Jennings et al., 2009; Pooley et al., 2009). However, lines of evidence for aerobic cometabolism (oxic redox conditions, presence and activity of TCE cometabolic bacteria as proven through qPCR tests, TCE degradation during microcosm experiment, and decreasing concentrations, Table 2-2) do not correlate with $\delta^{13}\text{C}$ -TCE significant enrichment ($>2 \text{‰}$), except when DCEs are detected (see Section 2.4.2.1). Nevertheless, some TCE could degrade through TCE cometabolism without producing significant $\delta^{13}\text{C}$ -TCE enrichment. For instance, the net enrichment resulting from degradation depends on two parameters: 1) the fraction of the contaminant mass degraded; and 2) the enrichment factor of the reaction. For example, if TCE was degraded cometabolically with toluene, the enrichment factor would be in the higher range (-11.6‰ to -20.7‰ (Barth et al., 2002; Clingenpeel et al., 2012)). Consequently, limited enrichments is associated with limited degradation, as enrichments below the significance threshold of 2‰ would represent less than 16% of TCE degradation (calculated from eq. 2-3). However, for TCE cometabolism with methane, ϵC is in the smaller range ($\epsilon\text{C} = -1.1 \text{‰}$, (Chu et al., 2004)), hence TCE mass conversion will reach more than 85% before significant enrichment is detected. Consequently, the lack of $\delta^{13}\text{C}$ -TCE enrichment in aerobic zones of the shallow aquifer rules out TCE aerobic cometabolism in presence of toluene as an important degradation pathway, but not cometabolism by methane monooxygenase. Additionally, where cis-DCE is detected, the overall occurrence of TCE reductive dechlorination (large ϵC) hinders the detection of TCE cometabolism.

TCE aerobic cometabolism is also suspected in the deep aquifer (CH2MHILL, 2009). Specifically, aerobic cometabolism with methane could occur at the interface of the aerobic sand layers and the low-permeability layers in which methane is produced from organic matter degradation, reaching concentrations up to $1.2 \text{mg}\cdot\text{L}^{-1}$, while toluene concentrations remain below $20 \mu\text{g}\cdot\text{L}^{-1}$. As DCEs are detected at all wells in the deep TCE plume, cometabolism with methane (low ϵC) might not be distinguishable. Hence, C CSIA by itself is not sufficient to detect TCE cometabolism in the deep aquifer.

TCE direct metabolism was proven possible only in 2014 (Schmidt et al., 2014), and was therefore not considered as a potential degradation pathway in the prior CSM, published in 2009. Direct metabolism could hypothetically occur in all aerobic zones of the shallow and

the deep aquifer, provided enough oxygen is available. However, an enrichment factor was evaluated to -11.4 ‰ for this pathway (Schmidt et al., 2014), in a similar range of that of toluene. Therefore, similarly to cometabolism with toluene, C CSIA does not support strong aerobic metabolism where no significant $\delta^{13}\text{C}$ -TCE enrichment is detected.

An additional potential tool for the detection of TCE (or other CEs) aerobic oxidation is the CIMB. The CIMB is considered enriched when higher than -24 ‰ (higher than $\delta^{13}\text{C}$ -TCE_{source} added with the uncertainty (~0.5‰)). The CIMB was significantly enriched (up to 6.5 ‰ with respect to $\delta^{13}\text{C}$ -TCE_{source}) at about 20 % of the shallow wells and 30 % of the deep wells, always in presence of DCEs (Fig. 2-4b and Fig. 2-4d). In the shallow plume, only wells detecting DCEs presented an enriched CIMB (S4, S5, S10, S17, S22, and S39, Fig. 2-1, Fig. 2-4a, and Fig. 2-4b). In the deep plume, where all wells detect DCEs, enriched CIMB values are found in only two areas, which are the most upgradient extent of the plume (wells D1 and D2) and near the plume front (D12, D14, D18, and D19) (Fig. 2-1 and Fig. 2-4d). Since in both plumes the CIMB is enriched only in presence of DCEs, the observed CIMB enrichments do not specifically point to TCE aerobic oxidation, but are instead likely related to (partial) aerobic or anaerobic degradation of the daughter product(s) from TCE reductive dechlorination (see Section 3.3), with or without additional TCE aerobic oxidation. While CIMB enrichment in the vicinity of an aquitard can also result from differential transport of the CEs (Thouement et al., 2019), the presence of VC at the site and other signs of further cis-DCE degradation which could result in CIMB enrichment are discussed in Section 4.6.

Surprisingly, CIMB lower than -27 ‰, i.e. lower than the lower range of $\delta^{13}\text{C}$ -TCE_{source} added with the uncertainty (~0.5‰) is detected at seven wells in the deep plume (5 wells during 2011 campaign, 2 wells (D9, D14) during 2014 campaign, results not shown). Such depleted CIMB is generally not expected during CEs degradation. Although oxidation is likely faster for cis-DCE than TCE (Clingenpeel et al., 2012; Semprini, 1997), the complex behaviour of microorganisms does not entirely exclude a faster TCE than cis-DCE oxidation. Only in the latter case, the combined decreasing molar fraction of the TCE (enriched in carbon-13) and increasing molar fraction of DCE (depleted in carbon-13) might generate a depleted CIMB. Since most DCEs detected at the site are depleted in carbon-13, a balanced combination of TCE reductive dechlorination, followed by relatively fast TCE cometabolic oxidation compared to DCE oxidation could produce a depleted CIMB. Although this explanation, which requires rare balanced microorganisms diversity, is not impossible, an alternative and more likely interpretation is based on CEs transport processes and described in Section 4.8.2.

2.4.4 TCE transformation - Chlorine isotopes

Similarly to carbon isotopes, the sensitivity of chlorine isotopes to transformation provides supplementary information on degradation. Two main trends are observed on the dual C-Cl CSIA plot (Fig. 2-3a). The trend with lowest slope, describing data from both the shallow and the deep plumes, covers the range of previous dual Cl-C isotope slopes observed for TCE reductive dechlorination in the literature (Cretnik et al., 2013; Kuder et al., 2013; Lihl et al., 2019; Wiegert et al., 2013) (Fig. 2-3a). The trend with highest slope applies to various wells situated in the shallow TCE plume. This group shows $\delta^{37}\text{Cl}$ -TCE enrichment with minor $\delta^{13}\text{C}$ -TCE enrichment, which can be approximated by a 2:1 Cl/C isotope slope. To date, such a pattern is not explained by degradation processes; more specifically, to our knowledge, no large $\delta^{37}\text{Cl}$ enrichment was reported without simultaneous larger $\delta^{13}\text{C}$ enrichment. Relatively large $\delta^{37}\text{Cl}$ fractionation might reflect mass transport processes, and is further described in Section 4.8.1.

The large variation of the dual Cl-C slopes attributed to TCE reductive dechlorination could be explained through three different conceptual models. Each conceptual model involves at least two pathways leading to different relative carbon and chlorine isotopes fractionation. In a first model, two different coexisting RD pathways linked to different dual Cl-C isotope slopes might be detected, as observed in Wiegert et al. (Wiegert et al., 2013). The presences of two reductive dechlorination pathways seem plausible based on the large variations of the tDCE/cDCE concentration ratios. As second model a process preferentially fractionating $\delta^{37}\text{Cl}$ -TCE could occur additionally to a reductive dechlorination process with a small $\epsilon_{\text{Cl}}/\epsilon_{\text{C}}$ slope (for instance 0.20 or lower, Fig. 2-3a). Preferential $\delta^{37}\text{Cl}$ -TCE enrichment compared to $\delta^{13}\text{C}$ -TCE could be related to mass transport as observed in the shallow plume. As third model, an additional process such as TCE aerobic cometabolism in presence of toluene could enrich $\delta^{13}\text{C}$ -TCE more strongly than $\delta^{37}\text{Cl}$ -TCE, sequentially with a TCE reductive dechlorination process resulting to a large $\epsilon_{\text{Cl}}/\epsilon_{\text{C}}$ slope (for instance 0.37, Fig. 2-3a).

In order to further elucidate whether one of the aforementioned three degradation hypotheses is responsible for the large Cl/C isotope variation, the dual Cl-C isotope trends were determined for specific clusters of samples. The third conceptual model hypothesis was tested at first using CIMB as a potential indicator of TCE cometabolism (Section 4.3). Wells were sorted in clusters assuming that wells with constant CIMB (A) would reflect uniquely TCE reductive dechlorination, while both wells with enriched (B) and depleted (C) CIMB might indicate some extent of TCE aerobic cometabolic oxidation (section 4.3). Wells duplicates were employed only if different between sampling events (i.e., 2014 data for D11, D13, and D15 were not employed (SI Fig. S2-17)). The resulting dual Cl-C isotope slope, obtained through York fit regression, is reported in Table 2-1. The use of the York fit instead of a simple regression seems appropriate for obtaining dual isotope slopes as the

York fit takes into account the uncertainty specific to each sample on both the x and y axis (here C and Cl isotope ratios) (York et al., 2004). The York fit is specifically appropriate here as the uncertainty varied from one data point to the other (for example, due to improvement of the analytic method for Cl-CSIA) (see SI for a correction of proto-code to the York fit published in (Wehr and Saleska, 2016)). Note that all trends lines are compatible with the carbon and chlorine isotope signature assigned for the TCE source in section 4.1 (Fig. 2-6a).

For both the wells showing constant CIMB (cluster A, 11 wells, black symbols, black line) and depleted CIMB (cluster C, grey symbols, grey line), the dual Cl/C isotope slope of TCE reached small values, respectively 0.14 ± 0.05 and 0.18 ± 0.05 (Table 2-1, Fig. 2-6a). Those slopes are smaller than the literature range for reductive dechlorination ($0.21 - 0.37$, see Fig. 2-3a). Wells from cluster B (white symbols, red line) yield a significantly larger dual Cl/C isotope slope of 0.27 ± 0.04 compared to cluster A (Table 2-1: group B). The similarities between cluster A and C infers that the processes fractionating both C and Cl are similar for those two groups.

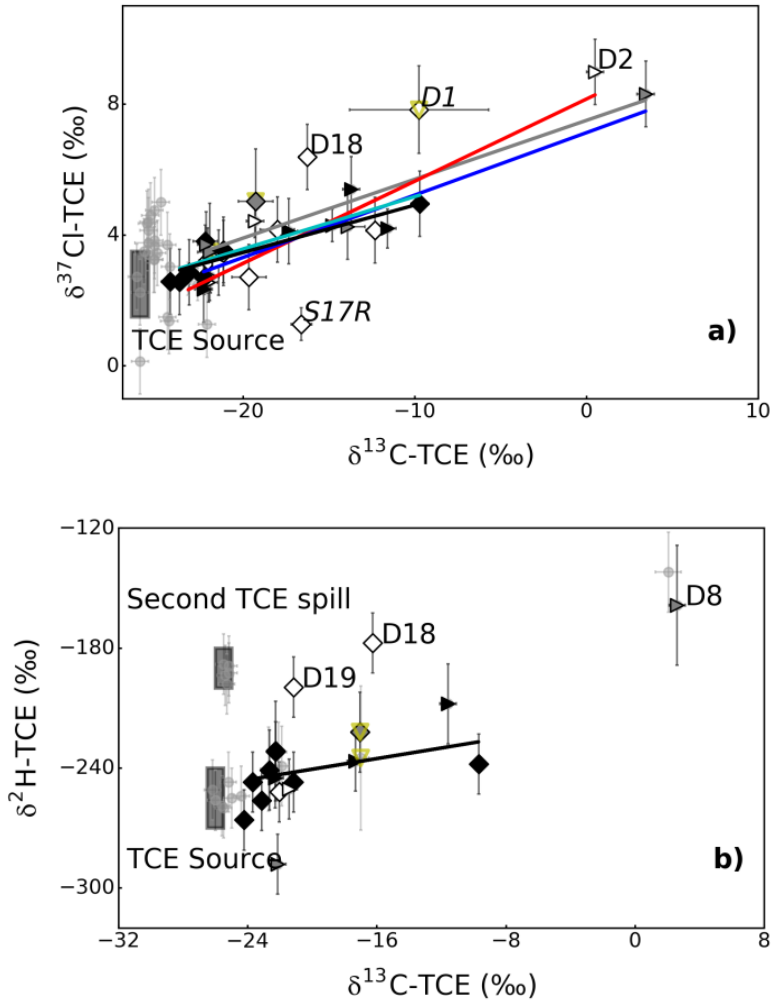
Table 2-1 : Dual isotope slopes of TCE and DCE for subgroups as determined by York fit regression.

Subgroups based on CIMB	Additional condition	TCE		cis-DCE	
		Dual Cl-C isotope slope	n	Dual Cl-C isotope slope	n
A, Constant CIMB ($-26.5\% < \text{CIMB} < -24\%$)	-	0.14 ± 0.05	11	0.26 ± 0.09	8
B, Enriched CIMB ($> -24\%$)	-	0.27 ± 0.04	12	0.12 ± 0.04	13
C, Depleted CIMB ($< -26.5\%$)	-	0.18 ± 0.05	5	0.1 ± 0.1	8
Wells subgroups based on trans-DCE to cis-DCE ratios					
AC1, CIMB $< -24\%$	tDCE/cDCE < 0.12	0.16 ± 0.08	7	0.17 ± 0.07	10
AC2, CIMB $< -24\%$	tDCE/cDCE > 0.12	0.19 ± 0.05	9	0.3 ± 0.1	13
		Dual H/C isotope slope			
A, Constant CIMB ($-26.5\% < \text{CIMB} < -24\%$)	-	1.3 ± 1.1	10	-	-

n : number of samples

Note: The fits are not forced through a same origin; therefore they differ both in their slopes and intercepts.

Cluster B shows the largest scattering around the average line; therefore the data collected at those wells likely reflect more than one pathway. An additional process fractionating Cl relatively more than during TCE reductive dechlorination might also occur, for instance TCE cometabolism in presence of methane ($\epsilon_{\text{Cl}}/\epsilon_{\text{C}} = 0.58$, Gafni et. al, 2018). Large Cl isotope fractionation compared to C isotope might also detect the effects of mass transport, with enrichment of $\delta^{37}\text{Cl}$ -TCE above a small $\epsilon_{\text{Cl}}/\epsilon_{\text{C}}$ TCE reductive dechlorination slope as hypothesized for the second conceptual model. Based on the current state of knowledge, well S17R, at which $\delta^{13}\text{C}$ -TCE is relatively enriched, might be the only well at which strong TCE aerobic oxidation on toluene is detected through CSIA data.



Legend

- | | | | | |
|--|------------------|---|---|----------------------------|
| — A, CIMB near source value | tDCE/cDCE < 0.12 | ◆ | ▶ | CIMB near source value |
| — B, CIMB enriched in carbon-13 | > 0.12 | ◇ | ▷ | CIMB enriched in carbon-13 |
| — C, CIMB depleted in carbon-13 | | ◊ | ▷ | CIMB depleted in carbon-13 |
| — AC1, tDCE/cDCE < 0.12, CIMB not enriched | | ▼ | | PDB well |
| — AC2, tDCE/cDCE > 0.12, CIMB not enriched | | | | |

Fig. 2-6 : TCE dual CI-C (a) and H-C (b) isotope plots. When applicable, York-fit regression results are shown for the different clusters of wells with constant CIMB (A, black), enriched CIMB (B, red), depleted CIMB (C, grey), small (AC1, cyan) and large (AC2, blue) tDCE/cDCE concentration ratios (for AC1 and AC2, CIMB < -24 ‰). For location of wells, refer to Fig. 2-1 and Fig. 2-12.

In order to test the first conceptual model, a cluster of wells based on tDCE/cDCE concentration ratios were built from the merged A and C clusters, as it seemed that the process leading to CIMB depletion in cluster C let unchanged TCE chlorine and carbon isotope ratios. The small (AC1, diamonds, cyan line) and large (AC2, triangles, dark blue line) tDCE/cDCE clusters show similar trends (Fig. 2-6a, Table 2-2). Consequently, the large scatter on the dual Cl-C plot is not explained by the potential existence of two TCE reductive pathways (first conceptual model).

As a result, the trend corresponding to TCE reductive dechlorination is small, and the scattering of the data around this trend seem to illustrate the impact of both $\delta^{37}\text{Cl}$ -TCE and $\delta^{13}\text{C}$ -TCE preferential enrichment through at least two supplementary processes.

2.4.5 TCE transformation - Hydrogen isotopes

The H-CSIA data presented here is the first extensive set of field data for a site detecting intense TCE degradation. The dual H-C isotope plot shows a large scatter of the data (Fig. 2-3). The positive trend for wells with constant CIMB (cluster A) on the dual H-C isotope plot signals that TCE degradation leads to $\delta^2\text{H}$ -TCE enrichment (Table 2-1, Fig. 2-6b). This is different from earlier results showing $\delta^2\text{H}$ -TCE depletion during dechlorination with a mixed culture (Bio-Dechlor Inoculum) capable of total transformation from TCE to ethene in a microcosm (Kuder et al., 2013). Hence, TCE reductive dechlorination likely follows a different mechanism than the one involved during complete CEs reductive dechlorination with Bio-Dechlor Inoculum.

The most enriched $\delta^2\text{H}$ -TCE data (wells D8, D18, D19, and the secondary TCE spill) are likely not related to each other's as the wells and the secondary spill are not on the same flowline (Fig. 2-1). Consequently, wells D8, D18 and D19 are likely strongly enriched from the TCE primary source. Specifically, $\delta^2\text{H}$ -TCE enrichment at D18 and D19 seem significantly larger than for cluster A. These data suggest that $\delta^2\text{H}$ may provide further indication concerning transformation pathways, offering ground for future research. D18 notably combines large C, Cl, and H isotope enrichment which were not observed yet for any degradation pathway.

2.4.6 Potential for DCE and VC transformation

2.4.6.1 DCE transformation - Carbon isotopes

Additionally to limited cis-DCE and VC reductive dechlorination (as proved by the presence of low VC and ethene/ethane concentrations in few wells), cis-DCE and VC cometabolic oxidation were expected at the site. Variations in tDCE/cDCE concentration ratios could be related to spatially-varying preferential formation, which was although not detected through the study of TCE CSIA data (Section 4.4), and/or degradation of the one

or the other isomer. These aspects of DCEs degradation are further studied using C, Cl, and H-CSIA of both DCE isomers.

DCE degradation through both aerobic and anaerobic pathways usually leads to $\delta^{13}\text{C}$ fractionation. For cis-DCE, ϵC for aerobic and anaerobic degradation is in the range of -2.4 ‰ to -30.5 ‰ (Abe et al., 2009b; Bloom et al., 2000; Fletcher et al., 2011; Gafni et al., 2018; Jennings et al., 2009; Schmidt et al., 2010; Tiehm et al., 2008), with the exception of two very small enrichment factors reported for cis-DCE aerobic cometabolism with methane (-0.4 ‰, (Chu et al., 2004)) and with toluene (-0.9 ‰ to -1.2 ‰ (Clingenpeel et al., 2012)). For trans-DCE, ϵC is in the range of -3.5 ‰ to -30.3 ‰ (Brungard et al., 2003; Fletcher et al., 2011; Hunkeler et al., 2002; Lee et al., 2007). The assessment of DCEs degradation through C CSIA is not as straightforward as for TCE, as DCEs isotope ratios' are simultaneously influenced by formation and degradation. DCEs degradation is only obvious when the originally depleted $\delta^{13}\text{C}$ -cDCE enriches beyond $\delta^{13}\text{C}$ -TCE_{source} (-26.5 ‰ to -25.5 ‰). Only two wells (D1 and D2) show $\delta^{13}\text{C}$ -cDCE values more enriched than $\delta^{13}\text{C}$ -TCE_{source} ($\delta^{13}\text{C}$ -cDCE values of -25.0 ‰ and -19.3 ‰ respectively), whereas all $\delta^{13}\text{C}$ -tDCE values are depleted with respect to $\delta^{13}\text{C}$ -TCE_{source}. Therefore, based on C CSIA only, DCEs degradation seems to be limited.

Nonetheless, the simultaneous study of $\delta^{13}\text{C}$ -cDCE and $\delta^{13}\text{C}$ -tDCE fractionation might inform on the suspected presence of a DCE isomer-specific degradation pathway as elaborated before (Section 2.5.3.1), as degradation could result in the independent enrichment of $\delta^{13}\text{C}$ of the one or the other DCE isomer. For instance, the offset between $\delta^{13}\text{C}$ -tDCE and $\delta^{13}\text{C}$ -cDCE tends to decline with the increase of the tDCE/cDCE concentration ratio (Fig. 2-7). The offset is about 6-10 ‰ (grey box on the left Fig. 2-7, $\delta^{13}\text{C}$ -tDCE < $\delta^{13}\text{C}$ -cDCE) for smaller tDCE/cDCE concentration ratios (< 0.5) but decreases abruptly, reaching near 0 ‰ (grey box on the right Fig. 2-7 $\delta^{13}\text{C}$ -tDCE \sim $\delta^{13}\text{C}$ -cDCE), for larger tDCE/cDCE concentrations ratios (Fig. 2-7).

The large offset observed for smaller tDCE/cDCE concentration ratios is likely due to the DCEs formation pathway, as it was observed that TCE reductive dechlorination to a trans-DCE and cis-DCE mixture with both small and large (up to 3.4) tDCE/cDCE concentration ratios produces more depleted $\delta^{13}\text{C}$ -tDCE compared to $\delta^{13}\text{C}$ -cDCE (Marco-Urrea et al., 2011; Song et al., 2002). Would the larger tDCE/cDCE concentration ratios result from preferred cis-DCE degradation, a larger offset between $\delta^{13}\text{C}$ -tDCE (originally < $\delta^{13}\text{C}$ -cDCE) and $\delta^{13}\text{C}$ -cDCE (enriching due to degradation) is expected (Fig. 2-7). As the offset is in fact smaller (near 0 ‰) for larger tDCE/cDCE concentration ratios, C CSIA does not support preferred cis-DCE degradation as an explanation for the variations of tDCE/cDCE concentration ratios.

Similarly, the reversed hypothesis (smaller tDCE/cDCE concentration ratios obtained from preferred trans-DCE degradation) would enrich $\delta^{13}\text{C}$ -tDCE. As the initial offset for larger

tDCE/cDCE concentration ratios is of about 0 ‰, this would produce a negative offset (Fig. 2-7) with decreasing tDCE/cDCE concentration ratios. However, the inverse pattern is observed (Fig. 2-7).

Therefore, C CSIA does not support an isomer-specific degradation pathway for explaining the variations of tDCE/cDCE concentration ratios throughout the aquifers, but would support that TCE degrades through at least two different pathways. The variations of the $\delta^{13}\text{C}$ -cDCE to $\delta^{13}\text{C}$ -tDCE offsets would then reflect different sets of DCEs ϵC values associated with TCE reductive dechlorination. The pathway producing small tDCE/cDCE ratios would then be associated with a larger ϵC during trans-DCE production than during cis-DCE production, while the pathway producing large trans-DCE fractions results in similar isotopic composition for both daughter products. Intermediary values would then be due to mixing of DCEs from the different pathways. The expression of different degradation pathways might result in variations of overall TCE enrichment factor through the plume.

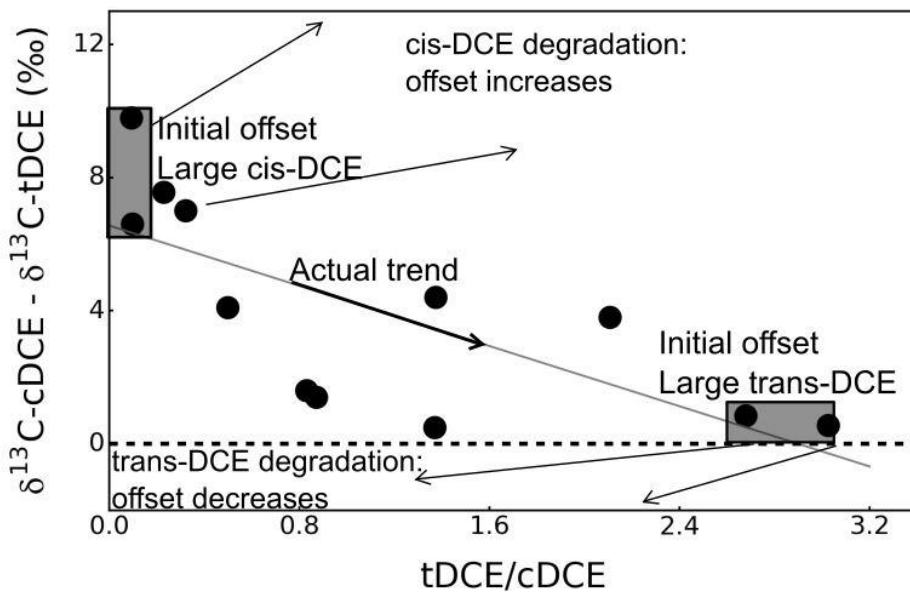


Fig. 2-7 : Offset between $\delta^{13}\text{C}$ -cDCE and $\delta^{13}\text{C}$ -tDCE versus tDCE/cDCE concentration ratios. Top left: arrows show the expected increase of the offset with larger tDCE/cDCE concentration ratio from preferred cis-DCE degradation, starting from 6-10 ‰ (grey box on the left) and increasing. Bottom right: the expected decrease of the offset with smaller tDCE/cDCE concentration ratios from preferred trans-DCE degradation, starting from about 0 ‰ (grey box on the right) and decreasing. In the middle, the actual trend (simple regression) is a decreasing of the offset with increasing tDCE/cDCE concentration ratios (regression line), resembling a mixing line.

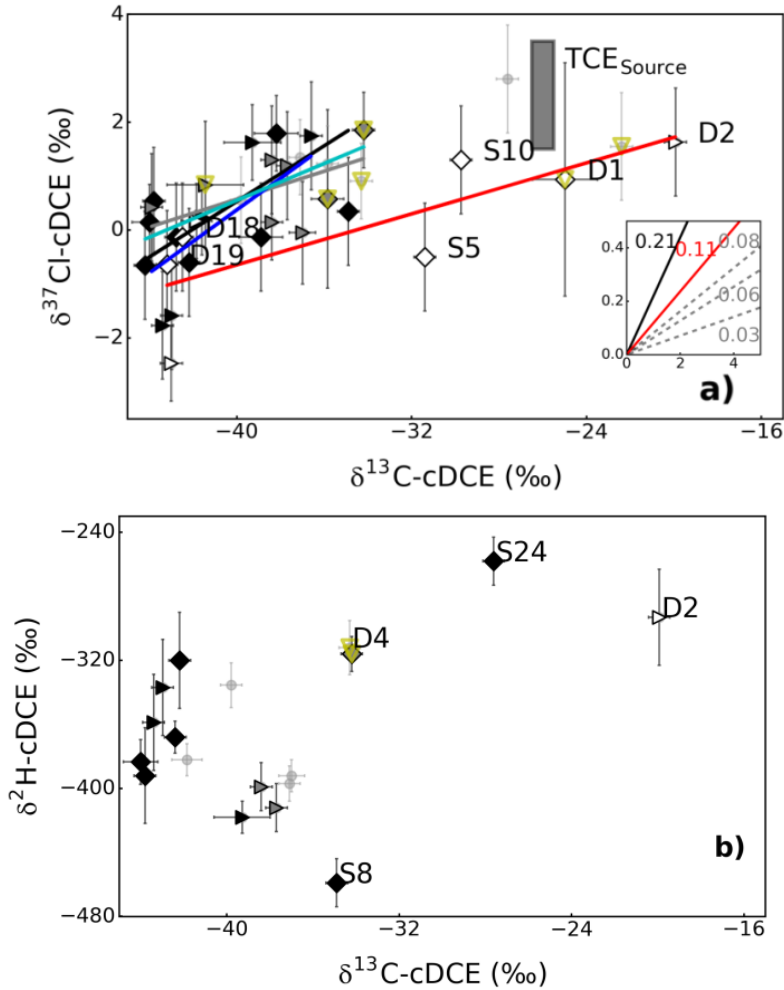
2.4.6.2 DCE transformation - Chlorine isotopes

The study of dual C-Cl CSIA patterns also can bring supplementary information on cis-DCE degradation. The selection of wells' clusters (A, B, C, AC1, and AC2) follows the same approach as for the study of TCE dual Cl-C isotope trends (Section 4.4). Duplicates from the second sampling campaign for wells D1, D4, D8, D11, and S21, were discarded as they were similar to the data obtained during the first sampling campaign.

Interestingly, similarly to what was observed for TCE, wells detecting depleted CIMB (grey symbols, cluster C) and constant CIMB (black symbols, cluster A) present similar dual Cl-C isotope trends (Fig. 2-8a). The process leading to depleted CIMB seems not related to degradative processes as no detectable fractionation of C or Cl isotopes are detected for both TCE (Section 4.4) and cis-DCE. The trends represented by those wells could correspond to $\delta^{37}\text{Cl}/\delta^{13}\text{C}$ for cis-DCE when produced through TCE reductive dechlorination without further degradation.

On the contrary, wells at which CIMB is enriched (white symbols, cluster B) present a significantly different dual Cl-C isotope trend compared to cluster A. Similarly to the large $\delta^{13}\text{C}$ -TCE enrichment relatively to $\delta^{37}\text{Cl}$ -TCE observed for well S17R during TCE oxidation (Fig. 2-3a), those wells show more enriched $\delta^{13}\text{C}$ -cDCE, or more depleted $\delta^{37}\text{Cl}$ -cDCE, than other wells (Fig. 2-8a). Both DCE oxidation and reductive dechlorination produce stronger $\delta^{13}\text{C}$ enrichment than $\delta^{37}\text{Cl}$ enrichment ($\epsilon_{\text{Cl}}/\epsilon_{\text{C}} = 0.03$ to 0.08 , see Fig. 2-8a). Those small slopes correspond to laboratory experiments where cis-DCE was only substrate for degradation. However, at this site cis-DCE is both produced and consumed. Combined production and degradation on the Cl/C isotope slopes could lead to intermediary values between the $\epsilon_{\text{Cl}}/\epsilon_{\text{C}}$ of the degradation process relative to the reactant (here TCE) and to the intermediary product (cis-DCE). The calculated dual Cl-C trend for cluster B of 0.12 ± 0.04 (Table 2-1) is similar to the cis-DCE dual Cl-C isotope trend 0.12 calculated for a microcosm experiment of TCE degradation to ethene (Kuder et al., 2013). However, the larger carbon isotope enrichment during cis-DCE oxidation could also lead to a shift towards more enriched carbon isotopes. Hence, the observation of the dual Cl-C isotope trends supports that some degradation beyond cis-DCE occurs, without revealing the degradation pathway. The connection between cis-DCE isotope enrichment and CIMB enrichment suggests that cis-DCE degradation through oxidation or reductive dechlorination is a necessary step towards CEs mineralization.

Finally, wells separated based on their tDCE/cDCE concentration ratios (clusters AC1 and AC2) do not strongly differ from their dual Cl-C isotope trends (Table 2-1, Fig. 2-8a). This supports that larger tDCE/cDCE concentration ratios are likely not related to preferred cis-DCE degradation. As both cis-DCE and TCE dual Cl-C isotope patterns do not detect major differences between the clusters AC1 and AC2, both TCE dechlorination pathways might present relatively similar $\epsilon_{\text{Cl}}/\epsilon_{\text{C}}$ ratios.



Legend

- | | | | |
|--|---|---|----------------------------|
| — A, CIMB near source value | ◆ | ▶ | CIMB near source value |
| — B, CIMB enriched in carbon-13 | ◇ | ▷ | CIMB enriched in carbon-13 |
| — C, CIMB depleted in carbon-13 | ◊ | ◂ | CIMB depleted in carbon-13 |
| — AC1, tDCE/cDCE < 0.12, CIMB not enriched | ▼ | | PDB well |
| — AC2, tDCE/cDCE > 0.12, CIMB not enriched | | | |

Fig. 2-8 : Cis-DCE dual Cl-C (a) and H-C (b) isotope plots. The lines represent the York-fit regression results for the different clusters of wells with constant CIMB (A, black), enriched CIMB (B, red), depleted CIMB (C, grey), small (AC1, cyan) and large (AC2, blue) tDCE/cDCE concentration ratios (for AC1 and AC2, CIMB < -24 ‰). On the insert on (a), the slopes for cluster A and C are plotted together with the ϵ_{Cl}/ϵ_C ratios for cis-DCE degradation from the literature (reductive dechlorination: 0.06 (Kuder et al., 2013), 0.08 (Abe et al., 2009b), oxidation: 0.03 (Abe et al., 2009b)). For location of wells, refer to Fig. 2-1 and Fig. 2-12.

2.4.6.3 DCE transformation - Hydrogen isotopes

A specificity of this field study is the strong variation of $\delta^2\text{H-cDCE}$, observed within a 200 ‰ range (-258 ‰ to -459 ‰, n=13) (Fig. 2-8b). This study presents also the first set of $\delta^2\text{H-tDCE}$. The two shallow wells S8 and S24 are at the extremities of the range (-459 ‰ and -258 ‰, respectively, Fig. 2-9), while values for the deep wells occur in a smaller range of about 125 ‰ (from -418 ‰ to -292 ‰, n= 11). In prior studies, $\delta^2\text{H-cDCE}$ varied within only 80 ‰ at field sites during PCE reductive dechlorination beyond cis-DCE (Audí-Miró et al., 2015; Filippini et al., 2018) and within 50 ‰ during a microcosm experiment with a consortium of *Dehalococcoides* species (Kuder et al., 2013). The dual H-C isotope plot seem to present an increasing trend towards D2 but the depleted $\delta^2\text{H}$ values of S8 suggest instead a decreasing trend (Fig. 2-8b). Additionally, while $\delta^2\text{H-cDCE}$ and $\delta^2\text{H-tDCE}$ reach depleted values for larger tDCE/cDCE concentration ratios, large variations of $\delta^2\text{H}$ are witnessed for small tDCE/cDCE concentration ratios.

During TCE simultaneous dechlorination and protonation, the resulting $\delta^2\text{H}$ of DCEs (both cis- and trans-) is expected to be much influenced by the $\delta^2\text{H}$ of the added hydrogen atom ($\delta^2\text{H}_{\text{addition}}$). The kinetic effect occurring on the H atom of TCE during the protonation step is small, as this H atom is not involved in the protonation step (Kuder et al., 2013). Although H_2 sources may vary, $\delta^2\text{H}$ of the dechlorination product is so far assumed to equilibrate with $\delta^2\text{H-H}_2\text{O}$, which is expected to be stable at the aquifer scale (Kuder et al., 2013). The large variations observed for $\delta^2\text{H-TCE}$ (-288 ‰ to -142 ‰) could then be a cause for the spreading of $\delta^2\text{H-cDCE}$ and $\delta^2\text{H-tDCE}$; however, variations in $\delta^2\text{H-TCE}$ do not relate to variations in $\delta^2\text{H-DCEs}$ (Fig. S2-15). Moreover, of all the wells represented on the dual H-C isotope plot (Fig. 2-6b), only S24 is likely to be detecting PCE dechlorination product, as PCE was not detected in the other shallow well S8 (sampled in 1996, 1999-2008, and 2011). Variations of $\delta^2\text{H-TCE}$ are therefore unlikely to be the cause of the large range observed for both $\delta^2\text{H-cDCE}$ and $\delta^2\text{H-tDCE}$.

As a result, the large variation observed for both $\delta^2\text{H-cDCE}$ and $\delta^2\text{H-tDCE}$ could relate to changes in the additional kinetic effects on $\delta^2\text{H}_{\text{addition}}$ occurring during the protonation stage, following from the microbial diversity at the site. Alternatively, enriched $\delta^2\text{H}$ could result from $\delta^2\text{H}$ -fractionating pathways degrading DCEs. Based on the dual H-C isotope plot, this pathway would require a very large $\epsilon\text{H}/\epsilon\text{C}$ ratio, as $\delta^2\text{H-cDCE}$ variations seem not linked to strong $\delta^{13}\text{C-cDCE}$ enrichment (Fig. 2-8b). As this potential degradation pathway is not related to enriched CIMB, it is likely not strongly degrading DCEs (Fig. 2-8b). While the exact cause for the large variations for both $\delta^2\text{H-cDCE}$ and $\delta^2\text{H-tDCE}$ is not unveiled, this study underlines that $\delta^2\text{H}$ might provide further information on CEs transformation (both TCE and DCEs) and should be further studied.

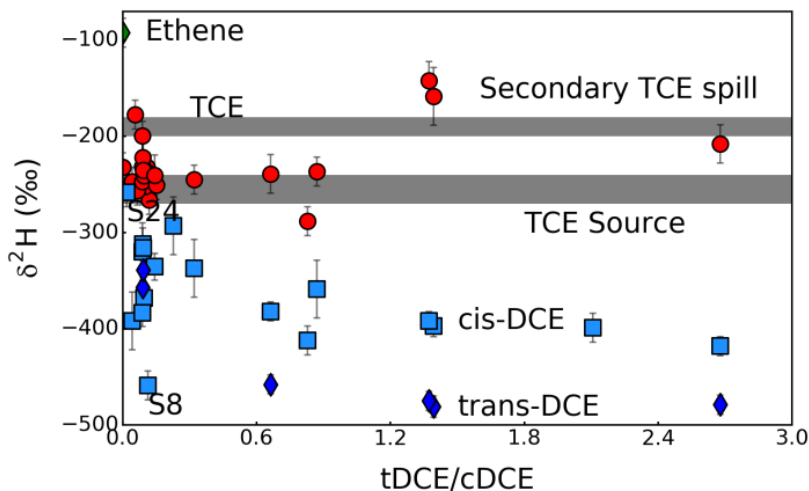


Fig. 2-9 : $\delta^2\text{H}$ of TCE (red circles), cis-DCE (cyan squares), trans-DCE (dark blue diamonds) and ethene (green diamond) versus tDCE/cDCE concentration ratio. Grey rectangles indicate $\delta^2\text{H}$ -TCE for the main source and for the potential secondary spill. For location of wells, refer to Fig. 2-1.

2.4.6.4 VC transformation

The general limited presence of VC could result from limited VC production or fast VC degradation once produced. While CSIA data was not available for VC, ethene concentration and CSIA data might inform on the production and fate of VC. Ethene concentrations, reported for 4 wells during the 2011 campaign, reached larger values (0.04 μM , 0.18 μM , 0.39 μM , and 0.53 μM for D12, D21, D16 and D18, respectively) than the largest reported ethene concentration of 0.03 μM prior to this study (D3 in 2007 (CH2MHill, 2011)). Ethene concentrations were also larger than the VC historical maximum (0.01 μM (CH2MHILL, 2009)). Moreover, $\delta^{13}\text{C}$ -Ethene (3 values reported, -54.5 ‰ to -52 ‰) are strongly depleted compared to $\delta^{13}\text{C}$ -TCE_{source}, which could reflect the incomplete TCE dechlorination.

However, the only reported $\delta^2\text{H}$ -Ethene of -92 ± 15 ‰ (well D16), is +50 ‰ more enriched than the most enriched $\delta^2\text{H}$ -TCE (max. -142 ± 15 ‰). This differs from a previous microcosm experiment yielding $\delta^2\text{H}$ -Ethene much more depleted than $\delta^2\text{H}$ -TCE (with 800 ‰) after sequential reductive dechlorination of TCE to ethene (Kuder et al., 2013). The highly enriched $\delta^2\text{H}$ -Ethene value suggests that the large ethene concentrations do not result from VC reductive dechlorination, although alternative sources for ethene were not identified.

Additionally, the depleted $\delta^{13}\text{C}$ -Ethene, similar in those three wells, seems to indicate that ethene is not degrading (aerobically or anaerobically) in this area, as both pathways would lead to $\delta^{13}\text{C}$ -Ethene enrichment (ϵC of -3‰ to -6.7‰ (Bloom et al., 2000; Mundle et al., 2012)). This shows that the low ethene and ethane concentrations detected in this area are likely due to little ethene and ethane production, and not to further ethene oxidation. Therefore, the low VC concentrations likely result from limited production of VC or a fast oxidation of VC following its production.

2.4.7 Interaction of transport and physical attenuation with CSIA.

2.4.7.1 *Large chlorine isotope enrichment as potential evidence for physical attenuation*

A large $\delta^{37}\text{Cl}$ enrichment compared to the source value ($\Delta^{37}\text{Cl}$ up to +2.5 ‰) is observed for TCE for a group of wells ($n = 13$) which simultaneously show small $\delta^{13}\text{C}$ enrichment ($\Delta^{13}\text{C} < +1$ ‰) (Fig. 2-9). The resulting ratios of the enrichments ($\Delta^{37}\text{Cl}:\Delta^{13}\text{C}$) are larger than 1, which is incompatible with TCE degradation (both reductive dechlorination and certainly for oxidation, Fig. 2-10). As $\Delta^{13}\text{C}$ are small, the $\Delta^{37}\text{Cl}:\Delta^{13}\text{C}$ ratios are strongly dependent on the assumed source isotope ratio. $\Delta^{37}\text{Cl}$ is larger than the $\delta^{37}\text{Cl}$ analytical error, in the range of the shift observed for TCE reductive dechlorination in the deep aquifer. Such relatively large chlorine isotope enrichments may reflect mass transport, as the mass difference between the two isotopes ^{37}Cl and ^{35}Cl is twice as large as the mass difference between the carbon isotopes (^{12}C and ^{13}C) (Hunkeler et al., 2011b; Jeannotat and Hunkeler, 2013, 2012; Kuder et al., 2009; van Breukelen and Rolle, 2012; Wanner and Hunkeler, 2015). The unusual pattern seems to be mostly observed in the upper zone of the shallow plume, near the water table. The shallow plume travels at the surface of an aquitard or near interbedded clay and silt layers, while also remaining near the groundwater table. Consequently, three physical processes were identified for rationalizing the isotopic patterns, namely diffusion into the aquitard, diffusion across the plume fringe, and volatilization from the groundwater, as elaborated below.

Volatilization from the groundwater is likely to be effective only when the plume is in contact with the unsaturated zone. Low groundwater levels which could have triggered volatilization were likely during the last decade, as rainfall was in average below normal since 2005 (Fig. S2-13). Volatilization impacts on carbon and chlorine isotopic patterns under different conditions (DNAPL volatilization, air-sparging) were reported in the literature (Jeannotat and Hunkeler, 2013, 2012). While multistep air-water partitioning of TCE likely represents best TCE volatilization from the groundwater table, it was linked to a small normal enrichment for chlorine but with an inverse enrichment for carbon ($\Delta^{37}\text{Cl}:\Delta^{13}\text{C} = -0.15$, Fig. 2-10, published as $\epsilon\text{Cl} = -0.06 \pm 0.05$ ‰ and $\epsilon\text{C} = +0.38 \pm 0.04$ ‰

(Jeannotat and Hunkeler, 2013)). Volatilization from the groundwater is therefore unlikely to explain the large chlorine isotope enrichment. The lack of clear trend corresponding to TCE volatilization from the groundwater is in agreement with the lack of detection of TCE in soil-gas samples off-base.

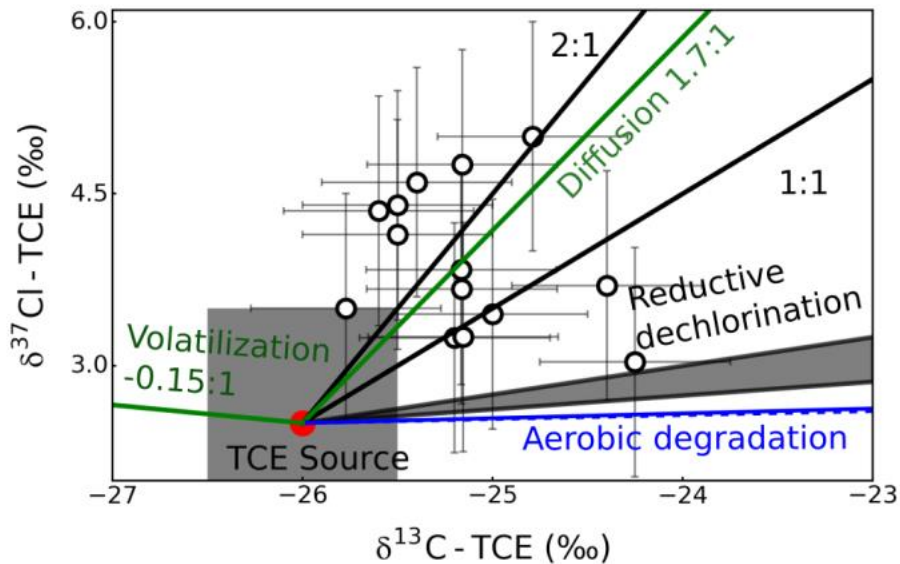


Fig. 2-10 : TCE dual Cl-C isotope plot for shallow wells with little $\delta^{13}\text{C}$ -TCE enrichment. The TCE isotope source value as determined in Section 4.1 is represented by the grey rectangle, the red dot being the middle of the rectangle. The plain lines 1:1 and 1:2 are a visual support showing the large enrichment of chlorine vs. carbon for some wells. $\epsilon\text{Cl}/\epsilon\text{C}$ slopes for physical attenuation are represented in green (volatilization: -0.15:1 (Jeannotat and Hunkeler, 2013), diffusion: 1.7:1 (Wanner and Hunkeler, 2015)). Range for $\epsilon\text{Cl}/\epsilon\text{C}$ during CEs degradation are represented in black (TCE reductive dechlorination, 0.12:1 to 0.25:1 as in Table 2-1) and blue (aerobic oxidation of VC and DCE, (dashed blue: DCE, 0.035; blue: VC, 0.042 (Abe et al., 2009b))).

Diffusion is faster for the light isotopes than for the heavy isotopes, which results in a pattern of slight isotope enrichment towards isotope depletion along the diffusion gradient (LaBolle et al., 2008). In prior field studies, $\delta^{13}\text{C}$ -TCE enrichment of up to +2.4 ‰ was suspected to be at least partially due to TCE diffusion into an aquitard, and $\delta^{13}\text{C}$ difference as large as 2 ‰ between the core and the fringe of the plume was attributed to diffusion as part of vertical transverse dispersion in the saturated zone for a PCE plume (Hunkeler et al., 2004; van Breukelen and Rolle, 2012). A large chlorine isotope enrichment relatively to carbon (near 2:1 for $\Delta^{37}\text{Cl}:\Delta^{13}\text{C}$) of the remaining fraction was predicted in a modeling experiment of fringe diffusion in a VC plume (van Breukelen and Rolle, 2012). A similar relative enrichment of about 1.7:1 ($\Delta^{37}\text{Cl}:\Delta^{13}\text{C}$) was observed for the remaining fraction during a diffusion cell experiment for TCE ($\Delta^{37}\text{Cl}:\Delta^{13}\text{C}$ of 1.7:1, published as the ratio of the diffusion effect of the heavy to the light isotopologue $\text{D132}/\text{D130} = 0.99963 \pm 0.00003$ for chlorine, and $\text{D131}/\text{D130} = 0.99978 \pm 0.00006$ for carbon (Wanner and Hunkeler, 2015)). Hence, the large chlorine and small carbon enrichment pattern observed at the Hill

Site could be explained by diffusion processes into the aquitard, as it was described in (LaBolle et al., 2008). As the lighter isotopologues would diffuse faster than the heavy isotopologues towards the low-permeability layers, the remaining fraction will get increasingly enriched. The depleted counterpart being situated in the low-permeability layer is not sampled for and therefore not reported. A similar process might be occurring in the deep plume, however the resulting isotope fractionation is likely masked by the fractionation resulting from degradation. Recent studies suggest that such diffusion-related isotope fractionation would not be detected without applying a sampling method targeted towards that goal (Xu et al., 2017); however, there is to date no other explanation for the large chlorine isotope enrichment observed at the site.

Unlike TCE, the ratios of the enrichments $\Delta^{37}\text{Cl}:\Delta^{13}\text{C}$ remain low for PCE (Fig. 2-5) in the range $\Delta^{37}\text{Cl}:\Delta^{13}\text{C}$ observed for PCE reductive dechlorination. The absence of a characteristic effect of diffusion be explained by the position of the PCE plume, which is above the TCE shallow plume, therefore away from the aquitard and close to the interface to the unsaturated zone. PCE would then not diffuse in the aquitard as TCE does. Provided PCE is more likely to volatilize, the lack of large $\Delta^{37}\text{Cl}:\Delta^{13}\text{C}$ would therefore support that no strong fractionation effect can be expected from volatilization.

2.4.7.2 Rationale for CIMB depletion: impacts of diffusion and sorption

CIMB (including ethene) is depleted by as much as -26.5 ‰ compared to the source value in some wells of the deep plume. Over the two sampling campaigns, 10 wells detected CIMB lower than -26.5 ‰, of which the uncertainty of the CSIA data at 3 wells still intersected the source value (D10, D11 (2011 campaign), and D20 (2014 campaign), see Fig. 2-4b for well D10). Although a sensitive balance between TCE reductive dechlorination and oxidation could also lead to depleted CIMB (see Section 4.3), it is more likely that depleted CIMB results from the preferential sorption of higher versus lower CEs (van Breukelen et al., 2005). As result, depleted daughter CEs are transported faster downgradient than their enriched precursors leading to depleted CIMB, as it was observed at a field site before (depletion by about 2.5 ‰) (Courbet et al., 2011).

Large molar fractions of strongly depleted ethene are observed at 3 out of the 10 wells for which depleted CIMB (if including ethene) is calculated (D16, D18, and D21, CIMB including ethene reaching -52.0 ‰, -37.6 ‰ and -52.8 ‰, respectively). Ethene could have travelled away from the enriched TCE (retardation factor of 3.0, 2.0, 1.7 and 1.2 for TCE, trans-DCE, cis-DCE and ethene, respectively, Table S2-2). Alternatively, this specifically depleted CIMB could be a sign of the disconnection between ethene and the CEs as evaluated in Section 2.4.6.4. Nonetheless, CIMB is strongly depleted (by 14.5 ‰) also when ethene is not considered as an end product (i.e., ethene not included in CIMB calculation). Depletion away from the source (for wells D8, D10, D11, D20, and D21) is

potentially explained by preferential sorption as above. However, preferential sorption cannot explain that CIMB shows depleted values also in the upgradient extent of the deep plumes (D3, D4, and in the southern well, D6).

Mass transport between the permeable sand layers and the low-permeability layers, which, according to the prior CSM conclusion, present different reactivity (Table 2-2), might explain CIMB depletion. In the prior CSM, reductive dechlorination in the deep aquifer was assumed to occur in the low-permeability layers (clay, silt), while the nearby permeable layers (sand) are less reactive (Table 2-2). Two processes, namely diffusion and sorption, might simultaneously impact the relative molar fractions of TCE and cis-DCE during mass transport between the low-permeability layers and the permeable layers. Diffusion processes are driven by concentration gradients. Consequently, as long as TCE concentrations in the permeable layers are lower than in the low-permeability layers, TCE will diffuse in the low-permeability layers. However, cis-DCE is initially not present in the permeable layers but is produced in the low-permeability layers through TCE reductive dechlorination; therefore diffusion of depleted cis-DCE out of the low-permeability layers to the permeable layers will occur already at the start of TCE dechlorination due to the increasing concentration gradient. Additionally, preferential sorption of TCE in the organic-rich clay or silt layers likely enhances the disconnection between the degrading, enriched source and depleted daughter products. As a result, carbon-13-depleted cis-DCE might be found in excess in the groundwater sampled within the sand layers. Consequently, the CIMB, which would otherwise remain constant, is also depleted in carbon-13. In this context, depleted CIMB would then support the relevance of TCE diffusion to low-permeability layers prior to TCE to reduce reductively, a main conclusion of the prior CSM.

Chapter 2. Verifying a conceptual model with 3D CSIA

Concept	Prior CSM	Evidence	CSM refinement with CSIA	Evidence
Source zones				
#1	PCE source is likely a spill of a 3.5 L PCE container (1 gallon).	PCE detected below a parking lot PCE concentrations profile in vadose zone Estimations of PCE transport direction and distances	Confirmed	Uniqueness of the source confirmed Limited $\delta^{13}\text{C}$ -PCE enrichment signifies that most of the spilled PCE is still detected (i.e. spilled volume supported).
#2	TCE source is likely a long duration leakage of TCE from an oil/water separator	Former presence of an oil/water separator TCE concentrations profile in vadose zone Estimations of TCE transport direction and distances	Limited TCE production from PCE degradation confirmed Potentially additional source	$\text{CIMB} \geq -26 \text{ ‰}$ through most of the shallow and deep aquifers $\text{CIMB} < -26 \text{ ‰}$ not due to PCE degradation ($\delta^{13}\text{C}$ - $\text{PCE}_{\text{source}} \approx -31 \text{ ‰}$) $\delta^2\text{H}$ -TCE analysis suggests an addition small spill near well S24.
PCE degradation				
#3	$\text{PCE} \rightarrow \text{CO}_2$	PCE present in aerobic zones	Not confirmed	$\delta^{13}\text{C}\text{-PCE} < \delta^{13}\text{C}\text{-PCE}_{\text{source}}$ in aerobic zones.
#4	$\text{PCE} \rightarrow \text{TCE}$	PCE present in anaerobic zones	Confirmed	$\delta^{13}\text{C}\text{-PCE} > \delta^{13}\text{C}\text{-PCE}_{\text{source}}$ detected near clay layers.
TCE degradation				
#5	Strong TCE \rightarrow DCE detected near the low-permeability layers (both shallow and deep aquifer)	DCEs detected TCE degradation rates calculated with Buscheck/Alcantar method	Confirmed	$\delta^{13}\text{C}\text{-TCE} > \delta^{13}\text{C}\text{-TCE}_{\text{source}}$, $\delta^{37}\text{Cl}\text{-TCE} > \delta^{37}\text{Cl}\text{-TCE}_{\text{source}}$ Dual Cl-C CSIA slopes.
#6	TCE \rightarrow DCE limited in the sand packs of the deep aquifer	Decreasing DCE concentrations and molar ratios with distance in the deep aquifer	Supported	Less enriched $\delta^{13}\text{C}$ -TCE with distance.
#7	TCE degradation pathway was not further defined	Large trans-DCE concentrations <i>Dehalobacter/Desulfuromonas</i> degrade TCE to cis-DCE exclusively	Presence of two reductive pathways for TCE	$\delta^{37}\text{Cl}$ and $\delta^{13}\text{C}$ (of both cis-DCE and trans-DCE) invalidate that local tDCE or cDCE degradation causes the tDCE/cDCE variations, but agree with two DCEs production pathways.
#8	Shallow aquifer: TCE aerobic cometabolism in presence of toluene/methane	Thiessen polygon analysis, Buscheck-Alcantar analysis, microcosms with aquifer material, molecular assays and enzyme-activity measurements	Cometabolism in presence of toluene is limited	$\delta^{13}\text{C}\text{-TCE} > \delta^{13}\text{C}\text{-TCE}_{\text{source}}$ simultaneous to DCE detection. Little correlation between changes in TCE isotope ratios/molar fractions and changes in TCE concentrations between two sampling event.

Concept	Prior CSM	Evidence	CSM refinement with CSIA	Evidence
#9	Deep aquifer: TCE cometabolism at the interface low/high-permeability layers in the deep aquifer	Large CH ₄ concentrations Methanotrophs detected Inflow of oxic water from the shallow to the deep aquifer	Not confirmed	CIMB > $\delta^{13}\text{C-TCE}_{\text{source}}$ supports CEs cometabolism (TCE, DCEs or VC) but $\delta^{37}\text{Cl-TCE}/\delta^{13}\text{C-TCE}$ plot contradicts TCE cometabolism (except S17).
DCE and VC degradation				
#10	DCE → VC incomplete	VC detected a only at trace concentration Absence of <i>Dehalococcoides</i> (4 wells tested) No tceA reductase	Confirmed	Only two wells with $\delta^{13}\text{C-DCE} > \delta^{13}\text{C-TCE}_{\text{source}}$.
#11	DCE → CO ₂ and/or VC → CO ₂	DCE degradation rates with Buschneck/Alcantar analysis VC detected	Confirmed	Locally CIMB > $\delta^{13}\text{C-TCE}_{\text{source}}$ and cis-DCE dual Cl-C isotope slope shows a smaller slope than where CIMB ≈ $\delta^{13}\text{C-TCE}_{\text{source}}$.
#12	VC → Ethene incomplete	No VC and bvcA reductase detected No <i>Dehalococcoides</i> (4 wells tested) Ethene and ethane detected only at trace concentration	Supported	$\delta^2\text{H-ethene}$ likely too enriched to be degradation product from TCE, although $\delta^{13}\text{C-ethene}$ is not contradictory. <i>No VC CSIA data available.</i>
Physical processes				
#13	TCE volatilization limited	Limited TCE in soil-gas Shallow TCE plume is deeper than PCE plume	Supported	$\delta^{37}\text{Cl-TCE} > \delta^{37}\text{Cl-TCE}_{\text{source}}$ likely linked to diffusion processes to the aquitard. Volatilization related patterns undetected.
#14	Deep plume: CEs back diffuse to permeable layers.	Heterogeneous lithology near recharge area + <i>Concept (#5 and #6) concerning TCE degradation</i> Anaerobic conditions in the low-permeability layers. TCE degradation rates with Buschneck/Alcantar analysis	Supported	CIMB < $\delta^{13}\text{C-TCE}_{\text{source}}$ detected upstream (wells D3, D4, D6) Best described by preferential diffusion of DCE out of impermeable layers. + <i>lines of evidence #5 and #6</i>
#15	TCE, and DCE sorb to organic matter	Presence of soil organic matter	Supported in the deep aquifer	CIMB < $\delta^{13}\text{C-TCE}_{\text{source}}$ is observed downstream in the deep aquifer, which is expected only in presence of strong sorption

2.4.8 CSIA-based refined interpretation of concentration decrease

In the absence of CSIA measurements, assessment of degradation extents and rate constants must rely on the temporal and spatial variations in CEs concentrations. For instance, in the prior CSM, an indirect evidence of TCE aerobic cometabolism in the shallow aquifer was the TCE mass decline through the shallow plume although the plume was not expending (Section 2.2.5). In order to retrieve whether concentration decreases (on which the calculations of mass decrease was based) can be linked to aerobic degradation (thus to $\delta^{13}\text{C}$ fractionation), TCE concentrations and molar fractions changes between the two sampling campaigns of 2011 and 2014 are compared to the evolution of $\delta^{13}\text{C}$ -TCE.

While concentrations decreased at most of the 16 wells (on average by -12 %) between 2011 and 2014, relatively steady $\delta^{13}\text{C}$ -TCE (changes < 1 ‰) is observed at about 2/3 of the wells (Fig. 2-11a). Moreover, the trend observed between the Δx_{TCE} (the change in the TCE molar fraction x_{TCE}) and $\Delta^{13}\text{C}$ -TCE show that at about half the wells, x_{TCE} increases while $\delta^{13}\text{C}$ -TCE depletes, which suggests that less degradation is observed at those wells in 2014 compared to 2011, and most wells show little changes (Fig. 2-11b). Hence, at 12 out of the 13 wells detecting a concentration decrease, this decrease likely reflects physical attenuation and/or variations in plume positioning relatively to the well screens.

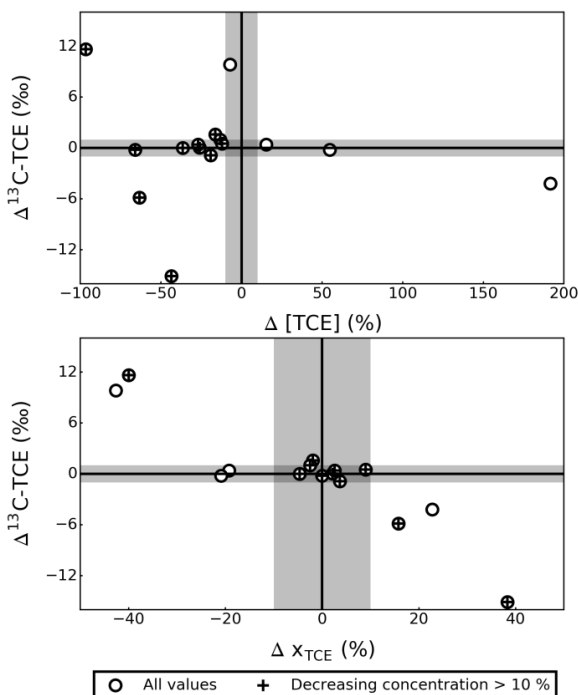


Fig. 2-11 : Change in $\delta^{13}\text{C}$ -TCE ($\Delta^{13}\text{C}$ -TCE) versus change in TCE concentration per well (2014 versus 2011) (a) and versus change in TCE molar fraction (x_{TCE}) (b). Shaded area represents a change of 10 % for concentrations and molar fractions or a change of 1 ‰ for isotope values.

These observations enter in conflict with the Buscheck-Alcantar method (Buscheck and Alcantar, 1995) which was employed in the prior CSM to quantify degradation rates at the site (both shallow and deep aquifer) (CH2MHILL, 2009). The method was applied to single wells, for the calculation of the pollutants attenuation rates using time-series of concentration data (regression of the concentration log through time). As a consequence, both positive (attributed to TCE accumulation) and negative rates (attributed to both degradative and non-degradative attenuation) were calculated in the shallow plume. Multiple-wells analysis, which was applied to pairs of wells situated on the plume's centre line, estimates the share of degradation to the total concentration decrease as the difference between the approximated physical attenuation (dispersion, advection, and adsorption) and the actual concentration decrease between the wells. In the prior CSM, multiple-wells analysis were produced between wells S28 and S33 for 7 sampling rounds (bi-annual sampling, 2003 to 2007), then averaged; however, negative half-lives (2 out of 7 sampling rounds), which represent accumulation of pollutant, were discarded. In the literature, the Buscheck-Alcantar method was criticized for considering only a one-dimensional transport of pollutants; in particular, neglecting transversal and vertical dispersion is likely to lead to an overestimation of the plumes degradation (McNab and Dooher, 1998; Stenback et al., 2004). In the case of the shallow plume, the greatest uncertainty was estimated to be the flow path assumption (CH2MHILL, 2009). The calculation of negative half-lives underlined the inconstancy of the two wells' connection.

Consequently, while in the prior CSM, TCE cometabolism occurrence was supported by enzyme-activity assessment and microcosm experiments, the related extent of TCE cometabolism was estimated through decay rates stemming from the decreasing concentrations with time. Since concentration decrease seemed generally unrelated to TCE degradation where reductive dechlorination is expected, it is possible that the concentration decrease observed in the shallow aquifer also reflects physical attenuation (such as dilution) and not TCE aerobic cometabolism. Specifically for this site, where the lack of isotope enrichment might contradict with the microcosm results and other lines of evidence, it would be relevant to evaluate whether the aerobic process degrading TCE in the microcosms leads to any isotope fractionation, and to evaluate the related C, Cl and H enrichment factors. Finally, this is an example for the application of CSIA for the detection of zones where mixing between flow-lines impact concentrations as opposed to degradation.

2.4.9 Summary discussion on the impacts of CSIA on the CSM

In this paper we confronted the prior CSM of this site with our results of the C-Cl-H CSIA of the CEs, as summarized in Table 2-2 and illustrated in Fig. 2-12. CSIA brought constructive insights in both source characterization and CEs degradation. Without H-CSIA, the additional source near the ERD zone would not have been detected (#2). Moreover, the

relatively large ethene concentrations detected in 2011 would have been unquestionably attributed to VC reductive dechlorination, but its enriched $\delta^2\text{H}$ suggests an alternative source for ethene, which could not be specified (#12). Concerning CEs mineralization, the dual Cl-C isotope plot and C CSIA confirmed that cis-DCE degradation (aerobic or anaerobic) was unlikely to be strong at the site, even though the dual Cl-C isotope plot could prove that cis-DCE degradation occurred locally (#10). Finally, although TCE aerobic cometabolism was much supported by the prior CSM, and PCE aerobic cometabolism was not rejected, both processes go mostly undetected through isotope fractionation (#3, #8, and #9). This is either due to the absence of TCE and PCE aerobic degradation (metabolic or cometabolic), or to the low associated isotope fractionation factor.

Physical attenuation presented unexpectedly large impact on CSIA interpretation. The large chlorine isotope enrichment observed in the shallow aquifer together with limited simultaneous carbon isotope enrichment resulted in a near 2:1 $\Delta^{37}\text{Cl}:\Delta^{13}\text{C}$ which could be attributed to diffusion processes. As lighter isotopologues of TCE diffuses faster, the detection of solely heavier TCE isotopologues suggests that only the remaining TCE is analysed, which is possible if TCE diffused to low-permeability layers (#13). In the deep aquifer, depleted CIMB in the upgradient extent of the deep TCE plume likely pointed to the back-diffusion of TCE and its daughter compounds (#14), supporting that reductive dechlorination occurred principally within low-permeability layers as suggested by the prior CSM. Depleted CIMB in the downgradient extent of the plume was ascribed to chromatographic separation of the CEs based on their respective retardation on organic matter (#15).

Although the prior CSM provided strong lines of evidence for PCE and TCE plumes source apportionment (#1, #2), and for PCE, TCE and DCE degradation extent (#4, #5, #10), CSIA could have been from the start a strong support for those hypotheses. Specifically, at the Hill site, the lack of reductive dechlorination products in the downgradient extent of the deep TCE plume could have been confused for daughter products degradation through oxidative processes (#6), while the lack of $\delta^{13}\text{C}$ -TCE enrichment in the same area is a strong line of evidence for limited TCE reductive dechlorination. Additionally, CSIA was a powerful tool for improving the understanding of the formation and degradation of the cis-DCE and trans-DCE isomers (#7). Finally, the present CSIA data set does not support a systematic correlation between TCE degradation and TCE concentration decrease, preferring the hypothesis that dilution could be involved in concentration decrease between two sampling events (#8). From this observation, it seems recommendable to employ CSIA to support or contradict that concentration changes is related to CEs degradation.

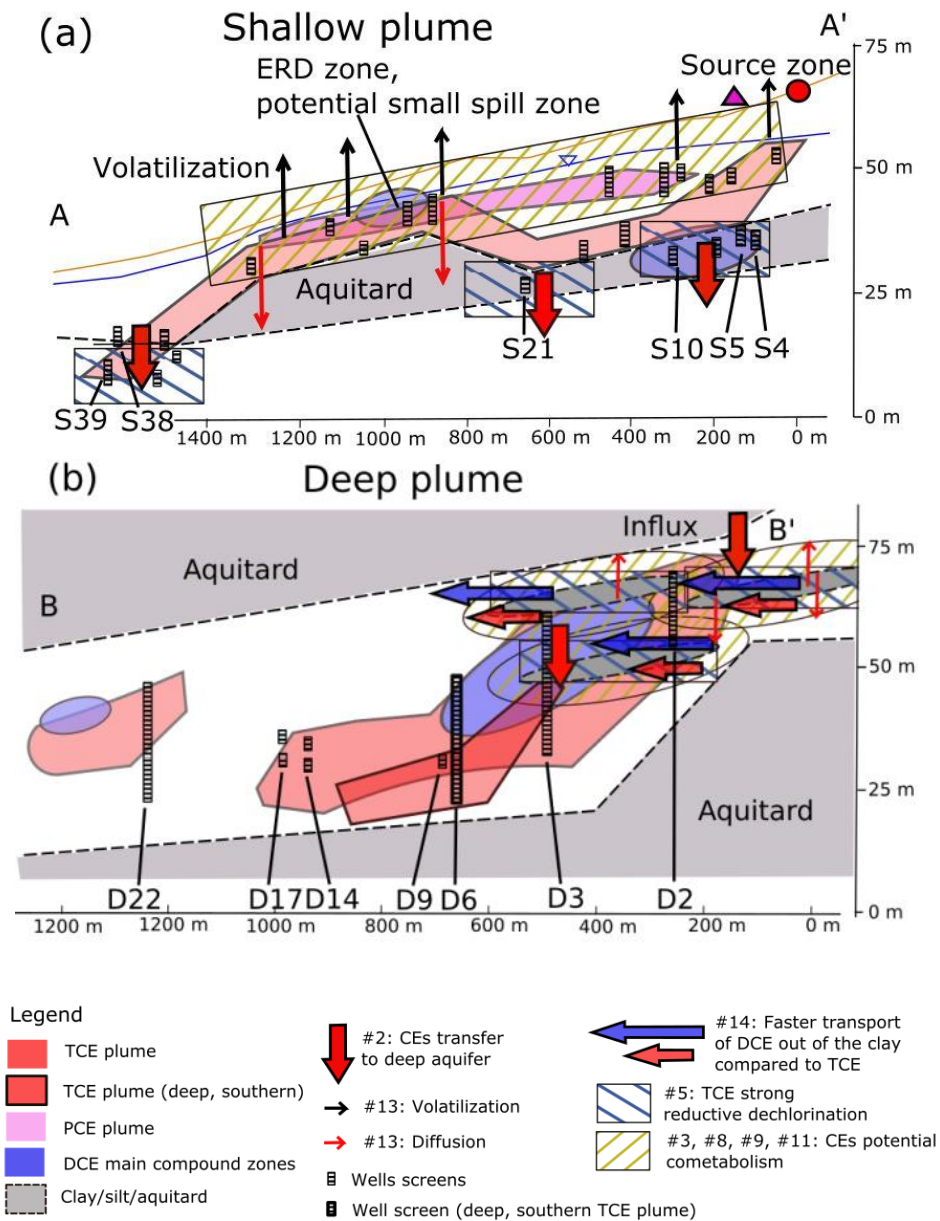


Fig. 2-12 : Subsurface view of the shallow (a) and deep plume (b) summarizing the processes affecting both TCE and DCE concentrations and isotope patterns. Only wells along the cross sections A-A' and B-B' (Fig. 2-1) are shown, the southern deep plume (sampled by D6 only) was added on top of the northern deep plume cross section. The different degradation processes estimated to occur at the site (reductive dechlorination, cometabolism) and the physical processes interacting with the isotope ratios (differential sorption, volatilization, and diffusion) are represented. Numbers indicated with # refer to Table 2-2.

2.5 Conclusion

Triple element CSIA field applications are not restrained to degradation assessment. Although physical processes have limited impact on carbon isotope ratios, their impact on chlorine isotope ratios and on the CIMB was substantial. At this heterogeneous site contaminated with chlorinated ethenes, dual Cl-C isotope trends detected both diffusive processes and cis-DCE and/or VC degradation. Furthermore CIMB indicated both CEs mineralization (enrichment) and CEs back-diffusion or preferential sorption (depletion). On the one hand, physical attenuation processes have impacts on degradation assessment, as the strong chlorine enrichment can be confused for degradation or presence of another CEs source, while a depleted CIMB might either mask CEs mineralization, or lead to confusion during the assessment of the source isotope signature. On the other hand, both strong chlorine enrichment and depleted CIMB, which were ascribed to physical attenuation processes, are generally unlikely to result from degradation processes, as degradative pathways lead to larger carbon than chlorine isotope enrichment according to literature, and mostly lead to CIMB enrichment. CIMB depletion from degradation is only possible given that there is a complex balance of degradation rates and enrichment factors allowing it. While strong chlorine enrichment and CIMB depletion patterns were unprecedented and made the present site interpretation difficult, the assessment of degradative processes was not hindered by those additional changes of CSIA patterns. Additionally, those patterns allowed detecting the presence of non-degradative processes as seen in the present field study. CSIA data was also shown to be a strong tool to support that the concentration changes between two sampling events are likely related to dilution and not to intense degradation.

The assessment of the occurrence of low-fractionating pathways, both degradative and non-degradative, relied on the precision of the source isotope signature. Extent of fractionation smaller than the uncertainty on the data will go undetected and present to some extent a limitation to CSIA applications. At this site, source characterization was crucially improved by H-CSIA for both TCE and ethene. Additionally, simultaneous enrichment of H and C CSIA during TCE degradation differed from a previous microcosm experiment showing $\delta^2\text{H-TCE}$ depletion during dechlorination, which could result from a different degradation mechanism. Further studies on the processes involved in H-CSIA fractionation as observed at the Hill Site are therefore necessary to ensure that field H-CSIA data remains a useful tool for source assessment at complex field sites.

Since back-diffusion is likely to be increasingly detected where aged sources are now exhausted or remediated (Seyedabbasi et al., 2012; Wanner et al., 2016), complex CSIA patterns such as depleted CIMB might be observed at other sites. The present study can help understanding those patterns and limit confusion. Triple element CSIA field studies

require an extensive understanding of both mass transport and degradative processes, respective interactions with CEs isotopes and molar fractions. Nevertheless, triple element CSIA has the potential to improve the understanding of degradation patterns at sites detecting multiple attenuation pathways despite the resulting intricate isotope fractionation patterns.

This page was intentionally left blank

Supporting information to chapter 2

S2.1 Hill AFB Hydrogeological Conditions

The hydrogeological conditions at the Hill AFB were previously thoroughly reported, stating that the aquifer present important heterogeneities (CH2MHILL, 2009). Slug tests and pump tests revealed that Unit A and Unit C showed distinct hydraulic conductivities between their western and the eastern parts (Table S2-1, Fig. S2-1). The median hydraulic conductivity of the eastern part of Unit A was estimated through slug tests to $2.8 \text{ m}\cdot\text{d}^{-1}$, while the western part of Unit A, which present finer grain sediments, showed a lower median hydraulic conductivity with 1.5 and $2.4 \text{ m}\cdot\text{d}^{-1}$, estimated from pump and slug tests, respectively. Similarly, the hydraulic conductivity of the sandy western part is lower ($3.0 \text{ m}\cdot\text{d}^{-1}$, pump tests) than in the eastern part (median $4.7 \text{ m}\cdot\text{d}^{-1}$, pump tests), which is heterogeneous with mixed thin sand and clay layers. The conductivity of those clay layers is extremely low ($< 0.01 \text{ m}\cdot\text{d}^{-1}$, slug tests).

The Unit B, situated between those two Units (Fig. S2-5 and S2-6), is a clay layer with a low conductivity of $0.1 \text{ m}\cdot\text{d}^{-1}$ (Fig. S2-1). The flow velocity v_x can be estimated by the application of the Darcy Law (S2-1):

$$v_x = \frac{K_x \frac{\partial h}{\partial x}}{n_e} \quad (\text{S2-1})$$

The effective porosity n_e was estimated to 0.2 for the whole aquifer based on average literature for sand aquifer matrix. The hydraulic gradients $\delta h/\delta x$ were obtained from the groundwater elevation detected in the monitoring wells (CH2MHill, 2009). The resulting flow velocities were averaged with the value calculated from the groundwater age, determined with tritium/helium-3 (Table S2-1). The final groundwater velocities are presented Fig. S2-1. In the main text, the Unit A and B are referred to as the “shallow aquifer” and Unit C as “deep aquifer”.

Table S2-1 : Estimation of the groundwater velocities based on the aquifer conductivities and groundwater age at the Hill Site (CH2MHill, 2009).

<i>Unit A</i>	West	East
	$0.15 \text{ m}\cdot\text{d}^{-1}$ (slug)	$0.18 \text{ m}\cdot\text{d}^{-1}$ (slug)
	$0.36 \text{ m}\cdot\text{d}^{-1}$ (pump)	$0.12 \text{ m}\cdot\text{d}^{-1}$ (age)
	$0.06 \text{ m}\cdot\text{d}^{-1}$ (age)	
<i>Unit C</i>	$0.15 \text{ m}\cdot\text{d}^{-1}$ (pump)	$1.06 \text{ m}\cdot\text{d}^{-1}$ (pump)
	$0.18 \text{ m}\cdot\text{d}^{-1}$ (age)	$0.09 \text{ m}\cdot\text{d}^{-1}$ (age)

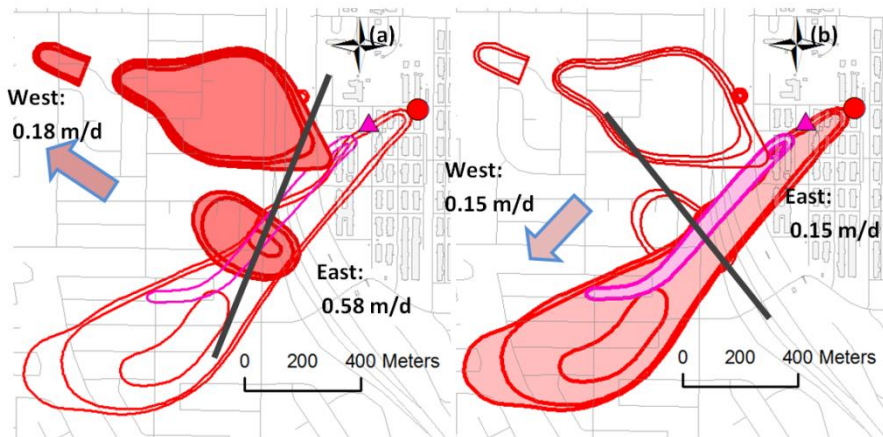


Fig. S2-1 : Final averaged groundwater velocities based on data from Table S2-1, (a) for the deep plumes, (b) for the shallow plumes). The grey line represents the approximate separation between the “eastern” and “western” area, the arrows represent the flow direction for the plumes.

S2.2 Retardation Factors.

Retardation factors R were calculated using the equation (S2-2) (CH2MHILL, 2009):

$$R = 1 + \frac{\rho_b \times K_d}{n_e} \quad (\text{S2-2})$$

The soil bulk density ρ_b was averaged to 1.65 gsd·mLsed from observations at the site. The solid-phase organic carbon-water partitioning (sorption) coefficient K_{oc} quantifies the affinity of a compound with soil. For CEs, K_{oc} decreases from PCE to VC (Table S2-2), ethene’s affinity with organic matter is negligible. K_d values are reported Table S2-2. Organic carbon content (f_{oc}) plays therefore also an important role for CEs retention. In the shallow aquifer, the f_{oc} is low in the sandy areas and retardation has a low impact on the compounds TCE to VC. However, the clay layers and the deep aquifer have a higher f_{oc} : TCE transport is retarded.

Table S2-2 : Parameters for the calculation of the retardation factors, and retardation factors (CH2MHILL, 2009).

	Molar mass (g/mol)	K_{oc} (mL/g)	Retardation factors (no unit)		
			Unit A + B (f_{oc} 0.07 %)	Unit A sand zones (f_{oc} 0.03 %)	Unit C (f_{oc} 0.2 %)
PCE	166	360	3.1	1.9	
TCE	131	120	1.7	1.3	3.0
Cis-DCE	97	36	1.2	1.1	1.6
Trans-DCE	97	59			2.0
VC	62	8			1.1
Ethene	28	10			1.2

S2.3 Redox conditions

Table S2-3 : Statistics on redox and groundwater quality parameters, 2007 sample set (CH2MHILL, 2009).

	Ferrous iron (mg·L ⁻¹)		Dissolved oxygen (mg·L ⁻¹)		Sulphate (mg·L ⁻¹)		ORP (mV)		Nitrate (mg·L ⁻¹)	
	Shallow	Deep	Shallow	Deep	Shallow	Deep	Shallow	Deep	Shallow	Deep
Average value	0.1	0.9	3.9	2.0	35.9	25.7	162	-91	11.5	1.9
Standard Deviation	0.1	0.8	2.1	1.2	20.1	26.5	137	118	10	6.3
Maximum Value	0.8	3.3	11.5	7.6	80	80	380	249	50.9	59.9
Minimum Value	0.0	0.0	0.1	0.1	0	0	243	-374	0.0	0.0
Number of observations	215	161	331	204	176	107	252	181	107	1111

NOTES:mg·L⁻¹= milligrams per Litre

Results correspond to the sampling campaign of 2007

mV = millivolt

Shallow corresponds to data collected in the Upper aquifer (Unit A and B)

Deep corresponds to the data collected in the Lower aquifer (Unit C)

S2.4 Groundwater sampling method

The drillings of the monitoring wells were operated between 1996 and 2008, in total 108 wells were monitoring the shallow plume, and 136 were monitoring the deep plume. During the 2011 sampling campaign, 82 of those wells presented CEs contamination. Most of the wells are long, between 3 and 6 m, with a diameter of 0.05 to 0.1 m. The wells are surrounded by a filter pack extended above and below the screen by 0.6 m, on the top of which 0.6 m of bentonite chips are disposed, topped by bentonite chips or bentonite grout until reaching the surface. Groundwater was sampled either through Low Flow (LF) sampling, Passive Diffusion Bags (PDBs), or Barcad wells. Those technologies are preferred to conventional purge and sample method (Barcelona et al., 2005; Vroblecky and Campbell, 2001).

- Low flow (LF) is the most common sampling method employed at the Hill Site. By applying a sufficiently low velocity to the water during its sampling to limit the drawdown, particulates settled at the bottom of the wells (i.e. artificial additional turbidity) are not mobilized. Furthermore, only a low quantity of stagnant water from above the screen is mixed to either the purged or the sampled water (Barcelona et al., 2005). The quality of the sample is high under the condition to withdraw groundwater until selected parameters (pH, ORP/EH, dissolved oxygen (DO), turbidity, specific conductance, and temperature) stabilize, or a minimum volume of water is withdrawn. The entire screen of the well (3-6 m) is then sampled, independently from the location

of the pump within the well (Varljen et al., 2006), therefore small well screens are recommended for the use of low-flow technologies.

- Four long wells (24 to 34 m), all in the deep aquifer, were sampled using passive diffusion bags (PDBs), i.e. LDPE bags (dimensions: 0.6 m), filled with deionized water and sealed, were placed in the well until equilibrium with the ambient concentrations. This method showed good results for VOCs, and can even detect stratification of the pollutant over depth (Vroblesky and Campbell, 2001). This sampling technic allows only for organic compound analysis.
- Eleven wells were sampled using Barcad technology. This method allows multiple samples at different depth from the same well by isolating the Barcad pumps from each other and reducing the portion of the screen which is sampled with bentonite chips or pellets. The pump themselves are set into fine grained sand. These smaller screens were generally monitoring thin interbedded sand zones.

S2.5 Enhanced Reductive Dechlorination zone

The Enhanced Reductive Dechlorination (ERD) program was launched in November 2007. Further information concerning the zone was not provided. The ERD zone is situated close to the highest TCE concentrations, at a mixing location with the PCE plume. It is likely that well S23 and S25 were control wells (Fig. S2-2). One well, S24, shows complete PCE and TCE transformation into DCE (Fig. S2-3). The other wells for which CE concentrations are known (S25, S26, S23) do not show similar trend (results not shown). At well S24, final $\delta^{13}\text{C-DCE}$ for S24 reaches -27.6 ‰ . This value is situated between PCE and TCE source values, which supports that degradation of PCE to TCE occurred. It is possible that DCE further degradation was a negligible process since the final isotope ratio is not enriched compared to TCE source value. At well S23, upstream from the ERD zone, PCE is enriched ($\delta^{13}\text{C-PCE} = -25.90\text{ ‰}$) but $\delta^{13}\text{C-TCE}$ is not significantly enriched (-25.3 ‰). Chlorine isotopes are not available for this well. At this location, the degradation pathway for PCE, which present a high molar fraction ($\approx 50\%$) is not clear. PCE could have oxidized, leading to no TCE production, but it is more likely that PCE reduced to TCE, which further degraded as well although no DCE is detected. Due to the little information concerning the ERD zone, S23 and S24 are generally not employed. S25 and S26 present $\delta^{13}\text{C}$ for TCE and PCE in the range of the source as determined Section 2.4.1 and are therefore not considered to be dramatically influenced by the actions taken at the ERD zone.

S2.6 Lithology



Fig. S2-4 : PCE and TCE plumes and cross section lines (A-A' and C-C' (C-C' is B-B' in the main text)).

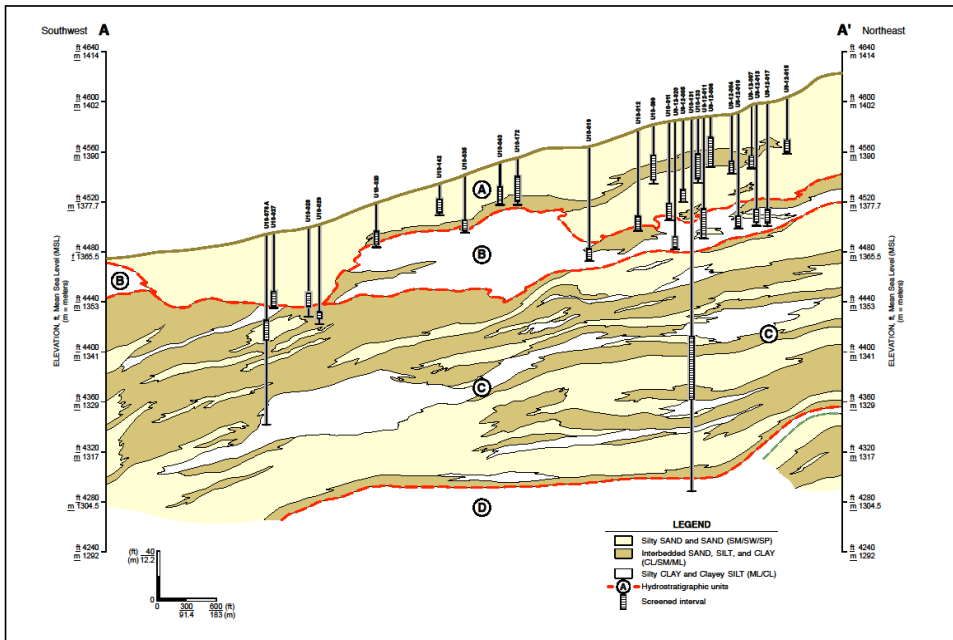


Figure S2-5 : Transect A-A' lithology (transect as in Fig. S2-4).

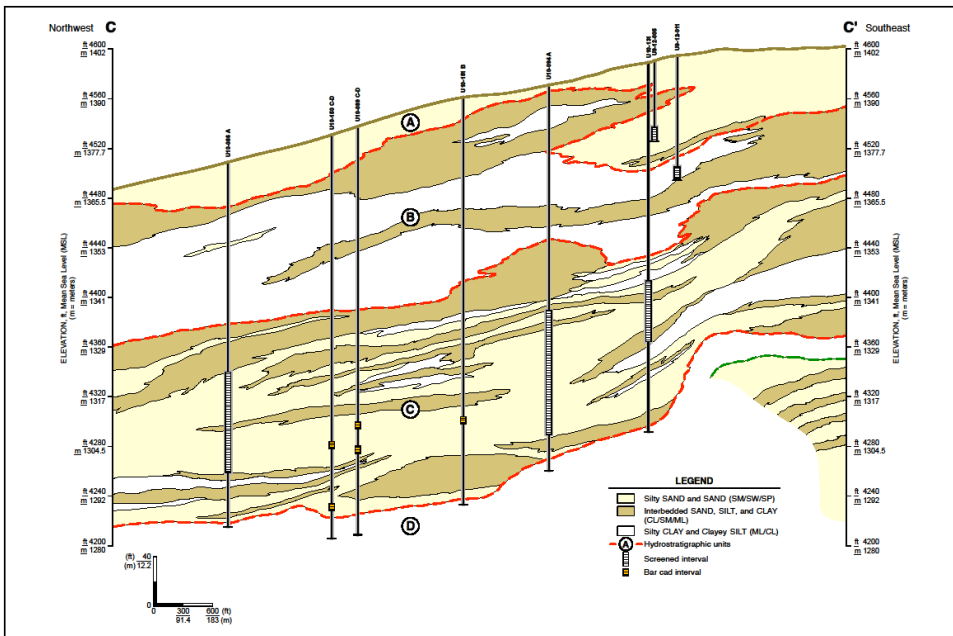


Fig. S2-6 : Transect C-C' lithology (transect C-C' as in Fig. S2-4, transect B-B' in the main document Fig. 2-1 and Fig. 2-14).

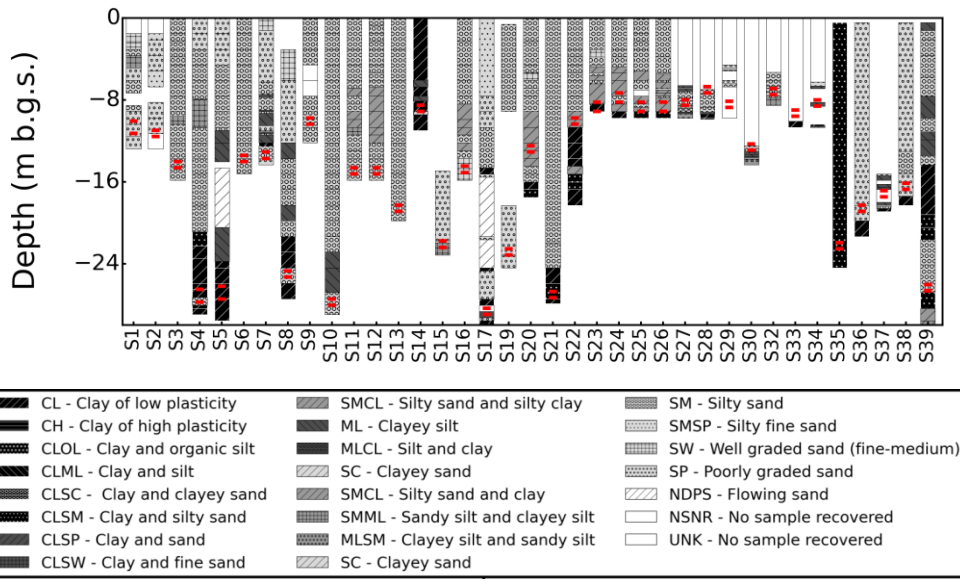


Fig. S2-7 : Lithology of the subsurface for shallow wells. The well screen top and bottom are indicated with a red symbol.

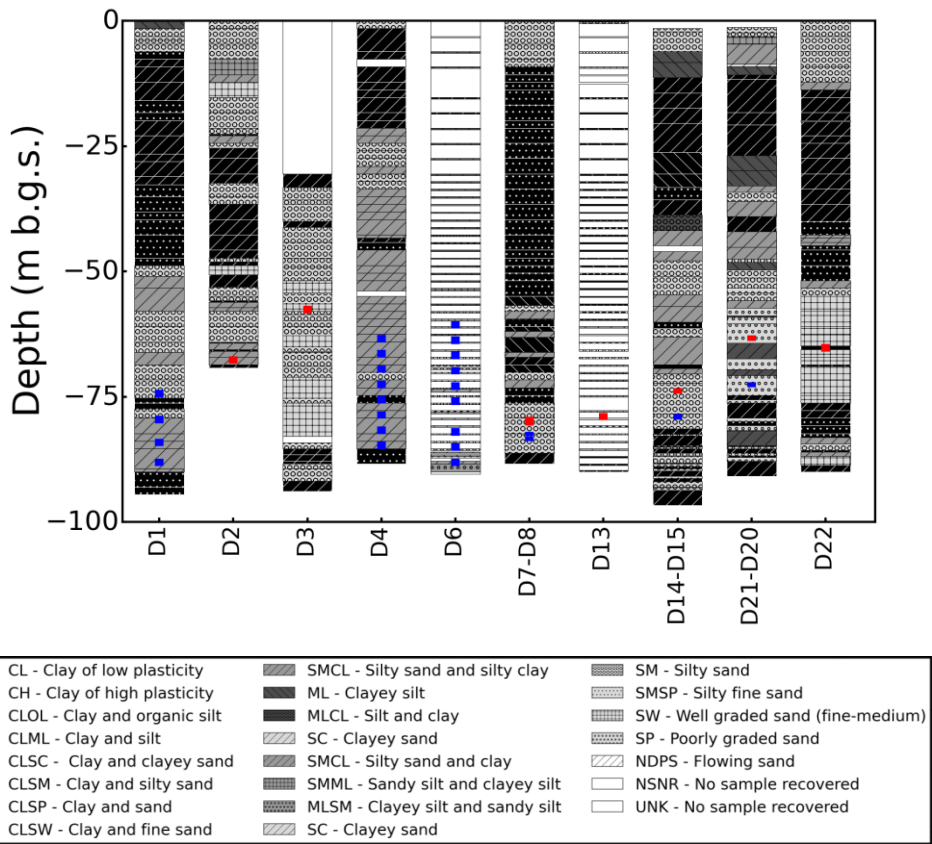


Fig. S2-8: Lithology of the subsurface for deep wells. The well screen top and bottom are indicated with a red symbol, except when two Barcad wells were set (D7-D8, D14-15, D20-21) in which case the second well is marked with a blue symbol. PDB wells (D1, D4, D6) are in blue.

S2.7 TCE attenuation through aerobic cometabolism

Enzyme-activity of aerobic TCE cometabolic bacteria was tested in groundwater samples from 8 different wells using the rapid fluorescence-based assay described in Miller et al. (Miller et al., 2002), which assesses both the presence and the activity of the soluble methane monooxygenase (sMMO). This enzyme is expressed by methane oxidizing bacteria, which are involved in cometabolic degradation of not only TCE but also other chloroethenes (Alvarez-Cohen 2001). Microbial DNA testing following the Baldwin et al. (Baldwin et al., 2003) procedure proves the potential degradation activity of a sample by detecting the presence of genes coding for biological oxygenase. Finally, 4',6-Diamidino-2-Phenylindole (DAPI), a stain that binds to DNA, was used to determine the total cells count. Results are presented on Fig. S2-10 (CH2MHill, 2009). Toluene oxygenase also was detected, following the same method.

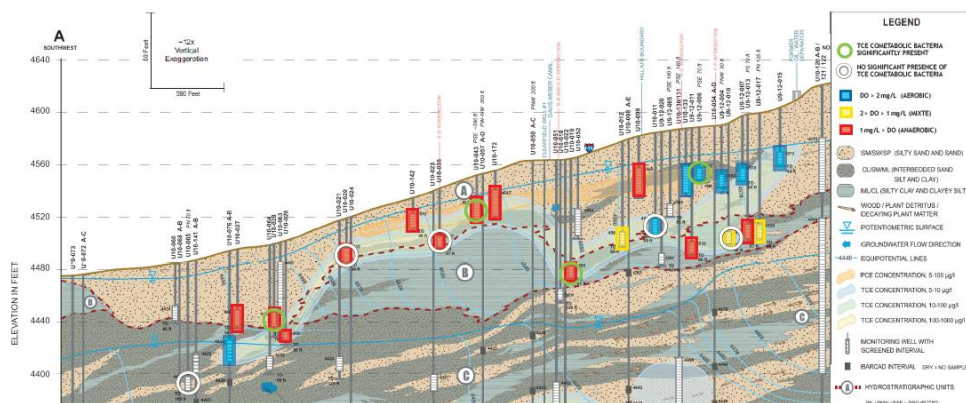


Fig. S2-9 : Enzyme-activity testing: Green circles: presence of TCE cometabolic bacteria, White circles: test did not reveal the presence of TCE cometabolic bacteria. Squares: levels of oxygen concentrations (red: 0 – 1 mg/L, yellow 1 – 2 mg/L, blue > 2 mg/L).

In plus of the enzyme-activity testing, the degradation rate of TCE by aerobic cometabolism was determined in laboratory batch tests using groundwater from 4 wells where both TCE and TCE cometabolic bacteria were detected. TCE and its daughter products were regularly measured. Since TCE concentrations decreased in the unamended vials, without production of DCE, the experiment proved the occurrence of clear aerobic degradation and, therefore, presence of TCE cometabolic bacteria. However, as mentioned above, the wells sampled for this experiment showed low DO concentrations, whereas the samples were reported to be potentially contaminated by atmospheric oxygen when sampled (CH2MHill, 2009).

S2.8 Characterization of Chlorinated Solvent Source Zones

For interpretation of CSIA data of plume samples it is crucial to determine the isotope signatures of the original solvent spills as precisely as possible. The investigation of the historical sources is described in detail in (CH2MHill, 2009). Since the investigation of the site began in 1995, approximately 50 years after the both spills, the pure products were not available anymore for investigation. Therefore the source isotope signatures had to be approximated. For this purpose, candidate source samples were selected based on the following criteria: (i) their carbon isotope ratio complied with known source values for industrial PCE and TCE (-30 to -25 ‰ (Kuder and Philp, 2013; Shouakar-Stash et al., 2003), (ii) relatively high concentrations, (iii) relatively low $\delta^{13}\text{C}$ (iv) absence of mixing between the TCE and PCE plumes (Table S2-4 and S2-5) for the shallow plume, or (iv) low DCE concentrations for the deep plume. Finally, a unique value was used for $\delta^{13}\text{TCE}$ without distinction between shallow and deep plumes.

Table S2-4 : Locations presenting the potential source values for TCE.

Location	Distance to TCE source (m)	C_{TCE} ($\mu\text{mol/L}$)	x_{TCE} (%)	$\delta^{13}\text{C-TCE}$	Comment	$\delta^{37}\text{Cl-TCE}$	$\delta^2\text{H-TCE}$
S15*	405	0.152	97	-26.2	Lowest carbon isotope ratio, but PCE is enriched ($\delta^{13}\text{C} = -20$ ‰). PCE degradation might, therefore, have depleted this TCE carbon isotope ratio.	2.7	-251
S2	67	0.110	99	-26.0	Second most depleted isotope ratio for TCE	2.3	-256
S28	971	0.719	98	-25.5	Second highest concentration and one of the most depleted carbon isotope ratio value, nearly pure TCE.	4.1	-260
S29	979	0.135	100	-25.4		4.6	-193
S26	895	0.749	88	-25.2	Highest concentration, relatively high carbon isotope ratio, $X_{\text{TCE}} < 90\%$	4.7	-192
S33	1248	1.05	100	-25.6		4.3	-259
D15	900	2.72	94	-24.2		2.6	-266
D11	771	0.822	85	-23.7		2.6	-247

* *Lowest isotope ratio.*

Table S2-5 : Locations presenting the potential "source values" for PCE.

Location	Distance to PCE source (m)	C _{PCE} (μmol/L)	X _{PCE} (%)	δ ¹³ C-PCE	Comment	δ ³⁷ Cl-TCE
S12*	197	0.078	99	-32.70	Lowest isotope ratio for PCE highest molar fraction.	-0.53
S9**	132	0.771	89	-31.50	Highest concentration	-1.40
S18	108	0.274	87	-31.38		-0.67

* *Lowest isotope ratio.* ** *Selected source signature.*

The selected source signature (δ¹³C-TCE = -26 ‰, δ³⁷Cl-TCE = 2.5 ‰, δ²H-TCE = -255 ‰) for the TCE plumes (both shallow and deep), is similar to the signature of wells such as S2, upgradient from the PCE plume (Fig. S2-3). The uncertainty on the source value was set to be equal to the standard analytic uncertainty (i.e.: carbon ± 0.5 ‰, chlorine ± 1 ‰ and hydrogen ± 15 ‰).

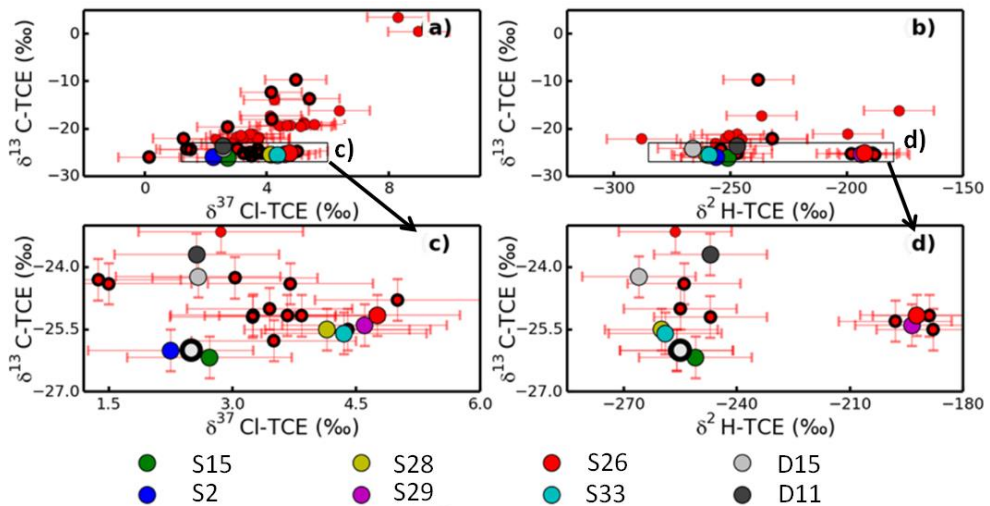


Fig. S2-10 : Repartition of TCE potential sources values on dual C-Cl and C-H plots. Final source value (white circle with back contour) was finally chosen.



Fig. S2-11 : Map of the wells presenting TCE $\delta^{13}\text{C}$ and $\delta^{37}\text{Cl}$ potentially similar to the original solvent signature (Fig. S2-10).

S2.9 CIMB and oxygen levels

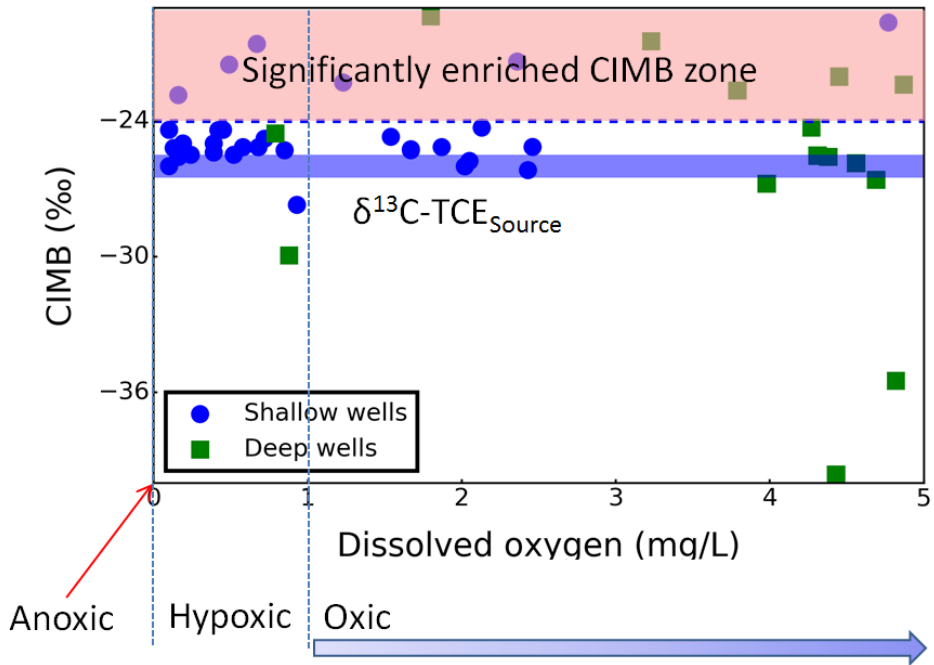


Fig. S2-12 : CIMB versus dissolved oxygen (data from 2011 sampling campaign) (CH2MHill, 2011). The dissolved oxygen concentrations in the deep aquifer are surprisingly high compared to the previously produced data (average dissolved oxygen concentrations was 2 mg/L (CH2MHILL, 2009)). Enriched CIMB is detected throughout the observed range of dissolved oxygen at the site, minimizing the importance of dissolved oxygen concentrations as a line of evidence for aerobic degradation.

S2.10 Precipitations

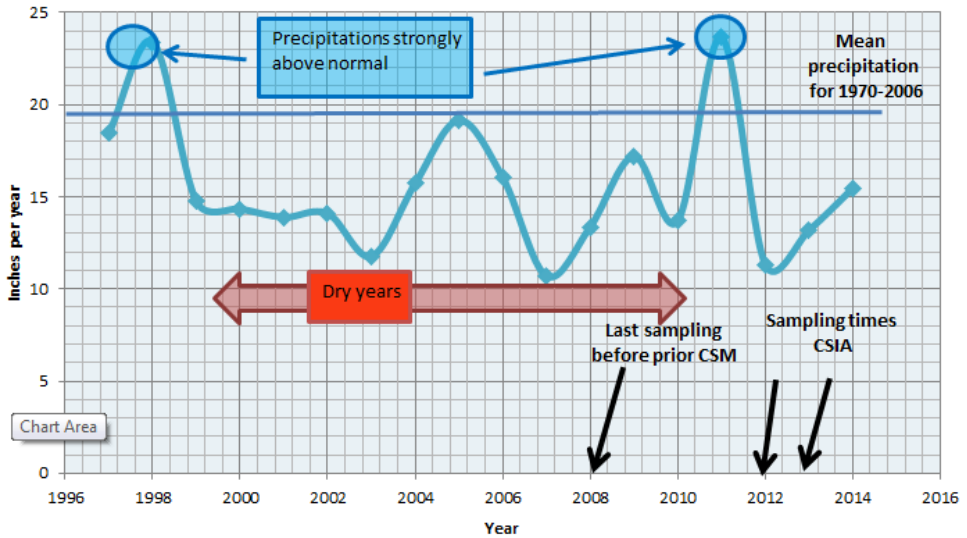


Fig. S2-13: Precipitations at the Hill Air Force Base (Utah) 1996-2014 (IAEA/WMO, 2014).

S2.11 TCE enrichment in chlorine-37 with distance

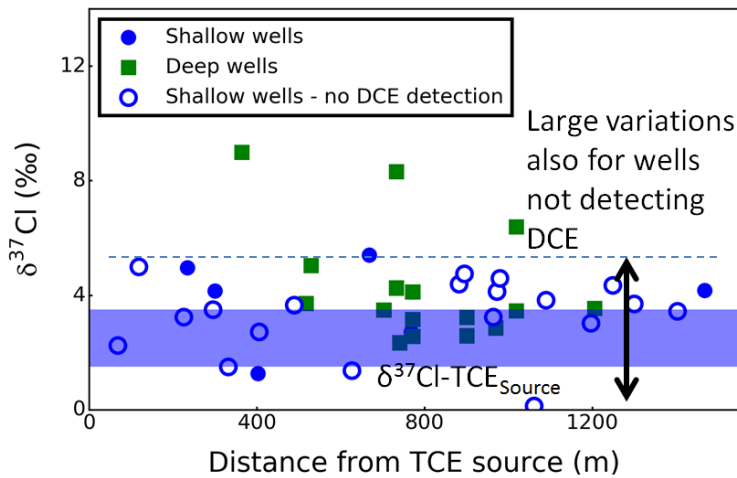


Fig. S2-14 : $\delta^{37}\text{Cl-TCE}$ versus distance from the TCE source.

S2.12 CIMB uncertainty calculation

The uncertainty of the CIMB was calculated based on the error propagation using the error reported for each carbon isotope measurement ($\Delta\delta^{13}C_i$, 0.5 ‰ to 4 ‰) and the error on concentrations (ΔC_i , 10 %) of the concentration (Stelzer et al., 2009):

$$\Delta_{CIMB} = \frac{\sqrt{\sum (C_i \times \Delta\delta^{13}C_i)^2 + \sum ([\delta^{13}C_i - CIMB] \times \Delta C_i)^2}}{\sum C_i} \quad (S2-3)$$

Where CIMB is calculated following eq. 2-1 (main document).

S2.13 Relation between $\delta^{13}C$ -tDCE and $\delta^{13}C$ -cDCE

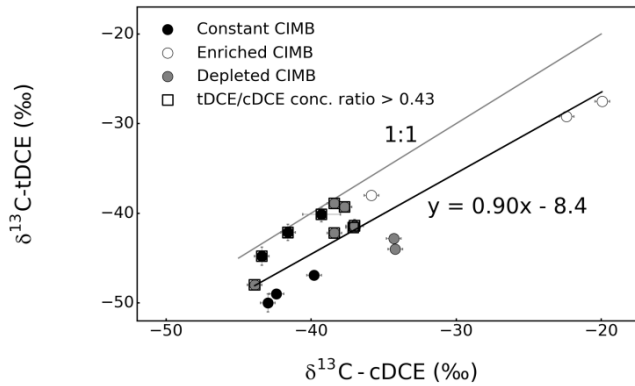


Fig. S2-15 : $\delta^{13}C$ -tDCE vs. $\delta^{13}C$ -cDCE. Constant CIMB (white, $-26.5 \text{ ‰} < CIMB < -24 \text{ ‰}$), enriched CIMB (white, $CIMB > -24 \text{ ‰}$), depleted CIMB (grey, $CIMB < -26.5 \text{ ‰}$). The York fit of the data (all data) is indicated on the plot. Additional squares are plotted for wells detecting very large tDCE/cDCE concentration ratio (>0.43 , i.e. trans-DCE represents more than 30 % of the DCEs).

S2.14 Relation between $\delta^2\text{H-tDCE}$ and $\delta^2\text{H-TCE}$.

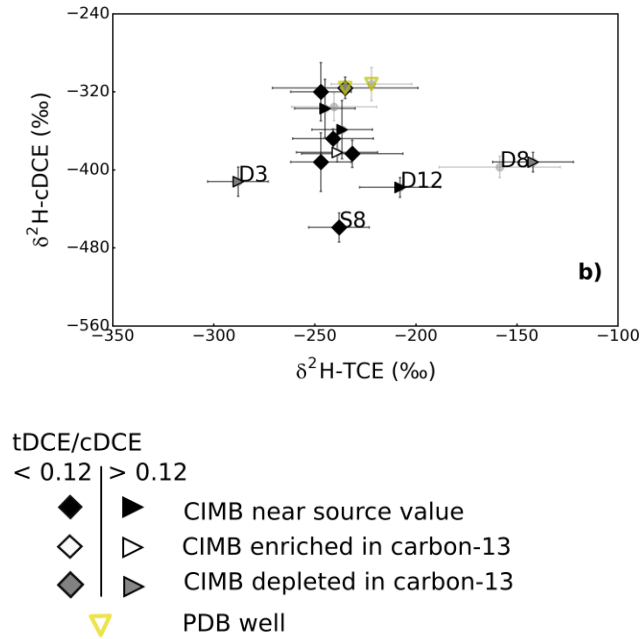


Fig. S2-16 : $\delta^2\text{H-cDCE}$ vs. $\delta^2\text{H-TCE}$.

S2.15 2014 versus 2011 data.

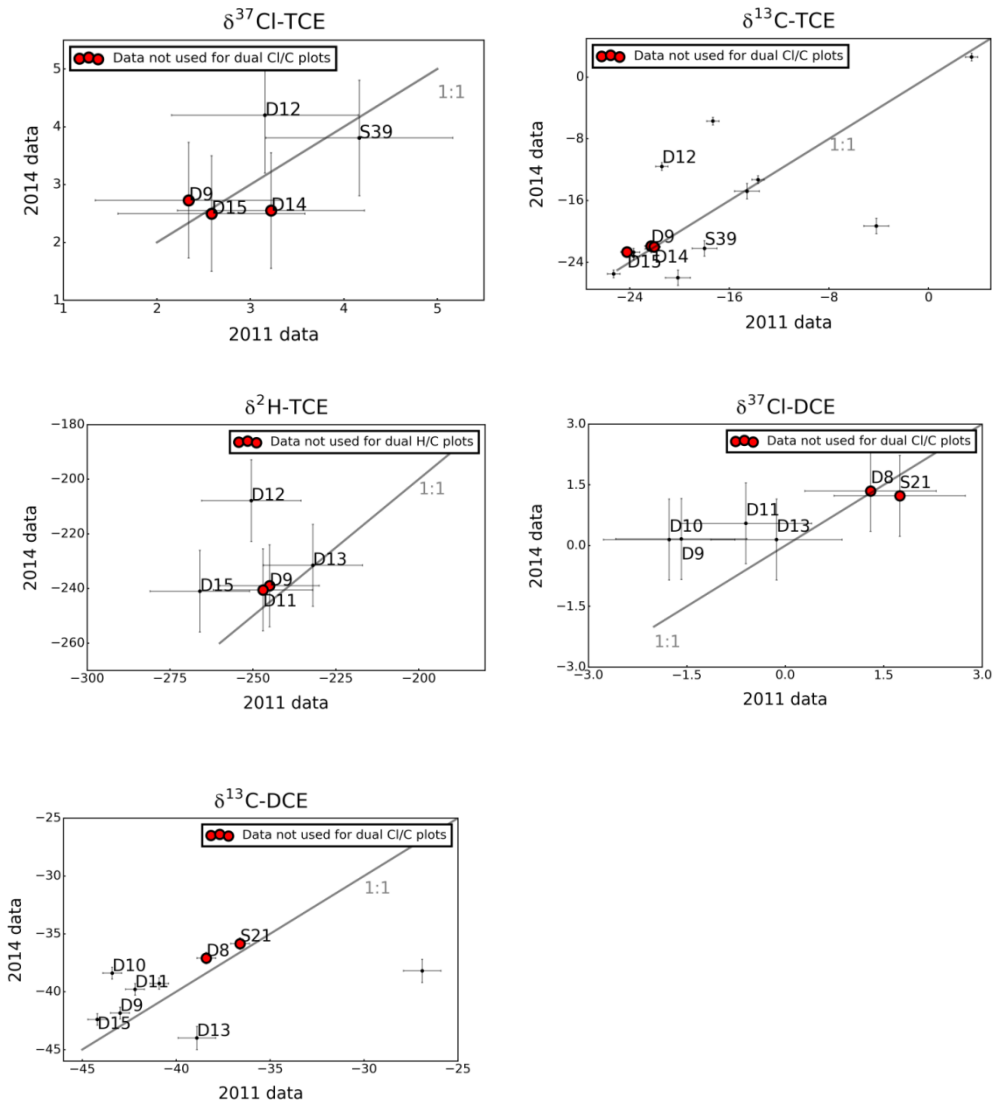


Fig. S2-17 : 2014 vs. 2011 data for $\delta^{37}\text{Cl-TCE}$ and $\delta^{13}\text{C-TCE}$, $\delta^2\text{H-TCE}$, $\delta^{37}\text{Cl-DCE}$ and $\delta^{13}\text{C-DCE}$.

S2.16 CIMB for the detection of CEs plumes mixing

Isotope signatures were already successfully employed for studying plumes mixing in presence of degradation (Blessing et al., 2009; Lutz and Van Breukelen, 2014). This section illustrates the specific potential of carbon isotope mass balance (CIMB) for detecting

plumes mixing, using the example of the shallow PCE and TCE plumes. Since $\delta^{13}\text{C-PCE}_{\text{source}}$ is depleted compared to $\delta^{13}\text{C-TCE}_{\text{source}}$, the mixing of both plumes will cause the complete carbon isotope mass balance including PCE (CIMB_{PCE}) to take any value between both source values, provided reductive dechlorination is the sole transformation process. The mixing lines representing the expected isotope ratio of the CEs mixture in the absence of degradation are plotted in Fig. S2-18. From the left to the right, the mixing lines (which include the uncertainty on the sources $\delta^{13}\text{C}$ values) show how TCE evolves from being negligible, with PCE being the main pollutant, to being the main pollutant controlling the CIMB_{PCE} .

For 9 wells, CIMB_{PCE} takes value in the range of the dominant compound's source isotope signature. One well, S6, is situated in the middle of the mixing lines, signalling strong mixing of the plumes.

CIMB_{PCE} plots above the mixing lines for 3 wells, namely S5, S20 and S23. If reductive dechlorination was the only pathway impacting CEs, PCE degradation to TCE or TCE degradation to DCEs should conserve the CIMB_{PCE} value, while TCE concentrations will increase (towards the right) or decrease (towards the left), respectively. Those 3 wells therefore might detect TCE degradation to DCEs. On the other hand, CEs mineralization (likely through cis-DCE degradation, according to the manuscript) will lead to CIMB_{PCE} enrichment. Only then it would be impossible to detect TCE production from PCE degradation, if any, as CIMB_{PCE} might enrich above the mixing line. Consequently, CIMB_{PCE} confirms little mixing occurs between both plumes.

Of the 3 wells, only one well detects DCEs (S5, with molar fractions of cis-DCE ~ 60 % and of trans-DCE < 5 %). The strong enrichment of the CIMB_{PCE} calculated at this well likely expresses degradation beyond DCEs. At well S23, the highly enriched PCE and the lack of DCEs would suggest that TCE production was intense and TCE did not degrade further, which is in contradiction with the enriched value for CIMB_{PCE} . This intricate pattern is difficult to explain but could relate to the processes that occurred at the enhanced reductive dechlorination zone where S23 was drilled. At S20, both TCE and PCE show strong $\delta^{13}\text{C}$ enrichment while the CIMB_{PCE} is enriched. The lack of detection of DCEs could be due to the very low concentrations its parents compounds ($[\text{PCE}] = 0.004 \mu\text{M}$ and $[\text{TCE}] = 0.03 \mu\text{M}$), as the concentrations of produced DCE might fall below quantification limits. Similarly, at well S15 where strong PCE degradation is expected, PCE concentration are so low that its degradation might not have strongly impacted $\delta^{13}\text{C-TCE}$. Consequently, CIMB_{PCE} confirms little mixing occurs between both plumes.

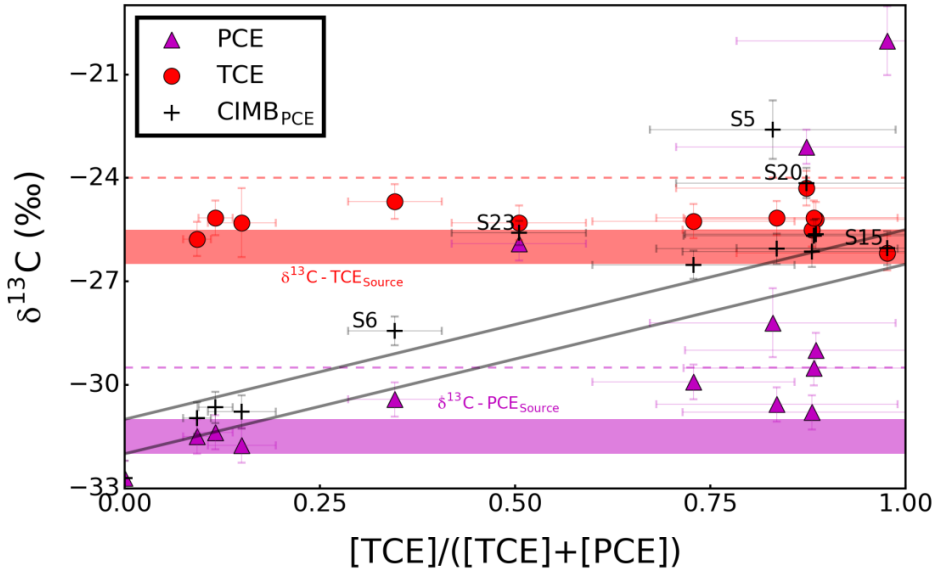


Fig. S2-18 : Complete carbon isotope mass balance (PCE values included) (black crosses), $\delta^{13}\text{C}$ -PCE (purple triangles), and $\delta^{13}\text{C}$ -TCE (red circles), plotted versus TCE proportion compared to the sum TCE and PCE concentrations. Only wells at which $\delta^{13}\text{C}$ -PCE was reported are represented. The isotope source values are represented by their uncertainties range, in purple for PCE and red for TCE. The dashed lines represent the value above which CIMB_{PCE} is significantly enriched compared to $\delta^{13}\text{C}$ - $\text{TCE}_{\text{source}}$ (red) and $\delta^{13}\text{C}$ - $\text{PCE}_{\text{source}}$ (magenta). Grey lines show the expected range for CIMB_{PCE} provided PCE and TCE are not degrading. Wells numbers signal atypical CIMB_{PCE} values.

S2.17 York-fit pseudo code

An algorithm in pseudo-code for computing the slope and intercepts of the best fit line through the York fit is published in the Appendix in (Wehr and Saleska, 2016). While we encourage the reader to employ this pseudo-code, it requires a small correction, presented below.

When defining W_i in the 10th line of the pseudo code, the following equation is employed:

$$W_i = \alpha_i^2 / (b^2 \omega_{Y,i}) + \omega_{X,i} - 2br_i \alpha_i, \text{ which is wrong.}$$

The correct equation is:

$$W_i = \alpha_i^2 / (b^2 \omega_{Y,i} + \omega_{X,i} - 2br_i \alpha_i)$$

This correction is published with the agreement of the authors R. Wehr and S. R. Saleska.

This page was intentionally left blank

Chapter 3

Dual C and Cl CSIA batch modeling for refinement of a conceptual site model on chlorinated ethene degradation

Abstract

This modeling study sets out to illustrate the potential and limitations of multiple compound-specific stable isotope analysis (CSIA) modeling for testing hypotheses and finding proof for specific degradation pathways and the extent of chlorinated ethenes (CEs) degradation in groundwater. For that purpose, CEs datasets obtained at the Hill air force base (Utah) were modelled. Carbon (C) and chlorine (Cl) CSIA data of trichloroethene (TCE) and cis-dichloroethene (cis-DCE), as well as C CSIA data of trans-DCE were available from a previous study for a large number of groundwater wells. A first study of the CSIA data without additional modeling brought further insights to a prior concentration-based conceptual site model (CSM). This previous CSIA-enabled CSM improvement confirmed the spatial distribution of CEs reductive dechlorination (RD) priority described as occurring at the site. Whether DCE isomers or vinylchloride (VC) oxidized was not clear. Although unlikely, faster TCE than cis-DCE cometabolism could cause the carbon isotope mass balance (CIMB) decrease as observed at the site; alternatively low CIMB could result from differential transport during back-diffusion effects. Simulations were envisaged to support the hypothesis that TCE degraded through two different reductive pathways, to determine cis-DCE degradation pathway (oxidative or reductive), and to investigate further the potential TCE degradation through the methane-oxidizing pathway.

The complexity of the site made reactive transport modelling of the CSIA data unfeasible due to the spatial heterogeneity of the degradation rate constants. Instead, simulations were obtained with a batch model and compared to the available dataset. This method required neither the additional transport hypotheses, nor the computational effort of multi-dimensional models. Simulations of C and Cl CSIA during TCE degradation to DCE isomers matched the DCE data for wells with constant CIMB, at which DCE isomers degradation stalled. The ranges of CSIA and molar fraction patterns could correspond to TCE degradation through two pathways differing from their relative tDCE/cDCE ratios and TCE enrichment factor. Where degradation beyond DCE isomers was expected, simulations of cis-DCE either via RD or oxidation matched best cis-DCE data when the corresponding carbon isotope enrichment factor was set to a large value. The limited

isotope fractionation of chlorine isotopes for both reductive and oxidative pathways of cis-DCE prevented the investigation of cis-DCE degradation using chlorine isotope ratios modeling. Additionally, simulating simultaneously TCE and cis-DCE RD seemed to match best the observed patterns, with some exception as for instance at the extremity of the shallow plume. Under the hypothesis that VC quickly degraded further, the TCE and DCE RD model helped narrowing the maximum CSIA-based CEs mineralization expected at the different wells to roughly 45 %. A low fractionation pathway such as methane induced TCE cometabolism could have influenced CEs molar fractions, however, it is insufficient to explain the isotope and molar fraction patterns in the deep aquifer. The simulations allow concluding that the process leading to CIMB decrease impacted all the wells upgradient in the deep plume, also when the calculated CIMB was enriched due to further CEs mineralization. Low CIMB could be linked to the intense CEs RD which might occur in the aquitard in this area. Differential back-diffusion due to sorption remains a preferred explanation to the CIMB decrease for those wells. In this study, batch models offer a first and computational less extensive modelling approach for process interpretation of multiple-CSIA data at sites presenting complex sub-surface conditions and multiple degradation pathways.

3.1 Introduction

Chlorinated solvents, widely used as degreasing agents in industry and for dry-cleaning, are toxic and ubiquitously present in groundwater due to spills or inadequate disposal. Recent developments in the understanding of naturally occurring CEs transformation pathways allowed relying on natural degradation pathways for polluted site remediation (Bradley, 2003; Mulligan and Yong, 2004). In order to rely on the natural capacity for the aquifers to degrade CEs, it is necessary to prove the occurrence of sustained degradation to non-toxic compounds. For this purpose, the study of the isotope composition of the CEs is increasingly employed. Different reaction speeds for the heavy (^{13}C , ^{37}Cl) and for the light (^{12}C , ^{35}Cl) isotopes lead to change in the isotope composition of the source compound which can be linked to its extent of degradation. The extent of isotope fractionation also depends on the degradation pathway (Abe et al., 2009a; Chu et al., 2004; Fox et al., 1990). Simultaneous chlorine and carbon isotope enrichment provided the opportunity to employ combined Cl/C CSIA slopes for identifying CEs degradation pathways at field sites (Badin et al., 2016; Clark et al., 2016; Hunkeler et al., 2011b; Wiegert et al., 2013, 2012). Metabolites from biotic reductive dechlorination are initially depleted in carbon-13 (Hunkeler et al., 1999; Sherwood Lollar et al., 2001), and might also present a different chlorine isotope composition than its precursor as a result from chlorine isotope fractionation at non-reactive bonds or even intramolecular heterogeneity (Cretnik et al., 2014; van Breukelen et al., 2017). Consequently, degradation assessment is increasingly intricate in presence of sequential degradation, as formation and degradation simultaneously impact the isotope ratios of the metabolites.

Combining isotope fractionation with analytical or numerical reactive transport models (IF-RTM) was highly beneficial for degradation assessments at field sites, as it unravelled the complex isotope patterns resulting from combined production and degradation during reductive dechlorination. The common simplifying modeling assumption that degradation rate constants are spatially homogeneous (Hunkeler et al., 1999) is now unsatisfying as aquifers reveal heterogeneous degradation zones (Atteia et al., 2008; Clement et al., 2000; Höhener et al., 2015; Sherwood Lollar et al., 2001). Facing the complexity of the modeling task, studies of field data often focus on a single flow line with 1-D or 2-D simulations, resulting in the modeling of CSIA data from 3 to 7 wells, with a maximum of 9 wells (Audí-Miró et al., 2013; Höhener, 2016; Höhener et al., 2015; Hunkeler et al., 1999; Pooley et al., 2009; Wiegert et al., 2013). However, CSIA is currently meant to be an additional tool where concentration patterns are complex to interpret; therefore, exploiting all available data would help evaluating the requirements for improving the performance of IF-RTM under more complex subsurface settings. A potential way to quickly model most data while bypassing limitations relative to aquifer complexity is to employ simpler batch-

models focusing on degradative pathways, using the relative CEs concentrations instead of the absolute CEs concentrations.

Batch models are limited for data interpretation as they do not include physical processes. Non-destructive processes such as sorption, diffusion and dispersion were also shown to result in isotope fractionation (Höhener, 2016; Jin et al., 2014; Kopinke et al., 2005; Wanner and Hunkeler, 2015). Mass-transfer processes such as diffusion impact chlorine isotope ratio to greater extent as the mass difference between both isotopes is larger for chlorine ($^{37}\text{Cl}/^{35}\text{Cl}$) than for carbon ($^{13}\text{C}/^{12}\text{C}$) (Wanner and Hunkeler, 2015). Hence, CSIA-based degradation assessments have to be handled with care where those processes interact with isotope ratios. Alternatively, the resulting enrichments might reveal zones impacted by physical attenuation processes (Chapter 2). When using batch-modeling, the impact of physical processes on the molar fractions and isotope ratios cannot be modelled. Systematic variations of the field data compared to a model focused on degradation pathways could be employed to discuss the occurrence of those processes. Batch modeling was applied before at a field study with complex and poorly defined hydrogeological conditions where all carbon isotope data from wells near a CE source could be simulated in this way (van Breukelen et al., 2005). Batch modeling was yet neither applied to the study of combined CEs reductive dechlorination and oxidation nor to multiple-element CSIA data.

The objective of this paper is to employ dual-CSIA modeling to thoroughly exploit the available dual CSIA data, notably for assessing the occurrence of CEs degradation via reductive and oxidative transformation. To this end, modeling was applied to dual CSIA data from an intensively sampled site which was already well described. At this site, reductive dechlorination of TCE occurred, cis-DCE reductive degradation occurred, but the occurrence of both TCE and cis-DCE oxidative degradation was uncertain (Chapter 2). Additionally, the prior study implied that TCE reductive dechlorination rates varied in the aquifer, and that TCE degraded through two different reductive pathways producing different amount of DCE trans- and cis- isomers. Trans-DCE is rarely a focus of degradation studies, as it is generally produced in lesser quantity than cis-DCE. However, microorganisms reducing TCE dominantly to trans-DCE are usually inefficient to degrade CEs beyond DCEs (Cheng et al., 2010; Cheng and He, 2009; Kittelmann and Friedrich, 2008; Marco-Urrea et al., 2011; Miller et al., 2005). Therefore, assessing TCE degradation is crucial to assess complete reductive dechlorination to non-toxic products at the site. Moreover, whether trans-DCE degraded further was unclear. The simulation of different plausible degradation pathways using sound input parameters could bring further insights to this first study. The acquirement of the aquifer parameters necessary to reproduce the spatial distribution of concentrations and isotope enrichment at the site seemed to be a highly complicated task for little reward. With a batch model, the paper aims at i) modeling C and Cl isotope fractionation and relative concentrations for multiple degradation

pathways using site derived (or when necessary literature-derived) enrichment factors, ii) testing the potential of a batch model for discussing degradation hypotheses.

3.2 Methodology

3.2.1 Field site description

The Operational Unit 10 (OU10) is an area of the Hill air force base (Utah) which was intensively monitored before and being sampled for triple element (C/Cl/H) CSIA. The CSM presented in a report prior to the CSIA campaign (CH2MHILL, 2009) is briefly summarized in Chapter 2 were the CSIA-based update of CSM from the CSIA study is presented. Beneath the Hill Site Operational Unit 10 lie two aquifers, on top of each other, separated by an aquitard (Fig. 2-1 in Chapter 2 and Fig. 3-1). The shallow aquifer is unconfined, and composed of fine to coarse sand and clay lenses. The eastern extent of the deep aquifer is composed of interbedded sand, silt and clay layers, while the western extent presents large sand packs. Groundwater velocity is about constant through the shallow aquifer ($0.15 \text{ m}\cdot\text{d}^{-1}$), but decreases from the eastern ($0.58 \text{ m}\cdot\text{d}^{-1}$) to the western part of the deep aquifer ($0.18 \text{ m}\cdot\text{d}^{-1}$).

TCE likely leaked from an oil/water separator between 1940 and 1959. The leak formed a shallow plume which travels at the surface of the aquitard, the latter being sufficiently porous to have transported TCE from the shallow aquifer to the deep aquifer at three locations (red arrows in Fig. 3-1). The leakages result in two deep TCE plumes, a large plume to the North and a small plume to the South. Both the shallow and the deep northern plumes travelled about 1000 m. Cis- and trans-DCE were detected in both the shallow and deep aquifer. VC, ethene and 1,1-DCE were detected punctually (both spatially and temporally) (Fig. 3-1), mostly at trace concentration, except for four wells in the deep aquifer at which concentrations of 0.04 to $0.53 \text{ }\mu\text{mol}\cdot\text{L}^{-1}$ were detected. The highest total CEs concentration is now detected at well D3 in the deep aquifer. A small shallow PCE plume present at the site was estimated to have a negligible impact on other CEs concentrations and is not further discussed.

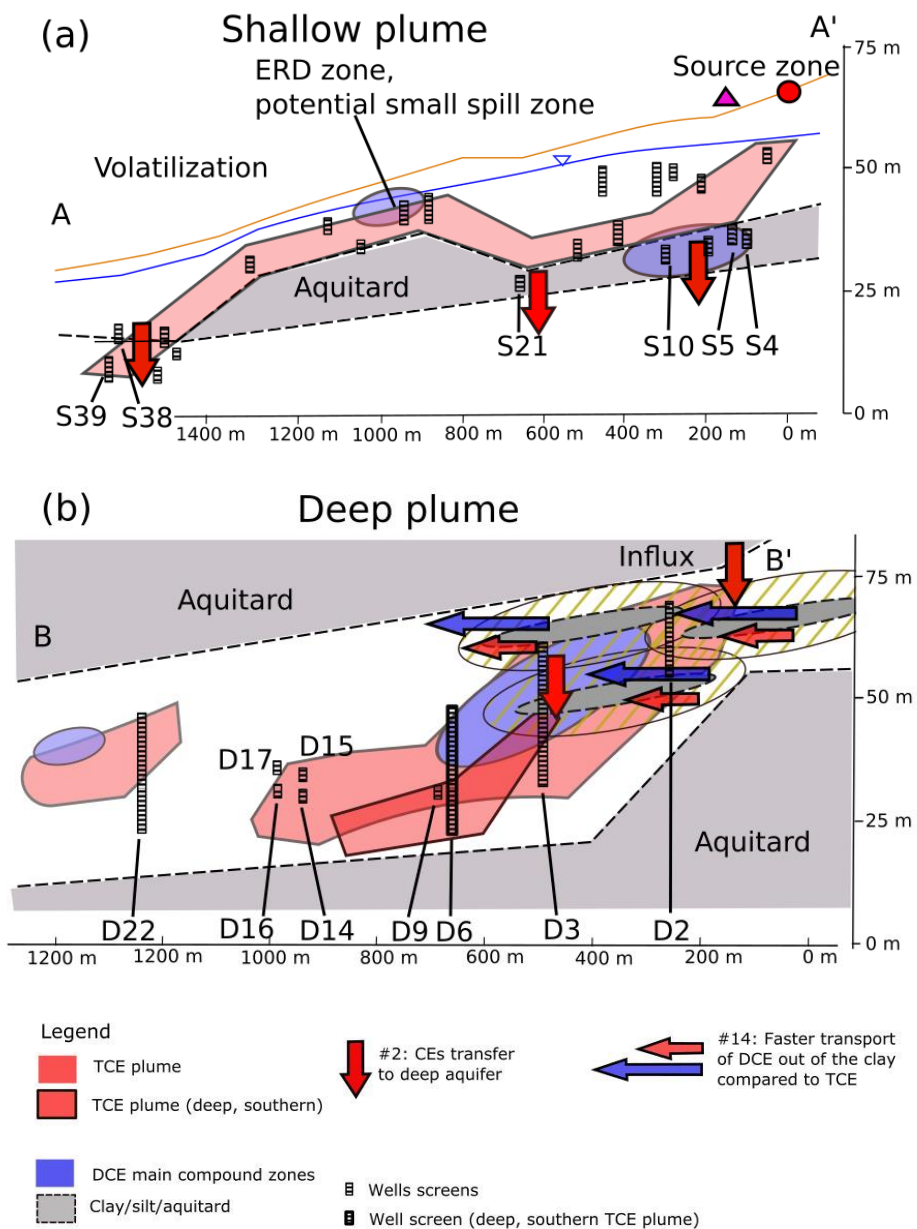


Fig. 3-1 : Subsurface view of the shallow (a) and deep plume (b) summarizing the processes affecting both TCE and cis-DCE concentrations and isotope patterns (defined Chapter 2). Only wells along the cross sections A-A' and B-B' (Fig. 2-1 Chapter 2) are shown, the southern deep plume (sampled by D6 only) was added on top of the northern deep plume cross section. The different degradation processes estimated to occur at the site (reductive dechlorination, cometabolism) and the physical processes interacting with the isotope ratios (differential sorption, volatilization, and diffusion) are represented.

Carbon, chlorine and hydrogen isotope ratios ($\delta^{13}\text{C}$, $\delta^{37}\text{Cl}$, and $\delta^2\text{H}$) of the different CEs were collected during two sampling campaigns at three year interval (2011 and 2014) (Kuder et al., 2016). TCE isotopic source values of the main TCE source were reconstructed for each element (in the delta notation, $\delta^{13}\text{C-TCE}_{\text{Source}}$, -26.5 ‰ to -25.5 ‰, $\delta^{37}\text{Cl-TCE}_{\text{Source}}$, 1.5 ‰ to 3.5 ‰; $\delta^2\text{H-TCE}_{\text{Source}}$, -270 ‰ to -240 ‰ (Chapter 2).

3.2.2 Summary of the conceptual site model for CEs degradation and isotope fractionation

Isotope fractionation at the site was investigated in Chapter 2. The background information supporting the assumptions relatively to isotope fractionation at the site is summarized here.

3.2.2.1 TCE reductive dechlorination

Occurrence of TCE reductive dechlorination in both aquifers was clear based on the presence of DCEs (both cis- and trans-). TCE reductive dechlorination seems strongest near or in the low-permeability zones (clay or silt lenses) of the deep aquifer, and at the bottom of the shallow aquifer near the aquitard. Because large DCEs concentrations were detected in the upgradient extent of the deep plume but not in its downgradient extent, the sand layers of the deep aquifer were assumed to present inadequate conditions to reductive dechlorination (CH2MHILL, 2009). The first CSM therefore hypothesised that TCE reductive dechlorination took place in the low-permeability layers of the deep aquifer. Large $\delta^{13}\text{C-TCE}$ enrichments (>-24 ‰) and $\delta^{37}\text{Cl-TCE}$ enrichments confirmed stronger TCE degradation in the upgradient extent of the deep plume compared to the downgradient extent. Interestingly, depleted CIMB was detected in the upgradient extent of the deep plume, for which two conceptual models were suggested (Chapter 2). The first conceptual model involved TCE cometabolism as detailed next paragraph, while the second was in line with TCE degradation in low-permeability layers. During TCE reductive dechlorination in the low-permeability layers, DCEs could diffuse out of the low-permeability layer faster than TCE, following the concentration gradient. The resulting excess of carbon-13-depleted DCEs in the high transmissivity zone would lead to the depletion of the CIMB as suggested in Chapter 2 before. Finally, the prior CSIA study also suspected TCE to have degraded reductively through two different pathways producing DCE isomers (the cis- and the trans-) in different proportions. Trans-DCE represents 0 % to 75 % of all DCE isomers (i.e. tDCE/cDCE concentration ratios varies from 0 to 3). Based on the relatively constant tDCE/cDCE concentration ratio of about 0.11 at 15 different wells, one of the pathway likely yields about 10 % of trans-DCE. 18 other wells displayed tDCE/cDCE concentration ratios in the range 0.12-3 (with in average 35 % of trans-DCE), suggesting a second TCE reductive dechlorination pathway yielding as much as 75 % of trans-DCE could also occur. The tDCE/cDCE ratio variation between 0.11 and 3 would then result from the mixing of the products of both pathways (Chapter 2). Additionally, tDCE/cDCE concentrations ratios

of 0 % (i.e. 100% cDCE) are found only at wells where cis-DCE concentrations are low ($1.6 \mu\text{g}\cdot\text{L}^{-1}$ and lower). Trans-DCE might in fact be present but undetected at those wells as a tenth of $1.6 \mu\text{g}\cdot\text{L}^{-1}$ nearly falls below the detection limit of $0.1 \mu\text{g}\cdot\text{L}^{-1}$. In the following, simulations of TCE reductive dechlorination explore the potential co-existence of two TCE reductive dechlorination pathways at the site. Those simulations set to evaluate the potential for CSIA to inform over CE degradation extent in presence of multiple TCE degradation pathways.

3.2.2.2 *TCE aerobic cometabolism*

TCE cometabolism in the aerobic zone of the shallow aquifer was suspected in the first CSM. A microcosm study effectuated with un-amended groundwater sampled at 4 wells in the shallow plume resulted in near complete TCE degradation after 32 days, without noticeable reductive dechlorination daughter products. Additionally, functional genes and enzyme activity tests targeting both toluene and methane monooxygenase supported that aerobic cometabolism might contribute to TCE degradation in the shallow aquifer. However, the CSIA study detected no significant $\delta^{13}\text{C}$ -TCE enrichment where TCE aerobic degradation was expected. It is possible that TCE degraded through a pathway leading to little $\delta^{13}\text{C}$ -TCE enrichment, such as aerobic cometabolism by methanotrophs (Kuder et al., 2016). Low isotope fractionation might also reveal limited TCE cometabolism in the shallow aquifer. TCE aerobic cometabolism was also suspected in the deeper aquifer based on the presence of functional genes of methane monooxygenase (CH2MHILL, 2009). Where cis-DCE is present, reductive dechlorination enriched $\delta^{13}\text{C}$ -TCE. TCE and cis-DCE aerobic cometabolism might influence molar fraction and consequently modify the CIMB while having a limited influence on the $\delta^{13}\text{C}$ -TCE and $\delta^{13}\text{C}$ -DCE.

In the deep aquifer, TCE aerobic cometabolism was deemed possible by both CSMs. The process could take place at the upgradient extent of the deep plume which presents a strongly heterogeneous lithology. The presence of interbedded low-permeability layers (clay or silt lenses) and permeable layers (sand layers) may create the required contact between high methane concentrations (produced from wood decomposition in the clay) with oxygen (from the influx of oxic groundwater from the shallow aquifer) at their interfaces. Detection of any TCE cometabolism through CSIA was hindered by the isotope enrichment relative to TCE reductive dechlorination in the same area. Additionally, enriched CIMBs detected through the plumes could also result from TCE daughter products mineralization and was not necessary assigned to TCE cometabolic degradation. The detection of depleted CIMB in the upgradient extent of the deep plume could interestingly be the result of TCE oxidation, as it could result in theory in the excess of carbon-13-depleted daughter product. The TCE chlorine isotope relative enrichment compared to the TCE $\delta^{37}\text{Cl}/\delta^{13}\text{C}$ reductive dechlorination slope at some of the wells at which CIMB is enriched could correspond to TCE cometabolism by methanotrophs (Chapter 2).

3.2.2.3 Daughter compounds degradation

DCE isomers might accumulate but might also degrade through either aerobic cometabolism or through reductive dechlorination, or a combination of both. For instance, microorganisms able of TCE oxidation, which are suspected to be present and active, are also able of both DCE isomers cometabolism (Alvarez-Cohen and Speitel, 2001; Jesus et al., 2016). Additionally, the sparse presence of VC indicates that some cis-DCE and/or trans-DCE reductive dechlorination occurred. As $\delta^{13}\text{C}$ -cDCE or $\delta^{13}\text{C}$ -tDCE enrichment beyond $\delta^{13}\text{C}$ -TCE_{source} was only detected at one well, C CSIA suggests that reductive dechlorination beyond DCEs was limited (Chapter 2). The calculation of enriched CIMB, which signals CE mineralisation, seemed to coincide with a different isotopic pattern for cis-DCE compared to wells with constant CIMB, which could indicate cis-DCE degradation. Consequently, two conceptual models might explain the observed patterns and notably the limited detection of VC, either cis-DCE oxidized, or VC quickly degraded further after being produced by cis-DCE reductive dechlorination.

3.2.2.4 Physical processes interaction with CSIA

Additionally to degradative pathways, some non-degradative pathways impacted chlorine isotope ratios and the relative concentrations (molar fractions). In the shallow aquifer, chlorine isotope enrichment detected in the aquifer seemed related to the faster diffusion of the light isotopologues of TCE compared to the heavy isotopologues towards the nearby low-permeability layers. This process might also have impacted wells in the deep aquifer, without being easily distinguishable as the resulting $\delta^{37}\text{Cl}$ -TCE enrichment then overlaps with the $\delta^{37}\text{Cl}$ -TCE enrichment resulting from TCE reductive dechlorination. Additionally to back-diffusion processes, preferential sorption of TCE over DCEs (generally depleted in the heavy isotopes) could also lead to some CIMB depletion in the downgradient extent of the deep aquifer.

3.2.3 Groups of wells with similar isotope patterns

The presence of several expected degradation pathways required considering multiple degradation models. Wells were sorted in relevant subgroups to facilitate the creation of adequate models for each group. The present study focussed only on wells at which significant enrichment of $\delta^{13}\text{C}$ -TCE or the presence of DCEs isomers is detected. This represents about 25 % of the shallow wells and 90 % of the deep wells. Wells are separated in groups based on two criteria, both likely point to different degradation pathways, (1) their relative trans-DCE to cis-DCE (tDCE/cDCE) concentration ratio, and (2) their carbon isotope mass balance (CIMB) (Table 3-1). The CIMB is the isotope ratio calculated over TCE and its daughter products cis-DCE and trans-DCE. Provided the CIMB is constant, all

daughter products are therefore included in the CIMB and no CEs mineralisation is expected.

Table 3-1 : Wells groups based on companion paper. Bold wells: 2011 sampling. Italic: 2014 sampling.

Wells criteria	[tDCE]/[cDCE]	CIMB	Wells names	Number of different wells
G1 TCE RD	< 0.12	-26.5 ‰ to -24 ‰ (Constant CIMB)	S8, D11, D13, D15, D17, D22, <i>S39,</i> <i>D13, D15</i>	7
G2 TCE RD and DCEs degradation	< 0.12	> -24 ‰ (Enriched CIMB)	S5, S10, S14, S17, S39 D1, D14, D18, D19, <i>S17R,</i> <i>D1</i>	9
G3 TCE RD	> 0.12	-26.5 ‰ to -24 ‰ (Constant CIMB)	S21, D9, D10, <i>D11, D12, D20</i>	6
G4 TCE RD and DCE degradation	> 0.12	> -24 ‰ (Enriched CIMB)	S4 D2, D12, <i>S21,</i> <i>D14</i>	5
G5 Alternative behaviour	< 0.12	< -27 ‰ (Depleted CIMB)	D4 <i>D4</i>	1
G6 Alternative behaviour	> 0.12	< -27 ‰ (Depleted CIMB)	D3, D6, D7, D8 <i>D8, D8S, D10</i>	5

3.2.4 Rationale for batch modelling

TCE reductive dechlorination is detected at wells scattered in both aquifers (Fig. 3-1, and Section 3.2.2.1). Those wells have little or no hydraulic connection; for instance S39 (end of the shallow plume) and D21 (end of the deep plume), are not on the same flow line (Fig. 3-1). The site combines lines of evidence of large zones without any degradation (specifically in the shallow plume), of multiple degradation pathways, and of potential back diffusion of CEs from the clay. This strong heterogeneity of degradation is visible when the CSIA data are plotted against distance but also when compared to the groundwater age data (Fig. 3-2). As a result, the site complexity is beyond the scope of prior published models including CSIA during CEs degradation and transport (Höhener et al., 2017, 2015; Pooley et al., 2009). In order to circumvent the site complexity and still simulate degradation, a batch model approach is employed for describing carbon (C) and chlorine (Cl) CSIA of TCE and both DCE isomers, as well as their molar ratios patterns.

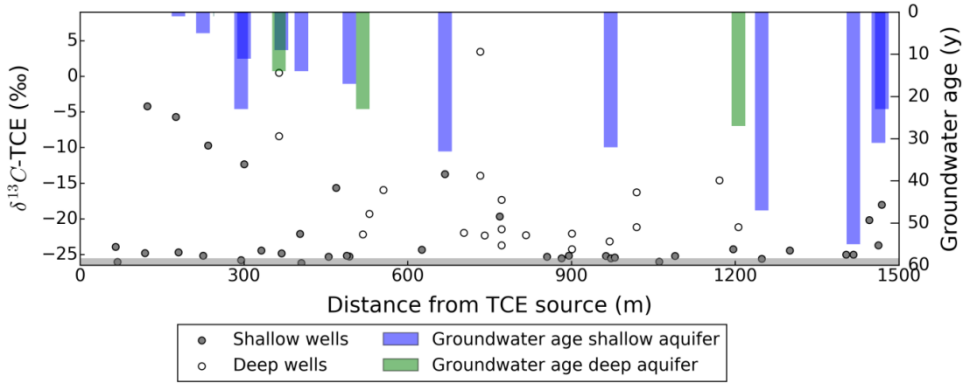


Fig. 3-2 : Groundwater age and $\delta^{13}\text{C-TCE}$ against the distance from the source for wells in the shallow and in the deep aquifer. In grey the $\delta^{13}\text{C-TCE}_{\text{source}}$ uncertainty.

3.2.5 Acquisition of enrichment factors for reductive dechlorination pathways

Isotope ratios R are expressed using the internationally recognized δ -notation in permil (‰) (eq. 3-1), with R_{std} the standards for isotopic ratios of carbon and chlorine isotopes being the Vienna Pee Dee Belemnite (VPDB), and Standard Mean Ocean Chloride (SMOC), respectively.

$$\delta = R/R_{std} - 1 \quad (3-1)$$

During degradation, the change in isotope ratio or isotope fractionation results from the relatively slower reaction rate constants of the heavy isotope (hk) compared to the light isotopes (lk). Isotope fractionation's magnitude therefore depends on the difference between those rates, and on the extent of degradation. The rate difference is often reported through the enrichment factor $\varepsilon = ^hk/^lk - 1$ (Coplen, 2011). Enrichment factors are employed for expressing both position-specific effects and bulk effects, i.e. effects averaged at the molecule level. Bulk isotope enrichment factor of one element E is calculated by eq. 3-2, where δ_{CE} and $\delta_{CE,source}$ are isotope ratios for the element E of a CE at a time t and initially (at the source), respectively, and f_{CE} is the remaining fraction of the CE at time t .

$$\ln\left(\frac{\delta_{CE}}{\delta_{CE,source}}\right) = \ln(f_{CE}) \times \varepsilon \quad (3-2)$$

In the environment, concentration changes are influenced also by physical processes such as sorption, dilution or dispersion. Employing relative concentrations as an estimate of the

remaining fraction f_{TCE} can circumvent the risk of overestimating degradation. At the Hill Site, DCE isomers might accumulate, therefore $x_{TCE} = [TCE] / \sum_i [CE]_i$, where $[CE]_i$ is a

CE's aqueous concentration, is appropriate for approximating f_{TCE} at those wells and it circumvents the influence of non-degradative attenuation effects such as dilution (Aeppli et al., 2010). For TCE, the dilution-corrected Rayleigh equation for one element is then written as in eq. 3-3:

$$\frac{\delta_{TCE} - \delta_{TCE,source}}{\ln(x_{TCE})} = \varepsilon_{bulk} \quad (3-3)$$

During reductive dechlorination, carbon and chlorine isotope ratios of CEs might present a stepped pattern in which the daughter compound is initially more depleted than the source compound. This stepped pattern is informative of isotope effects during dechlorination. For carbon, the difference $\varepsilon \approx \delta_{parent,t=0} - \delta_{daughter,t=0}$ is in theory equal to the carbon isotope enrichment factor of the substrate during its sequential dechlorination ($\varepsilon_{C_{TCE}}$) (Hunkeler et al., 1999).

For chlorine, as only non-reactive chlorine atoms are transmitted to the daughter product, eq. 3-4 provides the average of the position-specific isotope effects of the two Cl atoms on the non-reactive bonds $\varepsilon_{NRB(MEAN)}$ (Hunkeler et al., 2009; Kuder et al., 2013; van Breukelen et al., 2017). The isotope effect relative at the reactive bond ε_{RB} was calculated for TCE as in (van Breukelen et al., 2017) following eq. 3-4.

$$\varepsilon_{RB} = 3 \times \varepsilon_{Cl_{TCE,bulk}} - 2 \times \varepsilon_{NRB(MEAN)} \quad (3-4)$$

3.2.6 Reaction networks modelled

Based on the known potential degradation pathways (Section 3.2.2), the degradation model was required to include: (i) TCE reductive dechlorination to cis-DCE and trans-DCE (Section 3.2.2.1), (ii) both cis-DCE degradation pathway hypotheses (reductive dechlorination or oxidation) (Section 3.2.2.3), (iii) and TCE aerobic cometabolism (Section 3.2.2.2), with and without simultaneous cis-DCE aerobic cometabolism. The model speculates that TCE and cis-DCE reductive dechlorination reaction are simultaneous processes, but that TCE or cis-DCE oxidative degradation occurs after reductive dechlorination. One exception is VC transformation, which nature is unknown, and was modelled through rapid oxidation following its production. Fast VC oxidation is a reasonable assumption since VC oxidation rates are generally relatively high (Alvarez-Cohen and Speitel, 2001).

In order to better interpret CSIA results from the Hill OU10 field site, a RTM for CSIA was employed, based on a model priority developed with the PHREEQC code (Hunkeler et al., 2009; van Breukelen et al., 2017, 2005) for biotic reductive dechlorination of PCE, and is briefly presented here. In the model, TCE dechlorination to each DCE isomer (cDCE and tDCE) operates through two different pathways, each of them yielding 100 % of one or the other DCE isomer. There is therefore no common DCE isomer. The model considers a bulk isotope approach for carbon and an isotopologue approach for chlorine. The model is extended to oxidative transformation of TCE, cis-DCE, and VC. The current model includes carbon and chlorine isotope fractionation, during both TCE sequential reductive dechlorination to ethene and CEs oxidation. The isotope shifts during degradation are obtained in the model by assigning different rates to each isotopologue/isotope. As carbon and chlorine isotope fractionations are modelled independently, a correction term is employed to insure that the reaction progress is at similar rates for all isotopes/isotopologues (van Breukelen et al., 2017).

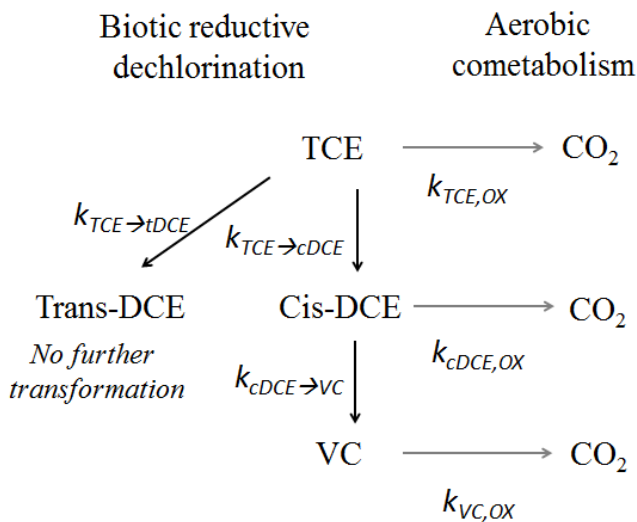


Fig. 3-3 : Reaction pathways and respective rate constants.

Table 1-1 : Degradation pathways included in the model.

Model	Reactions	Description	Models variations
TCERD	TCE \rightarrow cis-DCE and TCE \rightarrow trans-DCE	TCE reductive dechlorination to cis-DCE with or without trans-DCE simultaneous production, no DCEs degradation.	Relative rates change to reproduce the variations of trans-DCE to cis-DCE ratios.
DCERD	TCE \rightarrow cis-DCE \rightarrow VC \rightarrow CO ₂	TCE reductive dechlorination to cis-DCE with simultaneous cis-DCE degradation to VC. VC quickly oxidized. Trans-DCE omitted.	Enrichment factors relative to cis-DCE reductive dechlorination and relative rates of cis-DCE production and degradation are varied
DCEOX	TCE \rightarrow cis-DCE \rightarrow CO ₂	TCE reductive dechlorination to cis-DCE followed by sequential cis-DCE oxidation. Trans-DCE omitted.	Enrichment factors relative to cis-DCE oxidation are varied. Variations in start/stop times for the transition from reductive to oxidative pathways.
TCEOX	TCE \rightarrow CO ₂ and TCE \rightarrow cis-DCE \rightarrow CO ₂	TCE reductive dechlorination to cis-DCE followed by TCE aerobic cometabolism with or without simultaneous cis-DCE cometabolism. Trans-DCE omitted.	Enrichment factors relative to cis-DCE oxidation and relative rates for TCE and cis-DCE oxidations are varied.

3.2.7 Simulation of TCE and DCEs degradation and isotope fractionation

For modeling bulk carbon isotope fractionation, both the light (^lTCE) and heavy (^hTCE) carbon isotopes in the TCE molecule were simulated. First-order degradation kinetics was applied. Assessment of the pollutants isotope ratio changes is based on the Rayleigh equation (Mariotti et al., 1981; Rayleigh, 1896). The kinetic isotope fractionation factor

$\alpha_k = \varepsilon + 1$ describes the difference in degradation rate constants associated with the heavy and the light isotopes, ^h k_{bulk} and ^l k_{bulk} , respectively, as $\alpha_k = {}^h k_{bulk} / {}^l k_{bulk}$. The difference in degradation rate constants is incorporated in the reactive transport model by setting the degradation rates of the heavy and the light isotopes, ^l r and ^h r , respectively, following van Breukelen et al., (2005):

$$-{}^l r = -r \frac{[{}^l TCE]}{[TCE]} \quad (3-5)$$

$$-{}^h r = -r \frac{[{}^h TCE]}{[TCE]} \alpha_k \quad (3-6)$$

where r is the overall first-order degradation rate of TCE:

$$r = k [TCE] \quad (3-7)$$

where k is the first-order degradation rate constant of TCE.

The “isotopologue” method employed for chlorine isotope fractionation modeling accounts for the secondary isotope effects, i.e., isotope effects on non-reactive Cl atoms (Badin et al., 2018; Cretnik et al., 2014; Elsner et al., 2005; Hunkeler et al., 2009; Kuder et al., 2013; van Breukelen et al., 2017). The reaction rate for each isotopologue/isotopomer r_{mi} was obtained as:

$$r_{mi} = r_m \cdot \left(\frac{C_i}{C_m} \right) \cdot \left[\frac{n_i - H_i}{n_i} \Pi(\varepsilon_{NRB_i} + 1) + \frac{H_i}{n_i} \Pi(\varepsilon_{NRB_i} + 1) \right] \quad (3-8)$$

Where r_m is the degradation rate of the corresponding parent compound and C_m its concentration, C_i is the concentration of the isotopologue/isotopomer of interest, n_i is the number of Cl atoms at reactive positions (undergoing C-Cl cleavage) in the isotopologue/isotopomer i , H_i is the number of heavy chlorines at reactive positions in the isotopologue/isotopomer i . The isotope effects at reactive and non-reactive bonds were obtained from eq. (3-4) and (3-5). Further details can be found in (Hunkeler et al., 2009; van Breukelen et al., 2017). The initial C isotope composition and Cl isotopologue composition were calculated as described in the Appendix (Section S3-5, Table S3-5, S3-6 and S3-7).

3.3 Results and discussion

3.3.1 Field based assessment of TCE C and Cl isotope enrichment factors during reductive dechlorination

3.3.1.1 Bulk carbon enrichment factors

The bulk carbon enrichment factor during TCE reductive dechlorination ($\varepsilon_{C_{TCE, RD, bulk}}$) followed from the dilution-corrected Rayleigh equation (eq. 3-3), i.e. using the molar ratio of TCE to total CEs instead of the TCE concentration. Only values from wells having constant carbon isotope mass balance (CIMB) were employed Fig. S3-3. A constant CIMB means that all the daughter products are included in the CIMB calculation and implies that only CEs reductive dechlorination is detected. The uncertainties on both TCE molar fraction and TCE isotope ratio were taken into account in a York fit regression (York et al., 2004). The obtained value of -18 ± 2 ‰ is large but in the literature range (-3.3 ‰ to -18.9 ‰, see Table S3-1).

The product-related isotope enrichments for carbon ($\varepsilon_{C_{parent \rightarrow product}}$) specific to each DCE isomers are acquired through eq.3-3 applied to the data of 6 wells selected for their limited TCE enrichment (See Table S3-1). The resulting enrichment factor during TCE degradation to cis-DCE $\varepsilon_{C_{TCE \rightarrow cDCE}}$ is of -19.4 ± 0.9 ‰ and for TCE degradation to trans-DCE $\varepsilon_{C_{TCE \rightarrow tDCE}}$ of -26 ± 1.2 ‰ (see Table S3-1 for details and Fig. 3-4a). A larger $|\varepsilon_{C_{TCE \rightarrow DCE}}|$ compared to

$|\varepsilon_{C_{TCE \rightarrow cDCE}}|$ is in line with previously published data (Marco-Urrea et al., 2011). Theoretically, the product-related enrichment factors should be isotopically balanced around the bulk enrichment factor (Elsner et al., 2008). However, $\varepsilon_{C_{TCE \rightarrow cDCE}}$ and $\varepsilon_{C_{TCE \rightarrow tDCE}}$ are both more negative than $\varepsilon_{C_{TCE, RD, bulk}}$, which could result from the flaws in the product-related method which does not obtain the instantaneous difference between TCE and DCE, and yields a value larger than epsilon when cis-DCE accumulates (Elsner, 2010).

The difference of about 6 ‰ between $\varepsilon_{C_{TCE \rightarrow cDCE}}$ and $\varepsilon_{C_{TCE \rightarrow tDCE}}$ is in line with the prior CSM Chapter 2, in which an offset of 6 ‰ to 10 ‰ was described between $\delta^{13}C$ -cDCE and $\delta^{13}C$ -tDCE. However, it was suggested in the updated CSM that the offset was negligible where trans-DCE dominated. The distinction was not possible between groups of wells with large or small proportions of trans-DCE because only one of those wells displays limited TCE and CIMB enrichment. As mentioned in Chapter 2, two pathways might occur at the site, yielding different proportions of simultaneous trans-DCE and cis-DCE production. For the pathway in which trans-DCE is dominant, $\varepsilon_{C_{TCE \rightarrow cDCE}}$ and $\varepsilon_{C_{TCE \rightarrow tDCE}}$ might be in the same range. Simulations in Section 3.4.3 further explore this hypothesis.

3.3.1.2 Bulk chlorine enrichment factor

Bulk chlorine isotope enrichment factor ($\varepsilon_{Cl_{TCE, RD, bulk}}$) was obtained similarly to $\varepsilon_{C_{TCE, rd, bulk}}$ (eq. 3-3, Fig. S3-3b). The subsequent $\varepsilon_{Cl_{TCE, RD, bulk}}$ reaches -3.0 ± 0.5 ‰, at the lower end of the previously reported literature range (-2.7 ‰ to -5.7 ‰, Table S3-1).

3.3.1.3 Bond-specific chlorine isotope effects

The enrichment factors for non-reactive bonds $\varepsilon_{NRB(MEAN)}$ and reactive bonds ε_{RB} were estimated as -3.0 ‰ (standard deviation of 0.3 ‰) and -3.0 ‰, respectively (eq. 3-4 and 3-5). Such similar values contrast with prior microcosm studies which yielded larger ε_{RB} than $\varepsilon_{NRB(MEAN)}$ (Cretnik et al., 2014; Kuder et al., 2013). However, the contrast is lesser if the $\varepsilon_{NRB(MEAN)}$ of the present study is varied within its uncertainty. For instance, the difference between initial $\delta^{37}Cl$ -cDCE and $\delta^{37}Cl$ -TCE, which yield $\varepsilon_{NRB(MEAN)}$, varies between -2 ‰ and -3 ‰ through the plume (Fig. 3-4b). A slightly smaller $\varepsilon_{NRB(MEAN)}$ of -2.5 ‰ instead of -3 ‰, within the uncertainty of 0.7 ‰, would yield a ε_{RB} of -4 ‰, i.e. larger than $\varepsilon_{NRB(MEAN)}$. Nonetheless, TCE $\varepsilon_{Cl_{Bulk}}$, ε_{RB} and $\varepsilon_{NRB(MEAN)}$ are not excessively different from the values obtained from a microcosm experiment degrading CEs with a *Dehalococcoides (Dhc.)* consortium in which TCE reduced to ethene mainly through cis-DCE (-3.6 ‰, -4.2 ‰, and -3.3 ‰, respectively (Kuder et al., 2013).

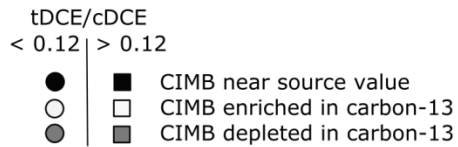
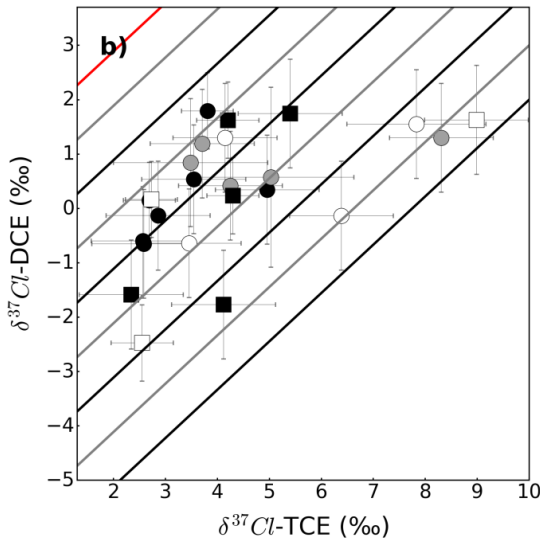
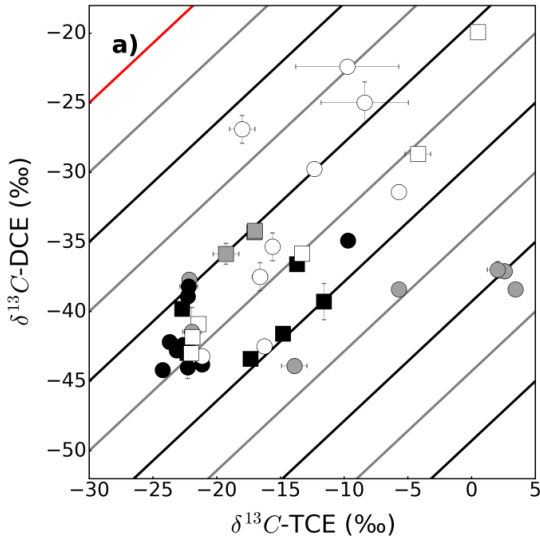


Fig. 3-4 : $\delta^{13}\text{C}$ -cDCE vs. $\delta^{13}\text{C}$ -TCE (a), and $\delta^{37}\text{Cl}$ -cDCE vs. $\delta^{37}\text{Cl}$ -TCE (b). Lines represent a visual indication of the difference between the TCE and DCEs isotope values starting from 0 ‰ (red line) then a line every 5 ‰ for $\delta^{13}\text{C}$ and every 1 ‰ for $\delta^{37}\text{Cl}$.

3.3.2 Modeling TCE degradation and DCE isomers production – C CSIA

In order to model the two potential TCE degradation pathways which differ from their simultaneous production of cis-DCE and trans-DCE, the model simulates degradation of TCE to trans-DCE and cis-DCE through two reductive dechlorination pathways, each producing uniquely either cis-DCE or trans-DCE and occurring simultaneously at different rates. One simulation (TCERd1) does not include trans-DCE production, while TCERd2 and TCERd3 differ from their relative rates $k_{TCE \rightarrow DCE}/k_{TCE \rightarrow cDCE}$ value (0.11 and 3, respectively; Table 3-1) in order to illustrate limited and large trans-DCE production.

For the simulation of low tDCE/cDCE concentration ratios, TCE enrichment factors were calculated in Section 3.3.1 with $\epsilon_{C_{TCE \rightarrow DCE}}$ of -26 ‰ and $\epsilon_{C_{TCE \rightarrow cDCE}}$ of -19 ‰. Ideally, the simulations employing those enrichment factors as inputs should describe the ranges for $\delta^{13}C$ and $\delta^{37}Cl$ of both DCEs (when data are available) for the 16 wells at which CIMB is constant (groups G1 and G3, symbolised with black markers in Fig. 3-5). Differences in the appropriate simulations are expected between wells with low (7 wells in group G1, small circle markers Fig. 3-5) or high (9 wells in G3, small square markers in Fig. 3-5) tDCE/cDCE concentration ratios. TCE reductive dechlorination simulations stop running when $\delta^{13}C$ -TCE reaches -9.7 ‰, the most enriched value detected for the well groups at which CIMB is constant (G1 and G3).

The simulation matches with the most depleted $\delta^{13}C$ -cDCE and $\delta^{13}C$ -tDCE values at wells with both high and low tDCE/cDCE concentration ratios (Fig. 3-5c, 5d, 5e, 5f). The lack of $\delta^{13}C$ -cDCE and $\delta^{13}C$ -tDCE values more depleted than the simulation suggests that the calculated enrichment factors relative to TCE reductive dechlorination are sufficiently low, and therefore conservative for TCE degradation estimates.

For the simulation of large tDCE/cDCE concentration ratios, both $\epsilon_{C_{TCE \rightarrow DCE}}$ and $\epsilon_{C_{TCE \rightarrow cDCE}}$ are set to -19 ‰. The simulated relation between $\delta^{13}C$ -TCE and TCE molar fraction is similar for both simulations (Fig. 3-5a). The simulation of high tDCE/cDCE concentration ratio displays also a good match with the two wells D12 and D20 (Fig. 3-5), which have the highest trans-DCE ratio and a constant CIMB. The simulation also corresponds better to the linear relation between $\delta^{13}C$ -cDCE and $\delta^{13}C$ -tDCE for those wells (Fig. 3-5b). The intermediary pattern observed for other wells at which tDCE/cDCE concentration ratios are larger than 0.12 and the CIMB is constant or depleted could illustrate a mixture of DCEs yielded by both degradation pathways.

Although a perfect fit is unreachable with such a simple model, the model supports that some of the spread observed on plots of DCEs molar fractions versus $\delta^{13}C$ -cDCE for data with constant CIMB (black symbols) could be due to the co-production of both DCE

isomers. The variation of tDCE/cDCE concentration ratios reflects the occurrence of two coexisting pathways or more, one of which producing about 10 % of trans-DCE, and a second pathway producing at least about 75 % of trans-DCE. The simulation of the daughter products molar ratios and isotope ratios patterns acts as a visual confirmation of the isotope enrichment factors estimated through the dilution-corrected Rayleigh equation and the difference daughter-parent compounds. The simulations support that $\delta^{13}\text{C-tDCE}$ could be initially more depleted when cis-DCE is the dominant product than when trans-DCE is dominantly produced; however the large amount of $\delta^{13}\text{C-tDCE}$ data more depleted than the simulation (Fig. 3-5f) indicates that $\varepsilon_{\text{TCE} \rightarrow \text{DCE}}$ might be less enriched than simulated here.

As expected, the TCE reductive dechlorination model show a poor agreement with data from wells at which CIMB is enriched (white symbols) or depleted (grey symbols) (Fig. 3-5). Compared to the simulations of TCE reductive dechlorination, wells with enriched CIMB present either smaller x_{DCE} and/or more enriched $\delta^{13}\text{C-cDCE}$ (Fig. 3-5). Both observations could correspond to the presence of a pathway degrading cis-DCE, investigated in the following. At wells with enriched CIMB, some trans-DCE degradation might have to be accounted for as shown by the enrichment of $\delta^{13}\text{C-tDCE}$ compared to the simulation, which was not possible to determine without the simulation of the daughter products carbon isotope ratios.

Wells at which the CIMB is depleted reach visibly lower x_{TCE} values than in the case of TCE reductive dechlorination only based on the simulations (Fig. 3-5a). The pattern could correspond to the presence of a third reductive dechlorination pathway for TCE, with a smaller $|\varepsilon_{\text{TCE,bulk}}|$. However, this would result in initially less depleted $\delta^{13}\text{C-cDCE}$ values than observed, and would not explain the depleted CIMB (results not shown). At the contrary, only a larger enrichment factor in absolute value, similar to the estimated for these scenarios, yields sufficiently depleted $\delta^{13}\text{C-cDCE}$. Consequently, it is more likely that the low x_{TCE} compared to the simulations results from an excess of depleted cis-DCE, which would also explain the depleted CIMB. In the prior study of the CSIA data, the depleted CIMB was suspected to be linked to a slower back-diffusion of the source compound (TCE) from the aquitard or to its fast aerobic cometabolism (Chapter 2). The potential role of TCE cometabolism to yield an excess of depleted cis-DCE and therefore to a depleted CIMB is investigated in Section 3.4.3

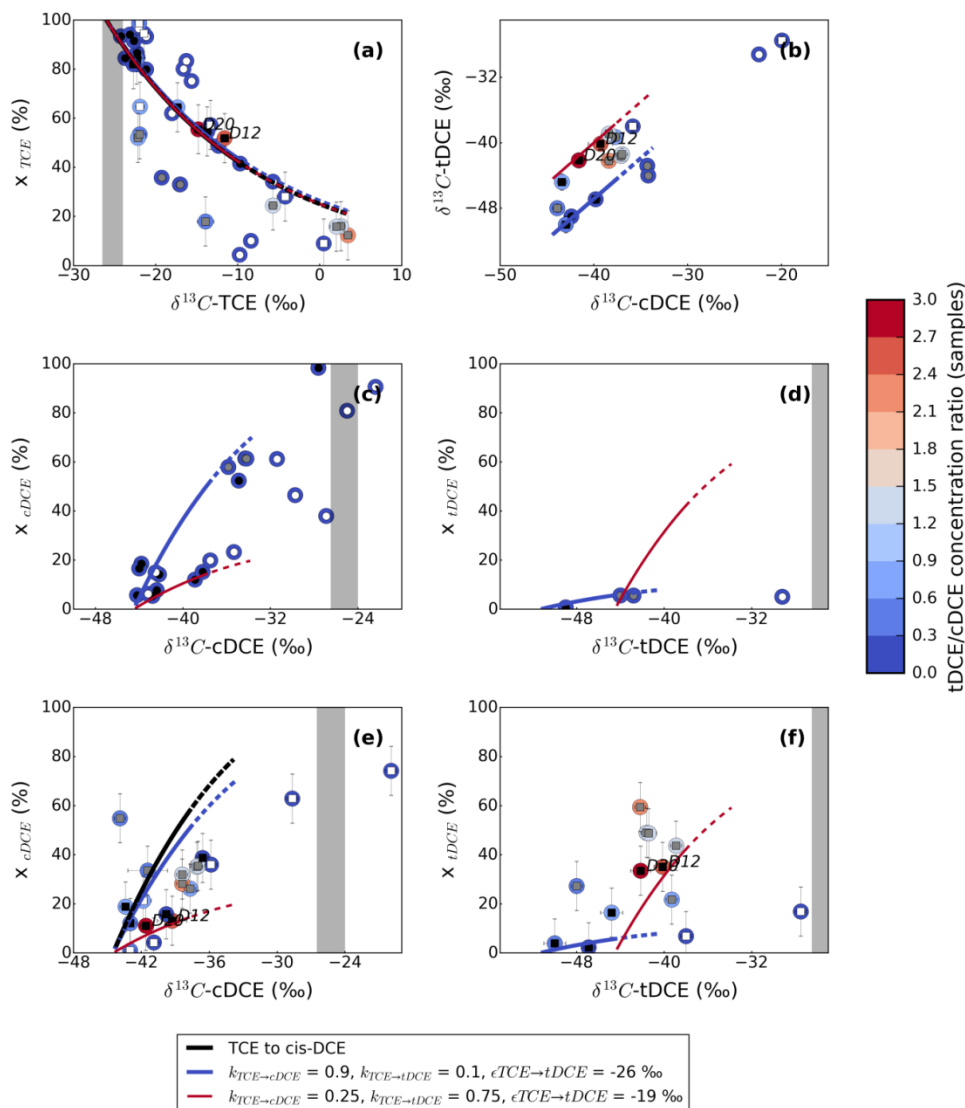


Fig. 3-5: Site data vs. the batch model simulations results for three different scenarios of TCE reductive dechlorination: TCE reductive dechlorination to cis-DCE only, and TCE degradation to both trans-DCE and cis-DCE, with two different tDCE/cDCE relative rate constant ratios: 0.11 and 3. The simulations therefore aim at fitting the data only for wells with constant CIMB indicated by the small black markers (detail below). For all the wells: $\delta^{13}\text{C-TCE}$ vs. TCE molar ratio (a), and $\delta^{13}\text{C-cDCE}$ vs. $\delta^{13}\text{C-tDCE}$ (b). DCEs $\delta^{13}\text{C}$ vs. their respective molar ratio for wells with tDCE/cDCE concentration ratios > 0.12 and < 0.12 in (c,d) and (e,f), respectively. The enrichment factors relative to TCE to trans-DCE degradation is set to -26 ‰ and -19 ‰ for tDCE/cDCE concentration ratios of 0.11 and 3, respectively (details in Appendix). The larger markers (red to blue circles) indicate the tDCE/cDCE concentration ratio. The smaller markers indicate whether the CIMB is enriched (white), constant (black) or depleted (gray). Circles and squares indicate wells with tDCE/cDCE concentration ratios $<$ and $>$ to 0.12, respectively. The isotope signature of the source $\delta^{13}\text{C-TCE}_{\text{source}}$ is indicated by the grey shaded zone. The dashed line corresponds to the parts of the simulations between $\delta^{13}\text{C-TCE}$ values of -9.7 ‰ (most enriched data for wells at which CIMB is constant) and 3.5 ‰ (most enriched $\delta^{13}\text{C-TCE}$ at the site).

3.3.3 Modeling TCE degradation and cis-DCE production - Cl CSIA

Similarly to the previous simulations of C CSIA, simulations of Cl CSIA employ as inputs the enrichment factors determined in Section 3.3.1. The simulations do not include trans-DCE production notably because no $\delta^{37}\text{Cl-tDCE}$ value was available for this site. The omission of trans-DCE production mostly impacts cis-DCE molar fraction as it can be seen for carbon isotopes simulation in Fig. 3-5a (difference between the blue and the black line), under the condition that chlorine isotope fractionation during TCE transformation to cis-DCE is similar for both TCE reductive dechlorination pathways. Considering that in Chapter 2, the dual carbon-chlorine isotope slopes were not strongly different between the data corresponding to the one or to the other pathway and that the carbon isotope enrichment pathways are also similar, this hypothesis is acceptable at this stage. The simulations run until $\delta^{13}\text{C-TCE}$ reached +3.5 ‰, the most enriched $\delta^{13}\text{C-TCE}$ value reported at the site. The simulations differ from their initial $\delta^{13}\text{C-TCE}$ which illustrates the uncertainty on $\delta^{37}\text{Cl-TCE}_{\text{source}}$ of ± 1 ‰ (Fig. 3-6).

The simulated $\delta^{37}\text{Cl-cDCE}$ corresponds to the range of the data reported for wells with constant CIMB (groups G1 and G3, black symbols) (Fig. 3-6b). The simulated envelop englobes most of the data on the dual C-Cl CSIA plot (Fig. 3-6d). However, some data features are not described properly by the simulations, as the simulated $\delta^{37}\text{Cl-cDCE}$ overestimates (S21, S39, D12) or underestimates (D9, D10) the data (Fig. 3-6b and 27c). Several processes could explain the limited match of the simulations. The isotope ratios of the source compound TCE could be altered by fractionating processes before its degradation to DCE isomers, impacting $\delta^{37}\text{Cl-cDCE}$ final value. For instance at well S21, the simulation results are low compared to the $\delta^{37}\text{Cl}$ values of both cis-DCE and TCE (Fig. 3-7). Alternatively, $\delta^{37}\text{Cl-cDCE}$ might be affected by isotope fractionation resulting from degradative or non-degradative processes combined.

Wells at which the CIMB was calculated to be enriched do not display strong $\delta^{37}\text{Cl-TCE}$ or $\delta^{37}\text{Cl-cDCE}$ enrichment compared to the model when plotted against the molar ratios with the exception of one well (Fig. 3-6a and 6b). Larger $\delta^{37}\text{Cl-TCE}$ enrichment relatively to $\delta^{13}\text{C-TCE}$ compared to the simulations (Fig. 3-6c) was assigned to isotope fractionation during diffusion to the aquitard in Chapter 2 as no degradation pathway described yet in the literature would lead to larger chlorine than carbon isotope enrichment. At the field site, $\delta^{37}\text{Cl-cDCE}$ varies in a limited range (~ -2 ‰ to +3 ‰) compared to the uncertainty of 1 ‰. The limited isotope fractionation prevents the use of $\delta^{37}\text{Cl-cDCE}$ for the identification of degradation pathways notably as cis-DCE degradation pathways are generally linked to limited chlorine isotope fractionation. Chlorine isotope enrichment is therefore not investigated during the simulations of cis-DCE further degradation.

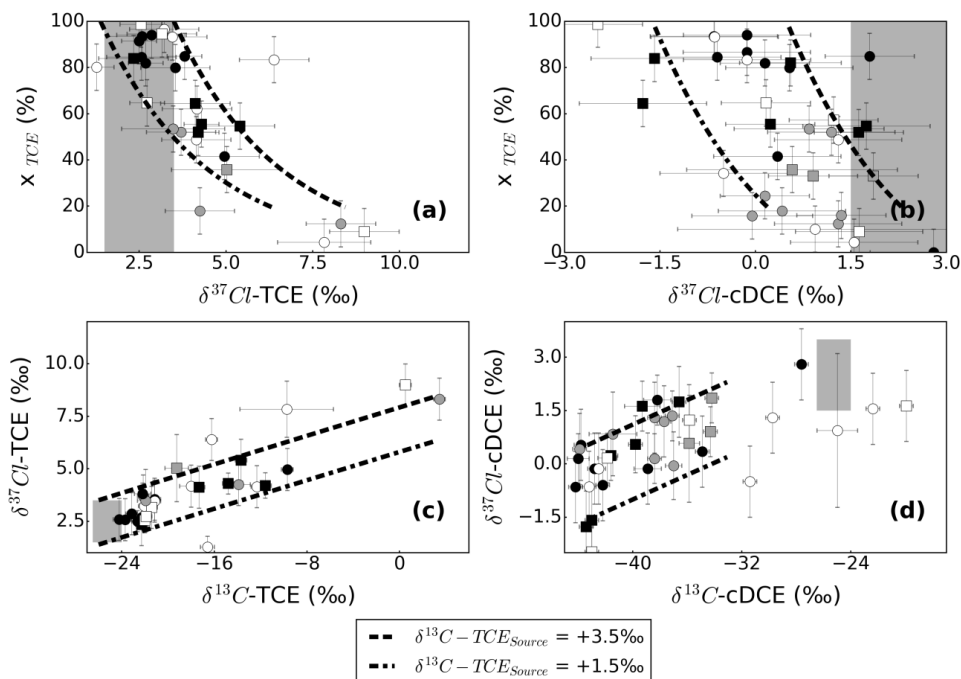


Fig. 3-6 : Model of TCE reductive dechlorination to cis-DCE (TCERd1) with varying initial $\delta^{37}\text{Cl-TCE}$ (small and large dashed black line $\delta^{37}\text{Cl-TCE}_{\text{source}} = +1.5\text{‰}$, large dashed black line $\delta^{37}\text{Cl-TCE}_{\text{source}} = +3.5\text{‰}$).

3.3.4 Modeling cis-DCE degradation

The cis-DCE degradation model is based on the TCE to cis-DCE model simulated in the prior sections to which additional degradation pathways for cis-DCE were implemented using literature values. Due to the limited number of wells concerned by trans-DCE degradation, this pathway was not simulated and trans-DCE was not included in this simulation for simplification. The lack of independent parameters like time or distance from the source was a limit for the visualization of the batch modeling results. It was therefore necessary to visualize the extent of CEs mineralization (B_{CE}) on the plots in order to improve the visual comparison between the models and the data.

Enrichment factors for cis-DCE degradation were obtained from the literature. Cis-DCE reductive dechlorination was simulated using $\varepsilon_{C_{DCE} \rightarrow VC}$ values within $\pm 1\sigma$ of the average of published enrichment factors for cis-DCE biotic reductive dechlorination (-15 ‰ for DCERd2 and DCERd4, and -25 ‰ for DCERd1 and DCERd3; Table S3-1).

Cis-DCE reductive dechlorination to VC is simulated simultaneously to TCE reductive dechlorination. The relative rates of cis-DCE degradation $k_{c_{DCE} \rightarrow VC}$ were varied between 0.2 (TCERd1 and TCE rd2) and $0.5 \cdot k_{TCE \rightarrow cDCE}$ (TCERd3 and TCERd4) based on previously

published degradation rates at field sites (Höhener, 2016; van Breukelen et al., 2005). Since VC detection was limited, VC is considered to degrade simultaneously to its production with a relatively large rate constant of $k_{VC} = 50 \cdot k_{TCE \rightarrow cDCE}$, which maintains VC concentrations 2 orders of magnitude lower than the other CEs.

The simulations are stopped when $\delta^{13}\text{C-TCE}$ reached + 3.5 ‰, the most enriched $\delta^{13}\text{C-TCE}$ value reported at the site.

3.3.4.1 DCE reductive dechlorination with rapid VC conversion

For both large and small $|\varepsilon_{cDCE \rightarrow VC}|$ values, the modeling of simultaneous cis-DCE production and degradation through reductive dechlorination matches the ranges observed for $\delta^{13}\text{C-cDCE}$, $\delta^{13}\text{C-TCE}$, and x_{TCE} of the groups of wells where CIMB is enriched (white symbols, G2 and G4, Fig. 3-7 and 3-8).

For all simulations, cis-DCE reductive dechlorination leads to an increasingly larger x_{TCE} , to CIMB enrichment and to $\delta^{13}\text{C-cDCE}$ enrichment with increasing relative cis-DCE reductive degradation rate constants ($k_{cDCE \rightarrow VC}/k_{TCE \rightarrow cDCE}$) (Fig. 3-7 and 3-8). For each simulation, the extent of CEs mineralization B_{CE} is calculated for each point and serves as a marker of the extent of CEs degradation. Interestingly, for the most enriched $\delta^{13}\text{C-TCE}$ values of wells in the groups G2 and G4 (white wells), the expected B_{CE} for a given pair of $\delta^{13}\text{C-TCE}$ and $\delta^{13}\text{C-cDCE}$ in Fig. 3-7b is significantly higher than the B_{CE} for the calculated CIMB. For the small $|\varepsilon_{cDCE \rightarrow VC}|$, the most enriched $\delta^{13}\text{C-cDCE}$ value (D2) is reached only for a B_{CE} of around 40-45 % (Fig. 3-6b), which is twice as much as what would be expected based on the CIMB value for the same well ($B_{CE} = 20-25$ %, Fig. 3-7d). For the larger $|\varepsilon_{cDCE \rightarrow VC}|$, the difference between both estimates is quantitatively smaller although proportionally similar (about 30-35 % B_{CE} based on $\delta^{13}\text{C-cDCE}$ (Fig. 3-8b) vs. 15-20 % for the CIMB plot (Fig. 3-8d).

Provided the conceptual model of sequential TCE and cis-DCE reductive dechlorination is appropriate for describing degradation at the site, the lower CIMB than simulated underlines that a process additional to the degradation processes modeled here would lead to CIMB decrease. A clearly lower x_{TCE} compared to the simulations indicates that the cause for the CIMB decrease could relate to this change in x_{TCE} , the remaining cis-DCE being more depleted. Provided such a process affected only the molar ratios of the CEs and not the isotope ratios, isotope ratios can be employed for degradation assessment. Based on the simulation obtained with an enrichment factor $\varepsilon_{cDCE \rightarrow VC}$ from the literature, the maximum degradation would be between 30 % and 45 % when reading on the $\delta^{13}\text{C-cDCE}$ vs. $\delta^{13}\text{C-TCE}$ plot (Fig. 3-7c). The general lack of VC detection would be the result of its quick degradation.

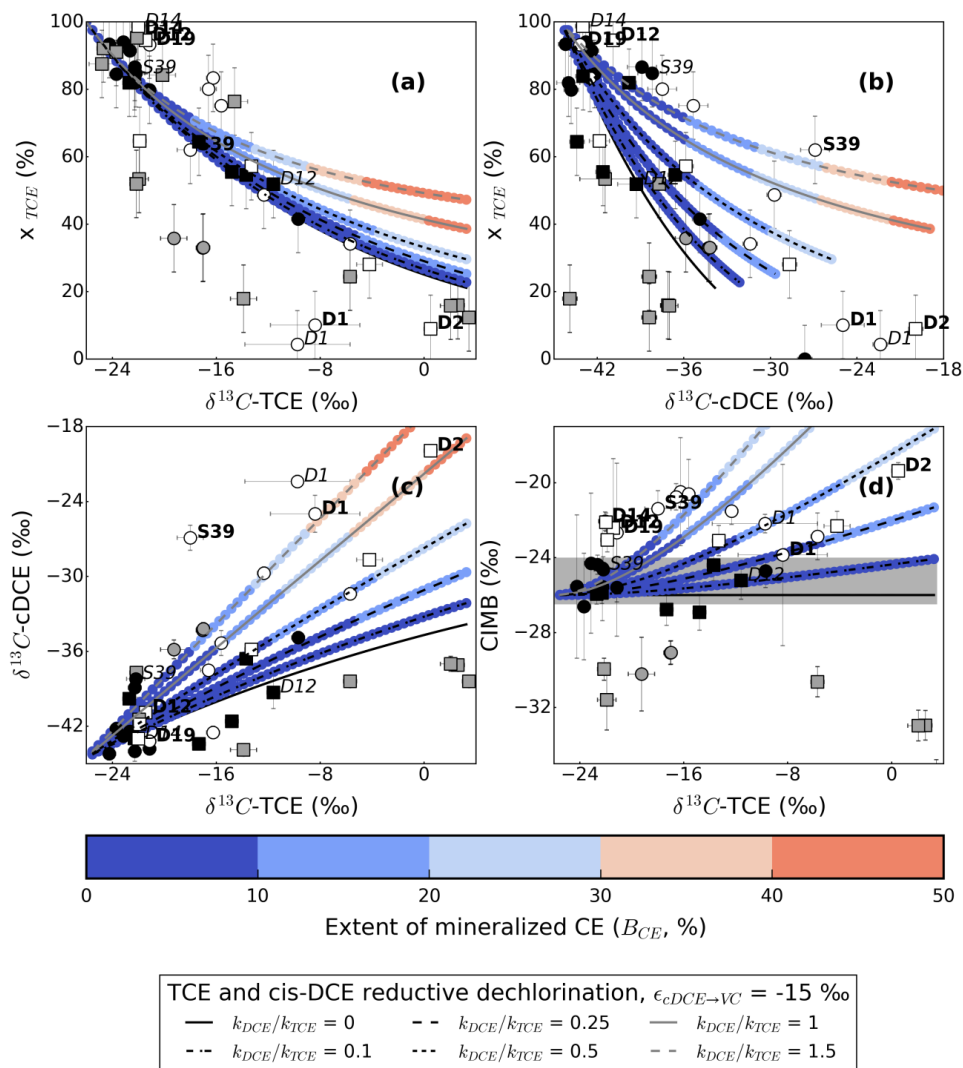


Fig. 3-7 : Simulations results for cis-DCE reductive dechlorination simultaneously to TCE reductive dechlorination to cis-DCE, with $\epsilon_{cDCE \rightarrow VC}$ set to -15 ‰. Detail of the simulations in text and Table 3-1. Different cis-DCE degradation rate constants were tested relatively to TCE degradation rate constant ($k_{cDCE \rightarrow VC}/k_{TCE \rightarrow cDCE}$ of 0.1, 0.25, 0.5, 1, and 1.25, detail in legend), and one model without further cis-DCE degradation (black line) is also presented. The coloured lines correspond to the different states of B_{CE} per 5%. The well data are represented by the markers, the description of the legend is similar to Fig. 3-4.

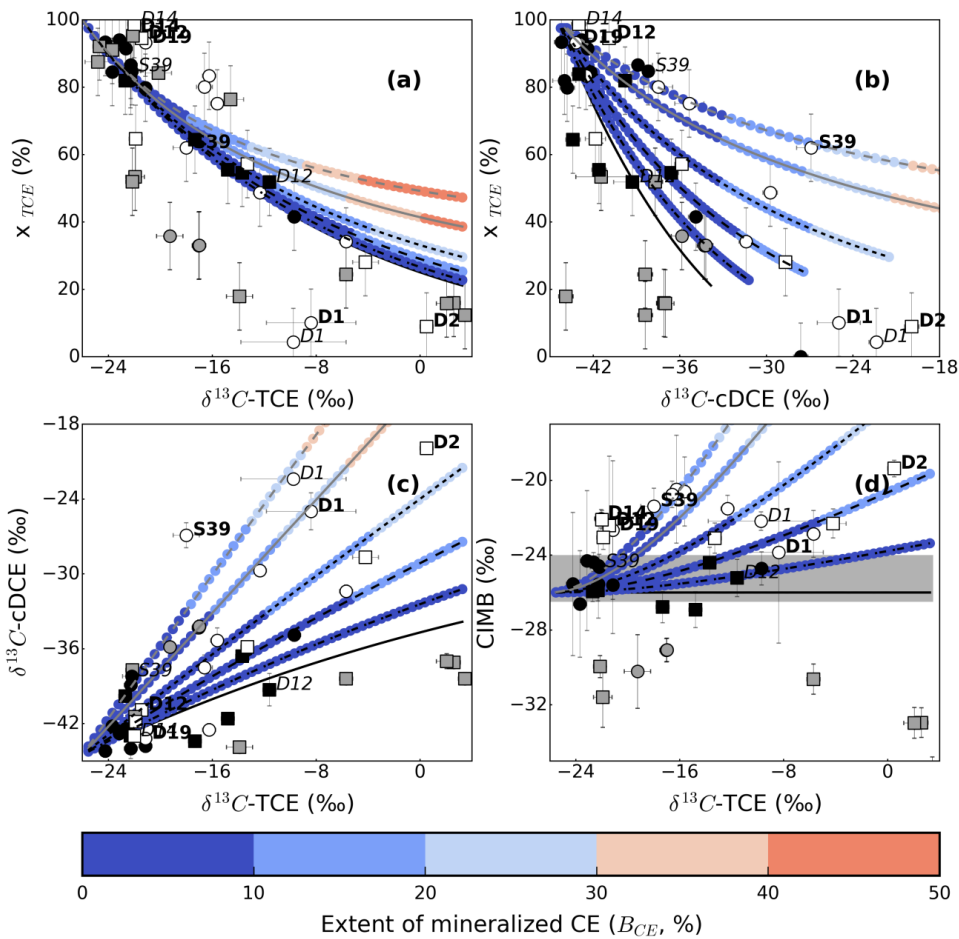


Fig. 3-8 : Simulations results for cis-DCE reductive dechlorination simultaneously to TCE reductive dechlorination to cis-DCE, with $\epsilon_{cDCE \rightarrow VC}$ set to -30 ‰. Detail of the simulations in text and Table 3-1. Different cis-DCE degradation rate constants were tested relatively to TCE degradation rate constant ($k_{cDCE \rightarrow VC}/k_{TCE \rightarrow cDCE}$ of 0.1, 0.25, 0.5, 1, and 1.25, detail in legend), and one model without further cis-DCE degradation (black line) is also presented. The coloured lines correspond to the different states of CEs mineralization (B_{CE}) per 5 %. The well data are represented by the markers similarly to Fig. 3-4.

3.3.4.2 DCE cometabolic or metabolic oxidation

TCE reductive dechlorination and cis-DCE oxidation are not expected to occur under the same redox conditions. For cis-DCE oxidation to be possible, it is assumed that the plume

travels in aerobic zones after having travelled in reductive zones where it was produced. The transition between both redox conditions could occur at any stage of TCE reductive dechlorination. In the simulations the transition occurs after 10 %, 30 %, 50 %, 65 %, and 78 % of TCE transformation. For simplicity, simultaneous cis-DCE reductive dechlorination is omitted in this scenario. The cis-DCE oxidation rate constant ($k_{cDCE,OX}$) is not a relevant parameter during this simulation and is set to $1 \cdot k_{TCE \rightarrow cDCE}$. Due the limited amount of published ϵC values during cis-DCE oxidation and the large variation in isotope enrichment, the minimum and maximum of the published values were employed for $\epsilon C_{cDCE,OX}$ (-22.4 ‰ for DCEox1 and -0.4 ‰ for DCEox2, see Table S3-2).

The simulations of cis-DCE oxidation using large $\epsilon C_{cDCE,OX}$ (-22 ‰) matches the ranges of $\delta^{13}C$ -cDCE, $\delta^{13}C$ -TCE and x_{TCE} values (Fig. 3-9). As cis-DCE oxidation can theoretically start at any stage of cis-DCE production, a small B_{CE} can be linked to strong $\delta^{13}C$ -cDCE enrichment when little cis-DCE was initially produced, i.e. for small $\delta^{13}C$ -TCE enrichment (Fig. 3-9c). For instance, for a TCE degradation to cis-DCE of 15 % ($\delta^{13}C$ -TCE = -22 ‰), a B_{CE} of 10 % requires that 66 % of the produced cis-DCE has degraded, therefore inducing intense $\delta^{13}C$ -cDCE enrichment. The lack of detection of any strongly enriched $\delta^{13}C$ -cDCE at wells with limited TCE reductive dechlorination infers that strongly enriching cis-DCE oxidation is unlikely to be an important degradation pathway when little cis-DCE was initially produced. Co-enrichment of $\delta^{13}C$ -cDCE and $\delta^{13}C$ -TCE which takes place when cis-DCE degrades reductively simultaneously to TCE reductive dechlorination seems more likely than sequential cis-DCE oxidation to explain the large $\delta^{13}C$ -cDCE fractionation. One visible exception is S39, at which $\delta^{13}C$ -cDCE enrichment is faster than $\delta^{13}C$ -TCE. S39 is situated at the very end of the shallow plume where the shallow plume sinks in the deeper aquifer; therefore S39 is hardly connected with other wells. At this well some cis-DCE oxidation could have been relevant to cis-DCE degradation.

Despite the limited $\delta^{13}C$ -cDCE enrichment in the simulation with the low $\epsilon C_{cDCE,OX}$ (-0.4 ‰), the simulations show that if this pathway was relevant to CEs mineralization, it could be detected as both the x_{TCE} and the CIMB increase during cis-DCE degradation (Fig. 3-10b and 10c). The simulations could theoretically match data from wells at which CIMB is slightly enriched and x_{TCE} larger than in simulations of TCE and cis-DCE simultaneous reductive dechlorination as D12, D14, or D19. However, those wells present little initial TCE degradation, therefore B_{CE} would remain limited (20-30 %, Fig. 3-9) for those wells even if all cis-DCE would be oxidised.

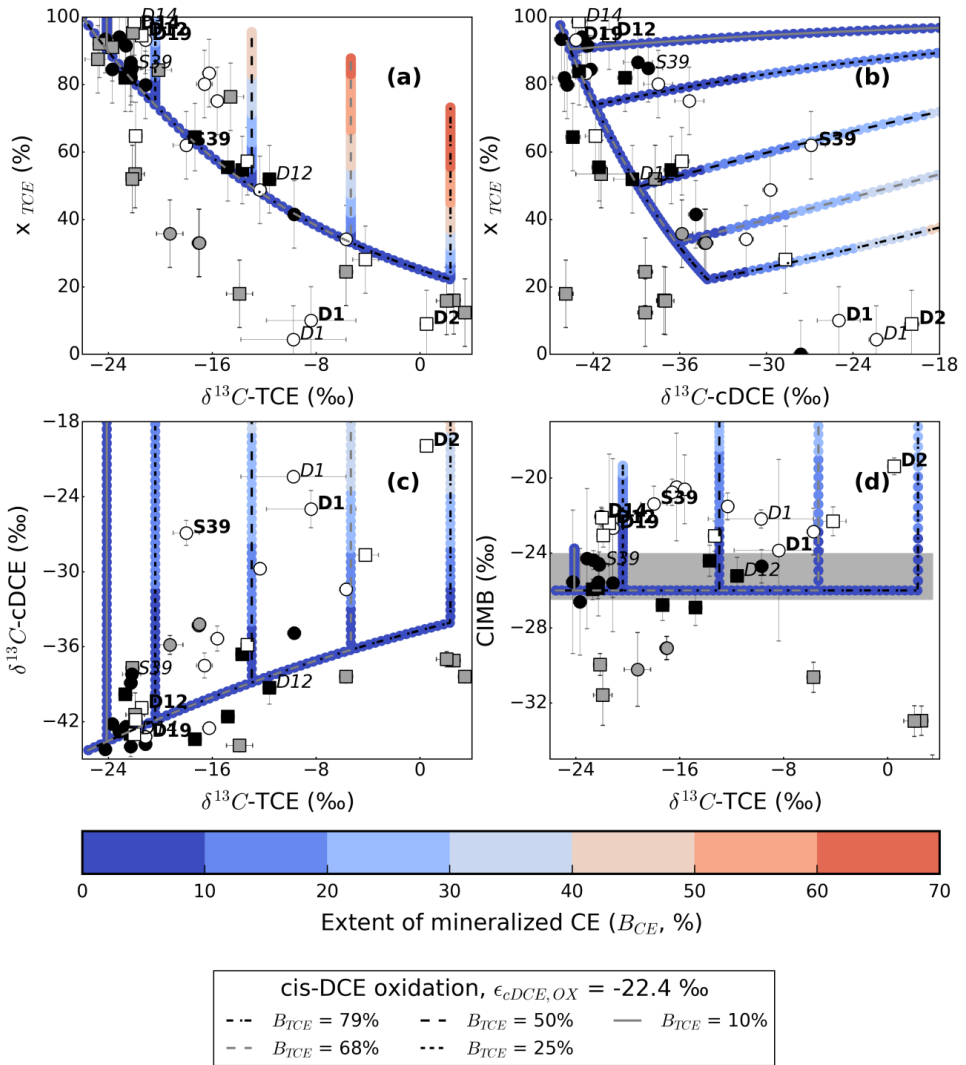


Fig. 3-9 : Simulations results for cis-DCE oxidation following sequentially TCE reductive dechlorination with $\epsilon_{cDCE,OX}$ of -22.4 ‰ . The simulations differ from the extent of TCE reduced before cis-DCE oxidation starts and TCE degradation stops (after TCE biodegradation extents (B_{TCE}) of 10%, 25%, 50%, 68 %, and 79%). The coloured lines correspond to the different states of CEs mineralization (B_{CE}) per 10 %. The well data are represented by the markers, the description of the legend is similar to Fig. 3-4.

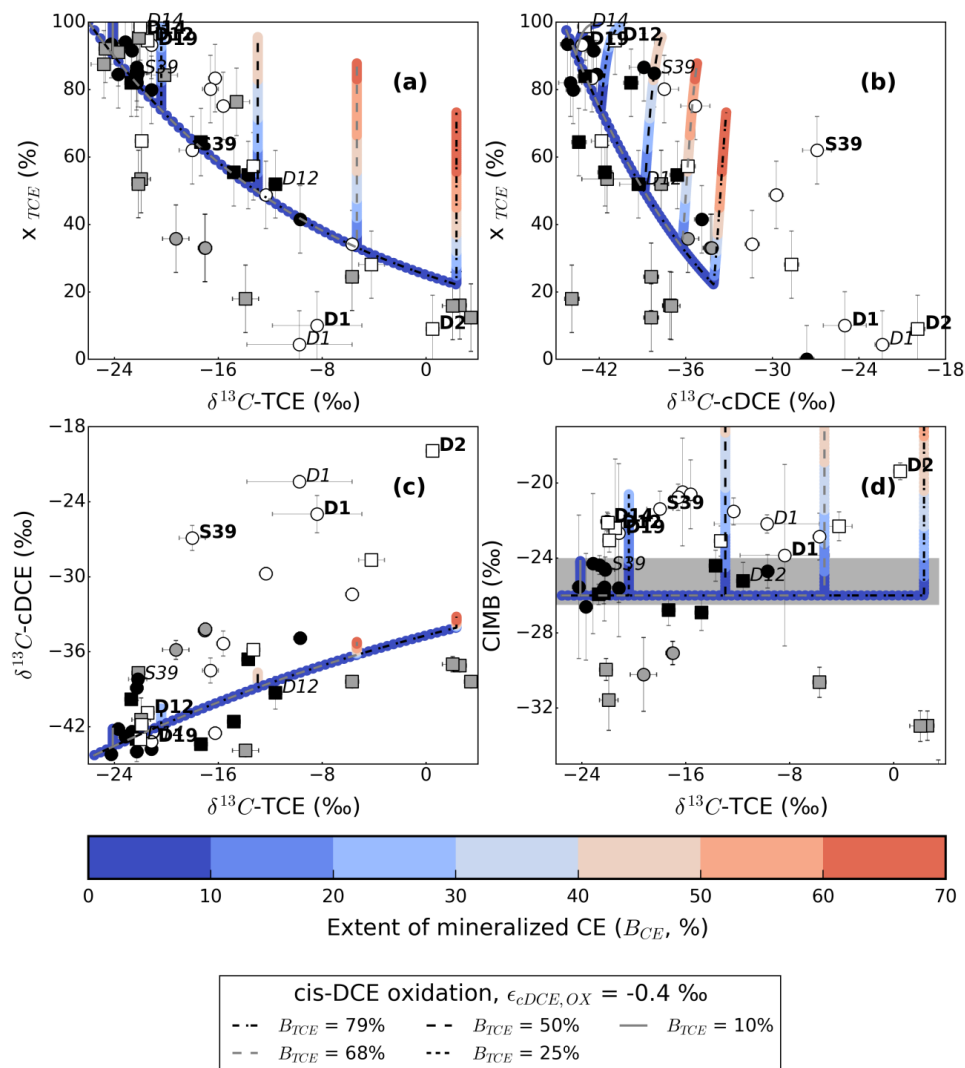


Fig. 3-10 : Simulations results for cis-DCE oxidation following sequentially TCE reductive dechlorination with $\epsilon_{cDCE,OX}$ of -0.4 ‰. The simulations differ from the extent of TCE reduced before cis-DCE oxidation starts and TCE degradation stops (after TCE biodegradation extents (B_{TCE}) of 10%, 25%, 50%, 68 %, and 79%). The coloured lines correspond to the different states of CEs mineralization (B_{CE}) per 10 %. The well data are represented by the markers, the description of the legend is similar to Fig. 3-4.

3.3.5 TCE cometabolic oxidation

This section aims at evaluating the potential of batch modeling for the detection and quantification of TCE oxidation through a low-fractionating pathway. Aerobic cometabolism of the CEs is expected to be detectable through changes of the CIMB

through changes of the CEs molar fraction. Oxidative degradation of the depleted cis-DCE would enrich the CIMB, while in the case of faster TCE oxidation once cis-DCE is produced CIMB decrease would be possible (Fig. 3-11d). The performance of aerobic cometabolism decreases with increasing chlorination. Therefore, TCE degradation is expected to be slower than of cis-DCE with this pathway (Jesus et al., 2016). The hypothesis of a faster TCE degradation was considered to answer the unusual decrease of the CIMB at the site. Additional TCE and cis-DCE cometabolism once TCE reduced reductively to cis-DCE are therefore simulated to evaluate isotope and molar fraction patterns are discernible. To simplify the model, cis-DCE reductive dechlorination is not simulated. Trans-DCE was also not included, and the bulk carbon enrichment factor $\epsilon_{C_{TCE, RD, bulk}}$ (-18 ‰) was used for the simulation of TCE reductive dechlorination. Based on the previous CSM (Chapter 2), $\epsilon_{C_{TCE, OX}}$ was set to -2 ‰. In each simulation, TCE degrades first to cis-DCE reductively. Reductive dechlorination stops once ~20 % of TCE is degraded ($\delta^{13}\text{C}$ -TCE enrichment is then of about 4 ‰), and TCE oxidation with or without co-occurring cis-DCE degradation starts. The scenarios tested to explain those patterns differ from their relative TCE and cis-DCE aerobic cometabolism rate constants $k_{DCE, OX}/k_{TCE, OX}$ (0.2 for TCEox1-2-3, 1.0 for TCEox4, 2.0 for TCEox4, and 0.0 for TCEox5), and from $\epsilon_{C_{DCE, OX}}$ (0 ‰ for all simulations (Chu et al., 2004) except for TCEox2 ($\epsilon_{C_{DCE, OX}} = -2$ ‰, (Clingenpeel et al., 2012) and TCEox 3 ($\epsilon_{C_{DCE, OX}} = -8$ ‰, (Abe et al., 2009b)).

Simulations of TCE cometabolism with low carbon isotope enrichment are compared to the data of several wells at which the CSIA patterns differed noticeably from the prior simulations. Those wells are found in two main groups in the deep aquifer. The depleted CIMB calculated for the samples from wells upgradient the deep plume D3, D4, D7, and D8 differ from the constant or positive CIMB obtained through prior simulations (Fig. 3-11d). At the wells D18, and D19 which are downgradient in the deep plume, the CIMB is constant or enriched although $\delta^{13}\text{C}$ -cDCE seems depleted in comparison with the simulated $\delta^{13}\text{C}$ -cDCE obtained from a TCE reductive model (Fig. 3-11c). The deep plume (mostly the downgradient part) is otherwise unlikely to host other degradation pathways than TCE reductive dechlorination.

The simulations show that for B_{CE} values > 80 %, $\delta^{13}\text{C}$ -TCE would enrich by about 6 ‰ compared to a scenario without TCE cometabolism. Provided cis-DCE degradation is faster than TCE (TCEox5), both x_{TCE} and the CIMB will increase as observed at D19. Equal aerobic degradation rate constant for both cis-DCE and TCE (TCEox4) yields unchanged molar ratios and enriched $\delta^{13}\text{C}$ -TCE compared to the TCE reductive dechlorination model (black line), as observed at D18. Finally, faster TCE aerobic cometabolism compared to cis-DCE degradation (TCEox1-2-3) leads to CIMB decrease and to lower x_{TCE} compared to a scenario without TCE aerobic cometabolism. Those simulations cover the ranges of molar fraction and isotope ratios observed at the wells D3, D4, D6, and D7. At wells D3 and D4, the noticeable $\delta^{13}\text{C}$ -cDCE enrichment compared to simulation of TCE reductive

dechlorination matches best the simulation with the largest $\varepsilon_{C_{DCE,OX}}$ (TCEox3). As $\delta^{13}\text{C}$ -cDCE enrichment seems to be an exception for wells at which CIMB decreased, this enrichment could instead be the result of another pathway such as cis-DCE reductive dechlorination. This assumption is line with the prior results as cis-DCE reductive dechlorination is expected for nearby wells D1 and D2 (Section 3.3.4). For D7 and D8, the pair of $\delta^{13}\text{C}$ -cDCE and $\delta^{13}\text{C}$ -TCE values differ strongly from the TCE RD simulation (Fig. 3-11c). $\delta^{13}\text{C}$ -TCE enrichment would have been of about 12 ‰ for D7 and 20 ‰ for D8 (Fig. 3-11c), which is at least twice larger than at the other wells.

The variation of molar fractions and isotope ratios is unlikely to result from a single degradation pathway. First, as it was already mentioned, the main condition for the CIMB to decrease would be a faster aerobic degradation for TCE than for cis-DCE which is unlikely. Additional contradictions are: (1) possible larger $\varepsilon_{C_{TCE,OX}}$ at two wells; and (2) lower $k_{DCE,OX}/k_{TCE,OX}$ upgradient the deep plume compared to downgradient. Either several aerobic pathways occur in the deep aquifer, such as TCE direct metabolism which is linked to a larger $\varepsilon_{C_{TCE,OX}}$ (Gaza et al., 2019), or other hypotheses than degradation have to be considered to explain the depleted CIMB. As developed in the prior CSM (Chapter 2), differential transport during back-diffusion might decrease the CIMB.

Those simulations point out that distinguishing degradation pathways would be nearly impossible in case low-fractionating degradation pathways occurred with similar rates constants for all CEs. In this case, both molar fractions and isotope ratios would be nearly constant with time unless degradation is advanced. Consequently, a risk remains that batch modeling is not sufficient to detect a certain combination of degradation rate constants and enrichment factors despite their relevance for the quantification of CEs biodegradation. However, when degradation rate constants are sufficiently different, the combined changes of the molar ratios and the CIMB can be indicative of degradation pathways with little isotope fractionation.

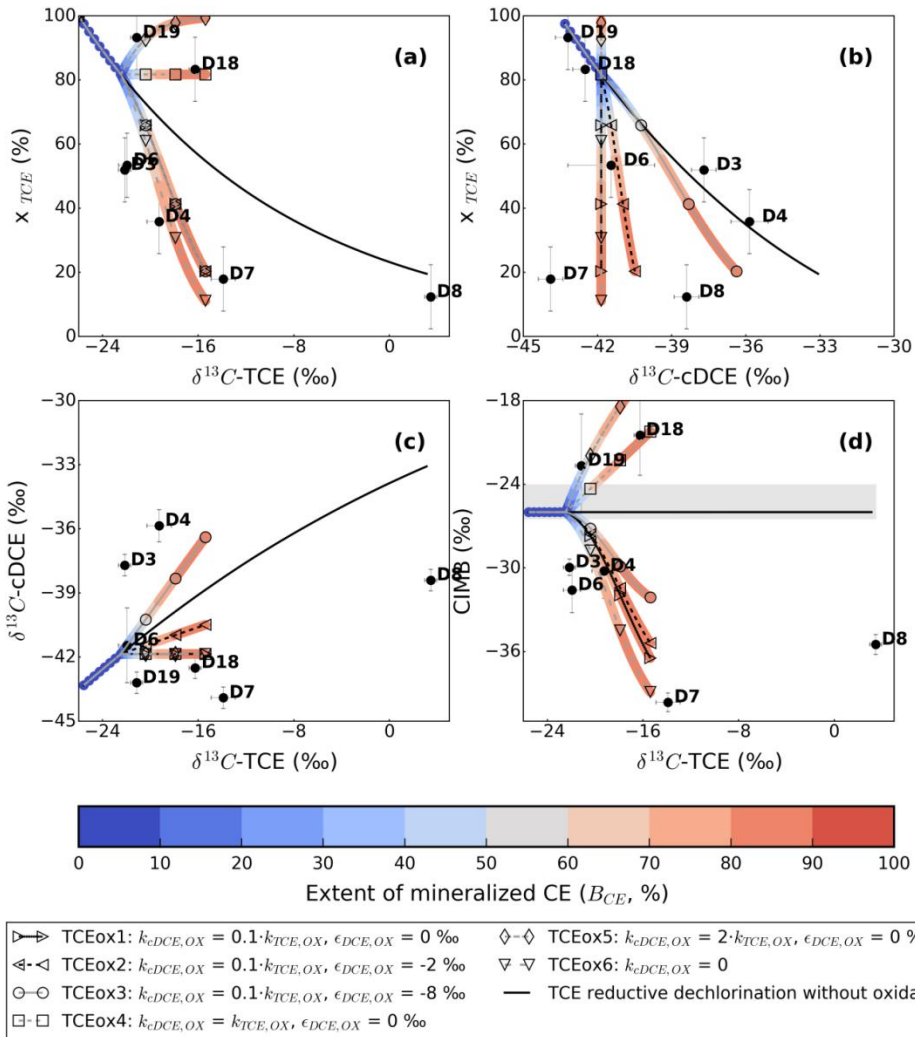


Fig. 3-11 : Simulation of TCE oxidative degradation through cometabolism, simultaneously, or not, to cis-DCE cometabolism. The coloured lines correspond to the different states of CEs mineralization (B_{CE}) per 10 %. The well data are represented by the markers, the description of the legend is similar to Fig. 3-4.

3.4 Conclusion

Modeling of carbon (C) and chlorine (Cl) compound specific isotope analysis (CSIA) data was employed in order to survey possible degradation pathways at a field site. Relative chlorinated ethenes concentrations and CSIA values were simulated based on the prior degradation hypotheses as part of the site’s conceptual model. The spatial heterogeneity of the degradation rate constants probably reflecting the heterogeneous lithology were

impeding the application of reactive transport models at this site. The present study therefore confronted the site data to simulations of degradative pathways obtained with a batch model. The simulations of trichloroethylene (TCE) reductive dechlorination (RD) to both the cis- and trans-dichloroethylene (cis-DCE and trans-DCE) isomers validated that the observed ranges of isotope ratios and molar fraction for TCE and for both DCE isomers could correspond to the occurrence of two different TCE degradation pathways at the site, one towards mainly trans-DCE and the other towards mainly cis-DCE, with slightly different isotope enrichment factors. The simulation supports here the hypothesis of the prior CSIA study and offers further insights, as enriched $\delta^{13}\text{C}$ -(t-/c-)DCE compared to the simulated DCEs isotope ratios (in the absence of further degradation) were an indicator of further degradation.

Both reductive and oxic degradation of cis-DCE were suspected degradation pathways at the site and were included in the model using isotope enrichment factors from the literature. The simulations allowed determining that the cis-DCE degradation pathway leading to strong $\delta^{13}\text{C}$ -cDCE fractionation and to most CEs mineralisation was likely RD as it seemed simultaneous to TCE RD. The limited chlorine isotope fractionation during cis-DCE both oxidative and reductive pathways prevented the use of $\delta^{37}\text{Cl}$ -cDCE modellisation for the identification of degradation pathways. Hardly detected at the site, VC would therefore be quickly degraded further. Based on the simulations, the maximum of CEs mineralisation calculated based on the isotope ratios at the site would be from 30 % to 45 % provided neither TCE nor cis-DCE oxidation occurred.

Aerobic cometabolism of TCE and cis-DCE with methane oxidation was also suspected at the site. Provided TCE aerobic cometabolism was faster than cis-DCE, such pathway could explain the unusual decrease of the CIMB in the deep aquifer. However, the comparison between the simulations of CEs oxidation and the data illustrated that a single oxidative degradation pathway could not yield the diversity of molar fractions and isotope ratios patterns for TCE and cis-DCE upgradient in the deep aquifer. Simulations illustrated that the CIMB depletion was generalised in this area and where the CIMB was enriched, its value was lower than expected based on the simulations of TCE and cis-DCE degradation. The alternative hypothesis that CIMB decrease was linked to differential transport during back-diffusion could be a preferred explanation to the complex isotope pattern upgradient the deep aquifer.

This study shows that to practitioners, the batch model linked to the data analysis might help the identification of key degradation and mineralisation processes, also in the presence of several degradation pathways. Additionally, such a batch model approach can provide a first idea of the possible extent of degradation pathways and is helpful for selecting the most reliable data for the calibration of a spatially explicit model, with or without including isotope fractionation.

Supporting information to chapter 3

S3.1 Calculations of different in isotope ratios between parent and daughter compounds

Table S3-1: Parent to daughter initial isotope difference.

Sample	$\delta^{13}\text{C-TCE}$	$\delta^{13}\text{C}_{\text{cDCE}}$	Difference TCE-cis-DCE	$\delta^{13}\text{C-tDCE}$	Difference TCE-trans-DCE	$\delta^{37}\text{Cl-TCE}$	$\delta^{37}\text{Cl}_{\text{cDCE}}$	Difference TCE cis-DCE	CIMB	xTCE
D13	-22.3±0.5	-44.0±0.8	-21.7			2.7±0.5	0.1±0.7	-2.5	-25.6	81.9
D9	-22.3±0.5	-43.0±0.5	-20.7	-50±1	-27.7	2±1	-2±1	-3.9	-25.9	83.9
D11	-23.7±0.5	-42.2±0.5	-18.5	-46.9±0.5	-24.2	3±1	-1±1	-3.2	-26.6	84.5
S39	-22.2±0.7	-38.2±1	-16.0			3.8±0.5	1.8±0.7	-2.0	-24.6	84.8
D15	-24.2±0.5	-44.2±0.5	-20.0	-49±0.5	-26.3	3±1	-0.7±1	-3.2	-25.5	93.4
D17	-23.1±0.5	-42.8±0.5	-19.6			3±1	-0.1±1	-3.0	-24.3	94.1

Table S3-2: Average parent to daughter initial isotope difference and uncertainty calculated using uncertainty propagation.

	TCE-cis-DCE $\delta^{13}\text{C}$	TCE-trans-DCE $\delta^{13}\text{C}$	TCE-cis-DCE $\delta^{37}\text{Cl}$
Average of the parent-daughter difference and uncertainty	-19.4±0.6	-26.1±0.8	-3±1.2

S3.2 Selection of redundant wells

Two sampling campaigns occurred for this study. The redundant values are not employed in the determination of enrichment factors. When the second sampling of a well yielded the same value than during the previous sampling campaign, the new values was not employed for the statistics. The plots below present the duplicates of wells at which the CIMB is constant.

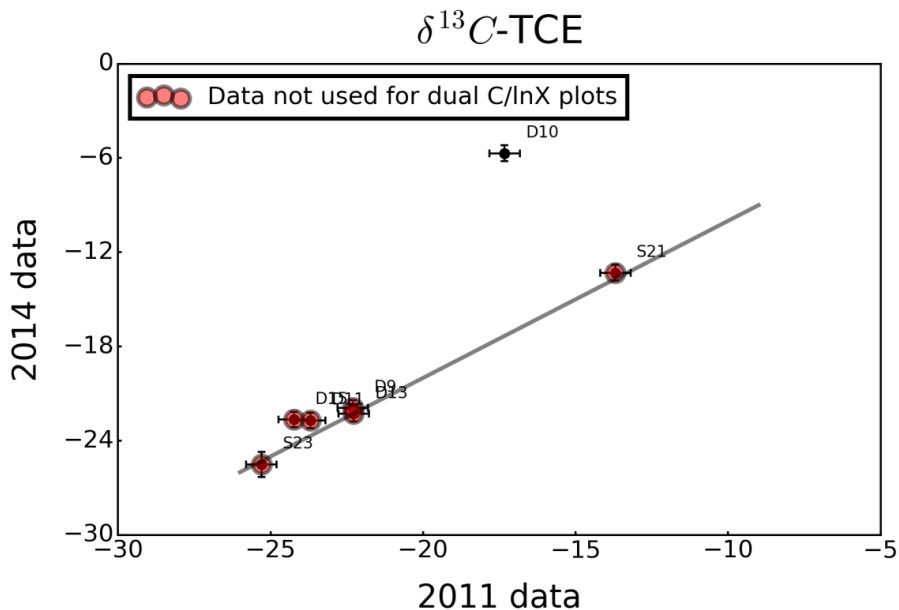


Fig. S3-1: Carbon isotope ratios during the 2011 campaign vs. 2014 campaign for wells with constant CIMB. Wells S21, S23, D9, D11, D13, and D15 present redundant data. For those wells only data from the 2011 sampling campaign are used for the calculation of TCE carbon isotope enrichment factor. For D10, data from both sampling campaigns are used.

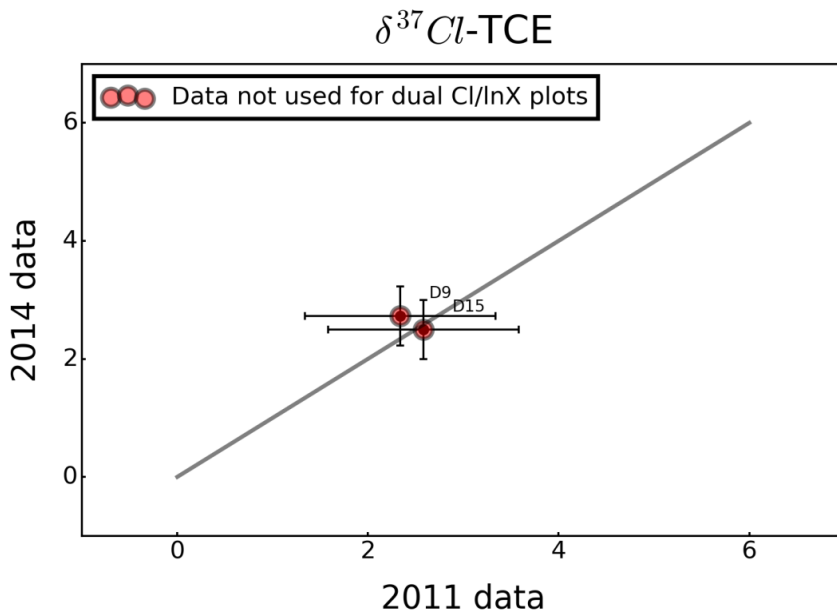


Fig. S3-2 : Chlorine isotope ratios during the 2011 campaign vs. 2014 campaign for wells with constant CIMB. Wells D9 and D15 present redundant data. For those wells only data from the 2011 sampling campaign are used for the calculation of TCE chlorine isotope enrichment factor.

S3.3 York fit of the wells with constant CIMB to obtain C and C isotope enrichment actors during TCE reductive dechlorination

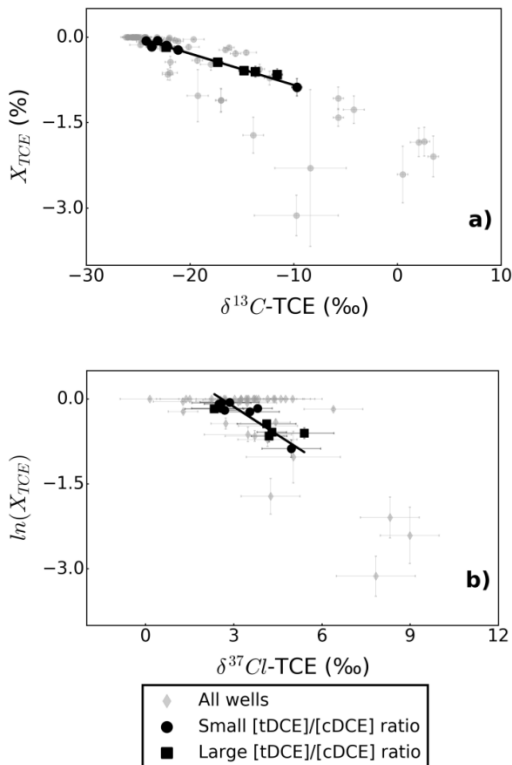


Fig. S3-3 : TCE molar fraction vs. TCE isotope ratios of carbon (a) and chlorine (b) with the York fit line for the selected wells (black line). The selected wells (black squares or circles) correspond to wells with constant CIMB sampled in 2011. If the 2011 data differs from the 2014 data, or if there is not data sampled in 2011 for that wells, the data from the 2014 sampling campaign is employed. The other wells are shown in grey.

S3.4 Carbon isotope enrichment factors (ϵ_C) for TCE and cis-DCE biotic reductive degradation

Table S3-3: Carbon isotope enrichment factor during TCE biotic reductive dechlorination in laboratory experiments.

ϵ_C	Reference
-18.9 ‰	(Cichocka et al., 2007)
-12.2 ‰	
-16.4 ‰	(Lee et al., 2007)
-9.6 ‰	
-3.3 ‰	
-12.8 ‰	(Liang et al., 2009)
-4.07 ‰	
-13.7 ‰	(Cichocka et al., 2008)
-8.5 ‰	
-6 ‰	
-3.5 ‰	
-8 ‰	(Fletcher et al., 2011)
-9.8 ‰	
-12.2 ‰	(Cretnik et al., 2013)
-9.1 ‰	
-12.2 ‰	(Cretnik et al., 2014)
-18.9 ‰(± 3.3 ‰)	Average (standard deviation)

Table S3-4: Carbon isotope enrichment factor during cis-DCE biotic reductive dechlorination in laboratory experiments.

ϵ_C	Reference
-16.1 ‰	(Bloom et al., 2000)
-14.1 ‰	
-20.4 ‰	(Slater et al., 2001)
-19.9 ‰	(Hunkeler et al., 2002)
-29.7 ‰	(Lee et al., 2007)
-21.1 ‰	
-16.9 ‰	
-18.5 ‰	(Abe et al., 2009b)
-25.3 ‰	(Fletcher et al., 2011)
-21.6 ‰	
-18.4 ‰	
-17.6 ‰	
-15.8 ‰	
-14.9 ‰	Average (standard deviation)
-20 ‰(± 5 ‰)	

S3.5 Calculation of initial carbon and chlorine isotopologue concentrations.

Isotope compositions are usually reported as isotope ratios relatively to an international

standard isotope ratio R_0 with the simplified delta notation $\delta E = \frac{R_{H/L}}{R_0} - 1$, where $R_{H/L}$ is the

ratio of the concentration of heavy to light isotopes. The international standards are for carbon: the Vienna Pee Dee Belemnite; and for chlorine : the Standard Mean Ocean Chloride), As described in (Hunkeler et al., 2009), the probability mass function is employed to calculate the source isotopologue concentrations and presented Table S3-1.

Table S3-5 : Calculation of the carbon bulk isotope concentrations of initial TCE^a.

Isotope	N1	Probability	Probability	Concentration (μM)
¹² C	L	P _L	0.989173655	118.7008386
¹³ C	H	P _H	1- P _L	1.299161448

$$^a[\text{TCE}] \approx 120\mu\text{M}, \delta^{13}\text{C-TCE}_{\text{source}} = -26.00\text{‰}$$

Table S3-6 : Calculation of the chlorine isotopologue/isotopomer concentrations of initial TCE^a ($\delta^{37}\text{Cl-TCE}_{\text{source}} = 1.5\text{‰}$).

Isotopologue	N1	N2	N3	Probability	Probability	Concentration (μM)
³⁵ Cl ₁ ³⁵ Cl ₂ ³⁵ Cl ₃	L	L	L	P _L	0.43454601	52.14552104
³⁵ Cl ₁ ³⁵ Cl ₂ ³⁷ Cl ₃	L	L	H	3·P _L ² ·P _H	0.41748441	50.09812869
³⁵ Cl ₁ ³⁷ Cl ₂ ³⁵ Cl ₃	L	H	L			
³⁷ Cl ₁ ³⁵ Cl ₂ ³⁵ Cl ₃	H	L	L			
³⁵ Cl ₁ ³⁷ Cl ₂ ³⁷ Cl ₃	L	H	H	3·P _L ·P _H ²	0.13369756	16.04370774
³⁷ Cl ₁ ³⁵ Cl ₂ ³⁷ Cl ₃	H	L	H			
³⁷ Cl ₁ ³⁷ Cl ₂ ³⁵ Cl ₃	H	H	L			
³⁷ Cl ₁ ³⁷ Cl ₂ ³⁷ Cl ₃	H	H	H	P _H ³	0.01427202	1.71264253

$$^a[\text{TCE}] \approx 120\mu\text{M}, \delta^{37}\text{Cl-TCE}_{\text{source}} = 1.5\text{‰}, P_L = 0.757434801; P_H = 1 - P_L.$$

Table S3-7 : Calculation of the chlorine isotopologue/isotopomer concentrations of initial TCE^a ($\delta^{37}\text{Cl-TCE}_{\text{source}} = 3.5\text{‰}$).

Isotopologue	N1	N2	N3	Probability	Probability	Concentration (μM)
³⁵ Cl ₁ ³⁵ Cl ₂ ³⁵ Cl ₃	L	L	L	P _L	0.43391513	52.06981594
³⁵ Cl ₁ ³⁵ Cl ₂ ³⁷ Cl ₃	L	L	H	3·P _L ² ·P _H	0.41771081	50.12529693
³⁵ Cl ₁ ³⁷ Cl ₂ ³⁵ Cl ₃	L	H	L			
³⁷ Cl ₁ ³⁵ Cl ₂ ³⁵ Cl ₃	H	L	L			
³⁵ Cl ₁ ³⁷ Cl ₂ ³⁷ Cl ₃	L	H	H	3·P _L ·P _H ²	0.13403721	16.08446498
³⁷ Cl ₁ ³⁵ Cl ₂ ³⁷ Cl ₃	H	L	H			
³⁷ Cl ₁ ³⁷ Cl ₂ ³⁵ Cl ₃	H	H	L			
³⁷ Cl ₁ ³⁷ Cl ₂ ³⁷ Cl ₃	H	H	H	P _H ³	0.01433685	1.72042215

$$^a[\text{TCE}] \approx 120\mu\text{M}, \delta^{37}\text{Cl-TCE}_{\text{source}} = 2.5\text{‰}, P_L = 0.757068074; P_H = 1 - P_L.$$

S3.6 Summary of the simulations input parameters

Table S3-8 : Degradation rate constants (γ^{-1}) and enrichment factors employed in the models. Parameters being subjects to variations are shaded in grey.

a. TCE reductive dechlorination: TCE→cis-DCE and/or TCE→trans-DCE						
	$k_{TCE \rightarrow DCE}$	$\epsilon C_{TCE \rightarrow DCE}$	$k_{TCE \rightarrow DCE}$	$\epsilon C_{TCE \rightarrow DCE}$		
TCErd1	1	-19 ‰	0	NA		
TCErd2	0.9	-19 ‰	0.1	-26 ‰		
TCErd3	0.25	-19 ‰	0.75	-19 ‰		
b. TCE reductive dechlorination and cis-DCE oxidation: TCE→cis-DCE→CO ₂						
	$k_{TCE \rightarrow DCE}$	$\epsilon C_{TCE \rightarrow DCE}$	$k_{DCE,OX}$	$\epsilon C_{DCE,OX}$		
DCEox1	1	-19 ‰	1	-22 ‰		
DCEox2	1	-19 ‰	1	-0.4 ‰		
c. TCE reductive dechlorination and TCE oxidation with or without cis-DCE oxidation TCE→cis-DCE and TCE→CO ₂ and cis-DCE→CO ₂						
	$k_{TCE \rightarrow DCE}$	$\epsilon C_{TCE \rightarrow DCE}$	$k_{TCE,OX}$	$\epsilon C_{TCE,OX}$	$k_{c,DCE,OX}$	$\epsilon C_{c,DCE,OX}$
TCEox1	1	-18 ‰	1	-2 ‰	0.2	0 ‰
TCEox2	1	-18 ‰	1	-2 ‰	0.2	-2 ‰
TCEox3	1	-18 ‰	1	-2 ‰	0.2	-8 ‰
TCEox4	1	-18 ‰	1	-2 ‰	1	0 ‰
TCEox5	1	-18 ‰	1	-2 ‰	2	0 ‰
TCEox6	1	-18 ‰	1	-2 ‰	0	NA

This page was intentionally left blank

Chapter 4

Do CSIA data from aquifers inform on natural degradation of chlorinated ethenes in aquitards?¹

Abstract

Back-diffusion of chlorinated ethenes (CEs) from low-permeability layers (LPLs) causes contaminant persistence long after the primary spill zones have disappeared. Naturally occurring degradation in LPLs lowers remediation time frames, but its assessment through sediment sampling is prohibitive in conventional remediation projects. Scenario simulations were performed with a reactive transport model (PHT3D in FloPy) accounting for isotope effects associated with degradation, sorption, and diffusion, to evaluate the potential of CSIA data from aquifers in assessing degradation in aquitards. The model simulated a trichloroethylene (TCE) DNAPL and its pollution plume within an aquifer-aquitard-aquifer system. Sequential reductive dechlorination to ethene and sorption were uniform in the aquitard and did not occur in the aquifer. After 10 years of loading the aquitard through diffusion from the plume, subsequent source removal triggered release of TCE by back-diffusion. In the upper aquifer, during the loading phase, $\delta^{13}\text{C}$ -TCE was slightly enriched (up to 2‰) due to diffusion effects stimulated by degradation in the aquitard. In the upper aquifer, during the release phase, (i) source removal triggered a huge $\delta^{13}\text{C}$ increment especially for higher CEs, (ii) moreover, downstream decreasing isotope ratios (caused by downgradient later onset of the release phase) with temporal increasing isotope ratios reflect aquitard degradation (as opposed to downstream increasing and temporally constant isotope ratios in reactive aquifers), and (iii) the carbon isotope mass balance (CIMB) enriched up to 4 ‰ as lower CEs (more depleted, less sorbing) have been transported deeper into the aquitard. Thus, enriched CIMB does not indicate oxidative transformation in this system. The CIMB enrichment enhanced with more sorption and lower aquitard thickness. Thin aquitards are quicker flushed from lower CEs leading to faster CIMB enrichment over time. CIMB enrichment is smaller or nearly absent when daughter

¹ This chapter is an edited version of Thouement, H.A.A., Kuder, T., Heimovaara, T.J., van Breukelen, B.M., 2019. Do CSIA data from aquifers inform on natural degradation of chlorinated ethenes in aquitards? *J. Contam. Hydrol.* 226, 103520. doi:10.1016/j.jconhyd.2019.103520

products accumulate. Aquifer CSIA patterns indicative of aquitard degradation were similar in case of linear decreasing rate constants but contrasted with previous simulations assuming a thin bioactive zone. The Rayleigh equation systematically underestimates the extent of TCE degradation in aquifer samples especially during the loading phase and for conditions leading to long remediation time frames (low groundwater flow velocity, thicker aquitards, strong sorption in the aquitard). The Rayleigh equation provides a good and useful picture on aquitard degradation during the release phase throughout the sensitivity analysis. This modelling study provides a framework on how aquifer CSIA data can inform on the occurrence of aquitard degradation and its pitfalls.

4.1 Introduction

Chlorinated ethenes (CEs) are widely spread toxic groundwater contaminants, due to their inadequate disposal and the spilling of the commercially widely used compounds perchloroethylene (PCE) and trichloroethylene (TCE). Their potential complete reductive dechlorination to ethene in anaerobic aquifers opened opportunities for monitored natural attenuation (MNA) as an alternative to invasive, energy-intensive technologies for polluted site remediation. MNA might be specifically relevant for the monitoring of back-diffusion from low-permeability layers, which is increasingly recognized as an important cause for increased CE source longevity (Chapman and Parker, 2005; Liu and Ball, 2002; Seyedabbasi et al., 2012). Back-diffusion corresponds to the mobilization of pollutants from silt or clay layers to transmissive zones (Chapman and Parker, 2005; Johnson and Pankow, 1992; Rivett et al., 2014). The low-permeability layers act as reservoirs for contaminants due to their diffusive and sorptive properties (Liu and Ball, 2002). Even a thin contaminated clay layer might maintain CE concentrations in the aquifer above maximum concentration limits (MCLs) for decades after source removal (Parker et al., 2008; Yang et al., 2015). Usual remediation technologies are not applicable to low-permeability layers notably due to their inherent low transmissivity (Khan et al., 2004). Fortunately, recent studies show that CE biotic reductive dechlorination can take place in low-permeability layers despite the small pore size (Chambon et al., 2010; Damgaard et al., 2013a, 2013b; Manoli et al., 2012; Takeuchi et al., 2011; Verce et al., 2015). At some sites low-permeability layers present better conditions for reductive degradation (RD) than the transmissive zone (Parker et al., 2008; Petitta et al., 2013; Wanner et al., 2016). Consequently, natural attenuation in the low-permeability layers may naturally mitigate ‘back-diffusion’ and thereby limit long remediation time frames (Carey et al., 2015; Damgaard et al., 2013a; Sale et al., 2008; Schaefer et al., 2013; Wanner et al., 2018a, 2018b; West and Kueper, 2010). MNA would benefit from tools able to detect and quantify the RD potential of the low-permeability layers. However, the study of RD in low-permeability layers requires coring them, which is usually prohibitive in regular site assessment (Chapman and Parker, 2005; Filippini et al., 2016; Parker et al., 2004). Compound specific isotope analysis (CSIA) of CEs, which is increasingly employed for MNA at field sites, could potentially help degradation assessment in the low-permeability layers as monitored from the transmissive zone as shown in a recent study simulating CSIA data at the Borden site (Wanner et al., 2018b).

As a result of kinetic effects, CE degradation leads to enrichment in heavy carbon isotopes (^{13}C) of the degrading compound (Hunkeler et al., 2011b, 1999). The degree of carbon isotope enrichment is influenced by both the advancement of the reaction and the kinetic isotope fractionation factor, characteristic of the degradation reaction, and therefore informs on the extent of degradation (Abe and Hunkeler, 2006; Hunkeler et al., 1999; van

Breukelen, 2007). Reaction products are initially depleted in ^{13}C , while the weighted sum of the carbon isotope ratios of the CEs (carbon isotope mass balance, CIMB) is theoretically constant during reductive dechlorination in batch experiments (Aeppli et al., 2010; Bloom et al., 2000; Hunkeler et al., 1999). The combination of these CSIA tools proved itself powerful for detection and quantification of CEs degradation in the subsurface (Höhener, 2016; Höhener et al., 2015; Hunkeler et al., 2011a; van Breukelen et al., 2005; Wiegert et al., 2013, 2012). One potential complication, however, is that several non-destructive processes might also lead to isotope fractionation as shown in small scale lab studies and aquifer scale model simulations. Those processes include highly relevant processes in low-permeability layers, i.e., sorption; with preferential sorption for isotopologues with light carbon isotopes (^{12}C) (Höhener and Atteia, 2010; Kopinke et al., 2005; Qiu et al., 2013; van Breukelen and Prommer, 2008; Wannner et al., 2017) and diffusion, with slightly smaller diffusion coefficients of the isotopologues containing ^{13}C , as diffusion is influenced among others by molecular weight (Jin et al., 2014; LaBolle et al., 2008; Rolle et al., 2010; Wannner and Hunkeler, 2015; Xu et al., 2017). Associated isotope fractionation effects were detected in low-permeability layers. Diffusion reportedly leads to depletion in ^{13}C with depth during short diffusion periods in clay (Wannner and Hunkeler, 2015). Sorption enriches chlorinated hydrocarbons in ^{13}C with depth (Wannner et al., 2017). While the effects are small compared to RD, sorption-induced isotope fractionation for instance could lead to significant enrichment in the aquitard (Wannner et al., 2017).

Both numerical and analytical modelling were proven useful to the study of volatile compounds or tracer concentrations in the subsurface during back-diffusion processes (Adamson et al., 2016, 2015; Liu and Ball, 2002; Parker et al., 2008; Yang et al., 2015). Modelling studies were shown essential for investigating aquifer parameters influencing TCE plume tailing (Carey et al., 2015; Maghrebi et al., 2015, 2014; Yang et al., 2017).

Reactive transport models (RTMs) extended with isotope fractionation were employed to retrieve carbon isotope patterns of CEs during combined degradation and transport in sandy aquifers (Höhener, 2016; Höhener et al., 2015; Höyng et al., 2015; Hunkeler et al., 2009, 1999; van Breukelen et al., 2005). Those models were extended in order to include isotope fractionation induced by non-degradative processes (Eckert et al., 2013; Höhener et al., 2017; Rolle et al., 2010; van Breukelen et al., 2005; van Breukelen and Prommer, 2008). Such models were also applied to the study of combined reaction (degradation or sorption) and diffusion in aquitards (Wannner et al., 2017, 2016), and aquifer-aquitard systems (Wannner et al., 2018a, 2018b). Recently, modelling of CSIA data enabled the differentiation and quantification of two specific degradation pathways of chlorohydrocarbons in an aquitard (Wannner et al., 2018a).

The isotope ratios of volatile organic compounds in the transmissive zone in the vicinity of a non-reactive aquitard were studied through such RTMs. Diffusion towards low-permeability layers was shown to have a potential for carbon isotope enrichment within the aquifer (LaBolle et al., 2008), the latter being likely attenuated and negligible compared to

potential degradation-induced enrichment that could occur in the transmissive zone, also after back-diffusion (Xu et al., 2017). However, processes leading to stronger isotope fractionation in the aquitard such as degradation could potentially lead to detectable enrichment at the aquifer level (Wanner et al., 2018b; Xu et al., 2017). Moreover, diffusion of daughter products from the low-permeability layers to the aquifer was shown to contribute to plume tailing (Rasa et al., 2011; Wanner et al., 2018b). It is relevant to investigate whether any CSIA data of TCE or of its degradation products sampled in the aquifer could be used for degradation assessment despite the low concentration levels. Recently, Wanner et al. (2018b) demonstrated with a modelling study that TCE to cDCE degradation in shallow bioactive zones of aquitards could cause unique CSIA patterns in above lying aquifers.

This study extends to the aforementioned work and sets out to illustrate to which extent spatial and temporal carbon CSIA patterns could be informative of CEs reductive degradation in aquitards despite the impacts of non-destructive processes on both the concentration and isotope ratios. To this end, we apply virtual experiments, i.e., run reactive transport models fed with sets of representative model parameters for common field conditions. For example, the hydraulic parameters chosen for the model were based on previous hydrological models predicting plume tailings for different types of low-permeability layers. Following up to the work of Wanner et al. (2018b), we simulated the full sequence of reductive dechlorination; assessed the effect of thinner aquifers and deeper bioactive zones; and evaluated the performance of the Rayleigh equation and CIMB as common CSIA data interpretation tools. The main objectives of this modelling study are (1) development of a model that simulates carbon CSIA and concentration patterns in an aquifer-aquitard-aquifer system before and after source removal, and (2) evaluating the potential of CSIA data to detect reductive dechlorination and the extent of TCE degradation as occurring in the aquitard while setting a sensitivity analysis on model parameters. With the sensitivity analysis we demonstrate the effect of critical model parameters like aquitard thickness and degree of sorption on simulation results. The performance of the Rayleigh-equation to determine TCE degradation and the use of the carbon isotope mass balance under these specific conditions is also assessed. Finally, we provide recommendations to practitioners on how CSIA data from aquifers can be used and interpreted for the detection and quantification of reductive dechlorination in low-permeability layers.

4.2 Methods

4.2.1 General model concept

Fig. 4-1 represents the general model concept for the base case scenario consisting of a 100 m long and 10 m high cross-sectional domain. A 1 m thick clay aquitard separates an 8 m

thick upper sand aquifer from a lower aquifer, of which only the upper 1 m is modelled. The model simulates two temporal phases: a *loading phase*, during which dissolution of a TCE DNAPL source present at the bottom of the upper aquifer leads to TCE advection through the aquifer following groundwater flow and TCE diffusion into the clay aquitard; followed by a *release phase*, which focusses on back-diffusion of CEs from the clay aquitard to the aquifer after the DNAPL is removed after 10 years (Adamson et al., 2016). A natural hydraulic gradient of $0.0042 \text{ m}\cdot\text{m}^{-1}$ was imposed through the boundary conditions, leading together with the selected permeability and porosity (see later) to a groundwater flow velocity of $0.12 \text{ m}\cdot\text{d}^{-1}$ in the sand aquifers. For simplicity, sorption of CEs is assumed to occur only in the aquitard. Likewise, sequential reductive dechlorination (from TCE to DCE, VC, and finally ethene) is only assumed to occur with a uniform rate constant across the aquitard (discussed further in Section 4.2.4). Localised reductive dechlorination (RD) in the aquitard in an otherwise unreactive aquifer is likely as the aquifer, unlike the aquitard, can be too oxic to host reductive processes, as it was previously observed at the Borden site (Wanner et al., 2016). Aquitards usually contain higher contents of soil organic matter, that can potentially act as electron donor in reductive dechlorination (Wanner et al., 2016). The model is described in detail in the following.

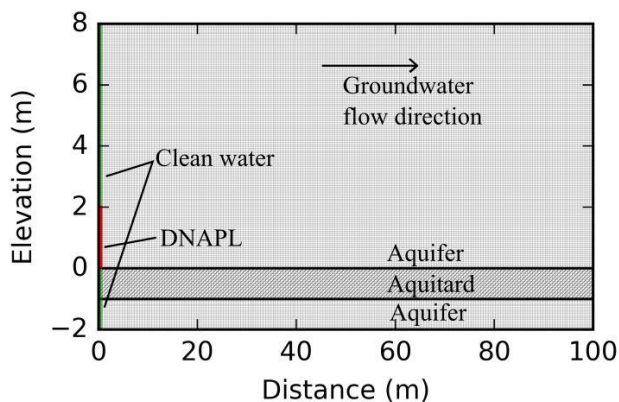


Fig. 4-5 : General model concept. A TCE DNAPL is present upgradient at the bottom of the upper aquifer until it is removed at year 10. Clean water flows above, below, and through the contaminated zone. Vertical discretization is finest in the aquitard and the underlying lower aquifer (only upper 1 m modelled, vertical lines). Horizontal discretization (horizontal lines) is constant with distance. In this figure and the following, zero elevation refers to the bottom of the upper aquifer.

4.2.2 Modelling approach

The multicomponent reactive transport code PHT3D (Prommer et al., 2001) was applied using the FloPy Python package (Bakker et al., 2016) as interface. PHT3D allows combining the geochemical model PHREEQC-2 (Parkhurst and Appelo, 1999) with the 3-D multicomponent transport model MT3DMS (Zheng et al., 2012). The implicit TVD method was used. Similarly as in prior publications (Hunkeler et al., 2009; van Breukelen et al., 2017, 2005), PHREEQC-2 was employed for modelling carbon isotope fractionation during sequential degradation of chlorinated ethenes. MT3DMS has been applied before to simulate back-diffusion and has been validated with analytical solutions and experimental data (Chapman et al., 2012). Each carbon isotopologue was simulated with different values of effective diffusion coefficients (D_e), solid-phase organic carbon-water partitioning (sorption) coefficients (K_{oc}), and first-order degradation rate constants (k). The selection procedure of the aforementioned model parameters is elaborated below.

4.2.3 General model settings

The model grid for the base case consists of 200 columns, 200 rows, and 1 layer. Grid discretization is of 0.5 m in the horizontal direction (columns) and of 0.05 m in the vertical direction (rows) (Fig. 4-1). Results obtained with grids of higher and lower resolutions are presented for comparison in Fig. S4-2 in the Appendix. For simplicity, the porosity was set to 0.35 for both the aquitard and aquifers. This value is typical for unconsolidated sands albeit at the lower end of clay layers. The dry bulk density was set to $1.855 \text{ kg}\cdot\text{L}^{-1}$ throughout the system. The aquifer and aquitard were given a hydraulic conductivity of $3650 \text{ m}\cdot\text{y}^{-1}$ and $1 \text{ m}\cdot\text{y}^{-1}$, respectively. The low hydraulic conductivity of the clay aquitard leads to negligible flow. Longitudinal and vertical transverse dispersivities were set to 1.0 m and 1.5 mm, respectively. These values are in the range of previously reported dispersivities values of plumes in sandy aquifers (Garabedian et al., 1991; Klenk and Grathwohl, 2002). The selected grid spacing (above) and time step (1 day) insure satisfying grid Peclet and Courant criteria.

Aqueous diffusion coefficient (D_w) values were calculated as $5.9\cdot 10^{-10} \text{ m}^2\cdot\text{s}^{-1}$, $6.9\cdot 10^{-10} \text{ m}^2\cdot\text{s}^{-1}$, $9.7\cdot 10^{-10} \text{ m}^2\cdot\text{s}^{-1}$, and $1.3\cdot 10^{-9} \text{ m}^2\cdot\text{s}^{-1}$ for TCE, DCE, VC, and ethene, respectively, as elaborated in Section 4.2.5. The fraction of organic content f_{oc} of the clay aquitard was set to 0.0033 (0.33 %), a representative value for fluvial sediments (Griffioen et al., 2016). Together with the selected values of other model parameter a retardation factor of 3.5 for TCE was obtained similar to prior back-diffusion studies (Carey et al., 2015; Parker et al., 2008). The calculation of the retardation factors is elaborated in Section 4.2.6. During the simulations linear sorption is assumed. The high CEs concentrations following the dissolution of the DNAPL could saturate the sorption capacity, in which case Freundlich or

Langmuir sorption isotherms would provide more realistic results. The implications of the model simplifications are described further in the discussion.

4.2.4 Pollutant source and degradation

A TCE DNAPL source was simulated as a constant concentration boundary condition at the lower 2 m of the upper aquifer for 10 years (Fig. 4-1). Such source positioning was previously used in the study of back-diffusion of both NAPL and DNAPL (Xu et al., 2017). The TCE source concentration ($\sim 0.6 \text{ g}\cdot\text{L}^{-1}$) was about half the TCE solubility ($1.28 \text{ g}\cdot\text{L}^{-1}$) and $\sim 6\cdot 10^5$ times larger than the typical carbon CSIA quantification limit ($1 \mu\text{g}\cdot\text{L}^{-1}$). Concentrations and isotope ratios are shown only for concentrations above this quantification limit.

The source was given a constant isotope composition $\delta^{13}\text{C-TCE}_{\text{Source}}$ of -30 ‰. Setting a constant isotope ratio for a dissolving DNAPL is acceptable as the model does not simulate degradation in the sand aquifer and therefore no weathering of the DNAPL (Hunkeler et al., 2004; Hwang et al., 2013). The three carbon isotopologues of each CE and ethene are simulated as done before for chlorine isotopologues (Hunkeler et al., 2009). The TCE carbon isotopologue concentrations in the source were calculated from the TCE concentration and isotope ratio of the source, as described in Appendix Section S4-3. After a simulation time of 10 years, the loading phase was stopped by setting the concentration of each CE at the constant concentration boundary condition to $0 \text{ g}\cdot\text{L}^{-1}$.

Biological reductive dechlorination in the aquitard degrades sequentially TCE to DCE, VC, and finally ethene. The model assumes that only the major cis-DCE isomer is formed. First-order degradation rate constants for biotic reductive dechlorination are selected in the line with the values employed in (van Breukelen et al., 2005), i.e., 1 y^{-1} , 0.2 y^{-1} , and 0.2 y^{-1} for TCE, DCE, and VC, respectively (Table S4 in Appendix). Although the high source concentration applied calls for Monod-kinetics (Bekins et al., 1997), first-order kinetics often used at field sites was chosen for simplicity, and also further additional complexity such as microbial growth, inhibition, and donor limitation (Chambon et al., 2013) was ignored. Degradation rate constants were assumed to remain constant with depth in the base case model as opposed to two recent studies where bioactivity was assumed to be (i) retrained a centimetres thin bioactive zone at the top of a thick aquitard as modelled by exponentially declining rate constants with depth (Wanner et al., 2018b), or (ii) declining gradually with depth as modelled by nearly linearly decreasing rate constants till about 1 m depth (Wanner et al., 2018a). In those previous studies, likely the microorganisms distribution, lead to decline of the degradation rate constants with depth. In the one study, the decreasing availability of nutrients and electron donors, diffusing from the aquifer to the aquitard, likely influenced the degradation rate constants (Wanner et al., 2018b). In the other study, the limited presence of microorganisms responsible for degradation of the

chlorohydrocarbons of concern deeper than 0.35 cm together with the near linearly decreasing degradation rate constants below this depth could indicate that transport of microorganisms remains a potential limitation for biotic degradation across thick aquitards (Wanner et al., 2018a). For thin aquitards (< 1 m) with rich organic carbon content, the contact with aquifers both above and below is likely to allow a more homogeneous bacterial distribution than for the aquitards described in those prior studies. Moreover, several bacterial strains including *Dehalococcoides* spp., a strain able of complete TCE to ethene degradation, were present across the studied depth of ~1.1 m (Wanner et al., 2018a). Unfortunately, at this stage studies on degradation and bacterial activity in aquitards are still limited. The choice of low uniform degradation rate constants in the aquitard is therefore a simplification which could be refined later once bacterial degradation in aquitard is better understood.

Each isotopologue degrades with a slightly different rate constant, leading to isotope fractionation of the CEs. For carbon, this fractionation is usually modelled as a bulk isotope fractionation, i.e., simplifying the model to the evolution of the compound's fraction of the light and the heavy isotope (van Breukelen et al., 2017, 2005). For this isotopologue model, we express the respective degradation rates of each isotopologue employing the bulk kinetic carbon isotope enrichment factor $\epsilon_{Degradation}$:

$$\frac{d^{LL}C}{dt} = k \cdot {}^{LL}C \quad (4-1)$$

$$\frac{d^{LH}C}{dt} = k \cdot (\epsilon_{Degradation} + 1) \cdot {}^{LH}C \quad (4-2)$$

$$\frac{d^{HH}C}{dt} = k \cdot (2 \cdot \epsilon_{Degradation} + 1) \cdot {}^{HH}C \quad (4-3)$$

where ${}^{LL}C$, ${}^{LH}C$, and ${}^{HH}C$ are the isotopologue concentrations (moles) of the carbon isotopologues containing two light (LL) carbon isotopes, one light (L) and one heavy (H) isotope (LH), and two heavy isotopes (HH), respectively; and k (y^{-1}) the first-order degradation rate constant.

Carbon isotope fractionation of chlorinated ethenes during biotic reductive dechlorination has been intensively studied. For this model, average values of bulk carbon isotope enrichment factors $\epsilon_{Degradation}$ obtained with microcosm experiments were used for the base case scenario, i.e., -12 ‰, -21 ‰, and -23 ‰ (Table S4-3), during biotic reductive dechlorination of TCE, DCE, and VC, respectively. The variability of enrichment factors reflects the diversity of degradative microorganisms. For instance, $\epsilon_{Degradation}$ during TCE reductive dechlorination was found to vary from -3.3 ‰ to 18.9 ‰ (Cichocka et al., 2008).

We restrained from assessing this variability on the model outcome, testing only a single lower value for each $\varepsilon_{\text{Degradation}}$ in an additional simulation in Section 4.3.5.

4.2.5 Diffusion and diffusion-induced isotope fractionation

Aqueous diffusion coefficients of each CE isotopologue were acquired from the aqueous diffusion coefficients of the CEs. Each CE's aqueous diffusion coefficient D_w was first calculated through (Worch, 1993):

$$D_w = \frac{3.595 \cdot 10^{-14} \cdot T}{\eta_T M_{CE}^{0.53}} \quad (4-4)$$

where T is the water temperature ($^{\circ}\text{K}$), set for the model to 283.15 $^{\circ}\text{K}$ (10 $^{\circ}\text{C}$), η_T the water's viscosity at T ($\text{Pa}\cdot\text{s}$), and M_{CE} is the CE's weighted molar mass using isotopologues abundances at 0 ‰ (Table S4-5 in Appendix).

Each isotopologue was then assigned a specific diffusion coefficient to model diffusion-induced isotope fractionation. Recent work showed that for a CE with N isotopologues, isotopologue-specific aqueous diffusion coefficients ($D_{w,n}$) of the isotopologue n are defined by (Jin et al., 2014):

$$D_{w,n} = D_w \cdot \sum_i^N A_i \left(\frac{m_i}{m_n} \right)^{\beta} \quad (4-5)$$

where A_i and m_i are the relative abundance and the mass of the isotopologue i , respectively, and β is an empirical coefficient determined experimentally for each compound. The abundances at 0 ‰ and masses of the isotopologues, given in Table S4-5 in Appendix, were then employed to calculate the diffusion coefficients of each isotopologue. The diffusion coefficient of the compound will be slightly modified by the change in its isotopologue composition.

Measurements obtained with a modified Stroke's diffusion cell (Wanner and Hunkeler, 2015) yielded β values of 0.029 ± 0.008 and 0.024 ± 0.002 for carbon and chlorine isotope fractionation of TCE, respectively. Through the modelling of diffusion experiments in gel diffusion tubes a slightly higher β value for chlorine isotope enrichment of TCE was obtained (0.043 ± 0.008 ; while of DCE = 0.088 ± 0.015 (Jin et al., 2014)). The difference between TCE and DCE might be explained by the role of the hydration shell in the extent of diffusion-induced isotope fractionation (Jin et al., 2014).

In the present model, we used the β values reported by Wanner et al. (Wanner and Hunkeler, 2015). Considering the similarity of β values for carbon and chlorine isotope fractionation of TCE, we assumed that the same applies to DCE. Therefore, we used $\beta = 0.088$ for the

carbon isotope effects of DCE. No experimental β values for VC and ethene are available. For those compounds, we used the value of 0.088, given that DCE in the closest available analogue for these compounds (Jin et al., 2014). Resulting diffusion-induced carbon isotope enrichment factors $\varepsilon_{\text{Diffusion}}$ are -0.2 ‰, -0.9 ‰, -1.4 ‰, and -3.1 ‰ for TCE, DCE, VC, and ethene, respectively (Table S4-4). Only $1 - D_{w,LH}/D_{w,LL}$ is given here for simplicity, where $D_{w,LH}$ and $D_{w,LL}$ are the aqueous diffusion coefficients for the isotopologue containing one heavy and one light and two light isotopes, respectively (Table S4-5 in Appendix lists the isotopologue-specific aqueous diffusion coefficients).

In porous media, molecules diffuse around the sediment grains of the rock matrix. Therefore, the effective diffusion coefficient D_e is smaller than D_w in order to account for the added travel distance. D_e was taken as $D_e = D_w \cdot \tau_{app}$, where D_w is defined for each isotopologue using eq. 4-4, and τ_{app} is the apparent diffusion tortuosity coefficient (also referred to as the tortuosity factor) (Carey et al., 2016). The coefficient τ_{app} is often written as a function of the accessible porosity for simplicity (Boving and Grathwohl, 2001). Recent work suggests that the coefficient τ_{app} is correlated to the permeability, not to the porosity of a media, with an average τ_{app} of 0.33 for low-permeability media (Carey et al., 2016). Fitting of TCE diffusion profiles in clay suggested much lower τ_{app} values (0.13, (Wanner and Hunkeler, 2015); 0.03, (Wanner et al., 2016)). In the present study, τ_{app} is taken equal to the porosity across the model (0.35) in the base case scenario.

4.2.6 Sorption and sorption-induced isotope fractionation

The retardation factor, R , represents the degree of retardation of a compound with respect to the local groundwater flow velocity and is calculated as follows:

$$R = 1 + \frac{\rho_b}{n} \cdot K_{oc} \cdot f_{oc} \quad (4-6)$$

where ρ_b is the bulk density across the aquifer-aquitard-aquifer system ($\text{kg} \cdot \text{L}^{-1}$), K_{oc} is the solid-phase organic carbon-water partition coefficient ($\text{L} \cdot \text{kg}^{-1}$), and n the porosity. K_{oc} values are usually derived from its correlation with the octanol-water partitioning coefficient, K_{ow} (Lu et al., 2011; Nguyen et al., 2005). The present study applied eq. 4-7 to the $\text{Log}K_{ow}$ values of 2.47, 1.98, 1.62, and 1.27 for TCE, DCE, VC and ethene, respectively, following the approach and the values reported in (van Breukelen et al., 2005). The K_{oc} values are then of $142 \text{ L} \cdot \text{kg}^{-1}$, $75 \text{ L} \cdot \text{kg}^{-1}$, $39 \text{ L} \cdot \text{kg}^{-1}$ and $27 \text{ L} \cdot \text{kg}^{-1}$ for TCE, DCE, VC and ethene, respectively (Table S4-4).

$$K_{oc} = 10^{0.81} \cdot K_{ow}^{0.56} \quad (\text{Valsaraj et al., 1999}) \quad (4-7)$$

The present simulation sets f_{oc} to 0.3 % in the aquitard so TCE retardation is of 3.5 as in prior modelling studies of aquifer-aquitard systems (see Table S4-1 in Appendix). The

selected f_{oc} value results in retardation factors, R , of 2.3, 1.8, and 1.5 for DCE, VC, and ethene, respectively, after applying eq. 4-6 and eq. 4-7.

Sorption-induced isotope fractionation results from the slightly stronger sorption to organic matter of molecules with light isotopes than those with heavy isotopes (Kopinke et al., 2005). The fractionation factor for linear equilibrium sorption, $\alpha_{Sorption}$, has been defined as the ratio of the K_{oc} of the heavy ($^H K_{oc}$) and the one of the light isotope ($^L K_{oc}$) (Höhener and Yu, 2012; Kopinke et al., 2005; van Breukelen and Prommer, 2008; Wanner et al., 2017). The resulting sorption-induced isotope fractionation is included in the model by attributing different K_{oc} values to each isotopologue (See Table S4-5 in Appendix). The calculation of isotopologue-specific K_{oc} values was inspired by (Höhener and Yu, 2012). We extended their approach for comparing data of differently deuterated compounds to carbon isotopologues, for which no specific relation was yet developed. The resulting relation is:

$${}^{LH} \alpha_{Sorption} = \left({}^{HH} \alpha_{Sorption} \right)^{\frac{1}{2}} \quad (4-8)$$

where ${}^{LH} \alpha_{Sorption}$ and ${}^{HH} \alpha_{Sorption}$ are the sorption-induced fractionation factors of the isotopologue containing one light (L) and one heavy (H), and two heavy (HH) carbon isotopes, respectively. The K_{oc} values of the two isotopologues containing at least one heavy carbon atom can be calculated from:

$${}^{LH} K_{oc} = {}^{LH} \alpha_{Sorption} \cdot {}^{LL} K_{oc} \quad (4-9)$$

$${}^{HH} K_{oc} = \left({}^{LH} \alpha_{Sorption} \right)^2 \cdot {}^{LL} K_{oc} \quad (4-10)$$

where ${}^{LL} K_{oc}$, ${}^{LH} K_{oc}$, and ${}^{HH} K_{oc}$ are the K_{oc} values of the isotopologue containing two light carbon isotopes, one light and one heavy, and two heavy, respectively. Isotopologue-specific K_{oc} values were estimated using the fractionation factor $\alpha_{Sorption}$ taken from the literature (see below) and the reported K_{oc} values. ${}^{LL} K_{oc} \approx K_{oc}$ was assumed, which is an acceptable approximation considering the large variation of K_{oc} . An example of the calculation of the isotopologue-specific K_{oc} is presented in the Appendix Section S4.5, and the values are reported in Table S4-5. Simulations of sorption-induced isotope fractionation during advection with an analytical solution (van Breukelen and Prommer, 2008) yielded identical results for the isotope and this isotopologue approach (see Fig. S4-1 in Appendix).

Laboratory experiments on homogeneous media yielded sorption-induced carbon isotope enrichment factors ($\varepsilon_{Sorption} = \alpha_{Sorption} - 1$) for 6 different organic compounds $\varepsilon_{Sorption}$ in the range of -0.9 ‰ to -0.1 ‰ (Imfeld et al., 2014). Unfortunately, little is known about the specific $\varepsilon_{Sorption}$ values of CEs. Only $\varepsilon_{Sorption}$ of TCE is available (-0.52±0.19 ‰ and -0.26±0.10 ‰), based on free energy linear relationships (Hoehener and Yu 2012). A recent

multi-step sorption study of DCM and 1,2-DCA reports $\varepsilon_{Sorption}$ values of about -0.54 ‰ and -0.4 ‰, respectively (Wanner et al., 2017). In the base case scenario, $^{LH}\varepsilon_{Sorption}$ for all CEs and ethene was taken at the upper predicted range -0.5 ‰ for TCE, consequently $^{HH}\varepsilon_{Sorption}$ was of -1 ‰.

4.3 Post-modelling calculations

4.3.1 Isotope ratio

The heavy to light carbon isotope ratios of a sample $R_{H/L}$ are calculated from the concentrations of the isotopologues as follow:

$$R_{H/L} = \frac{^{HH}C \cdot 2 + ^{LH}C}{^{LL}C \cdot 2 + ^{LH}C} \quad (4-11)$$

The isotope ratios are reported in the usual delta notation $\delta^{13}C$. The $\delta^{13}C$ is defined as $\delta^{13}C = R_{R/L} / R_{VPDB} - 1$ where R_{VPDB} is the carbon isotope ratio of an international standard. Isotope ratios are calculated only when the CEs concentration is above isotope quantification limit, taken as 1 µg/L for all CEs in this study.

4.3.2 Carbon isotope mass balance

The carbon isotope mass balance (CIMB) is the concentration-weighted average isotope ratio of the CEs and ethene combined:

$$CIMB = \frac{\sum [\delta^{13}C_i \cdot C_i]}{\sum C_i} \quad (4-12)$$

where $\delta^{13}C_i$ and C_i are carbon isotope ratios and concentrations, respectively, of the CEs and ethene. CIMB is not calculated when any of the CEs concentrations are below the minimum quantification limit for $\delta^{13}C$ (taken as 1 µg·L⁻¹ for all CEs for simplicity). The concept of CIMB has shown useful in other studies (Aeppli et al., 2010; Amaral et al., 2011; Hunkeler et al., 1999) as its enrichment points to, for example, oxidative transformation, whereas reductive dechlorination yields constant CIMB. The CIMB can also be calculated excluding ethene, which $\delta^{13}C$ is not always available, in which case constant CIMB would be a signal of a lack of VC transformation to ethene, for instance.

4.3.3 Performance of the Rayleigh equation to estimate TCE degradation

The Rayleigh equation is commonly applied to estimate the extent of biodegradation of a compound based on its degree of isotope enrichment and the applicable isotope enrichment factor (Hunkeler et al., 2002):

$$D_{Rayleigh} = 1 - \exp \left[\frac{1}{\varepsilon_{Degradation}} \ln \left(\frac{\delta^{13}C-TCE + 1}{\delta^{13}C-TCE_{Source} + 1} \right) \right] \quad (4-13)$$

where $D_{Rayleigh}$ is the Rayleigh-based estimate of TCE degradation, and $\varepsilon_{Degradation}$ is the bulk carbon enrichment factor during TCE degradation. A $D_{Rayleigh}$ of 0.1 signifies that 10 % of the initial TCE was degraded. The true extent of biodegradation as occurred in the model, D_{Sample} , is calculated from the simulated TCE concentration and the concentration of a non-degrading tracer with otherwise similar characteristics to TCE. D_{Sample} is calculated for a cell i of the non-sorbing aquifer as follows:

$$D_{Sample} = \frac{[TCE]_i}{[Tracer]_i} \quad (4-14)$$

where $[TCE]_i$ and $[Tracer]_i$ are the TCE and tracer concentrations, respectively, in cell i .

The Rayleigh equation systematically underestimates the true extent of degradation (Abe and Hunkeler, 2006; Höyng et al., 2015; van Breukelen and Prommer, 2008) but could under some conditions also overestimate if $\delta^{13}C$ enrichment resulting from non-degradative processes such as sorption at plume fronts or diffusion in plume cores would be attributed to degradation (Höhener and Yu, 2012; Kopinke et al., 2005; van Breukelen and Prommer, 2008; van Breukelen and Rolle, 2012). In order to decrease below the MCL of 5 $\mu\text{g/L}$, the initial TCE concentration of 0.6 g/L must be reduced by 99.999 %. At such a high number of decimals, the ratio of the extents of degradation $D_{Rayleigh}/D_{Sample}$ would be a poor quantifier of the underestimation at overall high extents of degradation. Using instead the ratio of the rate constants as a measure of the underestimation as done in previous studies (Lutz et al., 2013; van Breukelen and Prommer, 2008; van Breukelen and Rolle, 2012) circumvents this issue as it equals the ratio of the logarithms of the residual fractions, given that the rate constant k of a first-order reaction satisfies $-k \cdot t = \ln(1 - D)$ where D is the extent of degradation at the time t . In the present study, the deviation between the true extent of degradation and the Rayleigh-based estimate is addressed through the following measure θ , which quantifies the underestimation of the true first-order degradation rate

constant k_{Sample} by the Rayleigh-based estimate of the first-order degradation rate constant $k_{Rayleigh}$. The values of the rates themselves are not the subject of this paper.

$$\theta = \frac{\ln(1 - D_{Rayleigh})}{\ln(1 - D_{Sample})} = \frac{k_{Rayleigh}}{k_{Sample}} \quad (4-15)$$

A θ of 1 signifies that both rate constants are equal, i.e., no underestimation of D_{Sample} by $D_{Rayleigh}$; a θ of 0.8 indicates that the estimate $k_{Rayleigh}$ is 1.25 times smaller than the true k_{Sample} , whereas a θ of 0.1 means that $k_{Rayleigh}$ is 10 times smaller than the true k_{Sample} , i.e., $D_{Rayleigh}$ strongly underestimates D_{Sample} . θ is calculated only for significant $\delta^{13}\text{C}$ -TCE enrichment, i.e., the isotopic shift $\Delta^{13}\text{C}$ between $\delta^{13}\text{C}$ -TCE and $\delta^{13}\text{C}$ -TCE_{Source}, is beyond 1 ‰. A value below a threshold of 2 ‰ cannot be taken with certainty as an indication of degradation considering the analytical uncertainty of carbon CSIA and site heterogeneity (Hunkeler et al., 2008); however, in practice, enrichment beyond 1 ‰ is considered to be an indication of degradation.

Two additional concepts are defined for the sake of this study to estimate the true degradation effect at a larger scale than the scale of a sample. The total mass decrease of TCE versus the one of the tracer as occurred in the model is calculated at a certain distance downgradient for (1) the entire depth of the aquitard, $D_{Aquitard}$, and (2) the entire depth of the aquifer-aquitard-aquifer system, D_{System} . $D_{Aquitard}$ and D_{System} are therefore the ratios of TCE and the tracer's mass across a column of the model as in eq. 4-16:

$$D = 1 - \frac{\sum_i^N \left(1 + \frac{\rho_b}{\eta} \cdot f_{oc} \cdot K_{oc,TCE} \right) \cdot V_i \cdot \eta \cdot [TCE]_i}{\sum_i^N \left(1 + \frac{\rho_b}{\eta} \cdot f_{oc} \cdot K_{oc,TCE} \right) \cdot V_i \cdot \eta \cdot [Tracer]_i} \quad (4-16)$$

where N is the number of rows in the aquitard or in the aquifer column, respectively; $[TCE]_i$ and $[Tracer]_i$ the concentration for this column at the row i ($\text{mg} \cdot \text{L}^{-1}$); f_{oc} is the local fraction of organic carbon (only different between the aquifer and the aquitard); η is the porosity (dimensionless); $K_{oc,TCE}$ the solid-phase organic carbon-water partition coefficients of TCE (identical for the tracer) ($\text{L} \cdot \text{kg}^{-1}$); and ρ_b is the bulk density, V_i the the cells volume (m^3), the length and width of the model cells are always the same but the height of the cells varies accross depth. $D_{Aquifer}$ and $D_{Aquitard}$ are 0 % when there is no degradation and 100 % when degradation is maximal.

4.4 Results and discussion

4.4.1 Complete model including CEs degradation: loading phase

The base case scenario is employed to simulate CEs concentrations and isotope ratios following flow, diffusion, sorption, and degradation including associated carbon isotope effects. This section focusses on the loading phase, until the plume is removed. During the loading phase, the dissolving DNAPL forms a plume with high TCE concentration in the aquifer. The concentration gradient between the aquifer and the aquitard drives TCE diffusion into the initially pristine aquitard. In the aquitard, transport is governed by diffusion only; advective transport does not occur. At the end of the loading phase in year 10, daughter products show the highest concentration a few centimetres (2 cm to 15 cm) below the interface (Fig. 4-2a), resulting from their sequential production in the aquitard (close up of the aquitard available in the Appendix Fig. S4-4). The centres of the CEs masses are spatially separated, with ethene present the deepest, followed by VC, DCE, and TCE (Fig. 4-2a and 2b). CEs sequential reductive dechlorination, sorption, and diffusion create these patterns in concert. The more dechlorinated the compound, the later it is formed in the degradation sequence, the less it sorbs, and the faster it diffuses. For instance, ethene is the end product of reductive dechlorination, it sorbs least, and diffuses fastest compared to the other compounds. Whereas the peak concentration of TCE in the aquitard decreases downgradient, those of the daughter products remain remarkably similar (Fig. 4-2a, plain vs. dashed lines). Daughter products which back-diffused to upgradient parts of the aquifer are transported downgradient where they again diffuse into the aquitard. Consequently, daughter product concentration peaks remain high right below the aquifer-aquitard interface throughout the aquitard, also away from the source (dashed line Fig. 4-2a).

Simulations allow comparing the base case scenario DySy, which includes both the diffusion- and sorption induced isotope fractionation effects, to a model disregarding both those effects (DnSn), as well as two intermediary scenarios (DySn and DnSy, see description of these simulation codes in caption of Fig. 4-2). Details of additional simulations in the absence of degradation are presented in the Appendix Section S4.7. For all scenarios including TCE degradation, $\delta^{13}\text{C}$ -TCE enriches with depth in the aquitard with as much as +45 ‰ at 30 cm depth in year 10 (Fig. 4-2c). This enrichment is strongly larger than the negligible $\delta^{13}\text{C}$ -TCE enrichment predicted in the absence of reductive dechlorination (<0.5 ‰, Fig. S4-3c), resulting solely from the combined effects of sorption- and diffusion induced isotope fractionation. Each lesser chlorinated ethene presents a more depleted $\delta^{13}\text{C}$ than its precursor, which is the usual pattern for reductive dechlorination (Hunkeler and Aravena, 2000; Slater et al., 2000; van Breukelen et al., 2005). For the base

case scenario DySy, $\delta^{13}\text{C}$ of daughter products tend to curve with depth opposed to the straight enrichment of $\delta^{13}\text{C}$ -TCE. After initial enrichments compared to their starting values, $\delta^{13}\text{C}$ level off, and even show a declining trend deep in the aquitard (Fig. 4-2c). When DCE or VC eventually travels ahead of its precursor, the net $\delta^{13}\text{C}$ enrichment becomes smaller. Eventually, $\delta^{13}\text{C}$ decreases with depth below the $\delta^{13}\text{C}$ peaks for both the models including diffusion-induced isotope fractionation (Fig. 4-2c: DySy and DySn). The ethene $\delta^{13}\text{C}$ pattern is different as ethene does not degrade; $\delta^{13}\text{C}$ -ethene will not further enrich once it is away from its precursor VC. With the selected $\epsilon_{\text{Diffusion}}$, ethene shows stronger depletion in the base case scenario compared to the simulation omitting diffusion-induced isotope fractionation (Fig. 4-2c: $\sim -7\%$ for the base case model DySy vs. DnSy at 90 cm depth). Despite a f_{oc} of 0.3 %, $\epsilon_{\text{Sorption}}$ itself leads to a small enrichment for all CEs and is significant ($>2\%$) only in the deepest parts of the aquitard (Fig. 4-2c: DySy vs. DySn and DnSy vs. DnSn). In the aquifer, the upwards decline of $\delta^{13}\text{C}$ of DCE, VC, and ethene by a few ‰ (Fig. 4-2c) is caused by the faster diffusion of the light isotopes following the upward concentration gradients.

The CIMB increases just below the aquifer-aquitard interface where enriched TCE and DCE are dominant. The CIMB increase results from the faster downward diffusion of the depleted daughter products (Fig. 4-2c). Beneath, the CIMB strongly decreases with depth until being equal to $\delta^{13}\text{C}$ -Ethene once ethene is the dominant compound (depletion by about -25% at -0.9 m, Fig. 4-2c). The occurrence of depleted CIMB was described before in simulations of CEs transport and degradation through an aquifer in presence of sorption (van Breukelen et al., 2005). The different transport velocities of the CEs is the main reason for downwards CIMB decrease, further enhanced by diffusion-induced isotope fractionation (Fig. 4-2c: DnSy and DnSn). The most depleted CIMB predicted in this simulation (-55%) is close to the range of the lowest reported isotope signatures of PCE and TCE at a field site (-67.9% and -70% respectively (Nijenhuis et al., 2013)). As CEs isotope profiles in aquitards are employed for retracing CEs source history (Adamson et al., 2015), such low CIMB in a sorbing aquitard should not be confused for the prior presence of another strongly depleted TCE spill.

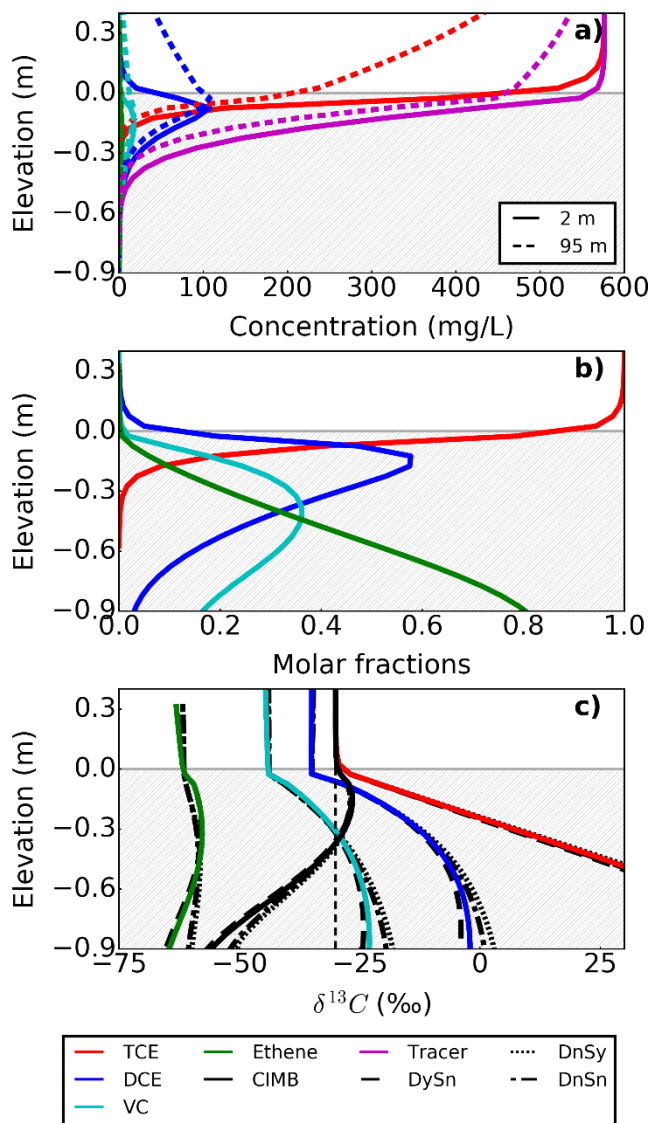


Fig. 4-2 : Depth profiles of concentrations (a), molar fractions (b), and carbon isotope ratios (c) of CE and ethene (TCE, red; DCE, blue; VC, cyan; ethene, green; CIMB, black) at the end of the loading phase (year 10), near the aquifer-aquitard interface, 2 m downgradient of the source (except indicated otherwise on (a)). (c) The base case simulation DySy is compared to simulations DySn, DnSy, and DnSn:

DySy is the base case scenario, with diffusion-induced (Dy) and sorption-induced (Sy) isotope fractionation; DySn includes diffusion-induced isotope fractionation (Dy) but omits sorption-induced isotope fractionation (Sn); DnSy includes sorption-induced isotope fractionation (Sy) but omits diffusion-induced isotope fractionation (Dn). DnSn does not include any isotope fractionation induced by physical processes.

The vertical dashed black line (c) represents $\delta^{13}C-TCE_{Source}$.

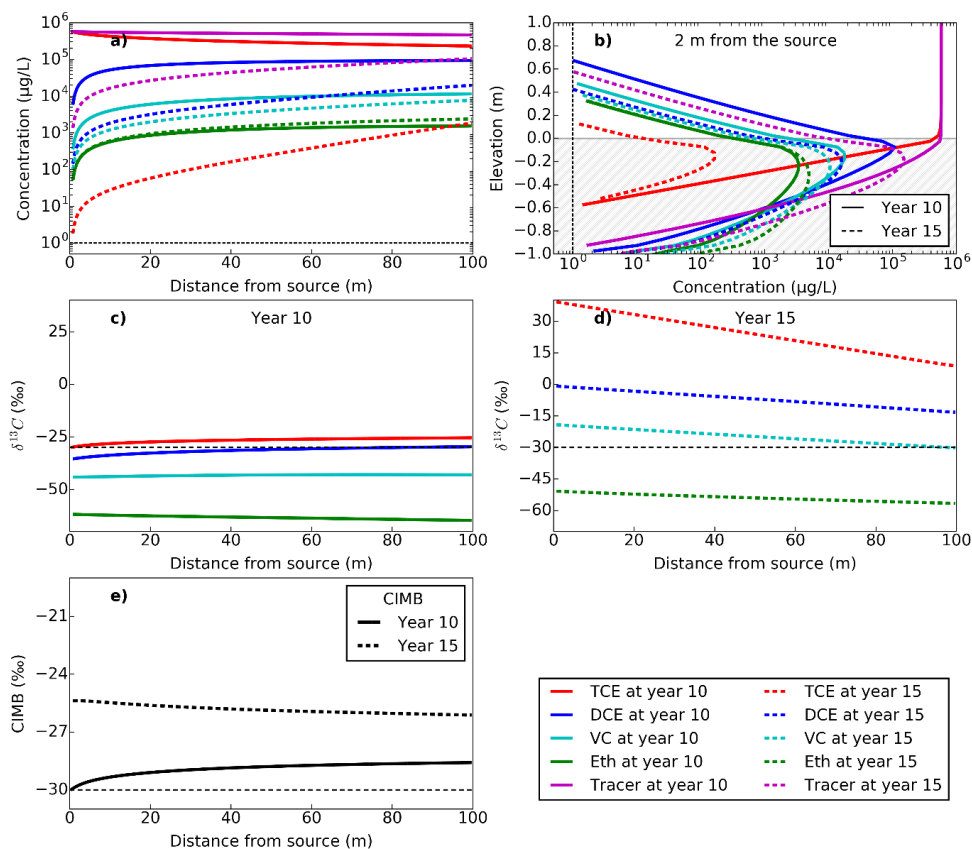


Fig. 4-3 : Concentration and carbon isotope ratio patterns of CEs and ethene right before (year 10) and 5 years after (year 15) source removal. The patterns are presented versus distance at the bottom of the aquifer in (a), (c), (d), and (e), and versus depth, 2 m downgradient from the source (b). Horizontal (a) and vertical (b) dashed black lines represent the minimum quantification limits for CEs isotopes ($1 \mu\text{g}\cdot\text{L}^{-1}$). Horizontal black lines (c, d, e) represent the $\delta^{13}\text{C}\text{-TCE}_{\text{source}}$.

Concentration and $\delta^{13}\text{C}$ patterns of CEs across the aquifer at the end of the loading phase (year 10) are presented in Fig. 4-3. Daughter products accumulate in the aquifer where their concentrations increase with distance from the source (Fig. 4-3a). At the end of the loading phase, daughter product concentrations at the bottom of the aquifer are already several orders of magnitude above the MCLs ($\text{MCL} = 70 \mu\text{g}\cdot\text{L}^{-1}$ for cis-DCE, $2 \mu\text{g}\cdot\text{L}^{-1}$ for VC) (Fig. 4-3a). At year 10, although no degradation occurs in the aquifer, $\delta^{13}\text{C}\text{-TCE}$ downgradient enrichment just above the aquifer-aquitard interface is strongly larger than in absence of degradation (isotope enrichment $\Delta^{13}\text{C} \sim 5 \text{‰}$ vs. $\sim 0.05 \text{‰}$; Fig. 4-3c and S3g, respectively). TCE degradation in the aquitard enhances the concentration gradient at the aquifer/aquitard interface. The resulting faster diffusion to the aquitard leads to a stronger isotope enrichment in the aquifer. The same process leads to the increase of $\delta^{13}\text{C}\text{-DCE}$ and $\delta^{13}\text{C}\text{-VC}$ with distance from the source (up to $\sim 5 \text{‰}$ for DCE, Fig. 4-3c). However, $\delta^{13}\text{C}\text{-Ethene}$

decreases with distance as ethene accumulates and as degradation is overall less advanced downgradient from the source (Fig. 4-3c). Until the release phase, daughter product concentrations are much lower than TCE concentrations in the aquifer and $\delta^{13}\text{C}$ -TCE is enriched. Consequently, the CIMB is dictated by $\delta^{13}\text{C}$ -TCE at the bottom of the aquifer at the end of the loading phase, and therefore enriches with distance (Fig. 4-3e).

4.4.2 Complete model including CEs degradation: release phase

After source removal, the main plume is flushed away from the 100 m long stretch of aquifer by upgradient uncontaminated groundwater within about 2.7 years (the groundwater flow velocity is of $44 \text{ m}\cdot\text{y}^{-1}$). The TCE concentration gradient is reversed and TCE diffuses now back from the aquitard to the aquifer. Prior to source removal, the high TCE concentration levels forced the $\delta^{13}\text{C}$ of CEs to low values. Five years after source removal, at year 15, $\delta^{13}\text{C}$ values of all compounds are considerably higher than during the loading phase and are above their minimum detection limit of $1 \mu\text{g}/\text{L}$. Interestingly, $\delta^{13}\text{C}$ now strongly decreases downgradient (Fig. 4-3d). The downgradient decline is as much as -10 ‰ for DCE and VC, and near -30 ‰ for TCE (Fig. 4-3d). The ongoing uniform degradation in the aquitard explains $\delta^{13}\text{C}$ -TCE enrichment over time in the entire system, while the overall downgradient $\delta^{13}\text{C}$ -TCE depletion relates to the delay in flushing of the downgradient parts of the aquifer (in Appendix; and discussed further in Section 4.3.3).

The temporal evolution of the CEs and ethene are evaluated near the aquitard, 95 m downgradient of the source. The TCE concentration drops below the MCL within 10 years after the source is removed (Fig. 4-4). Concentrations of daughter products near the aquitard also decline, but slower, and the accumulating product of CEs sequential degradation, ethene, resides in the aquifer nearly as long as the non-degrading tracer (Fig. 4-4a). VC concentration away from the source is still above its MCL at year 40, i.e., 30 years after source removal, although TCE declined below its MCL long before, at year 18 (Fig. 4-4a). Simulations of VC or DCE stall, presented in the Appendix, show that their concentrations would also remain nearly as high as that of the tracer in the aquifer (Fig. S4-7 and S4-8). Despite degradation occurs in the aquitard and not in the aquifer, the potentially high concentrations and the longevity of the degradation products in the aquifer should be considered in the study of back-diffusion.

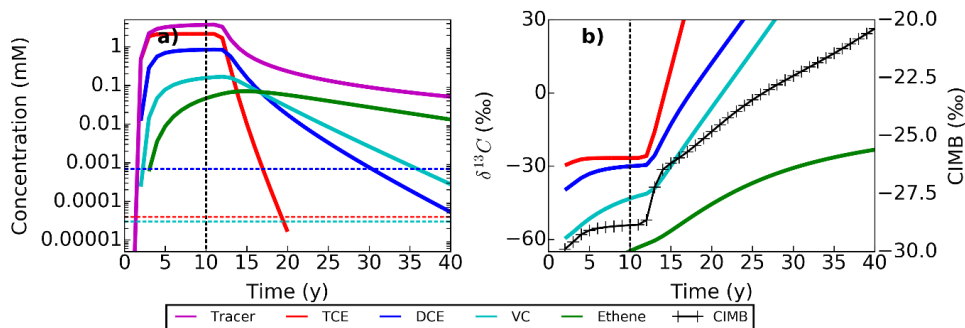


Fig. 4-4 : CEs, ethene, and tracer concentrations (a) and $\delta^{13}\text{C}$ (b), against time, at the bottom of the aquifer 95 m downgradient from the source. The vertical black line signals year 10 at which the source is removed. The horizontal lines correspond to the minimum concentration limits (MCL) for TCE (red); DCE (blue); and VC (cyan). The lines terminate when concentrations fall below detection limits.

Shortly after the clean-up, CIMB significantly increases by $\sim 3\%$ and remains high until the end of the simulation (Fig. 4-4b), also for different well screen lengths and positions (Fig. S4-5 in the Appendix). The CIMB increase points to the loss of depleted compounds from the aquifer during the release phase. The more dechlorinated and more depleted compounds have been transported deeper into the aquitard (see Section 4.3.1) and do not diffuse back to the aquifer as fast as the more enriched and chlorinated compounds. The difference in CIMB, ΔCIMB , was evaluated for several reaction chains, with DCE or VC as end product instead of ethene. ΔCIMB is smaller, but still $> 1.5\%$ after source removal when VC is the end product (Fig. S4-7). ΔCIMB decreases in a few years to near 0% when DCE is the end product (Fig. S4-8). At field sites, CIMB is expected to increase only in presence of degradation processes other than reductive dechlorination. For instance, DCE and VC are more readily oxidizable than TCE and could degrade in the aquifer provided the right conditions are met (Coleman et al., 2002a, 2002b). Therefore, such significant CIMB increase could be confused for alternative degradation pathways for the CEs.

4.4.3 Distinct CSIA patterns in the aquifer in presence of aquitard degradation

With the goal to assess spatial CSIA patterns characteristic of either aquitard RD or aquifer RD, the base case simulation on aquitard RD was compared with another simulation where RD only occurred in the aquifer (Fig. 4-5). Aquifer RD causes monotonously increasing CSIA patterns of all compounds in downgradient direction during both the loading and release phase (Fig. 4-5a,b) similarly as known for aquifer RD without aquitard interactions (van Breukelen et al., 2005). Strikingly, downgradient CSIA patterns and their magnitude remain almost unaffected after source removal and remain constant in time long after source removal (results not shown). During the loading phase, the CIMB is not increasing

downgradient, but it slightly increases by about 0.5 ‰ during the release phase. This minor CIMB increase after source removal can be explained by the lower back diffusion rates of the more dechlorinated and more depleted daughter products which have penetrated deeper into the aquitard as they diffuse faster and sorb less.

These patterns are in strong contrast with those of uniform aquitard RD as discussed shortly before, where carbon isotope ratios only limitedly increase downgradient during the loading phase, whereas most strikingly, after source removal huge isotope enrichment is simulated of all compounds as the aquitard serves as a reservoir of degraded CEs. As in both cases, concentration drop during the release phase, isotope ratios is more applicable to discriminate between both hypotheses. Furthermore, the CSIA patterns decreasing downgradient (Fig. 4-5b), and downgradient CIMB increase is substantial especially during the release phase with about 4‰ (Fig. 4-5c,d). A simulation assuming linear decreasing degradation rate constants dropping to zero at the base of the aquitard, showed similar CSIA patterns as the base case simulation (Fig. S4-6). Note that in the case bioactivity is limited to the upper centimetres of aquitards further isotope enrichment over time after the initial jump will not occur, while isotope ratios will also not decrease downgradient (Wanner et al., 2018b) because the residence time of back-diffusing TCE in the bioactive zone is invariant. Interestingly, CSIA patterns may thus inform on the depth of bioactive zones in aquitards, or in general the depth of reactivity as aquitards with potentially elevated contents of iron-sulphur minerals could also host chemical reductive dechlorination as CE attenuation process.

In the case RD occurs within the entire system (both in the aquitard and the aquifer(s)), the CSIA patterns become a mixture of the unique features of aquitard and aquifer RD. During the loading phase, downgradient CSIA patterns increase for the higher chlorinated CEs alike aquifer RD but are more stable for lower chlorinated CEs and ethene similar to aquitard RD. Whereas during the release phase aquifer RD shows increasing CSIA patterns, and aquitard RD shows strongly elevated but decreasing CSIA patterns, RD occurring within the entire system shows elevated but relatively constant CSIA patterns downgradient at least under the simulated conditions of spatially homogenous first-order rate constants. Even under those conditions aquitard RD is still noticeable as CSIA patterns of daughter products are much more enriched than in the absence of aquitard RD, notably near the source. The CIMB increase is in between those of purely aquitard and aquifer RD except near the source, where the increase is large which differs strongly from the aquifer RD pattern. Concluding, aquitard RD can still be clearly detected by aquifer CSIA in case also aquifer RD occurs because of (i) the significant CIMB increase, and especially (ii) the strong jump of CSIA ratios after source removal also near the source, and (iii) the absence of clear increasing and possibly decreasing CSIA trends downgradient.

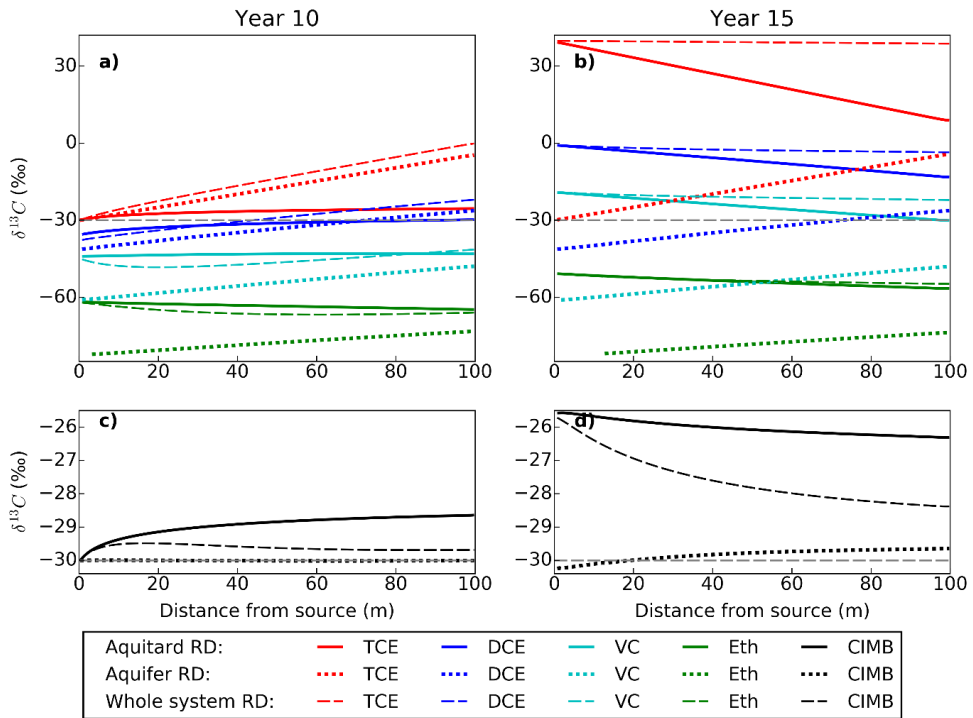


Fig. 4-5 : Carbon isotope ratio patterns of CE and ethene (top panels), as well as the CIMB (bottom panels), right before (left panels) and 5 years after source removal (right panels). The patterns are presented versus distance at the bottom of the aquifer. Horizontal dashed grey lines represent the $\delta^{13}C$ -TCE_{Source}.

4.5 Performance of the Rayleigh equation in assessing the extent of degradation

At contaminated sites with a predominant role of aquitard RD, CSIA of samples from conventional wells situated in the aquifer, but close to the aquifer-aquitard interface could detect and potentially be used to quantify the extent of degradation. The base case scenario shows that aquitard RD leaves an imprint on $\delta^{13}C$ -TCE in the aquifer. Additionally, daughter products are detected in the aquifer throughout the simulation. This section evaluates whether a CSIA calculation tool often used for biodegradation assessment at field sites, the Rayleigh equation, provides trustworthy information on the occurrence and degree of TCE degradation in the aquitard when based on CSIA samples from the aquifer.

4.5.1 Performance of the Rayleigh equation for local degradation assessment

The direct application of the Rayleigh equation to $\delta^{13}\text{C}$ -TCE data obtained from a polluted site is in theory sufficient to obtain a conservative estimate of TCE degradation as occurred in the samples, D_{Rayleigh} . The underestimation by the Rayleigh equation of the true extent of degradation for the simulated conditions can be assessed by comparing D_{Rayleigh} to the true extent of degradation D_{Sample} as both are obtained from the synthetic dataset (Lutz et al., 2013). Prior modelling studies pointed out that D_{Rayleigh} systematically underestimates the true extent of degradation under various conditions (Abe and Hunkeler, 2006; Höyng et al., 2015; Lutz et al., 2017; Lutz and van Breukelen, 2014a; van Breukelen and Prommer, 2008; van Breukelen and Rolle, 2012). The underestimation was then the result of the attenuation of degradation-induced $\delta^{13}\text{C}$ enrichment through mixing and dispersion of pollution plumes in aquifers. At high extents of degradation, for instance above 90 %, the ratio of the extents of degradation D_{Rayleigh} and D_{Sample} would be a poor indicator of the underestimation. The ratio of the Rayleigh-equation estimate to the true first-order degradation rate constant, θ , better qualifies the underestimation also at high extent of degradation (see Section 4.2.7).

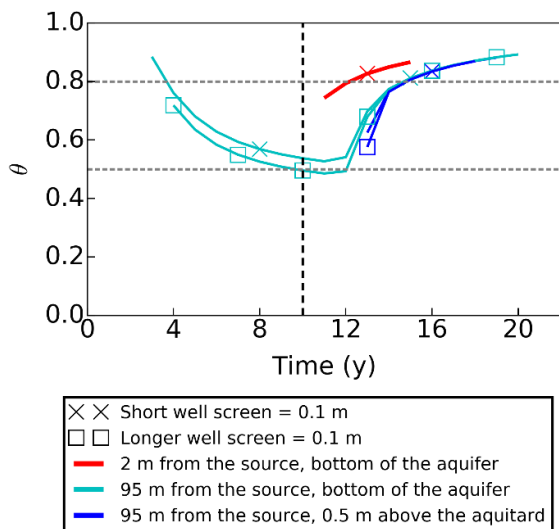


Fig. 4-6 : Ratio of the Rayleigh-equation estimate to the true first-order degradation rate constant (θ) as function of time and as calculated at 3 different positions in the aquifer (near the source and near the aquitard, red; 95 m downgradient the source near the aquitard, cyan; or 95 m downgradient the source 0.5 m above the aquitard; blue) for 2 different wells screen lengths (crosses: short well screens; squares: long well screens). θ cannot be computed at any moment in time as explained in the text.

Fig. 4-6 illustrates the variation of θ in the upper aquifer at various elevations and distances from the source, and screen lengths. Sampling from long well screens or near the source lowers the chance to detect significantly enriched $\delta^{13}\text{C}$ -TCE, either because of the high TCE concentration during the loading phase, or due to strong dilution during the release phase. Because θ is only calculated for $\Delta^{13}\text{C} > 1\%$, the longest time series of θ can be computed for short screens, away from the source, and near the aquitard (Fig. 4-6). When calculated, θ varies between 0.5 and 0.9, *i.e.*, the Rayleigh equation underestimates the real first-order degradation rate constant with a factor 2 to 1.1, respectively.

Away from the source, θ is initially low and progressively decreases from ~ 0.65 to ~ 0.5 during the loading phase (Fig. 4-6a, cyan lines). In this initial stage, the TCE concentration and its isotope ratio have plateaued, while the tracer concentration keeps rising (Fig. 4-4a,b), indicating that the true extent of degradation, D_{Samples} , increases. Consequently, the gap increases between the CSIA-based degradation estimate and the true extent of degradation, causing θ to drop.

Within 10 years after source removal, θ increases to high values, meaning that the Rayleigh-equation only slightly underestimates degradation as occurred in samples and a close estimate is obtained. TCE back-diffusing from the aquitard where it has been partially degraded is now the main source of TCE in the aquifer, and the $\delta^{13}\text{C}$ -TCE enrichment corresponds better to the actual degradation at the level of the aquifer sample.

4.5.2 Can mass destruction in the aquitard be estimated with CSIA data?

It remains the question whether locally obtained D_{Rayleigh} values from the aquifer can be used in assessing the overall TCE mass decrease as occurred in the aquitard which would be highly valuable for estimating remediation time frames. For this analysis, we employ two additional concepts: the total mass decrease of TCE versus the one of the tracer as occurred in the model at a certain distance downgradient of the source for (1) the entire depth of the aquitard, D_{Aquitard} , and (2) the entire depth of the aquifer-aquitard-aquifer system, D_{System} . These mass decreases are calculated from the ratio of TCE mass versus the mass of the non-degradative tracer with similar properties as TCE following eq. 4-16. D_{System} and D_{Aquitard} are compared at both 2 m and 95 m from the source to D_{Rayleigh} and to the true extent of degradation D_{Samples} , both obtained at the bottom of the aquifer (Fig. 4-7).

During the loading phase and near the source, both the lack of detectable $\delta^{13}\text{C}$ -TCE enrichment and the high TCE concentration levels prevent D_{Rayleigh} and D_{Sample} to depart from 0 % (Fig. 4-7, black and cyan lines, respectively). However, the large D_{System} and D_{Aquitard} values of $\sim 15\%$ and $\sim 70\%$, respectively (Fig. 4-7a red and blue dashed lines, respectively) point to TCE mass decrease in both the aquitard and the aquifer.

During the loading phase and away from the source (95 m), $D_{Rayleigh}$ increases soon after the arrival of the plume but underestimates D_{Sample} considerably at year 10 (Fig. 4-7b). $D_{Rayleigh}$ even more strongly underestimates $D_{Aquitard}$. At year 10, $D_{Rayleigh}$ is in the range of D_{System} but those similar values are coincidental as D_{System} depends among others on the thickness of the plume. Although $\delta^{13}\text{C}$ -TCE enrichment is detectable in the aquifer already in the loading phase, $D_{Rayleigh}$ values may give pessimistic views on the actual high degree of mass destruction in the aquitard, $D_{Aquitard}$.

Once the source is removed after 10 years, $D_{Aquitard}$ quickly increases both near and away from the source as a result of the continuous TCE degradation in the aquitard without further admixing of non-degraded TCE from the source. The poorly degraded TCE mass in the aquifer is flushed by clean water, therefore the mass remaining in the system is mostly contained in the reactive aquitard and D_{System} converges towards $D_{Aquitard}$. Both D_{System} and $D_{Aquitard}$ are large due to the ongoing degradation in the aquitard. Both D_{Sample} and $D_{Rayleigh}$ in the aquifer are now influenced only by the back-diffusing TCE and rapidly increase similarly to $D_{Aquitard}$. Once the source is removed, degradation assessment through CSIA is improved due to the enriched isotope signature of the back-diffusing TCE, which interestingly provides an insight to the state of degradation in the aquitard. Quickly after source removal, TCE mass effectively decreased in the aquifer system and $D_{Rayleigh}$ provides a conservative estimate of the state of degradation.

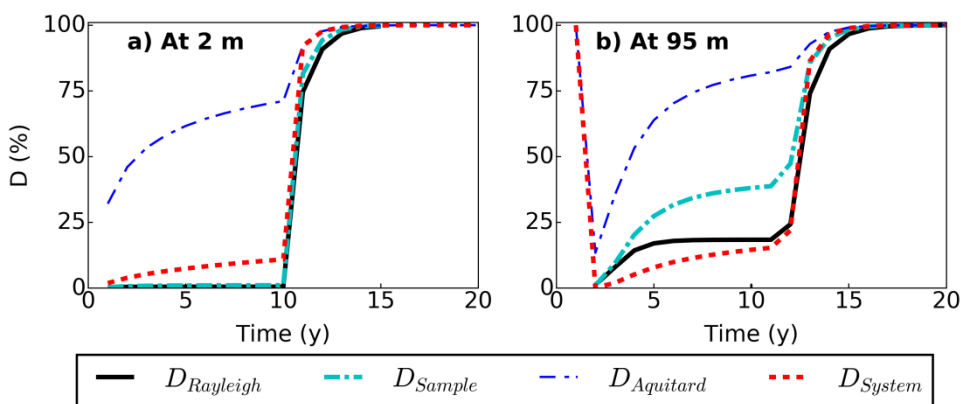


Fig. 4-7 : CSIA-based estimate of degradation ($D_{Rayleigh}$, black solid line), true extent of degradation (D_{Sample} , cyan dashed line), determined for short well screens at the bottom of the aquifer at two distances from the source (2 m, (a), and 95 m, (b)); true extents of TCE mass reduction at the respective distances across depth of the aquifer-aquitard-aquifer system (D_{System} , red dashed line), and across depth of the aquitard ($D_{Aquitard}$, blue dashed line).

4.6 Sensitivity analysis of degradation assessment

The results of a sensitivity analysis of key model parameters on CIMB and θ values are shown and discussed in detail in the Appendix. The main outcomes are reported here. With respect to CIMB, the most influential parameters appear to be the aquitard f_{oc} (Fig. S4-10c) and aquitard thickness (Fig. S4-10e). CIMB is sensitive to the spatial separation of the depleted daughter products from their more enriched precursors as discussed before. Especially during the release phase, a higher aquitard f_{oc} therefore yields a larger CIMB enrichment. Noteworthy, also without sorption, the CIMB is predicted to enrich in later stages of the release phase. Probably this is caused by the loss of depleted daughter products which have diffused through the aquitard and reached the lower aquifer. With respect to aquitard thickness, a thinner aquitard results probably in an increased mass loss of depleted daughter products to the underlying aquifer while the more enriched precursors sorb stronger and are still present in thinner aquitards during the back-diffusion phase causing a strong CIMB enrichment. Preferential mass loss of depleted daughter products to the underlying aquifer is thus another phenomenon contributing to high CIMB enrichments that could be observed in overlying aquifers. The CIMB of samples taken near aquitards is in most cases not a reliable indicator of the occurrence of alternative degradation pathways besides reductive dechlorination like oxidation. The sensitivity analysis further shows that Rayleigh-based estimates of degradation are always conservative. Moreover, we show that both $\delta^{13}\text{C}$ -TCE enrichment prior to source remediation and a sudden change in $\delta^{13}\text{C}$ values once the source is remediated are to be expected under many different field conditions. The Rayleigh equation systematically underestimates the extent of TCE degradation in aquifer samples especially during the loading phase and for conditions leading to long remediation time frames (low groundwater flow velocity, strong sorption in the aquitard, thicker aquitards).

4.7 Model limitations

The simulations required simplifications which influence the results. The key assumptions concern mostly reaction, *i.e.*, the simulation of linear sorption, and of first-order and uniform degradation kinetics in the aquitard. Diffusion-related assumptions are also discussed. Their implications on the main results are described in this section.

As presented in the method section, the model simulates linear sorption of chlorinated ethenes in aquitards. Sorption is site-specific, and while CEs sorption was near linear in natural clayey tills (Lu et al., 2011), TCE sorption was best represented with Freundlich isotherms in several clay-rich aquitards in a prior study (Allen-King et al., 1996).

Freundlich or Langmuir sorption behaviour implies that high CE concentrations compared to the sorption site concentration would overwhelm the sorption capacity of the aquitard. The $\delta^{13}\text{C}$ patterns of the CEs would therefore tend towards the patterns observed in the absence of sorption as in Fig. 4-9c and 10c. A non-linear sorption behaviour would mainly limit the CIMB enrichment induced by the different sorption potentials of the CEs.

First-order kinetics were assumed for simplifying the transport model. The high source concentration calls for Monod kinetics, in which case degradation at the high CE concentration levels would comparatively be slower than in our simulation. In our simulations, slower degradation rates lead to better Rayleigh-based degradation assessment and to lesser increase of the CIMB during the release phase; therefore, our simulations provide a higher range of the overall impact of the aquitard on the CSIA data. Our assumption of biodegradation occurring throughout the aquitard (either uniform, or non-uniform as linear decreasing rate constants) yielded different CSIA patterns in the aquifer than under the assumption of a thin bioactive zone at the top of the aquitard except for the jump in isotope ratios after source release. Note that resulting CSIA patterns could be similar in case of abiotic RD. CEs can degrade abiotically in contact with ferrous minerals in aquitards made of clayey soils or rock matrix (Schaefer, 2016; Schaefer et al., 2017). While several parameters such as the magnetite susceptibility or the contact surface might influence degradation rates (Schaefer, 2016; Schaefer et al., 2017), those parameters are not necessarily related to the aquitard depth and degradation rate constants might be more uniform across such an aquitard. Clearly more research is needed to the depth distribution of bioactivity and chemical reactivity in aquitards both for interpretation of CSIA data and for assessing remediation time frames.

The aquifer could also be sufficiently oxic to oxidize the daughter products diffusing out of the aquitard. The detection of enrichment of $\delta^{13}\text{C}$ -TCE in the absence of daughter compounds could be confused for TCE oxidation in the aquifer. Provided chlorine isotope enrichment factors for TCE cometabolism are available, the study of combined carbon and chlorine CSIA data could prevent this uncertainty (Abe et al., 2009a; Wiegert et al., 2012). For instance, as the slopes of DCE carbon and chlorine CSIA data differ for biotic and abiotic reductive degradation, combined carbon and chlorine CSIA was employed to determine DCE degradation pathways at a field site (Audí-Miró et al., 2015). The study of carbon and chlorine isotope ratios is therefore promising for pathway distinction in this case.

Finally, the $\varepsilon_{\text{Diffusion}}$ values of DCE, VC, and ethene were estimated based on the literature. The variations of $\varepsilon_{\text{Diffusion}}$ had little impact on both the CIMB and θ . Provided they are in the selected range, an improved estimate of $\varepsilon_{\text{Diffusion}}$ values will not change the implications of the simulations.. Additionally, a lower τ_{app} value as suggested by Wanner and co-workers

for the aquitard would reduce the distance travelled in the aquitard by the CEs within the simulation time and reduce the diffusion-induced isotope effect.

4.8 Summary and implications

Scenario simulations performed with a reactive transport model illustrate the potential of CSIA data to detect and quantify naturally occurring reductive dechlorination of chlorinated ethenes (CEs) in an aquifer-aquitard-aquifer system. The model input parameters were based on an extensive literature review. During presence of a TCE DNAPL source, TCE sequential reductive dechlorination to ethene in the underlying reactive aquitard enhances TCE diffusion from the aquifer to the aquitard. A resulting $\delta^{13}\text{C}$ -TCE enrichment of a few permil ($\Delta^{13}\text{C} > 2 \text{‰}$) is detectable in the aquifer near the aquitard, while in the absence of degradation, $\delta^{13}\text{C}$ -TCE enrichment induced by TCE diffusion to the aquitard is negligible. This signifies that before source removal, large $\delta^{13}\text{C}$ -TCE enrichment is unlikely to be attributable to degradation only in the aquitard, but would correspond to degradation at the aquifer level.

After source removal, the diffusion of all CEs out of the aquitard is accompanied by a quick and steady increase of the $\delta^{13}\text{C}$ of all CEs and ethene with time, and a decreasing $\delta^{13}\text{C}$ of all CEs with distance from the source. These characteristic CSIA patterns during the loading and releases phases contrast strongly to those associated with reductive dechlorination occurring in the aquifer only. These characteristic aquitard degradation patterns remain visible when degradation co-occurs in the aquifer and could serve as a line of evidence for degradation in the aquitard. The sudden jump in isotope ratios in the aquifer after source removal was recognizable in most of the simulations during the sensitivity analysis, suggesting that practitioners could use this line of evidence at many sites for effective DNAPL source removal (Wanner et al., 2018b).

Our simulated CSIA patterns differ from those found in the modelling study of Wanner et al. (2018b) where it was assumed that major TCE degradation only occurred in centimetres to decimetres thick bioactive zones at the top of aquitards. Under those conditions $\delta^{13}\text{C}$ -TCE did not further increase over time after the initial jump that occurred after source removal and $\delta^{13}\text{C}$ -TCE also slightly increased instead of decreased downgradient. These aquifer CSIA patterns are characteristic for aquitards where bioactivity drops to zero already at shallow depth. In a more recent study it was shown that bioactivity can spread deeper into an aquitard and rate constants decrease near linearly below a certain depth (Wanner et al., 2018b). We demonstrate that also in the case of non-uniform degradation similar CSIA patterns are expected as in the case of uniform degradation provided that the aquitard remains sufficiently bioactive (or reactive in the case of abiotic degradation) until CEs spreading depths. CSIA patterns during the release phase are thus also informative over aquitard reactivity with depth. Note that our predicted characteristic spatiotemporal

CSIA patterns assuming relatively steady reactivity with depth could also be representative for abiotic chemical reductive dechlorination in aquitards where chemical reactivity as content of reactive minerals is likely to be relatively uniformly distributed.

The carbon isotope mass balance (CIMB) is influenced by the spatial separation of the CEs and ethene during transport. During the release phase, the CIMB increases in the upper aquifer as a result of the relatively limited back-diffusion of depleted daughter products. While this is the case also when degradation occurs only in the aquifer, the CIMB increase is stronger when degradation occurs only in the aquitard. The CIMB increase also occurs but to a lesser extent when VC is the end product of degradation, as such it only occurs for a short period when DCE stalls. The CIMB increase is strongest for thinner sorbing aquitards. Unfortunately for degradation monitoring, such increase could be confused with the degradation of the CEs through other pathways. Overestimating the daughter products' degradation is problematic as daughter products in the aquitard can act as a new contaminant source.

During the loading phase, application of the Rayleigh equation to $\delta^{13}\text{C}$ -TCE data sampled in the aquifer strongly underestimates TCE degradation in the aquitard, provided the aquifer is unreactive. Within only a few years after source removal the precision of Rayleigh-based degradation quantification is improved to reasonable levels of underestimation (< factor 1.25), and seems to well represent the extent of mass destruction in the aquitard at this stage. Unfortunately, conditions increasing remediation timeframes such as a higher f_{oc} in the aquitard, thicker aquitards, or a slower groundwater velocity increase degradation underestimation, especially before source remediation. Sorption- and diffusion-induced isotope fractionations have limited impact on TCE degradation assessment.

Scenario modelling provides insights into the potential of aquifer CSIA data for monitoring the reactivity of an aquitard. The study of a simplified conceptual site could be extended to more complex aquifer geometry, for instance multiple reactive clay beds of different thickness and lengths. Further work, including experimental work, should address the potential of chlorine and hydrogen isotope fractionation in identifying aquitard degradation and also to distinct between biological and abiotic degradation that might co-occur in aquitards (Wanner et al., 2018a). Further experimental research to both biological and chemical aquitard reactivity with depth is highly needed as this largely impacts resulting CSIA patterns in the release phase.

Supporting information to chapter 4

S4.1 Compilations from previous studies

Table S4-1 : Compilation of input parameters for the low-permeability (low-K) and high-permeability (high-K) layers in previous modelling studies of back-diffusion of CEs from aquitards. The case of MTBE degradation to TBA in a reactive aquitard (Rasa et al., 2011) is also presented.

Source compound	Porosity		Hydraulic conductivity (m·d ⁻¹)		Retardation factor source compound		Reference
	High-K	Low-K	High-K	Low-K	High-K	Low-K	
TCE	0.25	0.37	6.6	0.26	1	<1.2	(Matthieu et al., 2014)
MTBE/TBA	0.34	0.4	10.4	5·10 ⁻²	1	1	(Rasa et al., 2011)
PCE	0.36	0.55	8.64	0.15	1	1 3 15	(Sale et al., 2008)
TCE	0.35	0.4	2.16 to 4.32	1·10 ⁻³	1	3.5	(Carey et al., 2015)
TCE	0.35	0.4	n.a.	« negligible »	1	3.5	(Parker et al., 2008)
Tracer	0.45	0.6	17.28	9·10 ⁻⁶	1	1	(Chapman et al., 2012)
TCE	0.33	0.4	n.a.	9·10 ⁻⁵	n.a.	6 15	(Wanner et al., 2016)
TCE	0.35	0.35	10	3·10 ⁻³	1	3.5	This study, base case scenario

Table S4-2 : Compilation of input parameters in previous modelling studies of back-diffusion of CEs in an aquitard. The case of MTBE degradation to TBA in a reactive aquitard (Rasa et al., 2011) is also presented.

Source compound	Source duration (y)	Groundwater velocity (m·d ⁻¹)	Low-K type	D_w (m ² ·d ⁻¹)	First order degradation rate constant (y ⁻¹)	f_{oc} (-)	Reference
TCE	57	pump	Clay	$7.5 \cdot 10^{-5}$	No degradation	n.a.	(Matthieu et al., 2014)
MTBE	13	0.0026	Silt	$6.7 \cdot 10^{-5}$	16.79	« Low »	(Rasa et al., 2011)
PCE	2.7	0.19-0.36	Silt	-	0.023-0.23	1%	(Sale et al., 2008)
TCE	0.25-50	0.04-0.36	Clay	$7 \cdot 10^{-5}$	0-0.7	0.49%	(Carey et al., 2015)
TCE	35	0.12-0.06	Clay	n.a.	No degradation	0.57 % ^(a)	(Parker et al., 2008)
Tracer	0.06	0.17-0.29	Clay	$2 \cdot 10^{-9}$	No degradation	n.a.	(Chapman et al., 2012)
TCE	n.a.	0.12	Clay	$8.7 \cdot 10^{-5}$	Not first order	0.66 % ^(b)	(Wanner et al., 2016)
DCE				$9.3 \cdot 10^{-5}$			(Wanner et al., 2016)
TCE	10	0.12	Clay	$5 \cdot 10^{-5}$	1	0.3 %	This study, base case scenario

^(a)Geometric mean

^(b)Averaged

Table S4-3 : Compilation of bulk carbon isotope enrichment factors ($\epsilon_{Degradation}$) during the biotic reductive dechlorination of TCE to DCE, DCE to VC, and VC to ethene.

Microorganism	TCE→DCE	DCE→VC	VC→ethene	Reference
<i>Dehalococoides</i>	-16.4 ‰	-26.8 ‰	-26.7 ‰	(Kuder et al., 2013)
ANAS	-16 ‰	-29.7 ‰	-22.7 ‰	(Fletcher et al., 2011)
BDI	-15.3 ‰	-25.3 ‰	-19.9 ‰	(Fletcher et al., 2011)
KB-1, low	-2.5 ‰	-14.1 ‰	-21.5 ‰	(Fletcher et al., 2011)
KB-1, high	-13.8 ‰	-20.4 ‰	-26.6 ‰	(Fletcher et al., 2011)
KB-1, averaged	-4.6 ‰	-15.1 ‰	-24.1 ‰	(Bloom et al., 2000)
KB-1	-13.8 ‰	-20.4 ‰	-22.4 ‰	(Slater et al., 2001)
Adopted in the base case	-12 ‰	-22 ‰	-23 ‰	Adopted in this study
Adopted as lower end	-3 ‰	-14 ‰	-20 ‰	Adopted in this study

S4.2 Input parameters values

Table S4-4 : Model settings for the base case scenario.

Description				
Length model horizontal (m)	100			
Height model vertical (m)	10			
Discretization x×z (m)	1×0.05 0.1 0.25			
Number of columns×rows	100×93			
Groundwater velocity (m/d)	0.12			
Bulk density, ρ_b (kg/L)	1.855			
Porosity sand, n (-)	0.35			
Longitudinal dispersivity coefficient, α_x (m)	1			
Vertical transverse dispersivity coefficient (m)	0.0015			
	Lower aquifer	Aquitard	Upper aquifer	
Thickness (m)	1	1	8	
Hydraulic conductivity (m/d)	10	0.01	10	
Longitudinal dispersivity coefficient, α_x (m)	1	1	1	
Fraction of organic carbon, f_{oc} (-)	0	0.3 %	0	
	TCE	DCE	VC	Ethene
First order degradation rate constant, k (y^{-1})	1	0.2	0.2	n.a.
Aqueous diffusion coefficient, D_w ($m^2 \cdot s^{-1}$)	$5.9 \cdot 10^{-10}$	$6.9 \cdot 10^{-10}$	$9.7 \cdot 10^{-10}$	$1.3 \cdot 10^{-9}$
Solid phase organic carbon-water partitioning coefficient, K_{oc} ($L \cdot kg^{-1}$)	142	75	39	27
Degradation-induced carbon isotope enrichment factor, $\epsilon_{Degradation}$	-12 ‰	-21 ‰	-23 ‰	n.a.
Diffusion-induced carbon isotope enrichment factor, $\epsilon_{Diffusion}$	-0.2 ‰	-0.9 ‰	-1.4 ‰	-3.1 ‰
Sorption-induced carbon isotope enrichment factor, $\epsilon_{Sorption}$	-0.5 ‰	-0.5 ‰	-0.5 ‰	-0.5 ‰

Table S4-5 : Diffusion coefficient, K_{oc} , molar mass and abundance at 0 ‰ for each compound and for each isotopologue species.

	D_w at 10 ⁰ C ($\cdot 10^{-10}$ m ² /s)	K_{oc}	Molar mass (g/mol)	Abundance at 0 ‰
<i>TCE</i>	5.8696 ^(a)	142.56 ^(c)	131.39	1
^{LL} <i>TCE</i>	5.8695 ^(b)	142.56 ^(d)	131.37	0.977899
^{LH} <i>TCE</i>	5.8682 ^(b)	142.49 ^(e)	132.37	0.021977
^{HH} <i>TCE</i>	5.8669 ^(b)	142.42 ^(f)	133.37	0.000123
<i>DCE</i>	6.8958 ^(a)	74.81 ^(c)	96.94	1
^{LL} <i>DCE</i>	6.8959 ^(b)	74.81 ^(d)	96.92	0.977899
^{sLH} <i>DCE</i>	6.8937 ^(b)	74.78 ^(e)	97.92	0.021977
^{HH} <i>DCE</i>	6.8918 ^(b)	74.74 ^(f)	98.92	0.000123
<i>VC</i>	8.7022 ^(a)	39.26 ^(c)	62.50	1
^{LL} <i>VC</i>	8.7021 ^(b)	39.26 ^(d)	62.48	0.977899
^{LH} <i>VC</i>	8.6983 ^(b)	39.24 ^(e)	63.48	0.021977
^{HH} <i>VC</i>	8.6942 ^(b)	39.22 ^(f)	64.48	0.000123
<i>Ethene</i>	13.305 ^(a)	26.66 ^(c)	28.05	1
^{LL} <i>Eth</i>	13.305 ^(b)	26.66 ^(d)	28.03	0.977899
^{LH} <i>Eth</i>	13.291 ^(b)	26.65 ^(e)	29.03	0.021977
^{HH} <i>Eth</i>	13.278 ^(b)	26.64 ^(f)	30.03	0.000123

^(a) Calculated with eq. 4-4.

^(b) Calculated with eq. 4-5 for an isotope ratio of 0 ‰.

^(c) Calculated with eq. 4-8.

^(d) Taken equal to the K_{oc} calculated with eq. 4-8.

^(e) Calculated from eq. 4-10 and eq. 4-11.

^(f) Calculated from eq. 4-10 and eq. 4-12.

S4.3 Calculation of initial carbon isotopologue concentrations

Isotope compositions are usually reported as isotope ratios relatively to an international standard isotope ratio (for carbon: the Vienna Pee Dee Belemnite, with an isotope ratio

$R_{VPDB} = 1.1237 \cdot 10^{-2}$), with the simplified delta notation $\delta^{13}C = \frac{R_{H/L}}{R_{VPDB}} - 1$, where $R_{H/L}$ is

the ratio of the concentration of heavy to light isotopes. In the case of isotopologues,

$R_{H/L} = \frac{{}^{LH}C + 2 \cdot {}^{HH}C}{{}^{LH}C + 2 \cdot {}^{LL}C}$, where ${}^{LL}C$ is the concentration of the carbon isotopologue with

two light (LL) carbon atoms, ${}^{LH}C$, with one light and one heavy carbon atom (LH), and ${}^{HH}C$, with two heavy carbon atoms (HH). The isotopologues concentrations were set to obtain a source TCE isotope ratio $\delta^{13}C\text{-TCE}_{\text{Source}}$ of -30.00 ‰, in the range of industrially produced TCE. Initial concentrations of the TCE isotopologues were calculated following the probability mass function as described by Hunkeler et al, 2009. Based on the assumed isotope ratios of the three individual chlorine atoms, the probability and consequently concentration of each isotopologue and isotopomer was calculated as illustrated Table S4-2. TCE total concentration was precisely 4.400003 mM.

Table S4-6 : Calculation of the Isotopologue/Isotopomer Concentrations of Initial TCE^a

Isotopologue	N1	N2	Probability	Probability	Concentration (mM)
${}^{12}C_1{}^{12}C_2$	L	L	$P_L \cdot P_L$	0.9785515	4.3056300
${}^{12}C_1{}^{13}C_2$	L	H	$2 \cdot P_L \cdot P_H$	0.0213322	$9.38617 \cdot 10^{-2}$
${}^{13}C_1{}^{12}C_2$	H	L			
${}^{13}C_1{}^{13}C_2$	H	H	$P_H \cdot P_H$	0.0001162	$5.115 \cdot 10^{-4}$

^a[TCE] \approx 600 mg.L, $\delta^{13}C\text{-TCE}_{\text{Source}} = -30.00$ ‰, $P_L = 0.989217$; $P_H = 1 - P_L$.

S4.4 Verification of isotopologue versus isotope sorption model

Sorption-induced carbon isotope fractionation occurs as a result of stronger sorption of heavy-isotope containing molecules compare to the light-isotope containing molecules. The resulting fractionation effect was so far modelled through the attribution of different retardation factors for the fraction of heavy and light carbon isotopes. In this study, different retardation factors were attributed to each isotopologue (i.e. the isotopologues containing two light, one heavy and one light, or two heavy carbon isotopes). For verifying this second model, the analytical solutions of both models are compared (Fig. S4-1). The analytical solutions are based on the Ogata-Banks equation (Ogata and Banks, 1961), which

was already employed to study sorption-induced bulk isotope fractionation (van Breukelen and Prommer, 2008):

$$C(x,t) = \left(\frac{C_0}{2} \right) \operatorname{erfc} \left[\frac{R \cdot x - v \cdot t}{(2 \cdot \alpha_x \cdot v \cdot t \cdot R)^{1/2}} \right] \quad (\text{S4-1})$$

where $C(x,t)$ is the concentration at distance x (L) and time t (T), $\operatorname{erfc}()$ is the complementary error function, C_0 is the concentration of the continuous source, v is the pore water velocity ($\text{L} \cdot \text{T}^{-1}$), R is the retardation factor (dimensionless) and α_x is the longitudinal dispersivity (L).

The equation was applied for each isotope or isotopologue separately to enable the calculation of the isotopic ratios, adjusting the value of the retardation factor R to simulate the different retardation of each isotope or isotopologues. Both 1D models simulate a 700 m aquifer with v of $20 \text{ m} \cdot \text{y}^{-1}$ and α_x of 7 m. The total transport time is of 30 years. TCE concentration is set to $1 \text{ mg} \cdot \text{L}^{-1}$ on the left boundary with an initial isotope ratio of $\delta^{13}\text{C-TCE}_0$. The tracer of transport, chloride, which was given the same initial concentration, does not sorb.

The bulk density ρ_b is of $1.855 \text{ kg} \cdot \text{L}^{-1}$, the fraction of organic carbon f_{oc} is of 0.33 %, and the solid-phase organic carbon-water partition coefficient K_{oc} of $142 \text{ L} \cdot \text{kg}^{-1}$. The retardation factor R is calculated as in equation (4-6) in the main text and is of 3.5. The bulk sorption-induced carbon isotope enrichment factor $\varepsilon_{\text{Sorption}}$ was of -0.17 ‰ and defined as $1 - \frac{{}^H K_{oc}}{{}^L K_{oc}}$ with ${}^H K_{oc}$ and ${}^L K_{oc}$ the isotope-specific solid-phase organic carbon-water partitioning coefficients for the heavy and the light carbon isotope, respectively. The isotopologue-specific K_{oc} were determined as in the main text and in Section S4.5. The results validate our isotopologue approach.

Table S4-7 : Input parameters for the Ogata-Bank equation.

	Initial concentration	$K_{oc} = 142 \text{ kg} \cdot \text{L}^{-1}$
Isotope model		
${}^{13}\text{C}$	0.000989217637	K_{oc}
${}^{12}\text{C}$	0.000010782363	$K_{oc} / (1 - \varepsilon_{\text{Sorption}})$
Isotopologue model		
${}^{12}\text{C}-{}^{12}\text{C}$	0.000978551533	K_{oc}
${}^{12}\text{C}-{}^{13}\text{C}$	0.000021332208	$K_{oc} / (1 - \varepsilon_{\text{Sorption}})$
${}^{13}\text{C}-{}^{13}\text{C}$	0.000000116259	$K_{oc} / (1 - \varepsilon_{\text{Sorption}})^2$

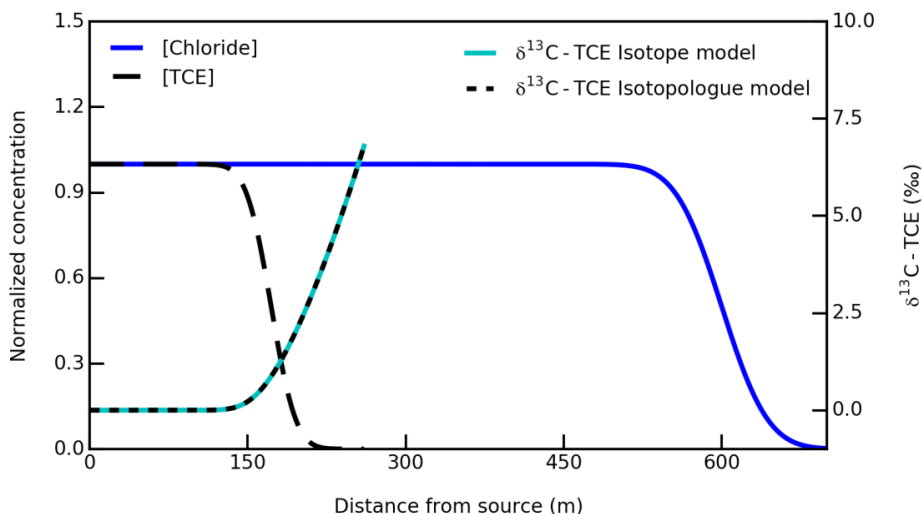


Fig. S4-1 : Sorption-induced isotope fractionation obtained with the isotopologue (as presented in the paper) against the bulk isotope model both using analytical solutions (van Breukelen and Prommer, 2008).

S4.5 Example for the calculation of isotopologue-specific K_{oc} .

The K_{oc} of TCE is $142 \text{ L} \cdot \text{kg}^{-1}$. The reported sorption-induced carbon isotope fractionation factor, α_{Sorption} , employed in this model for TCE is 0.9995, i.e., the enrichment factor $\epsilon_{\text{Sorption}}$ is then of -0.5 ‰. Then:

$${}^{LH} \alpha_{\text{Sorption}} = \alpha_{\text{Sorption}} = 0.9995$$

$${}^{HH} \alpha_{\text{Sorption}} = {}^{LH} \alpha_{\text{Sorption}}^2 = 0.9990$$

$${}^{LL} K_{oc} = K_{oc} = 142 \text{ L} \cdot \text{kg}^{-1}$$

$${}^{LH} K_{oc} = {}^{LL} K_{oc} \cdot 0.9995 = 141.93 \text{ L} \cdot \text{kg}^{-1}$$

$${}^{HH} K_{oc} = {}^{LL} K_{oc} \cdot 0.9990 = 141.86 \text{ L} \cdot \text{kg}^{-1}$$

The K_{oc} of the heavy carbon isotopologue is smaller, i.e., the light LL isotopologue sorbs more than the heavy HL isotopologue.

S4.6 Comparison of various model grid resolutions

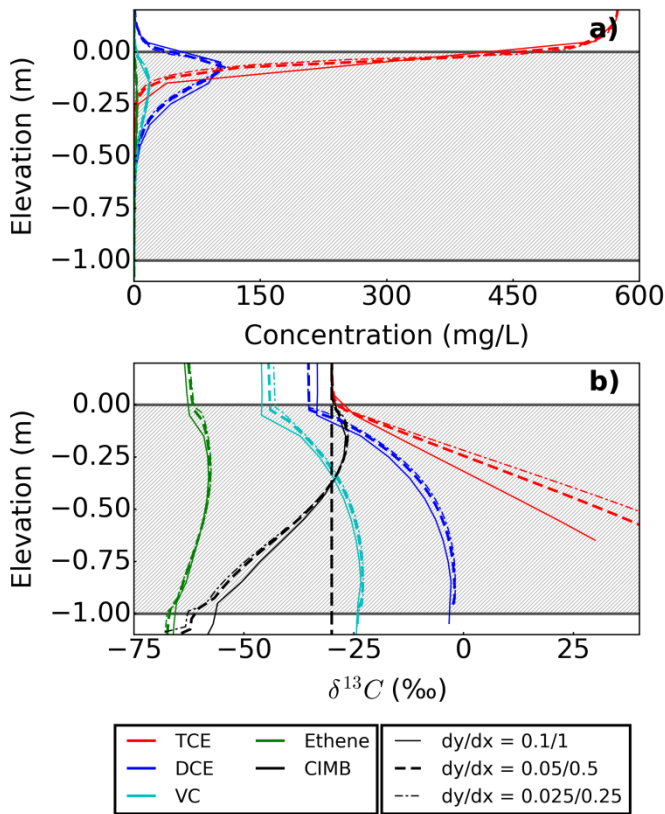


Fig. S4-2: Comparison of three different grid resolutions applied to the depth profiles of concentrations (a) and carbon isotope ratios (b) of CEs and ethene (TCE, red; DCE, blue; VC, cyan; ethene, green; CIMB, black). Simulations are shown at the end of the loading phase (year 10), near the aquifer-aquitard interface, 2 m downgradient of the source. The three grids are indicated in the legend, where dx is the discretization along the horizontal axis and dy along the vertical axis. The grid discretization employed in the manuscript is the middle grid (0.5 m in the horizontal direction (columns) and of 0.05 m in the vertical direction (rows)). The higher resolution grid yields a slightly more enriched $\delta^{13}C$ -TCE compared to the grid employed in the manuscript as a result of a slightly faster TCE concentration decrease with depth.

S4.7 Effects of non-degradative processes on TCE carbon isotope ratios

To assess the impact of solely physical processes on isotope ratio patterns of TCE, $\delta^{13}C$ -TCE was first modelled in the absence of degradation during the loading and back-diffusion/release phases. The simulations specifically assess the impact of isotope fractionation induced by sorption and/or diffusion (description in legend Fig. S4-3). During the loading phase, the dissolving DNAPL forms a plume with high TCE concentration in

the aquifer. The concentration gradient between the aquifer and the aquitard drives TCE diffusion into the initially pristine aquitard (Fig. S4-3a). In the aquitard, transport is governed by diffusion only; advective transport does not occur. TCE sorption occurs in the aquitard with a retardation factor of 3.5. Concentrations and carbon isotope ratio patterns are presented versus depth at 50 m from the source or at the bottom of the aquifer with distance (Fig. S4-3).

The net transport into the clay aquitard induces $\delta^{13}\text{C}$ -TCE enrichment with depth for the base case model (Fig. S4-3g: DySy but without degradation like the other simulations discussed in the Section 4.3.1 in the main text) compared to a model disregarding isotope fractionation induced by physical processes, which yields constant $\delta^{13}\text{C}$ -TCE with depth (Fig. S4-3g: DnSn). The net effect results from the combination of the effects induced by diffusion and sorption. The DySn model disregards sorption-induced isotope fractionation and illustrates that diffusion-induced isotope fractionation leads to isotope depletion with depth due to the slower diffusion of isotopologues containing heavy isotopes (^{13}C) (Fig. S4-3g). On the contrary, sorption-induced isotope fractionation (DnSy) leads to enrichment with depth resulting from stronger retardation of the light isotopologues (Fig. S4-3g). Under the selected set of parameter values, $\delta^{13}\text{C}$ -TCE is stronger fractionated by sorption ($\Delta^{13}\text{C} \sim +1.7 \text{ ‰}$ for DnSy) than by diffusion ($\Delta^{13}\text{C} \sim -1 \text{ ‰}$ for DySn) yielding a net enrichment of less than 1 ‰ in the aquitard at an arbitrarily reference depth of 40 cm after 10 years (Fig. S4-3g). Recently, a similar pattern was observed, modelled, and described for DCM and DCA (Wanner et al., 2017). The effect of varying model parameter values on net isotope fractionation in the aquitard by physical processes is further explored in Section S4.3.6. The simulations names are employed similarly in the main text for the simulations including degradation, and the names are summarized Table S4-8.

Table S4-8 : Details of the simulations DnSn, DySn, DnSy (“n”, without fractionation; “y”, with fractionation). Simulations otherwise similar to the base case scenario (DySy).

	No sorption-induced isotope fractionation (Sn)	Sorption-induced isotope fractionation (Sy)
No diffusion-induced isotope fractionation (Dn)	DnSn no fractionation	DnSy
Diffusion-induced isotope fractionation (Dy)	DySn	Base case (DySy)

When transported along the aquifer-aquitard interface, TCE diffusion into the aquitard tends to preferentially strip the TCE in the aquifer from its light isotopologues. The resulting downgradient $\delta^{13}\text{C}$ -TCE enrichment is small ($\sim 0.04\text{--}0.05 \text{ ‰}$) (Fig. S4-3c: DySn, DySy). Additionally, preferential sorption of the light TCE isotopologues in the aquitard strips the dissolved TCE from its light isotopologues (Fig. S4-3g), which slightly enhances the diffusion of light isotopes from the aquifer to the aquitard. As a result, despite the lack

of sorption in the aquifer, sorption-induced isotope enrichment adds to the diffusion-induced isotope effects in the aquifer during the loading phase (Fig. S4-3c: DnSy, DySy).

After source removal, the TCE concentration decreases in the aquifer, propagating from the source zone downgradient, and triggering back-diffusion of TCE. The base case model DySy shows the occurrence of isotope depletion ($\Delta^{13}\text{C} = -0.4 \text{ ‰}$) in the upgradient part of the aquifer two years after source removal (Fig. S4-3d). A similar depletion is apparent in the model which considers only sorption-induced isotope fractionation (Fig. S4-3d: DnSy). The sorbed fraction is lighter than $\delta^{13}\text{C-TCE}_{\text{Source}}$, therefore the desorption leads to the remobilization of TCE that is relatively depleted in heavy isotopes. The model thus illustrates a stronger influence of sorption than of diffusion on isotope fractionation in the aquifer at the onset of the release phase.

Two years after source removal (year 12, Fig. S4-3e), $\delta^{13}\text{C-TCE}$ is more stable across the aquifer and back-diffusion results in $\delta^{13}\text{C-TCE}$ depletion by about 0.3 ‰ (year 12, Fig. S4-3e). This pattern stabilizes as the same values are observed 15 years after source removal (year 25, Fig. S4-3f). The simulations illustrate that the overall impact of physical processes on isotope fractionation in the aquifer and throughout the different phases leaves only a small imprint on $\delta^{13}\text{C-TCE}$ (<0.5 ‰). Although not significant for biodegradation assessment (< 2 ‰) this small depletion imprint by physical processes after source removal is long-lived. Moreover, the small depletion is also detected across depth above the aquitard-aquifer interface (Fig. S4-3h), suggesting that the depletion could be observed using a well screen of any length.

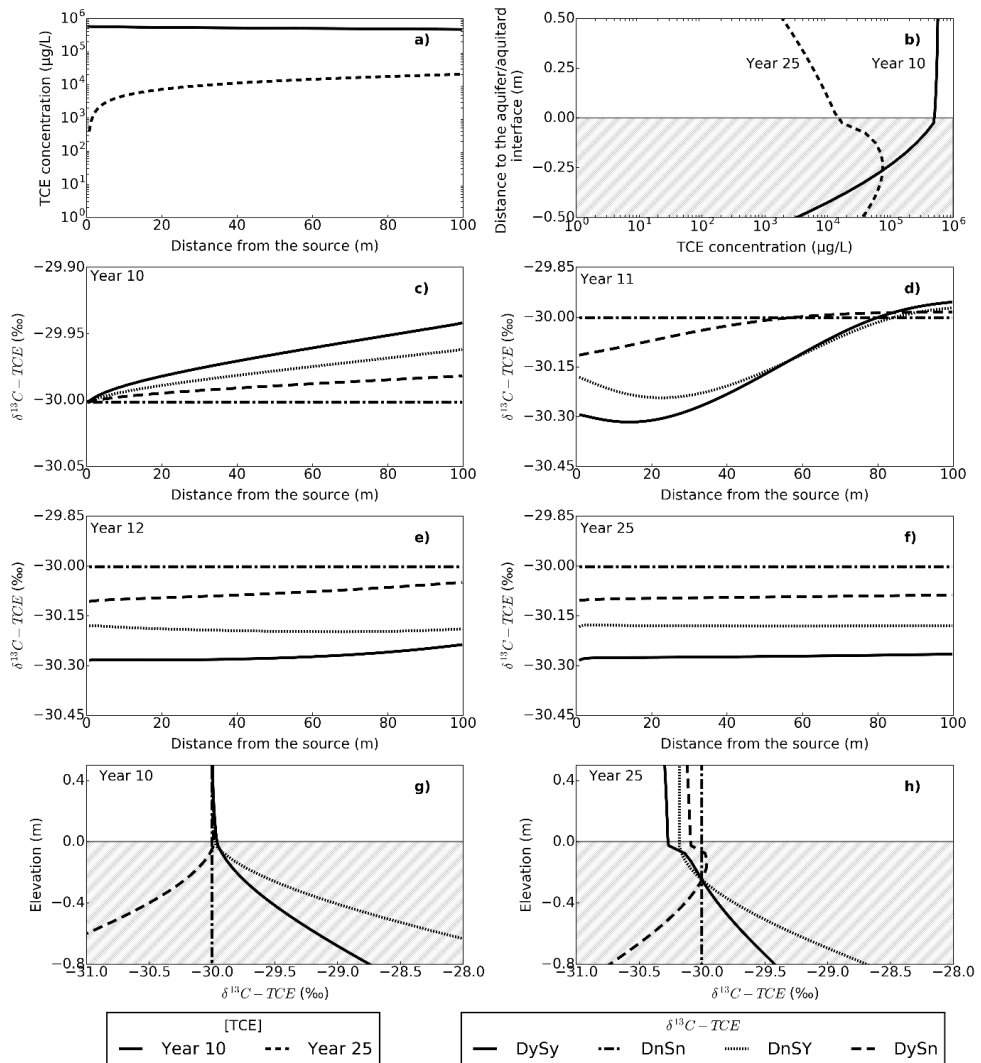


Fig. S4-3: TCE concentration for the base case model in the absence of TCE degradation at the bottom of the aquifer (a) and with depth 50 m downgradient from the source (b, a close-up of the aquifer/aquitard interface), at years 10 and 25 (TCE concentration patterns are similar for all four simulations). $\delta^{13}\text{C}-\text{TCE}$ with distance at the bottom of the aquifer for 4 different simulations (at year 10 (c), year 12 (d), year 15 (e), and year 25 (f)). $\delta^{13}\text{C}-\text{TCE}$ with depth 50 m downgradient from the source (close up of the aquifer/aquitard interface), at year 10 (g) and year 25 (h). Shaded area represents the aquitard. DySy is the base case scenario, with diffusion-induced (Dy) and sorption-induced (Sy) isotope fractionation. DySn includes diffusion-induced isotope fractionation (Dy) but omits sorption-induced isotope fractionation (Sn). DnSy includes sorption-induced isotope fractionation (Sy) omits diffusion-induced isotope fractionation (Dn). DnSn does not include any isotope fractionation induced by physical processes.

S4.8 Close up of the aquifer-aquitard interface (Fig. 4-2c in the manuscript).

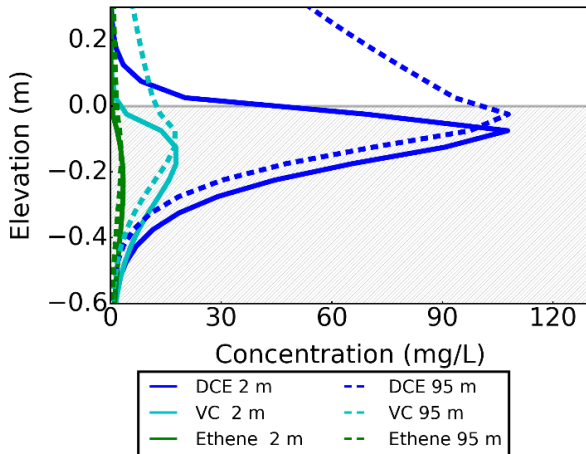


Fig. S4-4 : Close up of Fig. 4-2c in the main text. Depth profiles of concentrations of DCE, VC and ethene only (DCE, blue; VC, cyan; ethene, green) at the end of the loading phase (year 10), near the aquifer/aquitard interface, 2 and 95 m downgradient of the source. The model corresponds to the base case scenario (including degradation). The shaded area corresponds to the aquitard. The daughter products concentrations reach their maximum a few centimetres below the aquifer/aquitard interface, with increasing depth for decreasing chlorination, as a result of sequential reductive dechlorination in the aquitard.

S4.9 Influence of the well screen length and position on CIMB

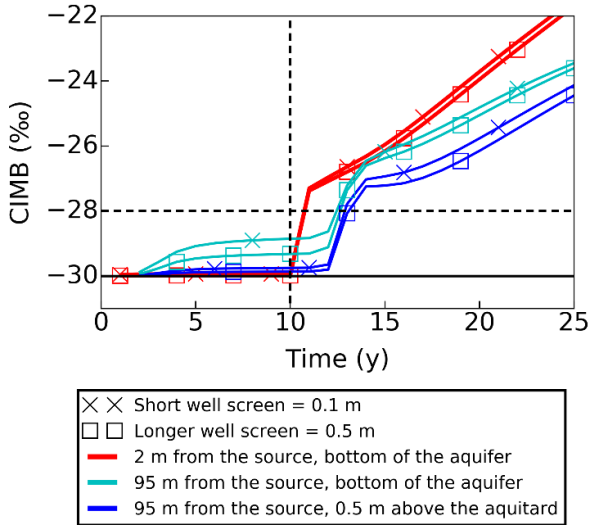


Fig. S4-5 : Carbon isotope mass balance (CIMB) as function of time and as calculated at 3 different positions in the aquifer (near the source and near the aquitard, red; 95 m downgradient the source near the aquitard, cyan; or 95 m downgradient the source 0.5 m above the aquitard; blue) for 2 different wells screen lengths (crosses: short well screens; squares: long well screens).

S4.10 Additional simulations comparing the base case scenario to a scenario with linear decreasing degradation rate constants

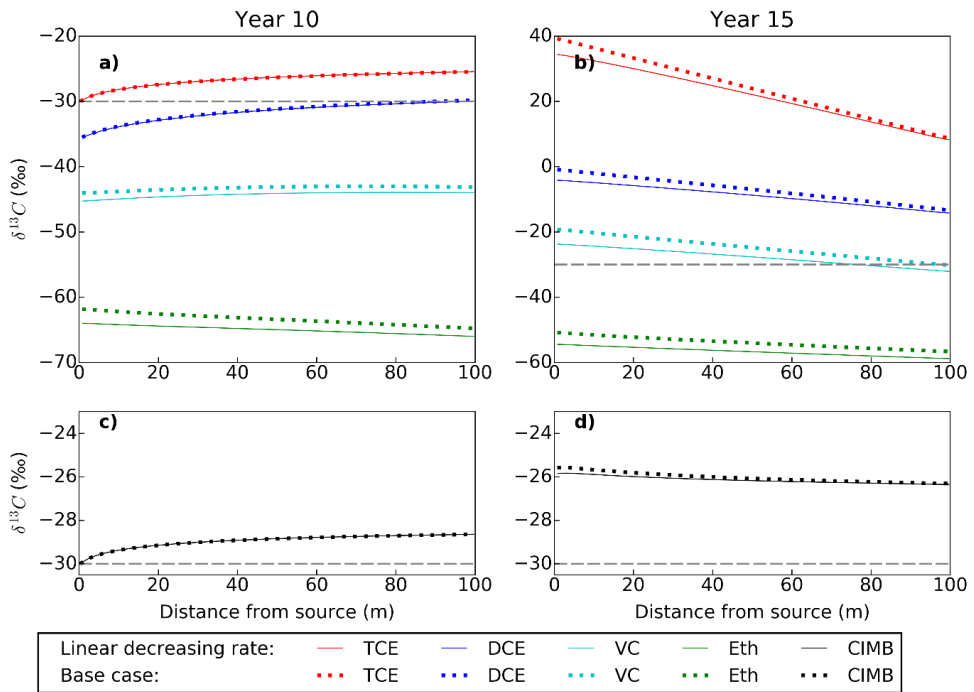


Fig. S4-6 : Carbon isotope ratio patterns of CEs and ethene (top panels), as well as the CIMB (bottom panels), right before (left panels) and 5 years after source removal (right panels). The patterns are presented versus distance at the bottom of the aquifer. Horizontal dashed grey lines represent the $\delta^{13}C$ -TCESource. The base case model is compared to a model with a linear decrease of the rate constant with depth. For the latter, the degradation rate constants of each CEs are multiplied by a factor decreasing incrementally from 1 at the top to 0.05 at the bottom of the aquitard.

S4.11 Additional simulations of TCE reductive dechlorination with DCE stall or VC stall

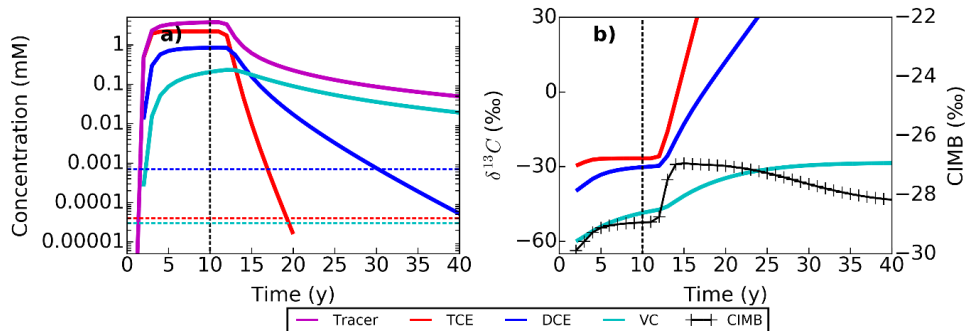


Fig. S4-7 : CEs, ethene, and tracer concentrations (a) and isotope ratios (b), against time, at the bottom of the aquifer 95 m downgradient the source, for a reaction chain including both TCE and DCE reductive dechlorination (VC is the accumulating product). The vertical black line signals year 10 at which the source is removed. The horizontal lines correspond to the minimum concentration limits (MCL) for TCE (red) and DCE (blue). The lines terminate when concentrations fall below detection limits.

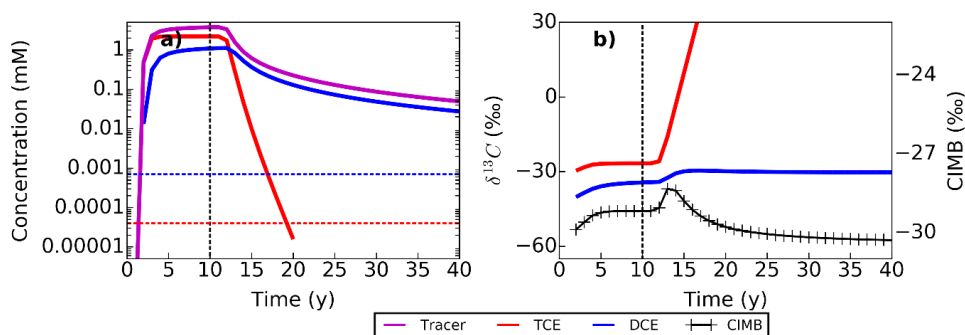


Fig. S4-8 : CEs, ethene, and tracer concentrations (a) and isotope ratios (b), against time, at the bottom of the aquifer 95 m downgradient the source, for TCE dechlorination to DCE (DCE is the accumulating product). The vertical black line signals year 10 at which the source is removed. The horizontal lines correspond to the minimum concentration limits (MCL) for TCE (red), DCE (blue), and VC (cyan). The lines terminate when concentrations fall below detection limits.

S4.12 Depth profiles of TCE concentration and isotope patterns

To obtain further insight in the concentration and isotope patterns and to shed light on the downgradient $\delta^{13}C$ decline (Fig. 3d,e), simulation results for TCE are shown as depth profiles at 3 distances from the source (2, 50, and 95 m) and at 3 moments in time (at the end of the loading phase, and 2 and 5 years into the release phase) (Fig. S4-9). At the end of

the loading phase (year 10), TCE concentration and $\delta^{13}\text{C}$ depth profiles are nearly identical across the aquifer as TCE has reached steady-state (Fig. S4-9a).

Two years after source removal, TCE concentrations near the source zone dropped in the aquifer and are then highest in the underlying aquitard (Fig. S4-9b). The TCE concentration gradient at the aquifer-aquitard interface becomes inverted as soon as the plume passes. The limited change at 95 m downgradient in two years of time illustrates the lag in onset of the release phase due to the later flushing of the downgradient parts of the aquifer (Fig. S4-9b, S9e).

Five years after removal of the source (year 15), the aquitard serves as a reservoir for TCE. TCE concentrations in the aquitard increase with distance from the source as back-diffusion starts later downgradient (Fig. S4-9c). The ongoing uniform degradation in the aquitard explains $\delta^{13}\text{C}$ -TCE enrichment over time in the entire system. The overall downgradient $\delta^{13}\text{C}$ -TCE depletion relates to the delay in flushing of the downgradient parts of the aquifer. Note that $\delta^{13}\text{C}$ depletion in the flow direction of groundwater is unusual at field sites as normally downgradient $\delta^{13}\text{C}$ enrichment is observed when degradation occurs. These spatiotemporal CSIA patterns also differ from those simulated recently under the assumption of a thin bioactive zone at the top of an aquitard (Wanner et al., 2018) as transfer of TCE back and forth through this shallow bioactive zone yields also a sudden and large but not further increasing isotope enrichment nor a decrease downgradient.

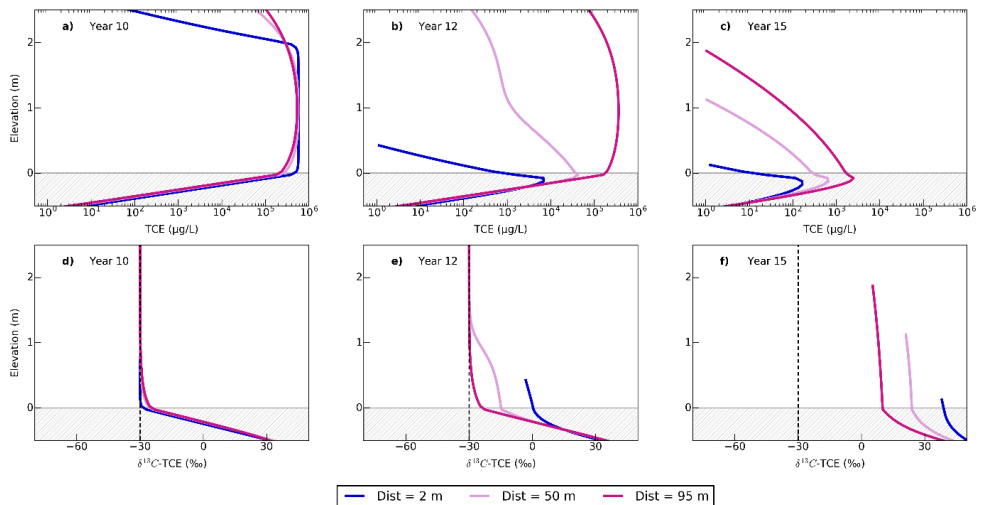


Fig. S4-9 : Depth profiles of TCE concentration and $\delta^{13}\text{C}$ -TCE at three distances (2, 50, and 95 m) from the source at three points in time (year 10, 12, and 15). The dashed line represents $\delta^{13}\text{C}$ -TCE_{Source}.

S4.13 Sensitivity analysis of degradation assessment

In the following section we discuss the effect of model parameter values on the simulated CIMB and θ values to assess the wider applicability of the simulated trends. The adjusted model parameters and their selected values are shown in Table S4-9. For each simulation, a single parameter is increased or decreased in comparison to the base case scenario values. This method disregards potential correlation effects of the parameters on the results, but this was not the aim of these simulations. Results are represented for the bottom of the aquifer, 95 m away from the source, where CE concentrations remain above MCLs long after source removal.

Table S4-9 : Model input parameters values for sensitivity analysis.

Model parameters	Lowest value	Lower value	Base case value	Highest value
Groundwater velocity (m·y ⁻¹)	NA	15 ^a	43.8	130
f_{oc} aquitard	0	NA	0.003 ^b	0.015 ^c
f_{oc} aquifer	NA	NA	0	0.0013 ^d
Thickness aquitard (m)	0.05	0.2	1	NA
Source duration (y)	NA	2	10	30
TCE initial concentration (mM) ^e	0.0088	0.44	4.4	NA
Degradation rate constant	NA	0.23/0.05/0.05	1/0.21/0.21	NA
TCE/DCE/VC (y ⁻¹) ^f	NA	-3 ‰/ -14 ‰/ -20 ‰	-12 ‰/-21 ‰/ -23 ‰	NA
$\epsilon_{\text{Degradation}}$ TCE/DCE/VC	NA	0 ‰/0 ‰/0 ‰/0 ‰	-0.2 ‰/-0.9 ‰/ -1.4 ‰	-1.1 ‰/-4.5 ‰/ -7.0 ‰
$\epsilon_{\text{Diffusion}}$ TCE/DCE/VC/Eth	NA	0 ‰/0 ‰/0 ‰/0 ‰	1.4 ‰/ -3.1 ‰ ^g	-1.1 ‰/-4.5 ‰/ -7.0 ‰
$\epsilon_{\text{Sorption}}$ all CEs	NA	0 ‰	-0.5 ‰	-2.5 ‰

^aTime step adjusted to comply to Peclet grid criteria (time step = 2.5 d).

Sets of retardation factors of ^b3.5/2.3/1.7/1.5, ^c12.3/6.9/4.1/3.1, and ^d2/1.5/1.3/1.2 for TCE, DCE, VC, and ethene, respectively.

^eTCE solubility is 9.7 mM (1.28 g·L⁻¹)

^fSee compilation of literature values Table S4-3.

^g β values of 0.029, 0.088, 0.088, and 0.088; and ^h β values 0.145, 0.44, 0.44, and 0.44 for TCE, DCE, VC, and ethene, respectively.

Despite the parameter variations, the simulated patterns of CIMB (Fig. S4-10) and θ (Fig. S4-11) look mostly similar from one simulation to the other with some exceptions. The presence of the aquitard impacts the CIMB the most after the source is removed, while the underestimation of the extent of degradation is the worst prior to source removal. Simulation confirmed that some parameters like $\epsilon_{\text{Sorption}}$ and $\epsilon_{\text{Diffusion}}$ had negligible effects on both CIMB and θ , despite that their assigned values varied between 0 ‰ and 5 times literature-based estimates and, in the case of sorption-induced fractionation, a relatively large f_{oc} (Fig. S4-10i,j and S4-11i,j). This is a favourable outcome as these values are not well known but clearly large variations hardly affect simulation results. Likewise, source concentration did not affect simulation results probably because of the assumed first-order kinetics and linear sorption (Fig. S4-10f and S4-11f, see also Section 4.3.7). For very low source concentrations, the sudden drop of CIMB at year 24 (Fig. S4-10f) is the result of the concentration of one or several enriched precursors falling below the detection limit. With respect to θ , a low source concentration resulted in lower θ values only during the loading phase. Some parameters mostly affect the timing of changes in the patterns after source removal, for instance sharp changes occur logically later with longer source duration (Fig. S4-10b and S4-10b). With respect to CIMB, groundwater flow velocity and aquifer f_{oc} also

had limited impact (Fig. S4-10a,d). A lower degradation rate constant and lower $\varepsilon_{Degradation}$ logically produce reduced increases of CIMB (Fig. S4-10g,h). Lower degradation rate constants improve the CSIA-based degradation estimate as shown by the increased θ , as shown in Fig. S4-11g and in line with the findings of Van Breukelen and Prommer (van Breukelen and Prommer, 2008). The $\varepsilon_{Degradation}$ should of course not affect θ as these values are assumed as known in the analysis (Figure S4-11h). In relation to source duration, the parameters groundwater flow velocity and aquifer f_{oc} seem mostly to cause a phase shift in the transition of the θ patterns (Figure S4-11a,d) but a higher groundwater flow velocity also causes a higher and thus better θ .

The most influential parameters appear to be the aquitard f_{oc} and aquitard thickness for both CIMB and θ (Fig. S4-10c,e and S4-11c,e). CIMB is sensitive to the spatial separation of the depleted daughter products from their more enriched precursors as discussed before. Especially during the release phase, a higher aquitard f_{oc} therefore yields a larger CIMB enrichment. Noteworthy, also without sorption, the CIMB is predicted to enrich in later stages of the release phase. Probably this is caused by the loss of depleted daughter products which have diffused through the aquitard and reached the lower aquifer. With respect to aquitard thickness, a thinner aquitard results probably in an increased mass loss of depleted daughter products to the underlying aquifer while the more enriched precursors sorb stronger and are still present in thinner aquitards during the back-diffusion phase causing a strong CIMB enrichment. Preferential mass loss of depleted daughter products to the underlying aquifer is thus another phenomenon contributing to high CIMB enrichments that could be observed in overlying aquifers.

This sensitivity analysis shows that Rayleigh-based estimates of degradation are always conservative. Moreover, we show that both $\delta^{13}\text{C}$ -TCE enrichment prior to source remediation and a sudden change in $\delta^{13}\text{C}$ values once the source is remediated are to be expected under many field conditions. However, the CIMB of samples taken near aquitards is in most cases not a reliable indicator of the occurrence of alternative degradation pathways besides reductive dechlorination like oxidation.

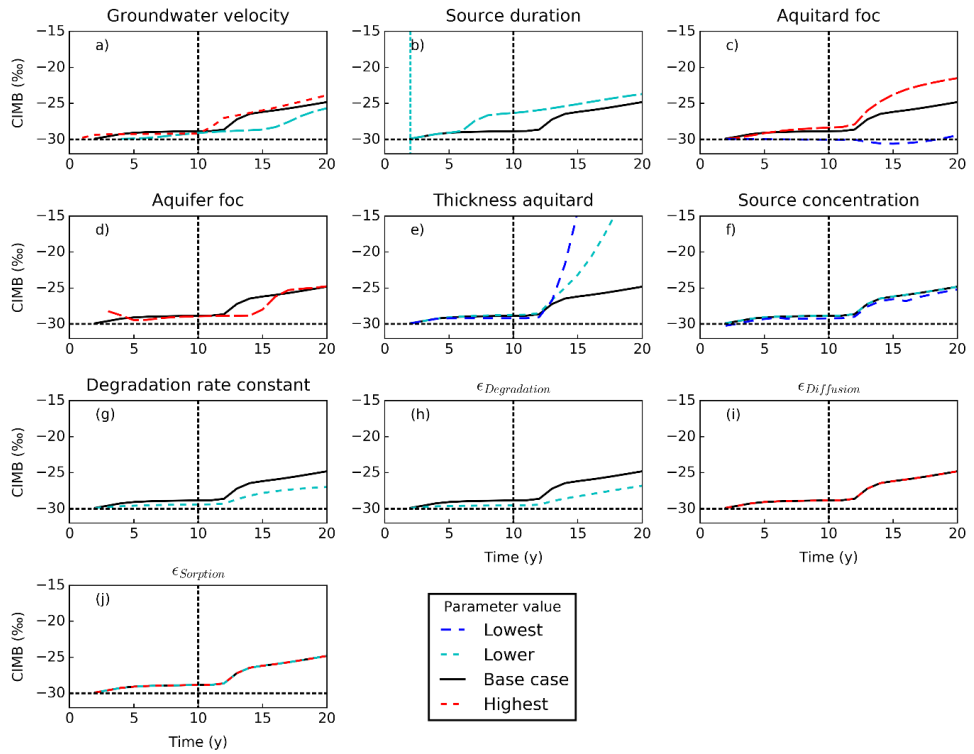


Fig. S4-10. Carbon isotope mass balance (CIMB) as depending on variations in model parameter values. CIMB is calculated versus time at the bottom of the aquifer at 95 m from the source. Model parameters were independently increased or decreased versus the base case scenario (see Table S4-9 for details).

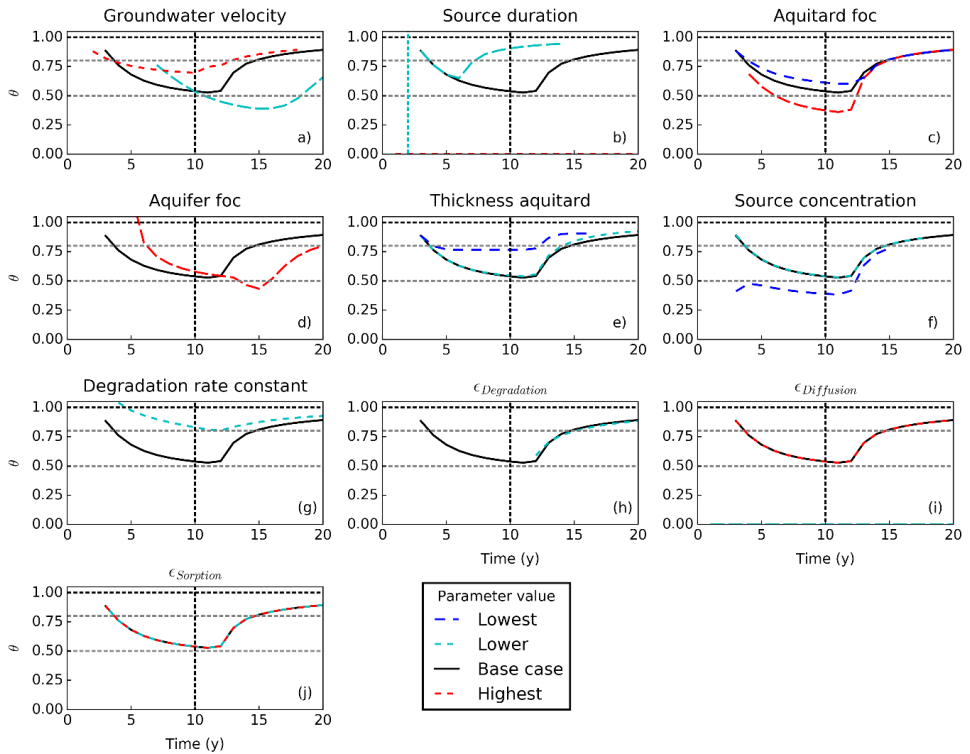


Fig. S4-11 : Ratio of the Rayleigh-equation estimate to the true first-order degradation rate constant (θ), as depending on variations in model parameter values. θ is calculated versus time at the bottom of the aquifer at 95 m from the source. Model parameter values were independently increased or decreased versus the base case scenario (see Table S4-9 for details).

S4.14 Abbreviations and symbols

Table S4-10 : Compilation of abbreviations and symbols used in the main article and the Appendix.

$\alpha_{Sorption}$	Sorption-induced carbon isotope fractionation factor		
$\epsilon_{Sorption}$	Sorption-induced carbon isotope enrichment factor		
f_{oc}	Fraction of organic carbon		
K_{oc}	Solid-phase organic carbon-water partitioning (sorption) coefficient		
${}^L K_{oc}, {}^H K_{oc}$	Isotope-specific K_{oc} for the light and heavy carbon isotope, respectively		
${}^{LL} K_{oc}, {}^{LH} K_{oc}, {}^{HH} K_{oc}$	Isotopologue-specific K_{oc} for the isotopologue containing two lights (LL), one light and one heavy (LH) and two heavy (HH) isotopes of carbon, respectively		
${}^{LH} \epsilon_{Sorption}, {}^{HH} \epsilon_{Sorption}$	Isotopologue-specific sorption induced enrichment factor for the isotopologue containing one light and one heavy (LH) and two heavy (HH) isotopes of carbon, respectively		
R	Retardation factor		
ρ_b	Bulk density	n	Porosity
$\epsilon_{Diffusion}$	Diffusion-induced carbon isotope enrichment factor		
β	Empirical coefficient (see Jin et al., 2014)		
D_w	Aqueous diffusion coefficient	η_T	Water viscosity at temperature T
D_e	Effective diffusion coefficient	T	Temperature
A_i	Activity of the isotopologue i	m_i	Mass of the isotopologue i
α_x	Longitudinal dispersivity	τ_{app}	Apparent diffusion tortuosity coefficient
M_{CE}	CE's weighted molar mass using isotopologues abundances at 0 ‰		
$D_{w,LH}, D_{w,LL}$	Aqueous diffusion coefficient of the isotopologue containing one light and one heavy carbon isotope, and two heavy carbon isotopes, respectively.		
$D_{w,n}$	Isotopologue-specific aqueous diffusion coefficient (isotopologue n)		
$\epsilon_{Degradation}$	Degradation-induced bulk kinetic carbon isotope enrichment factor		
k	First-order degradation rate constant		
θ	Ratio of the Rayleigh-equation estimate to the true first-order degradation rate constant		
${}^{LL} C, {}^{LH} C, {}^{HH} C$	Isotopologue concentrations of the carbon isotopologues containing two light (LL) carbon isotopes, one light (L) and one heavy (H) isotope (LH), and two heavy isotopes (HH)		
R_{VPDB}	International standard isotope ratio for carbon (Vienna Pee Dee Belemnite)		
$R_{H/L}$	Ratio of the concentration of heavy to light isotopes		
$D_{Rayleigh}$	Rayleigh-based estimate of TCE degradation		
D_{System}	Extent of degradation in a column of the aquifer system		
D_{Sample}	True extent of degradation		
$D_{Aquitard}$	Extent of degradation in a column of the aquitard		
DNAPL	Dense non-aqueous phase liquid	MCL	Minimum concentration limit
CIMB	Carbon isotope mass balance	MCL	Minimum concentration limit
Δ CIMB	Shift of the CIMB	LPLs	Low permeability layers
CEs	Chlorinated ethenes	$\delta^{13}C$	Carbon isotope ratio
PCE	Perchloroethene	$\Delta^{13}C$	Shift of the carbon isotope ratio
TCE	Trichloroethene	RD	Reductive dechlorination
DCE	Dichloroethene	$[TCE]_i$	Concentration in TCE at a cell i
VC	Vinyl Chloride	$[Tracer]_i$	Concentration in tracer at a cell i

This page was intentionally left blank

Chapter 5

Virtual experiments to assess opportunities and pitfalls of CSIA in physical-chemical heterogeneous aquifers

Abstract

Abiotic and biotic reductive degradation of chlorinated ethenes (CEs) in low conductivity layers reduces pollution plume tailing and accelerates natural attenuation timeframes. Such degradation pathways might go undetected when only highly conductive layers are targeted in site assessments. Reactive transport model simulations (PHT3D in FloPy) were executed to assess the performance of dual carbon and chlorine compound specific stable isotope analysis (CSIA) in degradation pathway identification and quantification in a coupled physical-chemical heterogeneous virtual aquifer. Degradation rate constants were assumed correlated to the hydraulic conductivity: positively for oxidative transformation (higher oxygen availability in coarser sands) and negatively for chemical reduction (higher content of reducing solids in finer sediments). Predicted carbon isotope ratios were highly heterogeneous. They generally increased downgradient of the pollution source but the large variation across depth illustrates that monotonously increasing isotope ratios downgradient, as were associated with the oxidative component, are not necessarily a common situation when degradation is favourable in low conductivity layers. Dual carbon-chlorine CSIA performed well in assessing the occurrence of the spatially separated degradation pathways and the overall degradation, provided appropriate enrichment factors were known and sufficiently different. However, pumping to obtain groundwater samples especially from longer well screens causes a bias towards overestimation of the contribution of oxidative transformation associated with the higher conductive zones. As degradation was less intense in these highly conductive zones under the simulated conditions, overall degradation was underestimated. In contrast, in the usual case of limited CSIA data, dual CSIA plots may rather indicate dominance of chemical reduction, while oxidative transformation could go unnoticed, despite being an equally important degradation pathway.

This page was intentionally left blank

5.1 Introduction

The potential degradation of chlorinated ethenes (CEs) through both biotic and abiotic redox-sensitive pathways in groundwater (Vogel et al., 1987) opened opportunities for monitored natural attenuation (MNA) as an alternative to invasive, energy-intensive technologies for the remediation of polluted sites. Until recently, MNA was focused on biotic reductive dechlorination (BRD) of TCE. Recent studies suspect that chloroethene degradation in the presence of iron(II) minerals might have been underestimated at field sites, including at sites where degradation occurs through simultaneous abiotic and biotic degradation (Brown et al., 2007). One of the reasons would be the general lack of detection of degradation products, either due to being indiscernible from the background concentrations or simply because they are not measured (He et al., 2009). For instance, when trichloroethylene (TCE) is in contact with the iron hydroxides green rust or magnetite, the daughter products acetylene, ethene, and ethane are likely to degrade further in aquifers (Han et al., 2012; Jeong et al., 2007; Lee and Batchelor, 2002a; Liang et al., 2009). For similar reasons, the aerobic cometabolism of TCE, which ultimately produces CO₂ and Cl, could have been overlooked (Schmidt et al., 2014).

Compound specific stable isotope analysis (CSIA) has been demonstrated to be a valuable tool for determining CE degradation pathways and extent of degradation (Bloom et al., 2000; Clark et al., 2016; Palau et al., 2014; Sherwood Lollar et al., 1999). For instance, during TCE degradation, the bond containing a heavy carbon isotope is cleaved slightly slower than the bond containing a light carbon isotope. The resulting carbon isotope fractionation depends on the extent of TCE degradation and on the fractionation potential of the reaction, characterized by the process-specific enrichment factor ϵ (Hunkeler et al., 2002). Both degradation by iron(II) minerals and the aerobic cometabolism of TCE are associated with large carbon isotope enrichment factors and could be detected and quantified at field sites using CSIA (Liang and Dong, 2007; Schmidt et al., 2014).

When two degradation pathways are co-occurring at a site, the CSIA data of a unique element does not allow a proper attribution of degradation to the one or the other pathway (Höyng et al., 2015). Dual carbon-chlorine CSIA (C-Cl CSIA) is specifically promising for the study of co-existing degradation pathways of CEs at field sites, as the relative extent of C and Cl isotope fractionation depends on the reaction mechanism. Where several processes were likely to occur, C-Cl CSIA slopes helped selecting the main degradation pathway (Badin et al., 2016; Clark et al., 2016; Hunkeler et al., 2011a). Provided that the enrichment factors of each reaction pathway are known and the relative chlorine to carbon isotope enrichments (ϵ_{Cl}/ϵ_C) are sufficiently different, the respective participation of each of the two different degradation pathways to overall degradation as well as the extent of overall degradation can be determined based on a C-Cl CSIA dataset (van Breukelen, 2007).

The physical and chemical heterogeneities of aquifers are directly impacting the reactive transport of pollutants. Physical heterogeneities induce preferential flow and therefore mixing of reactive components. Geochemical heterogeneity induces zones of either abundance or scarcity of reactive minerals and sedimentary organic matter. It is likely that zones of low conductivity will be more reductive, while conductive zones, where oxygen can be transported faster than it is consumed, will be more oxic. Additionally, different geological layers might present different mineralogy, specific surface areas, or host different microbial groups, inducing an additional correlation between hydraulic conductivity and reactivity. For example, at a field site sampled with high resolution, the reduction and therefore the immobilization of uranium was higher in low permeability zones than in permeable sediments (Janot et al., 2015). However, hydraulic conductivity is not the only parameter expected to be correlated with reactivity. For instance, the ferrous mineral content seemed to be an important parameter to explain the difference of reactivity of two clayey soils in the abiotic degradation of chlorinated ethenes (Schaefer et al., 2017). In both low-conductivity zones and in conductive zones, availability of substrate and bacterial activity plays a role in the biotic reduction or oxidation of pollutants (McMahon, 2001; Wanner et al., 2018a; Yan et al., 2016). With time, reduced conditions develop in chlorinated solvent plumes (Christensen et al., 2000). Such additional conditions influence reactivity while being potentially uncorrelated to the hydraulic conductivity, and were addressed in previous modeling studies (Atchley et al., 2014; Jang et al., 2017; Sanz-Prat et al., 2016). Despite those additional complexities, heterogeneity of hydraulic conductivity in aquifers plays a major role in degradation (Jang et al., 2017).

Well-characterized aquifers are rare, and aquifers are often considered as ‘black boxes’ in which the degradation and transport patterns of CEs must be determined through spatially and temporally sparse datasets. In this context, synthetic data sets created using models combining reactive transport with isotope fractionation are employed for advising practitioners on the optimal CSIA sampling strategies (Höyng et al., 2015; Xu et al., 2017). The effects of hydraulic conductivity heterogeneity on resulting C-CSIA patterns of toluene degrading with various electron-acceptors was assessed before by reactive transport modelling of aquifer analogues (Höyng et al., 2015). Using such a similar approach, the present study investigates whether dual C-Cl CSIA could detect TCE degradation through two different reaction pathways when those pathways occur dominantly in different conductivity zones. Low-permeability sediments such as clay lenses are more likely to present reductive conditions susceptible to host biotic reductive dechlorination of CEs (Damgaard et al., 2013a; Takeuchi et al., 2011; Wanner et al., 2018b), and might offer large reactive iron mineral contents and surfaces (Schaefer et al., 2017). High-conductivity zones as permeable sands are more likely to be aerobic and therefore can host TCE biotic oxidation, either directly or through aerobic cometabolism. Applying a simple correlation between the hydraulic conductivity and the two degradation rate constants of TCE (aerobic

transformation and chemical reduction), alike the approach of (Cunningham and Fadel, 2007), we investigate the resulting spatially heterogeneous carbon and chlorine isotope ratio patterns of TCE and the implications for polluted site investigation. The main objectives of this study are (1) to understand how spatially heterogeneous CSIA patterns evolve from physical-chemical heterogeneous conditions, (2) to assess the performance of dual C-Cl CSIA in detecting the occurrence of both degradation pathways and in calculating overall degradation under these conditions, and (3) to assess the effect of pumping (preferentially from the more permeable zones) on degradation assessment.

5.2 Methodology

5.2.1 General setup of model

The multicomponent transport and degradation is modelled with PHT3D (Prommer et al., 2001), which combines the 3-D multicomponent transport model MT3DMS with the geochemical model PHREEQC-2 (Parkhurst and Appelo, 1999). PHT3D was accessed through the python interface FloPy (Bakker et al., 2016). A TCE source with a thickness of 4 m is set at the upgradient boundary of the aquifer. The source includes a non-degradative tracer with otherwise similar characteristics to TCE. The degradation rate constants of aerobic cometabolism and chemical reduction of TCE are either positively (oxidation) or negatively (chemical reduction) correlated to the hydraulic conductivity (K). The first-order degradation rate constants range between 0 to 10 y^{-1} (discussed in detail later).

The simulated aquifer domain is 100 m long and 10 m thick, with a discretization of 0.5 m in the x (spreading) direction and 0.05 in the z (depth) direction. For simplicity, the porosity was set homogeneously to 0.35 across the aquifer. This value is typical for unconsolidated sands. The dry bulk density was set to $1.855 \text{ kg}\cdot\text{L}^{-1}$ throughout the aquifer system.

The heterogeneous hydraulic conductivity field was obtained using the field generator available in ModFlow (Chiang, 2013). In our model, the mean of the log-normally distributed K was set to $3.3\cdot 10^{-4} \text{ m}\cdot\text{s}^{-1}$, with a standard deviation for $\ln(K)$ of 1.5, in line with prior modeling studies (Atchley et al., 2014; Uçankuş and Ünlü, 2008). The correlation lengths were set to 7 m longitudinally and 1 m vertically. Those input parameters yield a medium heterogeneous aquifer with hydraulic conductivities corresponding to a sandy aquifer (see Fig. 5-1). The simulated conductivity field is presented in Fig. 5-2a and the distribution of K is presented in Fig. 5-1. The flow direction is from left to right, with an imposed average hydraulic gradient of $0.0033 \text{ m}\cdot\text{m}^{-1}$ calculated to achieve an average groundwater velocity of $30 \text{ m}\cdot\text{y}^{-1}$ based on the geometric mean of the simulated hydraulic conductivity of $3.2\cdot 10^3 \text{ m}\cdot\text{y}^{-1}$. The simulation duration is of 6 years, at which steady-state is reached. The longitudinal and vertical dispersivities were set to 1 m and 5 mm, respectively. The selected grid spacing (mentioned above) and time step (1.1

days) ensure that both Peclet and Courant criteria are satisfied for the median value of the permeability ($2.8 \cdot 10^3 \text{ m} \cdot \text{y}^{-1}$). TCE aqueous diffusion coefficient D_w was set to $5.1 \cdot 10^{-5} \text{ m} \cdot \text{d}^{-1}$. To account for tortuosity, the effective diffusion coefficient was calculated as $D_{eff} = D_w \times n$, where n is the porosity. Diffusion was expected to have negligible effects on TCE isotope fractionation under the simulated conditions. Sorption was not simulated.

5.2.2 Correlation between hydraulic conductivity and degradation rates

The modelling study relies on the hypothesis is that the spatial distribution of degradation pathways is connected to the hydraulic conductivity in the aquifer. Recent detailed studies of subsurface sediments in the Netherlands show that clays present a generally higher potential reactivity than sands, with notably higher contents of reactive iron, pyrite, and organic matter in clays versus sands (Griffioen et al., 2016, 2012). The more reduced clay zones are therefore likely to provide the necessary reactive iron minerals such as pyrite required for abiotic reductive dechlorination (Lee and Batchelor, 2002; Liang et al., 2009; Weerasooriya and Dharmasena, 2001). Biotic reductive dechlorination of CEs in clays profits from elevated contents of organic matter which serve as substrate to the bacterial population (Wanner et al., 2018b). Finally, TCE aerobic (co)metabolism, for instance on methane (Fogel et al., 1986), requires the presence of oxygen but might benefit from the vicinity of low-permeability layers provided they act as substrate source for the microbial population in the otherwise less reactive sand zones (McMahon, 2001). In this paper, the first-order degradation rate constants were therefore correlated to the spatially varying hydraulic conductivity following (Cunningham and Fadel, 2007). Despite the simplification of a perfect correlation, we expect that the employed correlation is sufficient for addressing our research objectives.

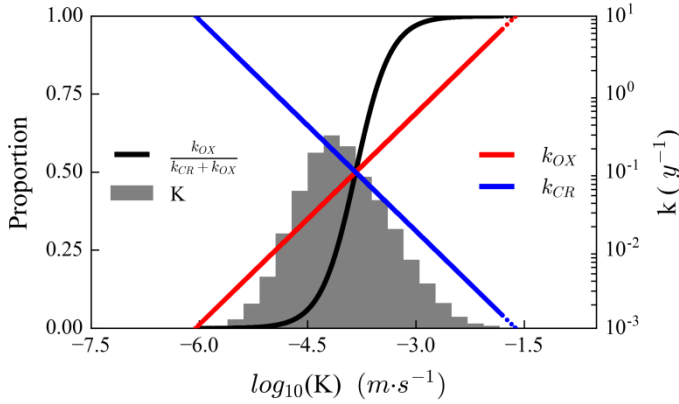


Fig. 5-1 : On the left axis, the distribution of the hydraulic conductivity K (grey histogram) and the proportion of the oxidative, k_{OX} , to chemical reductive, k_{CR} , first-order rate constants (black). On the right axis, the change of degradation rate constants for TCE chemical reduction (blue) and TCE oxidation (red) against the decimal logarithm of K (K in $m \cdot s^{-1}$).

The first-order rate constant of TCE oxidation (OX), k_{OX} , positively correlated with the hydraulic conductivity, is such as $\ln(k_{OX}) = f(\ln(K))$. The first-order rate constant of chemical reduction (CR), k_{CR} , negatively correlated to the hydraulic conductivity, is such as $\ln(k_{CR}) = f(-\ln(K))$. For the rate constants to evolve between $0 y^{-1}$ and $10 y^{-1}$, they were then defined at the aquifer scale such as $\ln k_{OX} = a_{OX} \cdot \ln(K) + b_{OX}$ and $\ln k_{CR} = a_{CR} \cdot \ln(K) + b_{CR}$, with each pair of a and b values being calculated as follows:

$$a_{OX} = \frac{10}{\max_{\ln(K)} - \min_{\ln(K)}} \quad (5-1)$$

$$b_{OX} = -a_{OX} \cdot \min_{\ln(K)} \quad (5-2)$$

$$a_{CR} = \frac{10}{\max_{-\ln(K)} - \min_{-\ln(K)}} \quad (5-3)$$

$$b_{CR} = -a_{CR} \cdot \min_{-\ln(K)} \quad (5-4)$$

where $\min_{\ln(K)}$, $\min_{-\ln(K)}$, and $\max_{\ln(K)}$, $\max_{-\ln(K)}$, represent respectively the minimums and the maximums of the values of the $\ln(K)$ permeability field and of $-\ln(K)$. The resulting distribution of the rate constants k_{OX} and k_{CR} are presented in Fig. 5-2b and 2c, respectively, and in relation with K in Fig. 5-1. Across the simulated aquifer, the average and median of the pathways rate constants are of the same order of magnitude (not shown). TCE chemical reduction is slightly more favourable than oxidation due to the skewness of the K values distribution (Fig. 5-1). Note that we simulated a medium heterogeneous sand aquifer which

not specifically included clay lenses but finer grained and more impermeable sections assumed to have a similar reactivity for CR as clay/silts as known from the literature. As a heterogeneous sandy aquifer was modelled, it was chosen not to increase the standard deviation and/or to lower the mean of K to produce zones with K values closer to clay hydraulic conductivity, as this would also have yielded more zones with K values representative of gravel. The outcomes of this study are not expected to change by this assumption.

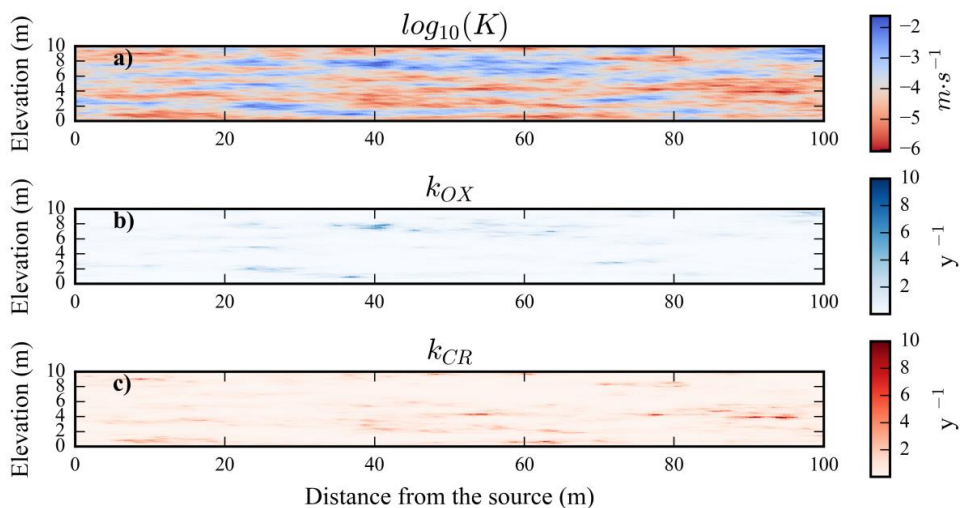


Fig. 5-2 : (a) Hydraulic conductivity (K) field; blue zones: high-conductivity zones, red zones: low-conductivity zones; (b) k_{OX} distribution; (c) k_{CR} distribution.

5.2.3 Simulation of isotope fractionation

The TCE source is modelled as a constant TCE concentration at the upgradient aquifer boundary. The initial TCE concentration is set to about half the solubility, i.e., $600 \text{ mg} \cdot \text{L}^{-1}$. The initial TCE carbon and chlorine isotope ratios are -30 ‰ and $+2.5 \text{ ‰}$, respectively, which corresponds to the isotope signature of industrially produced TCE (Shouakar-Stash et al., 2003). The initial concentration of each carbon and chlorine isotope is calculated following (Hunkeler et al., 2009) as presented in the supporting information in Section S5.1. Concentrations below the usual isotope quantification limit ($1 \text{ } \mu\text{g/L}$) are not reported.

First-order degradation kinetics was applied to both reaction pathways. Both carbon and chlorine isotope fractionation were modelled through the “bulk isotope” method. For each isotopic element (C and Cl), both the light (^lTCE) and heavy (^hTCE) isotopes in the TCE molecule were simulated. The difference in degradation rate constants associated with the heavy and the light isotopes, $^h k_{bulk}$ and $^l k_{bulk}$, respectively, is described by the kinetic isotope

fractionation factor $\alpha_k = {}^h k_{bulk} / {}^l k_{bulk}$, where $\alpha_k = \varepsilon + 1$. Isotope fractionation is incorporated in the reactive transport model by setting the degradation rate constants of the heavy and the light isotopes, ${}^l r$ and ${}^h r$, respectively, as follows Van Breukelen et al. (2005):

$$-{}^l r = -r \frac{[{}^l TCE]}{[TCE]} \quad (5-5)$$

$$-{}^h r = -r \frac{[{}^h TCE]}{[TCE]} \alpha_k \quad (5-6)$$

where r is the overall first-order degradation rate of TCE associated with a specific process:

$$r = k[TCE] \quad (5-7)$$

where k is the first-order TCE degradation rate constant of a specific process.

The magnitude of degradation-induced isotope effects is reported as the bulk effect, i.e., the average of all reactive and non-reactive positions of a molecule. As TCE reaction products were not the subject of this study and not much relevant for the simulated pathways either, position-specific isotope fractionation for both carbon and chlorine were not considered. Bulk isotope fractionation is sufficient for simulating isotope enrichment of parent compounds (Badin et al., 2018; Cretnik et al., 2014; Hunkeler et al., 2002; van Breukelen et al., 2017, 2005).

Bulk isotope enrichment factors of TCE CR were set to $\varepsilon C_{CR} = -15 \text{ ‰}$ and $\varepsilon Cl_{CR} = -2.5 \text{ ‰}$ for carbon and chlorine, respectively (Audí-Miró et al., 2013), which corresponds to degradation by zero-valent iron. For TCE OX, bulk isotope enrichment factors were set to $\varepsilon C_{OX} = -11.5 \text{ ‰}$ and $\varepsilon Cl_{OX} = +0.3 \text{ ‰}$ (Gafni et al., 2018), which corresponds to TCE aerobic cometabolism by the toluene degrader *Pseudomonas Putida F1*. These values correspond to $\varepsilon Cl/\varepsilon C$ slopes of +0.16 for TCE CR and -0.03 for TCE OX. Different $\varepsilon Cl/\varepsilon C$ slopes associated with each pathway as selected here are necessary to enable pathway identification with dual C-Cl CSIA (van Breukelen, 2007).

The slightly lower degradation rates of the heavy isotopes results in the total summed rate of all isotopes to be somewhat lower than the intended degradation rate of the molecule. As the reaction networks for carbon and chlorine isotopes are independent, the predicted C-Cl CSIA slopes gradually deviate from reality over time. Following Van Breukelen et al. (2017) a correction factor was applied to each isotope reaction rate in order to align the two independent isotope networks with the overall reaction progress (supporting information Section 5.2).

5.2.4 Post-simulation calculations

5.2.4.1 *Virtual groundwater samples*

The TCE concentrations and isotope ratios were calculated for virtual groundwater samples obtained from various virtual monitoring well networks. The concentration of TCE or of the tracer in each virtual sample, $C_{(sample)}$, were calculated as the pumping flow-rate-weighted mean concentrations of the model grid cells representing the immediate surroundings around the well screen (Höyng et al., 2015). It was assumed that the pumping local flow rate was proportional to the local hydraulic conductivity. This method takes into account the influence of the local hydraulic conductivity on the groundwater flux into the well screen during pumping:

$$C_{sample} = \frac{\sum C_i \cdot K_i}{\sum K_i} \quad (5-8)$$

where C_i is the concentration of the compound and K_i the hydraulic conductivity of a grid cell i .

The isotope ratio of element E (in this study, carbon or chlorine) in the sample is weighted according to the respective concentrations of TCE in each grid cell:

$$\delta_{(sample)} = \frac{\sum C_i \cdot \delta_i \cdot K_i}{\sum C_i \cdot K_i} \quad (5-9)$$

where $\delta_{(sample)}$ and δ_i are the heavy to light isotope ratio of the element E , of the sample and of a cell i , respectively, expressed in the δ notation ($\delta_{(sample)} = (R_{(sample)} - R_0) / R_0$), and where $R_{(sample)}$ and R_0 are the ratios of the heavy to light isotope concentrations of an element E in a sample and of the international standard, respectively.

5.2.4.2 *Degradation estimates and rate ratio*

Degradation estimates were obtained using the previously developed modified Rayleigh equation for assessing degradation through two different processes using dual isotope analysis (van Breukelen, 2007). With this concept, degradation can be attributed to the one or the other pathway, or to a combination of those, based on the dual C-Cl CSIA data, provided that their respective carbon and chlorine isotope enrichment factors ϵC and ϵCl are known. The proportion of the influence of the one pathway over the other is quantified through the rate ratio F as defined in Van Breukelen (2007).

The derivation of the modified Rayleigh equation is briefly summarized below. We refer to Van Breukelen (2007) for the details. Based on the commonly used Rayleigh equation, the isotopic shift of an element E , Δ , is calculated as follows:

$$\ln\left(\frac{\delta_{(sample)} + 1}{\delta_{source} + 1}\right) = \Delta = \varepsilon \cdot \ln f \quad (5-10)$$

where δ_{source} and $\delta_{(sample)}$ are the initial isotope ratio of the element E in the source and a downgradient sample, respectively, ε is the enrichment factor for the element E for a given reaction pathway, and f is the fraction of remaining (non-degraded) TCE. The ratio of the apparent enrichment factors Φ is estimated based on the ratios of the isotopic shifts:

$$\Phi = \frac{\Delta^{13}C}{\Delta^{37}Cl} \quad (5-11)$$

For our study, the rate ratio F of our two competing pathways is calculated as:

$$F = \frac{\Phi \cdot \varepsilon C_{CR} - \varepsilon Cl_{CR}}{(\varepsilon Cl_{OX} - \varepsilon Cl_{CR}) - \Phi(\varepsilon C_{OX} - \varepsilon C_{CR})} \quad (5-12)$$

where εC_{CR} , εC_{OX} , εCl_{CR} , and εCl_{OX} are the carbon and chlorine isotope enrichment factors of the chemical reduction and the aerobic cometabolism pathways, respectively. The distribution of the two degradation pathways can therefore be directly obtained from the relative isotopic shifts and from the enrichment factors of the two pathways, provided they are known.

The apparent carbon isotope enrichment factor εC_{app} is calculated as follows:

$$\varepsilon C_{app} = F \cdot \varepsilon C_{OX} + (1 - F) \cdot \varepsilon C_{CR} \quad (5-13)$$

The modified Rayleigh equation to quantify the remaining TCE fraction f using dual C-Cl CSIA is then:

$$f = \left(\frac{\delta^{13}C_{(sample)} + 1}{\delta^{13}C_0 + 1}\right)^{\frac{1}{\varepsilon C_{app}}} \quad (5-14)$$

The estimate of degradation based on the C-Cl CSIA data, $D_{Rayleigh}$, is calculated as $D_{Rayleigh} = 1 - f$. $D_{Rayleigh}$ is usually smaller than the true extent of degradation, D_{True} , the ratio of TCE to the concentration of the non-degradative tracer, i.e., $D_{True} = [TCE]/[Tracer]$.

5.3 Results and discussion

5.3.1 General patterns

Fig. 5-3 illustrates the impact of the coupled physical and chemical heterogeneity on the spatial distribution of the TCE concentrations, the carbon and chlorine isotope ratios, and the degree of overall degradation within the plume at steady-state. TCE concentrations are the highest in the high-conductivity zones which induce preferential flow (Fig. 5-3b). TCE carbon and chlorine isotope ratios show limited enrichment in the high-conductivity zones compared to the low-conductivity zones due to relatively lower residence times (Fig. 5-3d, 3e). Both carbon and chlorine isotopes display a net mean increase with distance but with a large variation with depth (Fig. 5-4a). The observed patterns differ from a prior study of heterogeneous toluene degradation where degradation and consequently isotope enrichment was concentrated at the fringes of the plume (Höyng et al., 2015).

Simulations in which either TCE chemical reduction (CR) or TCE oxidation (OX) occurs reveal a major difference in associated isotope patterns (Fig. 5-4bc). While the standard deviation of $\delta^{13}\text{C}$ values at a certain depth profile for TCE OX is smaller than 0.5 ‰ regardless of the travel distance (Fig. 5-4b), for TCE CR the standard deviation is large and varies between 2 ‰ and 10 ‰ (Fig. 5-4c). Interestingly, despite the heterogeneity of TCE OX degradation rate constants, isotope patterns for TCE OX (Fig. 5-4b) are similar to the monotonous enrichment expected in case of uniform degradation in the aquifer (Hunkeler et al., 1999). The contrasting large depth variation of isotope ratios associated with TCE CR is sustained by the inverse correlation of k_{CR} with the hydraulic conductivity. As degradation mostly occurs in the low conductivity zones, those zones will show high isotope enrichments especially when conductivity is relatively low and contaminants reside there for a long time. In contrast, limited isotope enrichment is observed in the connecting high permeability zones where degradation by CR is limited. The correlation between the chemical and the physical heterogeneity plays thus a determining role in the distribution of isotope enrichment.

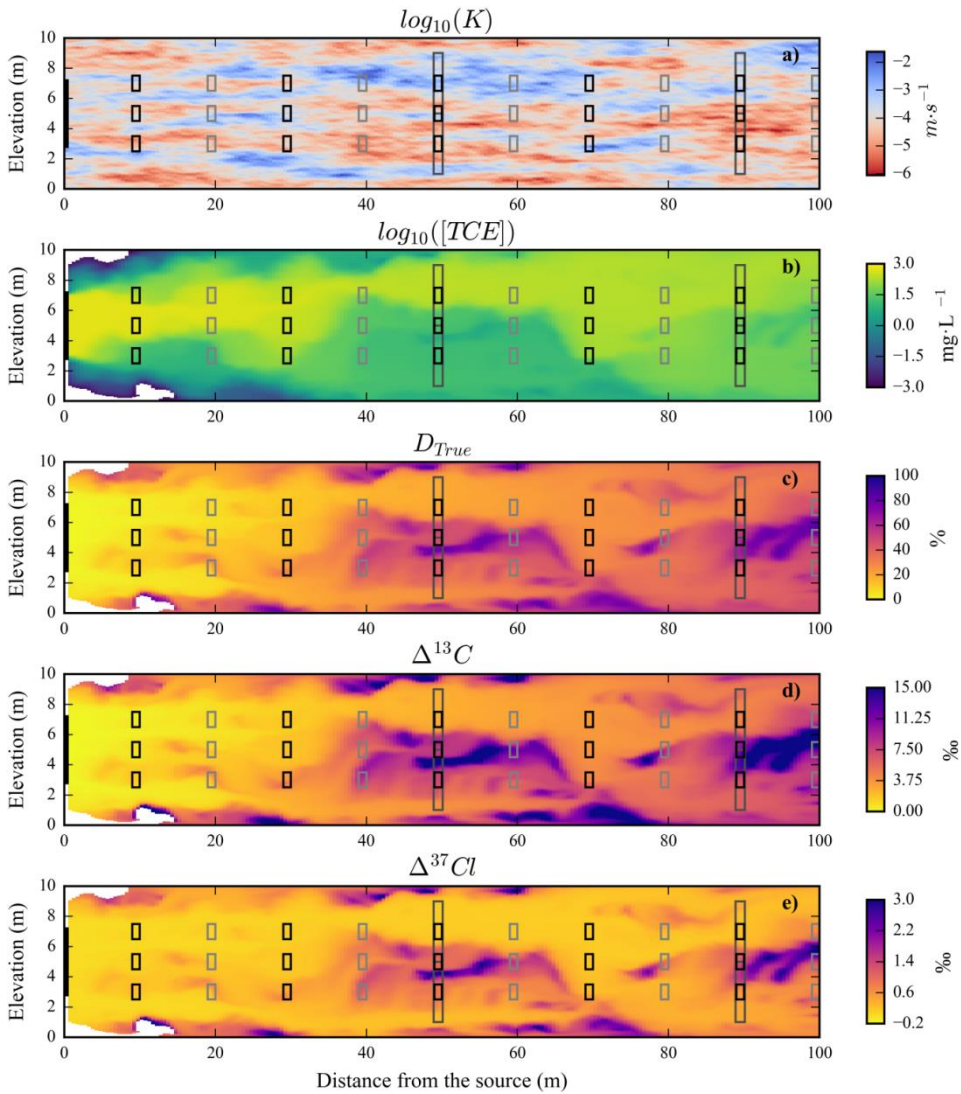


Fig. 5-3 : Cross section showing a case of combined TCE oxidation (in high-permeability layers) and chemical reduction (in low-permeability layers) at steady state of (a) K , (b) TCE concentration, (c) the true TCE degradation extent D_{True} , and of the isotopic shifts (d) $\Delta^{13}C$ and (e) $\Delta^{37}Cl$. The TCE source is indicated by the thick black line at the upgradient (left) boundary. The 6 different regularly spaced monitoring networks consisting of 5 wells of 1m long screens placed at equal depth (3m, 5m, or 7m) and with 20 meter spacing differing in their start position from the source (10m (black rectangles) or 20m (grey rectangles)). At 50 m and 90 m from the source the grey contours correspond to two 4-m-long wells with average screen elevation of 3 m and 7 m.

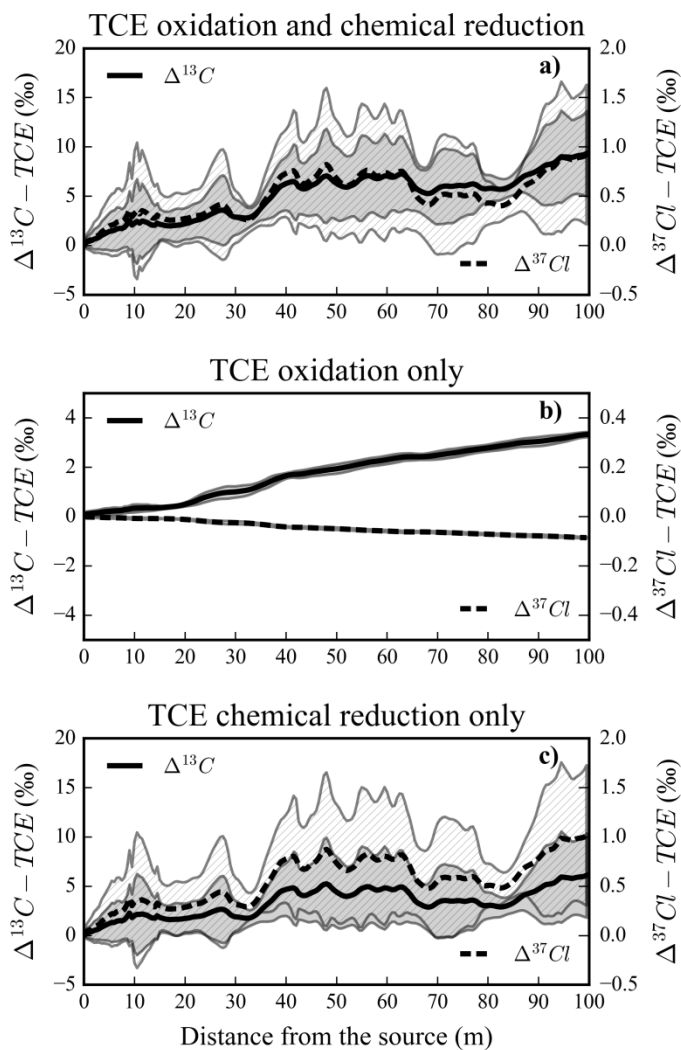


Fig. 5-4 : Means of the carbon (plain line) and chlorine (dashed line) isotope shifts with distance away from the source, for (a) combined TCE CR and OX, (b) TCE CR only, and (c) TCE OX only. The shaded areas represent the standard deviation at each distance of the carbon (light grey with hatches) and the chlorine isotope ratios (dark grey) depth profiles, respectively, illustrating the strong variations with depth.

Using the synthetic datasets, the true state of TCE degradation, D_{True} , is calculated at the point scale. D_{True} shows a pattern similar to the pattern of carbon and chlorine isotope ratios (Fig. 5-3c). In the conductive zones of the aquifer, D_{True} increases gradually with distance from the source, reaching up to 40 % degradation, while low-conductivity zones are hotspots of intense degradation with D_{True} varying from 60 % to 80 %.

The share of TCE degraded through oxidation versus reduction is estimated using the rate ratio, F , calculated using the isotope ratios $\delta^{13}\text{C}$ and $\delta^{37}\text{Cl}$ for each point of the model through eq. (5-10) to (5-12). The rate ratio F varies between 0 and 1, with 0 indicating that TCE degradation is entirely attributed to CR and 1 that TCE is entirely degraded through OX. At the source zone, the limited carbon isotope enrichment ($<0.5\text{‰}$) did not allow for calculating F . Despite zones of intense TCE oxidation, F reaches at most 0.73 in the simulated domain. F approaches 0 only in the upgradient zone of the aquifer where the aquifer is relatively impermeable and CR dominates. Downgradient, F bears the influence of the alternation of CR and OX across the aquifer and presents no extreme values as F varies approximately between 0.2 and 0.7. F as calculated from the isotope ratios poorly compares to the real local rate ratio $k_{OX} / (k_{OX} + k_{CR})$ which was set as input (Fig. 5-5b). F is therefore not an indicator of the local conditions of degradation but rather an integrator of the degradation processes acting on the pollutant from the source zone until the sampling location.

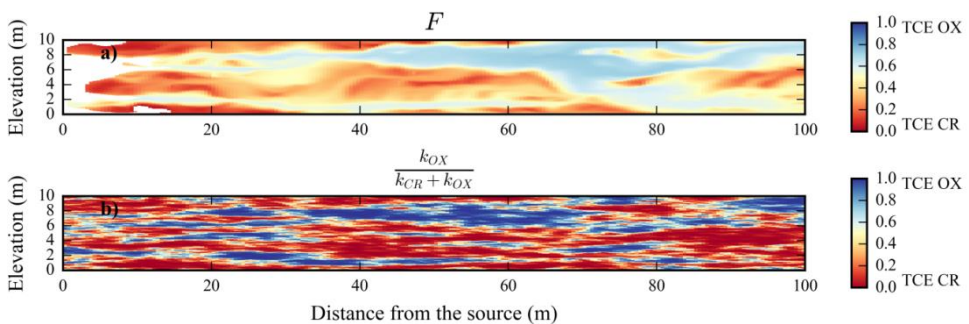


Fig. 5-5 : Cross sections showing (a) the calculated rate ratio F from the dual C-Cl CSIA data, and (b) the true local rate ratios following the k_{OX} and k_{CR} input values.

5.3.2 Sampling effect

Field investigation often relies on water samples obtained through pumping from (long) well screens. This approach might induce an overestimation of the importance of the degradation pathway (dominantly) occurring in the high-permeability zones as relatively more water is pumped from these zones compared to the low-permeability zones. Under the assumption that the obtained synthetic dataset is representative of realistic transport and

degradation behaviour of TCE, both the degradation extent and the contribution of each degradation pathway to TCE degradation were evaluated from synthetic sample CSIA data.

Dual C-Cl CSIA data plots are commonly used to determine degradation pathways likely to occur at field sites. The proportion of isotope enrichment of dual CSIA data is compared to compiled laboratory enrichment factors in order to identify which pathway(s) may be taking place. Dual C-Cl CSIA data are plotted for each of the 6 monitoring networks (each consisting of 5 wells placed at equal depth and with 20 meter spacing) differing in their start position from the source (10m or 20m) and well screen elevation (3m, 5m, or 7m) (Fig. 5-6). The slopes of $\delta^{37}\text{Cl}/\delta^{13}\text{C}$ linear regressions at each of the monitoring networks (+0.04 to +0.12) are always larger than the theoretical $\varepsilon_{\text{Cl}/\varepsilon\text{C}}$ slope of TCE OX (-0.03). A first result is that independently from the positioning of the monitoring network, the sampled C-Cl CSIA data are not only influenced by the process occurring in the high- but also by the process in the low-conductivity zones, and this despite the preferential flow through the high-conductivity zones. For practitioners, this implies that the presence of a degradation process occurring in low-conductivity zones might be revealed by a randomly set monitoring network.

A potential drawback for the assessment of degradation is that the small positive (inverse) chlorine isotope enrichment factor (+0.3 ‰) associated with TCE OX is overridden by the normal chlorine isotope enrichment factor (-2.5 ‰) induced by TCE CR (Fig. 5-6 and Fig. 5-4a). Each set of CSIA data displays strong chlorine isotope enrichment which could result in TCE OX going undetected. For instance, the slope of the network presented in Fig. 5-5d (+0.12±0.04) is not significantly different from the $\varepsilon_{\text{Cl}/\varepsilon\text{C}}$ slope for TCE chemical reduction (+0.16). The slopes values are in the range of recently published TCE $\varepsilon_{\text{Cl}/\varepsilon\text{C}}$ slopes during biotic reductive dechlorination (BRD) obtained after the microorganisms were precultivated on lesser chlorinated CEs in a laboratory experiment (range: ~0.05-0.11, published as $\varepsilon_{\text{Cl}/\varepsilon\text{C}}$ slopes of 9.0±1.1 to 18.2±4.3 (Lihl et al., 2019)). Those growth conditions and therefore the small slopes are not expected to be common at field site. However, when the observed slopes are lower than the previously published sets of $\varepsilon_{\text{Cl}/\varepsilon\text{C}}$ values both for TCE biotic and abiotic reductive degradation (Fig. 5-6), co-occurrence of oxidation and chemical reduction pathways may be suspected. The present simulation shows that the resulting $\varepsilon_{\text{Cl}/\varepsilon\text{C}}$ slope is in between the slopes of the reductive and the oxidative pathway. BRD as met so far at field sites has a much larger $\varepsilon_{\text{Cl}/\varepsilon\text{C}}$ slope than CR. A similar scenario with BRD in the low conductivity layers could produce $\delta^{37}\text{Cl}/\delta^{13}\text{C}$ slopes in the range of published $\varepsilon_{\text{Cl}/\varepsilon\text{C}}$ slopes of CR or the lower end of BRD. In that case, dual C-Cl CSIA would not be suitable for pathway distinction. The formation of the metabolites DCE and VC might inform that biotic degradation occurs unless they are consumed by oxidation. Additionally, this underlines that the $\varepsilon_{\text{Cl}/\varepsilon\text{C}}$ slopes of the degradation pathways must be sufficiently different to be able to use C-Cl CSIA data for pathway distinction as pointed out in Van Breukelen (2007).

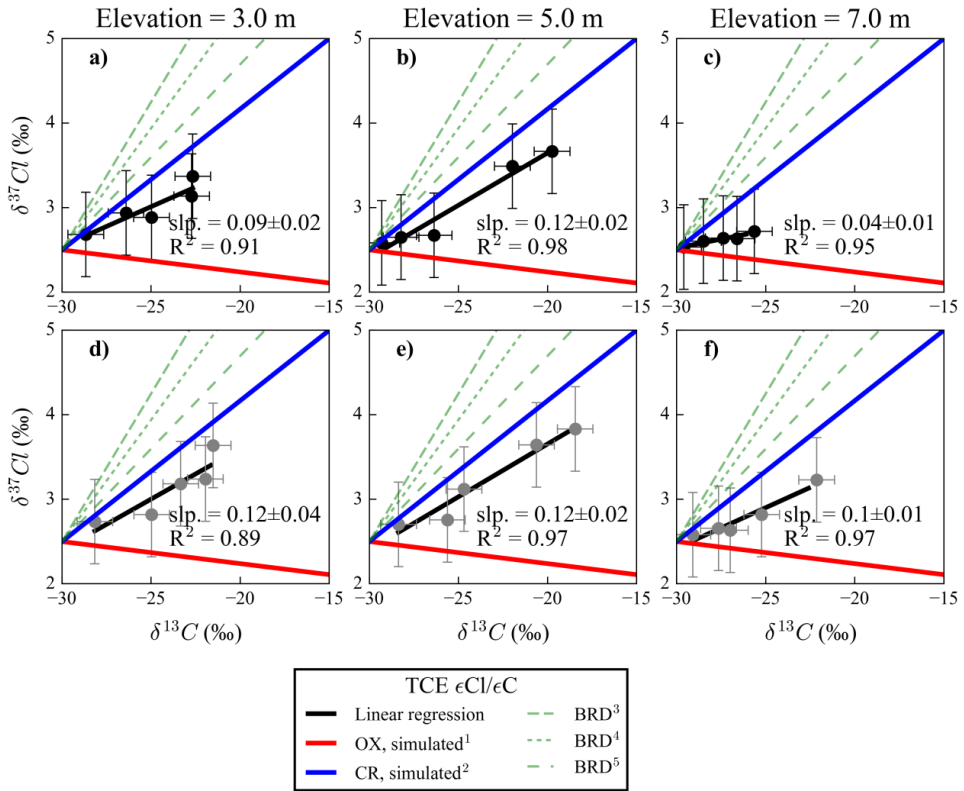


Fig. 5-6 : Dual element isotope plot ($\delta^{37}\text{Cl}_{(\text{sample})}$ vs. $\delta^{13}\text{C}_{(\text{sample})}$) representing simulated well data at steady-state for the 6 virtual monitoring networks consisting of 5 wells each, with the corresponding calculated linear regression (thick black line, slopes of the linear regression (slp.) indicated in the plot). Slopes of the colored lines correspond to selected sets of $\epsilon\text{Cl}/\epsilon\text{C}$ for biotic reductive dechlorination in the literature (thin green lines) and to the input parameters (thick red line: ⁽¹⁾TCE OX, -0.03 (Gafni et al., 2018); thick blue line: ⁽²⁾TCE CR, +0.16 (Audi-Miró et al., 2013)). Relative $\epsilon\text{Cl}/\epsilon\text{C}$ for TCE biotic reductive dechlorination (BRD) ⁽³⁾ *Dehalococcoides*: +0.21 (Kuder et al., 2013), ⁽⁴⁾ *Geobacter lovely* strain SZ: 0.3 (Cretnik et al., 2014), ⁽⁵⁾ mixed bacterial culture : +0.37 (Wiegert et al., 2013). The error bars on the well samples correspond to realistic uncertainties for field data: ± 0.5 ‰ for carbon and ± 1 ‰ for chlorine.

In order to illustrate the potential of dual CSIA data to inform on the importance of the two pathways occurring at the field site, the calculated rate ratio, F , as obtained from simulated flow-rate-weighted well data, $F_{(\text{sample})}$, is compared to the average of F in the pore water along the well screen, $F_{(\text{core})}$. The values are compared at two selected distances, 50 and 90 m, and for two well screen sizes, 1 m and 4 m (Fig. 5-7c, 7d). When sampling through long well screens, the importance of TCE oxidation in the aquifer was overestimated as result of sampling ($F_{(\text{sample})} > F_{(\text{core})}$) as groundwater is preferentially abstracted from the more permeable layers. Overestimation was the most at the lower plume fringe in zones of low-

conductivity (bottom long wells, Fig. 5-3), and was the least at the top wells screens, which are set in the core of the TCE plume and in high-conductivity zones (top long wells, Fig. 5-3) (Fig. 5-7c, 5-7d). Despite the overestimation, the $F_{(sample)}$ values (< 1) always indicate some co-occurrence of TCE CR (Fig. 5-5, 5-7c, 5-7d). For short wells, $F_{(sample)}$ matches well with $F_{(core)}$. Interestingly, some limited underestimation ($F_{(sample)} < F_{(core)}$) can be noticed for the top short well screen at 90 m from the source (Fig. 5-7d), likely due to TCE back diffusing from a low-conductivity zone a few meters upgradient from the screen (Fig. 5-3). In this modelling study, the virtual samples correspond to optimal sampling conditions. Under real conditions, insufficient pumping rates or durations might lead to the abstracted water to originate even more from the high-conductivity zones (McMillan et al., 2014), in which case overestimation of the importance of degradation processes associated with high-conductivity zones when sampling across low-conductivity zones is likely the rule.

The CSIA-based extent of degradation at point scale in the aquifer, $D_{Rayleigh}$, is calculated from applying eq. (5-9) to (5-12) to the local $\delta^{13}C$ and $\delta^{37}Cl$ values. When plotting $D_{Rayleigh}$ against depth, the $D_{Rayleigh}$ curves slightly underestimate D_{True} (Fig. 5-7e, 7f). The underestimation is a result of dispersion which fades the isotope ratio gradients resulting from degradation (Abe and Hunkeler, 2006; van Breukelen and Prommer, 2008). For the presented cross-sections, the underestimation of D_{True} is in the range of the previously estimated underestimations at field sites and of less than 5 % (Abe and Hunkeler, 2006). The limited difference between $D_{Rayleigh}$ and D_{True} suggests that flow segregation as described in (Kopinke et al., 2005) had little impact on the results as flow segregation limits the applicability of CSIA for degradation estimation. A similar simulation with larger reactive zones or rate constants is likely to exemplify flow segregation in which case CSIA-based degradation estimates would underestimate degradation (Kopinke et al., 2005).

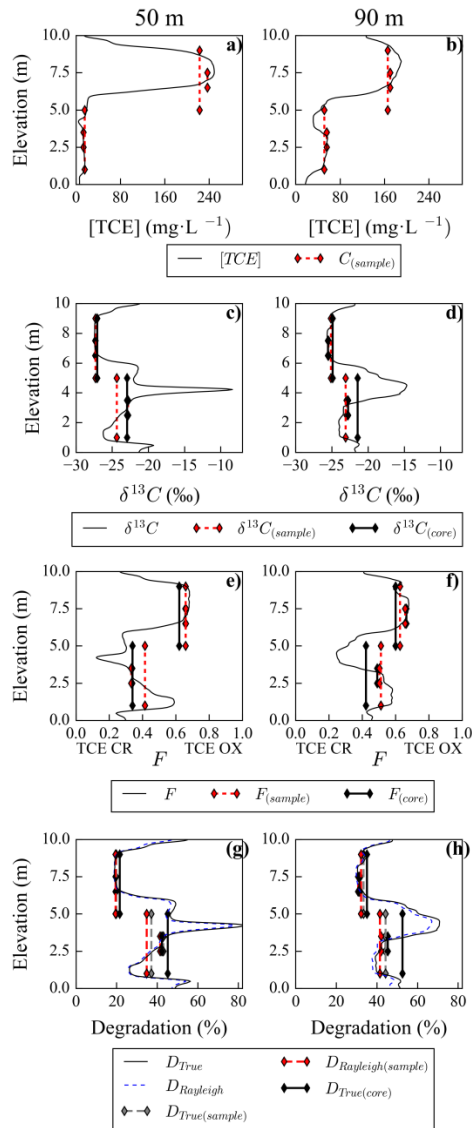


Fig. 5-7 : (a,b) TCE concentration; (c,d) TCE carbon isotope ratio; (e,f) CSIA-based rate ratio F , and (g,h) TCE extent of degradation: true (D_{True}) and CSIA-based ($D_{Rayleigh}$). For all plots, the value/parameter is given across depth at the point scale (thin black lines, blue dashed line for $D_{Rayleigh}$) and for flow-rate-weighted groundwater samples (dashed red vertical lines). Average pore water values along well screens are represented with thick black vertical lines for (e,f) F ($F_{(core)}$) and (g, h) D_{True} ($D_{True(core)}$). Values from flow-rate-weighted groundwater samples are represented with dashed red vertical lines for (a, b) TCE concentration, (c,d) F , and (e,f) $D_{Rayleigh}$. The true extent of degradation at the groundwater sample level $D_{True(sample)}$ is indicated by grey vertical lines in panels e and f. Results are shown at 50 m (left panel) and 90 m (right panel) downgradient from the source. At both locations, the shallow wells have been placed in more permeable zones than the deep wells. The positions of the shallow and deep wells are shown

in Fig. 5-3.

The overestimation of the occurrence of TCE OX in the sample illustrated by $F_{(sample)} > F_{(core)}$ (Fig. 5-7e, 7h) suggested that the εC_{app} calculated for the groundwater sample $\varepsilon C_{app(sample)}$ would be biased towards εC_{OX} . As $|\varepsilon C_{OX}| < |\varepsilon C_{RD}|$, $\varepsilon C_{app(sample)}$ is expected smaller in absolute value than εC_{app} calculated from the average pore water isotope values ($\varepsilon C_{app(core)}$). Such underestimation of $|\varepsilon C_{app}|$ would overestimate degradation extent ($D_{Rayleigh(sample)} > D_{True(core)}$), of which the opposite is observed as also the difference in isotope enrichment between the groundwater sample and the pore water needs to be taken into account. With the example of the deepest long well at 90 m from the source, which shows the most contrast between the sample and the core degradation values (Fig. 5-7h), the sampled isotope values ($\delta^{13}C_{(sample)} = -23.1 \text{ ‰}$ (Fig. 5-7c), $\delta^{37}Cl_{(sample)} = 3.1 \text{ ‰}$) yield a $\varepsilon C_{app(sample)}$ of -13.3 ‰ . In comparison, the apparent enrichment value for pore water is indeed slightly larger, with $\varepsilon C_{app(core)} = -13.6 \text{ ‰}$. However, the carbon isotope ratio in the sample (-23.1 ‰) is notably less enriched than in the core ($\delta^{13}C_{(core)} = -21.4 \text{ ‰}$). When applying the smaller $\varepsilon C_{app(sample)}$ to the less enriched $\delta^{13}C_{(sample)}$, the resulting $D_{Rayleigh(sample)}$ is underestimating degradation as occurred in the pore water ($D_{(core)} = 52 \%$, $D_{Rayleigh(sample)} = 41 \%$). The underestimation reflects the lesser degradation in the highly conductive zones (degradation of 30 % to 40 %) compared to the lesser conductive zones (up to 70 %) as shown by the depth profiles at 80 m from the source (Fig. 5-7h, the conductivity field is given in Fig. 5-3a). If degradation would be more intense in the highly conductive zones compared to the lesser conductive zones, pore scale degradation would be overestimated. Finally, the slight underestimation of $D_{True(sample)}$ by $D_{Rayleigh(sample)}$ is of 3 %, in the range of the underestimation seen for the depth profiles D_{True} and $D_{Rayleigh}$. The underestimation is likely due to dispersion. As shown by the smaller difference between $D_{Rayleigh(sample)}$ and $D_{True(core)}$ for smaller well screens or for the top long well (Fig. 5-7h), the ability to describe degradation in the aquifer depends strongly on the sample method and the lithology crossed by the well screen.

5.4 Conclusion and implications

This simulation study illustrates that CEs reductive degradation in low-permeability zones might be detected using dual carbon (C) and chlorine (Cl) CSIA, also when TCE oxidation occurs in highly conductive zones. Simulated degradation extent and isotope enrichments were heterogeneous, with the lesser conductive zone forming pockets of more intense degradation compared to the more conductive zones. When sampling sites presenting heterogeneous lithology, large variations of C CSIA values across depth and non-linear increase with distance could indicate that degradation is favourable in the less permeable layers. The $\delta^{37}Cl/\delta^{13}C$ slopes of the various virtual monitoring networks were intermediate between the published sets of $\varepsilon Cl/\varepsilon C$ slopes for TCE chemical reductive dechlorination and TCE oxidation. When the $\varepsilon Cl/\varepsilon C$ slopes of the pathways occurring at the site are known and sufficiently different, the contrast with the sampled data could point towards the presence

of two degradation pathways that are simultaneously occurring. Unfortunately, the combination of TCE biotic degradation and TCE aerobic oxidation could instead yield $\delta^{37}Cl/\delta^{13}C$ slopes matching previously published $\varepsilon Cl/\varepsilon C$ slopes. Additionally, the effect of sampling bias should not be neglected. The preferential abstraction from the more conductive layers led to the overestimation of TCE oxidation to overall TCE degradation in the aquifer. Despite this wrong attribution of degradation, dual CSIA from the sampled data provides a good estimate of the degradation state of the sampled TCE provided εC and εCl of both occurring pathways are known. Limiting sampling across layers of difference conductivities is critical to obtain a good estimate of degradation at the pore scale. Degradation might otherwise be over- or under-estimated, depending on whether the conductive layers are more or less reactive than the lesser conductive zones. In practice, the bias induced either by the sampling method or by a limited amount of CSIA data should be taken into account when designing sampling campaigns or interpreting data in view of determining to which extent various degradation pathways are taking place.

This page was intentionally left blank

Supporting information to chapter 5

S5.1 Calculation of initial carbon and chlorine isotopologue concentrations.

Isotope compositions are usually reported as isotope ratios relatively to an international standard isotope ratio R_0 (for carbon: the Vienna Pee Dee Belemnite; for chlorine : the

Standard Mean Ocean Chloride), with the simplified delta notation $\delta E = \frac{R_{H/L}}{R_0} - 1$,

where $R_{H/L}$ is the ratio of the concentration of heavy to light isotopes. The respective carbon and chlorine isotope concentrations were set to obtain a source TCE isotope ratio $\delta^{13}\text{C-TCE}_{\text{Source}}$ of -30.00 ‰ and $\delta^{37}\text{Cl-TCE}_{\text{Source}}$ of + 2.50 ‰, in the range of industrially produced TCE (Shoukar-Stash et al., 2003). Initial concentrations of the TCE isotopologues were calculated following the probability mass function as described by (Hunkeler et al., 2009) and presented Table S5-1.

Table S5-1 : Calculation of the carbon and chlorine bulk isotope concentrations of initial TCE^a

Isotope	N1	Probability	Probability	Concentration (mM)
¹² C	L	P _L	0.989217	4.352557
¹³ C	H	P _H	1- P _L	0.004744
³⁵ Cl	L	P _L	0.758169	3.331906
³⁷ Cl	H	P _H	1- P _L	1.068093

^a[TCE] ≈ 600 mg.L, $\delta^{13}\text{C-TCE}_{\text{Source}} = -30.00$ ‰, $\delta^{37}\text{Cl-TCE}_{\text{Source}} = 2.5$ ‰

S5.2 Correction factor for degradation rates.

The correction factor is further described in (van Breukelen et al., 2017). The two independent isotope networks were aligned with the overall reaction progress with the following simple correction term applied to each isotope/isotopologue reaction rate:

$$\times \frac{1}{(A_H \times \alpha + A_L)}$$

where A_H and A_L are the abundances of the heavy and light isotope, respectively, and α is the bulk isotope fractionation factor.

S5.3 List of abbreviations and symbols

Table S5-2: Compilation of abbreviations and symbols used in the main article and the Appendix.

CEs	Chlorinated ethenes
TCE	Trichloroethylene
CR	Chemical reduction
OX	Oxidation
BRD	Biotic reductive dechlorination
MNA	Monitored natural attenuation
α_k	Kinetic isotope fractionation factor
r	Overall TCE degradation rate
$^h r$ and $^l r$	Degradation rate constants of the heavy and the light isotope specie
k	First-order degradation rate constant
$^h k_{bulk}$ and $^l k_{bulk}$	Bulk degradation rate constants associated with the heavy and the light isotope, respectively
C_i	Compounds concentration in a grid cell i
K_i	Hydraulic conductivity of a grid cell i
C_{sample}	Concentration in a virtual sample
δ_i	Heavy to light isotope ratio of the element E in a cell i
δ_{sample}	Heavy to light isotope ratio of the element E in the sample
R_0	Ratios of the heavy to light isotope concentrations of an element E in the international standard
R_{sample}	Ratios of the heavy to light isotope concentrations of an element E in a sample
εC	Carbon isotope enrichment factor
εCl	Chlorine isotope enrichment factor
K	Hydraulic conductivity
n	Porosity
D_w	Aqueous diffusion coefficient
D_{eff}	Effective diffusion coefficient
k_{OX}	First-order rate constant of TCE oxidation
k_{CR}	First-order rate constant of TCE chemical reduction
εC_{OX}	Bulk TCE carbon isotope enrichment factor of TCE oxidation
εCl_{OX}	Bulk TCE chlorine isotope enrichment factor of TCE oxidation
εC_{CR}	Bulk TCE carbon isotope enrichment factor of TCE chemical reduction
εCl_{CR}	Bulk TCE chlorine isotope enrichment factor of TCE chemical reduction
F	Rate ratio
$F_{(sample)}$	Rate ratio in a sample
εC_{app}	Apparent carbon isotope enrichment factor at the point scale
$\varepsilon C_{app(core)}$	Apparent carbon isotope enrichment factor calculated for the pore water along the well screen
$\varepsilon C_{app(sample)}$	Apparent carbon isotope enrichment factor in a virtual sample
D_{True}	True extent of degradation
$D_{True(core)}$	True extent of degradation calculated for the pore water along the well screen
$D_{True(sample)}$	True extent of degradation in a virtual sample
$D_{Rayleigh(sample)}$	CSIA-based estimate of degradation in a virtual sample

This page was intentionally left blank

Chapter 6

Synthesis

6.1 Summary

Well-characterized aquifers are rare, and aquifers are often considered as ‘black boxes’ in which the degradation and transport patterns of chlorinated ethenes (CEs) must be determined through spatially and temporally sparse datasets. **Chapter 2** and **Chapter 3** illustrate the benefits of multiple-element (carbon (C), chlorine (Cl), and hydrogen (H)) compound specific stable isotope analysis (CSIA) data for the improvement of the conceptual site models (CSM) on sources and sinks of chlorinated ethenes (CEs). The presence of multiple sources, heterogeneous lithology, and multiple pathways, as found at the study site of interest (Hill Air Force Base, Utah) are shown to be challenging for CSIA data interpretation. To our knowledge, this data represents the first large TCE H CSIA field data set. Based on the site observations, **Chapter 2** illustrates the potential of multiple-element CSIA data of CEs in such complex conditions for source characterization, for pinpointing the relevant degradation pathways, and for detecting physical attenuation processes. Following up on Chapter 2, **Chapter 3** illustrates how C-Cl CSIA batch modeling can be used to further enhance the investigation of degradation pathways and their spatial extent at the study site. The CSIA-based field study developed in Chapters 2 and 3 connected unusual CSIA patterns to the physical and chemical heterogeneity of the aquifer. In order to further understand the field observations, **Chapters 4-5** utilize model simulations of hypothetical but field site inspired situations (i.e., virtual experiments) to verify whether CSIA-based degradation assessment would be possible when degradation occurs in low permeability sediments. **Chapter 4** focuses on the potential of CSIA data collected from an aquifer to evaluate the presence and extent of TCE degradation in an underlying reactive aquitard. In **Chapter 5** a simulation of intra-aquifer physical-chemical heterogeneity is presented in order to assess the performance of dual C-Cl CSIA in determining reaction pathways and the extent of degradation in the case of two competing processes (oxidative transformation dominating in permeable parts and abiotic reduction dominating in less permeable parts of the aquifer). In both Chapters 4-5, the input parameters of the reactive transport models were based on an extensive literature review to make the simulations as realistic as possible. Simulations were carried out using the freely available software PHT3D (Prommer et al., 2001), which combines the 3-D multicomponent transport model MT3DMS with the geochemical model PHREEQC-2 (Parkhurst and Appelo, 1999). PHT3D was accessed through the python interface FloPy

(Bakker et al., 2016). To our knowledge, this paper is the first publication of a reactive transport model obtained with FloPy.

Chapter 2 improves the prior CSM of the investigated research site presenting both a shallow and a deep plume through the thorough interpretation of the large C-Cl-H CSIA data set, illustrating several applications of CSIA for process determination. Source characterization was crucially improved using H CSIA for both trichloroethene (TCE) and ethene. Dual Cl/C isotope trends were employed to detect (further) cis-dichloroethene (cis-DCE) degradation. The connection between both carbon (C) and chlorine (Cl) isotope enrichment of cis-DCE and the carbon isotope mass balance (CIMB) enrichment suggested that cis-DCE degradation through oxidation or reductive dechlorination with subsequent rapid VC mineralisation was a necessary step toward CEs mineralization. CSIA also supported the hypotheses in a previously developed CSM concerning the locations of degradation hotspots for TCE. From the cis-DCE and trans-DCE C and Cl CSIA data, it also appeared that TCE possibly degraded through two different reductive dechlorination (RD) pathways which resulted in different trans-DCE/cis-DCE concentration ratios. The lack of C isotope ratio enrichment for TCE where TCE cometabolism was expected ruled out the strongly fractionating TCE aerobic cometabolism with toluene as an important degradation pathway, but not cometabolism by methane monooxygenase, which yields limited isotope changes. Chapter 2 also demonstrates that field applications using multiple-element CSIA are not restrained to source apportionment and degradation assessment, but may also enable the detection of physical attenuating processes. Although physical processes have a limited impact on carbon isotope ratios, their impact on chlorine isotope ratios and on the CIMB were shown to be substantial. Strong chlorine isotope enrichment relative to carbon isotope enrichment in the shallow plume was attributed to diffusion of CEs to an underlying aquitard. The unusual CIMB depletion pattern observed upgradient the deep plume was assumed to be linked to differential sorption of the CEs during back-diffusion. This latter hypothesis inspired the modeling experiment described in Chapter 4.

To underpin the conclusions of Chapter 2 and further explore the identified degradation pathways, C and Cl CSIA field data were simulated with a batch model in **Chapter 3**. Spatial modeling was challenged by the spatial heterogeneity of the degradation rate constants reflecting the heterogeneous lithology, which impeded the application of reactive transport models at this site. Chapter 3 presents the first application of batch modeling to the study of combined CEs reductive dechlorination and oxidation, and multiple-element CSIA data. Using the batch model fed with both field-derived and literature-based enrichment factors, it was possible to validate that the observed ranges of isotope ratios and molar fractions of TCE and of both DCE isomers corresponded to the occurrence of two different TCE degradation pathways at the site differing in their relative tDCE/cDCE ratios and TCE isotope enrichment factors. Modeling also offered further insights, as enriched $\delta^{13}\text{C}$ of trans- and cis-DCE observations compared to the simulated DCEs isotope ratios as

reference values (in the absence of further degradation) were an indicator of further degradation of DCE. Batch modeling also allowed determining that the cis-DCE degradation pathway leading to strong $\delta^{13}\text{C}$ -cDCE fractionation was likely RD as it seemed simultaneous to TCE RD. Low-fractionating pathways were also simulated using batch modeling, as aerobic cometabolism of TCE and cis-DCE on methane were also suspected at the site. Provided TCE aerobic cometabolism was faster than of cis-DCE, such a pathway might also explain the decrease of the CIMB in the deep aquifer. However, the comparison between the simulations of CEs oxidation and the field data illustrated that a single oxidative degradation pathway could not yield the diversity of molar fractions and isotope ratio patterns for TCE and cis-DCE upgradient in the deep aquifer. CSIA patterns attributed to physical processes (declined CIMB and strong Cl isotope fractionation relatively to C) were unprecedented and complicated the interpretation of the site data; however, the assessment of degradative processes remained possible.

The simulation described in **Chapter 4** illustrates the potential of aquifer CSIA data to detect and quantify naturally occurring reductive dechlorination of CEs in an aquifer-aquitard-aquifer system. The model simulates a TCE DNAPL diffusing in and out an underlying reactive aquitard (sorption and sequential RD to ethene) and the resulting TCE pollution plume. As a thought experiment, it was expected that such a setting would lead to depleted CIMB in the aquifer as observed in Chapters 2 and 3 at the Hill Air Force Base, provided the depleted daughter products would diffuse faster out of the reactive aquitard to the aquifer than the enriched source compound. The main conclusions to be drawn from the simulation in Chapter 4 were that (i) before source removal, large $\delta^{13}\text{C}$ -TCE enrichment corresponds to degradation in the aquifer as opposed to degradation only in the aquitard or to diffusion to the aquitard; (ii) CIMB increases during back-diffusion in the upper aquifer as a result of the relatively limited back-diffusion of depleted daughter products being present deeper in the aquitard; (iii) characteristic CSIA patterns during the loading and release phases (large CIMB enrichment, strong increase of all CEs isotope ratios after source removal, elevated isotope ratios across the aquifer after source removal) contrast strongly with those associated with reductive dechlorination occurring in the aquifer (limited to no CIMB enrichment, limited changes in isotope patterns after source removal, increasing isotope ratio with distance from the source); (iv) those characteristic patterns are recognizable in most of the simulations of the sensitivity analysis; (v) Rayleigh-based degradation quantification reaches reasonable levels of underestimation (< factor 1.25) shortly after the DNAPL removal is complete; and (vi) both sorption- and diffusion-induced isotope fractionations have limited impact on TCE degradation assessment.

Despite the discrepancy between the field site observations in Chapter 2 and 3 (CIMB decrease in aquifer) and the explorative model results of Chapter 4 (CIMB increase in aquifer), the simulation allows verification that an aquitard can affect the CIMB in the adjacent aquifer. The results of the simulation and its sensitivity analysis illustrate that the

processes governing the CIMB decrease at the Hill Site are not yet understood at this stage. While the disagreement might result from the simplifications employed to simulate the aquitard-aquifer system, the results from Chapter 4 do not provide directions for a new simulation which should be able to yield depleted CIMB. The cause of the depleted CIMB is therefore yet unclear.

Chapter 5 focuses on the model-based assessment of the performance of dual carbon and chlorine CSIA in degradation pathway identification and quantification in a coupled physical-chemical heterogeneous hypothetical aquifer. In contrast with Chapter 4, which presented an aquifer-aquitard-aquifer system, the simulation in Chapter 5 is based on a single aquifer with heterogeneous hydraulic conductivity. Degradation rate constants were assumed to be correlated with the hydraulic conductivity: positively for oxidative transformation (higher oxygen availability in coarser sands) and negatively for chemical reduction (higher content of reducing minerals in finer sediments). The simulation results illustrate that large variations of C CSIA values across depth and the non-linear increase with distance could indicate that degradation is favourable in the less permeable layers. Chapter 5 offers further insights for monitoring degradation in low-permeability zones, as the $\delta^{37}\text{Cl}/\delta^{13}\text{C}$ slopes of the data obtained through various virtual monitoring networks fell between the published sets of $\varepsilon\text{Cl}/\varepsilon\text{C}$ slopes for TCE chemical reductive dechlorination and TCE oxidation. The interpretation of the $\delta^{37}\text{Cl}/\delta^{13}\text{C}$ slopes and the subsequent degradation quantification is promising but could be complicated if the slope matches previously published $\varepsilon\text{Cl}/\varepsilon\text{C}$ slopes of other degradation pathways than present at the site or if the εC and εCl of both occurring pathways are not known.

Chapter 5 illustrates that the presence of hot spots of degradation in the low-permeability sediments in an aquifer would lead to heterogeneous enrichment of C CSIA in the aquifer. In Chapter 2, degradation at hot spots was suspected based on pointwise large C CSIA enrichment, large variations in isotope enrichment with depth, and C CSIA decrease with distance in the deep plume. Possibly, the observed decrease with distance of C CSIA in Chapter 2 instead of an increase as in the simulation of Chapter 5 could result from the presence of large non-reactive sand beds downgradient in the deep plume.

6.2 Implications and outlook

6.2.1 Refining conceptual site models with CSIA data and modelling

The data grouping operated in **Chapter 3** was an evident but crucial step to extract isotope enrichment factors and dual C-Cl CSIA slopes from the CSIA field data due to multiple pathways impacting the CEs. At sites where CSIA is employed to refine a CSM, the sampling strategy should ensure that each group would include a sufficient number of samples to characterize a process of interest. The sampling strategy therefore needs to be adapted to the CSIA study. Several advices for optimizations of well screens position and length based on the simulated experiments are presented in Chapters 4-5. In this thesis, concentration of CEs and carbon isotope ratios were the selected criteria for dividing the initial data set in groups of wells with similar characteristics. When applied to other sites, other measurements could constrain data grouping, such as aquifer chemical and physical parameters co-pollutants, proximity in the aquifer, lithology, or bacterial activity.

The observation of a 2:1 Cl/C isotope slope in the Hill Site data was ascribed to diffusion to the aquitard in **Chapter 2**. Chlorine isotope fractionation resulting from the diffusive process was strong in comparison to both the uncertainty on the data and to fractionation relative to degradation at the site, implying that (1) a degradation survey uniquely based on chlorine isotope enrichment, although not common, is discouraged in the vicinity of an aquitard; (2) the combination of both physical and degradation attenuation processes might increase the uncertainty of C-Cl CSIA slopes. This second point is specifically relevant for degradation pathway determination of CEs. The decrease of experimental CSIA measurement uncertainty (about 1‰ in this study for Cl) could help separating the different processes influencing chlorine isotope fractionation, as well as best practice for slope determination and comparison as presented with the York fitting approach applied in Chapter 2 and in (Ojeda et al., 2019).

In practice, CSIA is increasingly used at sites where the complexity of transport, degradation, or plume mixing challenges the interpretation of concentration data. The present work has several implications for practitioners who wish to increase their understanding of pollutant sources and sinks at sites with heterogeneous lithology. In the different chapters, CSIA-based degradation assessment was shown possible despite of the impact of the heterogeneous lithology on both CEs concentrations and isotope ratios. The main difficulty resides in identification of the relevant degradation pathways and associated enrichment factors. In Chapters 2 and 3, this determining step was supported by multiple element isotope analysis and batch modeling. Such approach can also be helpful for selecting the most reliable data for the calibration of a spatially explicit model, with or

without including isotope fractionation. Batch models have consequently a place in the practitioner's toolbox as they present a limited extra cost compared to more extensive 3D simulations.

Chapters 2, 3, and 4 warn for a potential misinterpretation when employing the CIMB to detect mineralization of CEs in the vicinity of a reactive aquitard. Previous studies based the detection of mineralization of CEs by CIMB enrichment: this study calls for caution for such practice in the vicinity of aquitards, with for instance the use of dual C-Cl CSIA in order to investigate the presence of additional degradation pathways as in Chapter 2. CIMB decrease as observed in Chapters 2 and 3 also limits the possibility to calculate the extent of degradation of CEs based on CIMB value as done in (Aeppli et al., 2010).

Despite the detailed dataset available for H CSIA data of TCE, cis-DCE and trans-DCE, the limited knowledge of the fractionating processes of H CSIA in the subsurface hindered data interpretation. Further studies of those processes are therefore necessary to ensure that field H CSIA data remains a useful tool for source assessment and pathway determination at field sites.

6.2.2 Exploring subsurface heterogeneity

The potential for assessing the extent of degradation in Chapters 4 and 5 was optimal as they were calculated using the simulated enrichment factors. The selection of an enrichment factor is therefore crucial. For that purpose, further work, including experimental work is necessary to improve our knowledge of isotope enrichment factors associated with relevant degradation pathways. Especially for the study of degradation in low permeability sediments, studies should address the potential of chlorine and hydrogen isotope fractionation in identifying aquitard degradation and distinguishing between biotic and abiotic degradation that might co-occur in reductive conditions.

The scenario simulations aimed to study realistic conditions without encompassing all possible aspects that may affect pollutant fate. Nonetheless, they succeed in designating influential parameters. Both Chapters 4 and 5 demonstrate that the distribution of degradation in the low permeability zones or layers crucially modifies CSIA patterns when sampling in permeable zones. Further experimental research into both biological and chemical aquitard reactivity at the interface between low- and high-permeability zones, as well as further characterization of degradation profiles within aquitards allows better understanding of CSIA patterns in the aquifer.

The sensitivity of CSIA data to the presence of multiple sources, the occurrence of multiple degradation pathways, and to some physical effects demonstrates the potential of CSIA to complement the interpretation of concentration data at field sites. This sensitivity also stresses the need for tools to interpret CSIA data themselves as complexity arises from the

simultaneous impact of several CSIA-modifying factors. This thesis demonstrates the applicability of CSIA data for degradation and source assessment also in complex settings and illustrates the use of various methods from data interpretation to virtual experiments to improve our understanding of CSIA data and the process information they contain.

This page was intentionally left blank

References

- Abe, Y., Aravena, R., Zopfi, J., Parker, B., Hunkeler, D., 2009a. Evaluating the fate of chlorinated ethenes in streambed sediments by combining stable isotope, geochemical and microbial methods. *J. Contam. Hydrol.* 107, 10–21. doi:10.1016/j.jconhyd.2009.03.002
- Abe, Y., Aravena, R., Zopfi, J., Shouakar-Stash, O., Cox, E., Roberts, J.D., Hunkeler, D., 2009b. Carbon and chlorine isotope fractionation during aerobic oxidation and reductive dechlorination of vinyl chloride and cis-1, 2-dichloroethene. *Environ. Sci. Technol.* 43, 101–107. doi:10.1021/es801759k
- Abe, Y., Hunkeler, D., 2006. Does the Rayleigh equation apply to evaluate field isotope data in contaminant hydrogeology? *Environ. Sci. Technol.* 40, 1588–1596. doi:10.1021/es051128p
- Adamson, D.T., Chapman, S.W., Farhat, S.K., Parker, B.L., DeBlanc, P., Newell, C.J., 2015. Characterization and source history modeling using low-k zone profiles at two source areas. *Groundw. Monit. Remediat.* 35, 52–69. doi:10.1111/gwmr.12090
- Adamson, D.T., de Blanc, P.C., Farhat, S.K., Newell, C.J., 2016. Implications of matrix diffusion on 1,4-dioxane persistence at contaminated groundwater sites. *Sci. Total Environ.* 562, 98–107. doi:10.1016/j.scitotenv.2016.03.211
- Adrian, L., Löffler, F.E., 2016. *Organohalide-respiring bacteria*. Springer-Verlag Berlin Heidelberg, Berlin. doi:10.1007/978-3-662-49875-0
- Aeppli, C., Hofstetter, T.B., Amaral, H.I.F., Kipfer, R., Schwarzenbach, R.P., Berg, M., 2010. Quantifying in situ transformation rates of chlorinated ethenes by combining compound-specific stable isotope analysis, groundwater dating, and carbon isotope mass balances. *Environ. Sci. Technol.* 44, 3705–3711. doi:10.1021/es903895b
- Allen-King, R.M., Groenevelt, H., Warren, C.J., Mackay, D.M., 1996. Non-linear chlorinated-solvent sorption in four aquitards. *J. Contam. Hydrol.* 22, 203–221. doi:10.1016/0169-7722(95)00089-5
- Alvarez-Cohen, L., Speitel, G.E., 2001. Kinetics of aerobic cometabolism of chlorinated solvents. *Biodegradation*. doi:10.1023/A:1012075322466
- Amaral, H.I.F., Aeppli, C., Kipfer, R., Berg, M., 2011. Assessing the transformation of chlorinated ethenes in aquifers with limited potential for natural attenuation: Added values of compound-specific carbon isotope analysis and groundwater dating. *Chemosphere* 85, 774–781. doi:10.1016/j.chemosphere.2011.06.063
- Atchley, A.L., Navarre-Sitchler, A.K., Maxwell, R.M., 2014. The effects of physical and geochemical heterogeneities on hydro-geochemical transport and effective reaction rates. *J. Contam. Hydrol.* 165, 53–64. doi:10.1016/j.jconhyd.2014.07.008
- ATSDR, 2016. Substance priority list (SPL) resource page [WWW Document]. URL <https://www.atsdr.cdc.gov/spl/resources/index.html> (accessed 1.4.17).

- Atteia, O., Franceschi, M., Dupuy, a., 2008. Validation of reactive model assumptions with isotope data: Application to the dover case. *Environ. Sci. Technol.* 42, 3289–3295. doi:10.1021/es071269m
- Audí-Miró, C., Cretnik, S., Otero, N., Palau, J., Shouakar-Stash, O., Soler, A., Elsner, M., 2013. Cl and C isotope analysis to assess the effectiveness of chlorinated ethene degradation by zero-valent iron: Evidence from dual element and product isotope values. *Appl. Geochemistry* 32, 175–183. doi:10.1016/j.apgeochem.2012.08.025
- Audí-Miró, C., Cretnik, S., Torrentó, C., Rosell, M., Shouakar-Stash, O., Otero, N., Palau, J., Elsner, M., Soler, A., 2015. C, Cl and H compound-specific isotope analysis to assess natural versus Fe(0) barrier-induced degradation of chlorinated ethenes at a contaminated site. *J. Hazard. Mater.* 299, 747–754. doi:10.1016/j.jhazmat.2015.06.052
- Badin, A., Braun, F., Halloran, L.J.S., Maillard, J., Hunkeler, D., 2018. Modelling of C/Cl isotopic behaviour during chloroethene biotic reductive dechlorination: limitations of simplified and comprehensive models. (Under Rev. 1–16. doi:10.1371/journal.pone.0202416
- Badin, A., Broholm, M.M., Jacobsen, C.S., Palau, J., Dennis, P., Hunkeler, D., 2016. Identification of abiotic and biotic reductive dechlorination in a chlorinated ethene plume after thermal source remediation by means of isotopic and molecular biology tools. *J. Contam. Hydrol.* 192, 1–19. doi:10.1016/j.jconhyd.2016.05.003
- Badin, A., Buttet, G., Maillard, J., Holliger, C., Hunkeler, D., 2014. Multiple dual C-Cl isotope patterns associated with reductive dechlorination of tetrachloroethene. *Environ. Sci. Technol.* 48, 9179–9186. doi:10.1021/es500822d
- Bakker, M., Post, V., Langevin, C.D., Hughes, J.D., White, J.T., Starn, J.J., Fienen, M.N., 2016. Scripting MODFLOW model development using python and FloPy. *Groundwater* 54, 733–739. doi:10.1111/gwat.12413
- Barth, J.A.C., Slater, G., Schüth, C., Bill, M., Downey, A., Larkin, M., Kalin, R.M., 2002. Carbon isotope fractionation during aerobic biodegradation of trichloroethene by *Burkholderia cepacia* G4: A tool to map degradation mechanisms. *Appl. Environ. Microbiol.* 68, 1728–1734. doi:10.1128/AEM.68.4.1728-1734.2002
- Bekins, B.A., Warren, E., Godsy, E.M., 1997. A comparison of zero-order, first-order, and Monod kinetics biotransformation models. *Groundwater* 36, 261–268.
- Bloom, Y., Aravena, R., Hunkeler, D., Edwards, E., Frappe, S.K., 2000. Carbon isotope fractionation during microbial dechlorination of trichloroethene, cis -1,2-dichloroethene, and vinyl chloride: implications for assessment of natural attenuation. *Environ. Sci. Technol.* 34, 2768–2772. doi:10.1021/es991179k
- Bradley, P.M., 2003. History and ecology of chloroethene biodegradation: a review. *Bioremediat. J.* 7, 81–109. doi:10.1080/10889860390246141
- Bradley, P.M., 2000. Microbial degradation of chloroethenes in groundwater systems. *Hydrogeol. J.* 8, 104–111. doi:10.1007/s100400050011
- Bradley, P.M., Chapelle, F.H., 2011. Microbial mineralization of dichloroethene and vinyl

- chloride under hypoxic conditions. *Ground Water Monit. Remediat.* 31, 39–49. doi:10.1111/j.1745-6592.2011.01339.x
- Bradley, P.M., Chapelle, F.H., 1997. Kinetics of DCE and VC mineralisation under methanogenic and Fe(III)-reducing conditions. *Environ. Sci. Technol* 31, 2692–2696.
- Bradley, P.M., Chapelle, F.H., 1996. Anaerobic Mineralization of Vinyl Chloride in Fe (III) -Reducing , Aquifer Sediments. *Environ. Sci. Technol.* 30, 2084–2086.
- Brungard, K.L., Munakata-Marr, J., Johnson, C. a., Mandernack, K.W., 2003. Stable carbon isotope fractionation of trans-1,2-dichloroethylene during co-metabolic degradation by methanotrophic bacteria. *Chem. Geol.* 195, 59–67. doi:10.1016/S0009-2541(02)00388-1
- Buchner, D., Behrens, S., Laskov, C., Haderlein, S.B., 2015. Resiliency of stable isotope fractionation ($\delta^{13}\text{C}$ and $\delta^{37}\text{Cl}$) of trichloroethene to bacterial growth physiology and expression of key enzymes. *Environ. Sci. Technol.* 49, 13230–13237. doi:10.1021/acs.est.5b02918
- Buscheck, T.E., Alcantar, C.M., 1995. Regression techniques and analytical solutions to demonstrate intrinsic bioremediation, in: Hinchee, RE and Wilson, JT and Downey, D. (Ed.), *Intrinsic Biodegradation, BIOREMEDIATION SERIES*. pp. 109–116.
- Carey, G.R., Chapman, S.W., Parker, B.L., McGregor, R., 2015. Application of an adapted version of MT3DMS for modeling back-diffusion remediation timeframes. *Remediat. J.* 25, 55–79. doi:10.1002/rem.21440
- Carey, G.R., McBean, E.A., Feenstra, S., 2016. Estimating tortuosity coefficients based on hydraulic conductivity. *Groundwater* 54, 476–487. doi:10.1111/gwat.12406
- CH2MHill, 2011. Hill AFB OU10 ERPIMS Database. Utah.
- CH2MHILL, 2009. Operable Unit 10 remedial investigation report. Salt Lake City, UT.
- Chambon, J.C., Bjerg, P.L., Scheutz, C., Baelum, J., Jakobsen, R., Binning, P.J., 2013. Review of reactive kinetic models describing reductive dechlorination of chlorinated ethenes in soil and groundwater. *Biotechnol. Bioeng.* 110, 1–23. doi:10.1002/bit.24714
- Chambon, J.C., Broholm, M.M., Binning, P.J., Bjerg, P.L., 2010. Modeling multi-component transport and enhanced anaerobic dechlorination processes in a single fracture-clay matrix system. *J. Contam. Hydrol.* 112, 77–90. doi:10.1016/j.jconhyd.2009.10.008
- Chapman, S.W., Parker, B.L., 2005. Plume persistence due to aquitard back diffusion following dense nonaqueous phase liquid source removal or isolation. *Water Resour. Res.* 41, 1–16. doi:10.1029/2005WR004224
- Chapman, S.W., Parker, B.L., Sale, T.C., Doner, L.A., 2012. Testing high resolution numerical models for analysis of contaminant storage and release from low permeability zones. *J. Contam. Hydrol.* 136–137, 106–116. doi:10.1016/j.jconhyd.2012.04.006
- Cheng, D., Chow, W.L., He, J., 2010. A Dehalococoides-containing co-culture that

- dechlorinates tetrachloroethene to trans-1,2-dichloroethene. *ISME J.* 4, 88–97. doi:10.1038/ismej.2009.90
- Cheng, D., He, J., 2009. Isolation and characterization of “Dehalococcoides” sp. strain MB, which dechlorinates tetrachloroethene to trans-1,2-dichloroethene. *Appl. Environ. Microbiol.* 75, 5910–5918. doi:10.1128/AEM.00767-09
- Chiang, W.H., 2013. 3D-Groundwater Modelinf with PMWIN: A Simulation System for Modeling Groundwater Flow and Transport Processes. doi:10.1017/CBO9781107415324.004
- Chiu, W.A., Jinot, J., Scott, C.S., Makris, S.L., Cooper, G.S., Dzubow, R.C., Bale, A.S., Evans, M. V., Guyton, K.Z., Keshava, N., Lipscomb, J.C., Barone Jr., S., Fox, J.F., Gwinn, M.R., Schaum, J., Caldwell, J.C., 2013. Human health effects of trichloroethylene: Key findings and scientific issues. *Environ. Health Perspect.* 121, 303–311. doi:10.1289/ehp.1205879
- Christensen, T.H., Bjerg, P.L., Banwart, S.A., Jakobsen, R., Heron, G., Albrechtsen, H.-J., 2000. Characterization of redox conditions in pollution plumes. *Contam. Soil* 2000 181–188.
- Chu, K.-H., Mahendra, S., Song, D.L., Conrad, M.E., Alvarez-Cohen, L., 2004. Stable carbon isotope fractionation during aerobic biodegradation of chlorinated ethenes. *Environ. Sci. Technol.* 38, 3126–3130. doi:10.1021/es035238c
- Cichocka, D., Imfeld, G., Richnow, H.H., Nijenhuis, I., 2008. Variability in microbial carbon isotope fractionation of tetra- and trichloroethene upon reductive dechlorination. *Chemosphere* 71, 639–648. doi:10.1016/j.chemosphere.2007.11.013
- Cichocka, D., Nikolausz, M., Haest, P.J., Nijenhuis, I., 2010. Tetrachloroethene conversion to ethene by a Dehalococcoides-containing enrichment culture from Bitterfeld. *FEMS Microbiol. Ecol.* 72, 297–310. doi:10.1111/j.1574-6941.2010.00845.x
- Cichocka, D., Siegert, M., Imfeld, G., Andert, J., Beck, K., Diekert, G., Richnow, H.H., Nijenhuis, I., 2007. Factors controlling the carbon isotope fractionation of tetra- and trichloroethene during reductive dechlorination by *Sulfurospirillum* ssp. and *Desulfitobacterium* sp. strain PCE-S. *FEMS Microbiol. Ecol.* 62, 98–107. doi:10.1111/j.1574-6941.2007.00367.x
- Clark, J.A., Stotler, R.L., Frape, S.K., Illman, W.A., 2016. Compound-specific isotope analyses to assess TCE biodegradation in a fractured dolomitic aquifer. *Groundwater*. doi:10.1111/gwat.12440
- Clement, T.P., Johnson, C.D., Sun, Y., Klecka, G.M., Bartlett, C., 2000. Natural attenuation of chlorinated ethene compounds: model development and field-scale application at the Dover site. *J. Contam. Hydrol.* 42, 113–140. doi:10.1016/S0169-7722(99)00098-4
- Clingenpeel, S.R., Moan, J.L., McGrath, D.M., Hungate, B.A., Watwood, M.E., 2012. Stable carbon isotope fractionation in chlorinated ethene degradation by bacteria expressing three toluene oxygenases. *Front. Microbiol.* 3, 1–7. doi:10.3389/fmicb.2012.00063

- Coleman, N. V., Mattes, T.E., Gossett, J.M., 2002a. Biodegradation of cis-dichloroethene as the sole carbon source by a β -Proteobacterium. *Appl. Environ. Microbiol.* 68, 2726–2730. doi:10.1128/AEM.68.6.2726
- Coleman, N. V., Mattes, T.E., Gossett, J.M., Spain, J.C., 2002b. Phylogenetic and kinetic diversity of aerobic vinyl chloride-assimilating bacteria from contaminated sites. *Appl. Environ. Microbiol.* 68, 6162–6171. doi:10.1128/AEM.68.12.6162-6171.2002
- Coplen, T.B., 2011. Guidelines and recommended terms for expression of stable-isotope-ratio and gas-ratio measurement results. *Rapid Commun. Mass Spectrom.* 25, 2538–2560. doi:10.1002/rcm.5129
- Courbet, C., Riviere, A., Jeannotat, S., Rinaldi, S., Hunkeler, D., Bendjoudi, H., de Marsily, G., 2011. Complementing approaches to demonstrate chlorinated solvent biodegradation in a complex pollution plume: Mass balance, PCR and compound-specific stable isotope analysis. *J. Contam. Hydrol.* 126, 315–329. doi:10.1016/j.jconhyd.2011.08.009
- Cretnik, S., Bernstein, A., Shouakar-Stash, O., Löffler, F., Elsner, M., 2014. Chlorine isotope effects from isotope ratio mass spectrometry suggest intramolecular C-Cl bond competition in trichloroethene (TCE) reductive dehalogenation. *Molecules* 19, 6450–6473. doi:10.3390/molecules19056450
- Cretnik, S., Thoreson, K.A., Bernstein, A., Ebert, K., Buchner, D., Laskov, C., Haderlein, S., Shouakar-stash, O., Kliegman, S., McNeill, K., Elsner, M., 2013. Reductive dechlorination of TCE by chemical model systems in comparison to dehalogenating bacteria: insights from dual element isotope analysis ($^{13}\text{C}/^{12}\text{C}$, $^{37}\text{Cl}/^{35}\text{Cl}$). *Environ. Sci. Technol.*
- Cunningham, J.A., Fadel, Z.J., 2007. Contaminant degradation in physically and chemically heterogeneous aquifers. *J. Contam. Hydrol.* 94, 293–304. doi:10.1016/j.jconhyd.2007.07.011
- D’Affonseca, F.M., Prommer, H., Finkel, M., Blum, P., Grathwohl, P., 2011. Modeling the long-term and transient evolution of biogeochemical and isotopic signatures in coal tar–contaminated aquifers. *Water Resour. Res.* 47.
- Damgaard, I., Bjerg, P.L., Bælum, J., Scheutz, C., Hunkeler, D., Jacobsen, C.S., Tuxen, N., Broholm, M.M., 2013a. Identification of chlorinated solvents degradation zones in clay till by high resolution chemical, microbial and compound specific isotope analysis. *J. Contam. Hydrol.* 146, 37–50. doi:10.1016/j.jconhyd.2012.11.010
- Damgaard, I., Bjerg, P.L., Jacobsen, C.S., Tsitonaki, A., Kern-Jespersen, H., Broholm, M.M., 2013b. Performance of full-scale enhanced reductive dechlorination in clay till. *Groundw. Monit. Remediat.* 33, 48–61. doi:10.1111/j.1745-6592.2012.01405.x
- Darlington, R., Lehmicke, L., Andrachek, R.G., Freedman, D.L., 2008. Biotic and abiotic anaerobic transformations of trichloroethene and cis-1,2-dichloroethene in fractured sandstone. *Environ. Sci. Technol.* 42, 4323–4330. doi:10.1021/es702196a
- Darlington, R., Lehmicke, L.G., Andrachek, R.G., Freedman, D.L., 2013. Anaerobic abiotic transformations of cis-1,2-dichloroethene in fractured sandstone. *Chemosphere* 90, 2226–2232. doi:10.1016/j.chemosphere.2012.09.084

- Dayan, H., Abrajano, T., Sturchio, N.C., Winsor, L., 1999. Carbon isotopic fractionation during reductive dehalogenation of chlorinated ethenes by metallic iron. *Org. Geochem.* 30, 755–763. doi:10.1016/S0146-6380(99)00058-3
- Dong, Y., Butler, E.C., Philp, P., Krumholz, L.R., 2011. Impacts of microbial community composition on isotope fractionation during reductive dechlorination of tetrachloroethylene. *Biodegradation* 22, 431–444. doi:10.1007/s10532-010-9416-2
- Eckert, D., Qiu, S., Elsner, M., Cirpka, O. a., 2013. Model complexity needed for quantitative analysis of high resolution isotope and concentration data from a toluene-pulse experiment. *Environ. Sci. Technol.* 47, 6900–6907. doi:10.1021/es304879d
- Eckert, D., Rolle, M., Cirpka, O. a., 2012. Numerical simulation of isotope fractionation in steady-state bioreactive transport controlled by transverse mixing. *J. Contam. Hydrol.* 140–141, 95–106. doi:10.1016/j.jconhyd.2012.08.010
- Elsner, M., 2010. Stable isotope fractionation to investigate natural transformation mechanisms of organic contaminants: principles, prospects and limitations. *J. Environ. Monit.* 12, 2005–2031. doi:10.1039/c0em00277a
- Elsner, M., Chartrand, M., Vanstone, N., Couloume, G.L., Lollar, B.S., 2008. Identifying abiotic chlorinated ethene degradation: Characteristic isotope patterns in reaction products with nanoscale zero-valent iron. *Environ. Sci. Technol.* 42, 5963–5970. doi:10.1021/es8001986
- Elsner, M., Zwank, L., Hunkeler, D., Schwarzenbach, R.P., 2005. A new concept linking observable stable isotope fractionation to transformation pathways of organic pollutants. *Environ. Sci. Technol.* 39, 6896–6916. doi:10.1021/es0504587
- Filippini, M., Amorosi, A., Campo, B., Herrero-Martín, S., Nijenhuis, I., Parker, B.L., Gargini, A., 2016. Origin of VC-only plumes from naturally enhanced dechlorination in a peat-rich hydrogeologic setting. *J. Contam. Hydrol.* 192, 129–139. doi:10.1016/j.jconhyd.2016.07.003
- Filippini, M., Nijenhuis, I., Kümmel, S., Chiarini, V., Crosta, G., Richnow, H.H., Gargini, A., 2018. Multi-element compound specific stable isotope analysis of chlorinated aliphatic contaminants derived from chlorinated pitches. *Sci. Total Environ.* 640–641, 153–162. doi:10.1016/j.scitotenv.2018.05.285
- Fletcher, K.E., Nijenhuis, I., Richnow, H.-H., Löffler, F.E., 2011. Stable carbon isotope enrichment factors for cis-1,2-dichloroethene and vinyl chloride reductive dechlorination by *Dehalococcoides*. *Environ. Sci. Technol.* 45, 2951–2957. doi:10.1021/es103728q
- Fogel, M.M., Taddeo, A.R., Fogel, S., 1986. Biodegradation of chlorinated ethenes by a methane-utilizing mixed culture. *Appl. Environ. Microbiol.* 51, 720–724.
- Fox, B.G., Borneman, J.G., Wackett, L.P., Lipscomb, J.D., 1990. Haloalkene oxidation by the soluble methane monooxygenase from *Methylosinus trichosporium* OB3b: mechanistic and environmental implications. *Biochemistry* 29, 6419–6427. doi:10.1021/bi00479a013
- Fries, M.R., Forney, L.J., Tiedje, J.M., 1997. Phenol- and toluene-degrading microbial

- populations from an aquifer in which successful trichloroethene cometabolism occurred. *Appl. Environ. Microbiol.* 63, 1523–1530.
- Gafni, A., Lihl, C., Gelman, F., Elsner, M., Bernstein, A., 2018. $\delta^{13}\text{C}$ and $\delta^{37}\text{Cl}$ Isotope Fractionation to Characterize Aerobic vs Anaerobic Degradation of Trichloroethylene. *Environ. Sci. Technol. Lett.* 5, 202–208. doi:10.1021/acs.estlett.8b00100
- Garabedian, S.P., Leblanc, D.R., Gelhar, L.W., Celia, M.A., 1991. Large-scale natural gradient tracer testing sand and gravel, Cape Cod, Massachusetts. *Water resources Res.* 27, 895–910.
- Gaza, S., Schmidt, K.R., Weigold, P., Heidinger, M., Tiehm, A., 2019. Aerobic metabolic trichloroethene biodegradation under field-relevant conditions. *Water Res.* 151, 343–348. doi:10.1016/j.watres.2018.12.022
- Gossett, J.M., 2010. Sustained aerobic oxidation of vinyl chloride at low oxygen concentrations. *Environ. Sci. Technol.* 44, 1405–1411. doi:10.1021/es9033974
- Griffin, B.M., Tiedje, J.M., Löffler, F.E., 2004. Anaerobic microbial reductive dechlorination of tetrachloroethene to predominately trans-1,2-dichloroethene. *Environ. Sci. Technol.* 38, 4300–4303. doi:10.1021/es035439g
- Griffioen, J., Klaver, G., Westerhoff, W.E., 2016. The mineralogy of suspended matter, fresh and Cenozoic sediments in the fluvio-deltaic Rhine-Meuse-Scheldt-Ems area, the Netherlands: An overview and review. *Geol. en Mijnbouw/Netherlands J. Geosci.* 95, 23–107. doi:10.1017/njg.2015.32
- Griffioen, J., Klein, J., Van Gaans, P.F.M., 2012. Reaction capacity characterization of shallow sedimentary deposits in geologically different regions of the Netherlands. *J. Contam. Hydrol.* 127, 30–46. doi:10.1016/j.jconhyd.2011.04.001
- Hamonts, K., Kuhn, T., Vos, J., Maesen, M., Kalka, H., Smidt, H., Springael, D., Meckenstock, R.U., Dejonghe, W., 2012. Temporal variations in natural attenuation of chlorinated aliphatic hydrocarbons in eutrophic river sediments impacted by a contaminated groundwater plume. *Water Res.* 46, 1873–1888. doi:10.1016/j.watres.2012.01.001
- Han, Y.S., Hyun, S.P., Jeong, H.Y., Hayes, K.F., 2012. Kinetic study of cis-dichloroethylene (cis-DCE) and vinyl chloride (VC) dechlorination using green rusts formed under varying conditions. *Water Res.* 46, 6339–6350. doi:10.1016/j.watres.2012.08.041
- He, Y., Su, C., Wilson, J., Wilkin, R., Adair, C., Lee, T., Bradley, P., Ferrey, M., 2009. Identification and characterization methods for reactive minerals responsible for natural attenuation of chlorinated organic compounds in ground water, *Risk Management*.
- Hofstetter, T.B., Berg, M., 2011. Assessing transformation processes of organic contaminants by compound-specific stable isotope analysis. *TrAC - Trends Anal. Chem.* 30, 618–627. doi:10.1016/j.trac.2010.10.012
- Höhener, P., 2016. Simulating stable carbon and chlorine isotope ratios in dissolved chlorinated groundwater pollutants with BIOCHLOR-ISO Ethene Ethene Chlorine :

- Standard approach. *J. Contam. Hydrol.* 195, 52–61. doi:10.1016/j.jconhyd.2016.11.002
- Höhener, P., Atteia, O., 2010. Multidimensional analytical models for isotope ratios in groundwater pollutant plumes of organic contaminants undergoing different biodegradation kinetics. *Adv. Water Resour.* 33, 740–751. doi:10.1016/j.advwatres.2010.03.016
- Höhener, P., Elsner, M., Eisenmann, H., Atteia, O., 2015. Improved constraints on in situ rates and on quantification of complete chloroethene degradation from stable carbon isotope mass balances in groundwater plumes. *J. Contam. Hydrol.* 182, 173–182. doi:10.1016/j.jconhyd.2015.09.006
- Höhener, P., Li, Z.M., Julien, M., Nun, P., Robins, R.J., Remaud, G.S., 2017. Simulating stable isotope ratios in plumes of groundwater pollutants with BIOSCREEN-AT-ISO. *Groundwater* 55, 261–267. doi:10.1111/gwat.12472
- Höhener, P., Yu, X., 2012. Stable carbon and hydrogen isotope fractionation of dissolved organic groundwater pollutants by equilibrium sorption. *J. Contam. Hydrol.* 129–130, 54–61. doi:10.1016/j.jconhyd.2011.09.006
- Höyng, D., Prommer, H., Blum, P., Grathwohl, P., Mazo D’Affonseca, F., 2015. Evolution of carbon isotope signatures during reactive transport of hydrocarbons in heterogeneous aquifers. *J. Contam. Hydrol.* 174, 10–27. doi:10.1016/j.jconhyd.2014.12.005
- Huang, B., Lei, C., Wei, C., Zeng, G., 2014. Chlorinated volatile organic compounds (Cl-VOCs) in environment - sources, potential human health impacts, and current remediation technologies. *Environ. Int.* 71, 118–138. doi:10.1016/j.envint.2014.06.013
- Hunkeler, D., Abe, Y., Broholm, M.M., Jeannotat, S., Westergaard, C., Jacobsen, C.S., Aravena, R., Bjerg, P.L., 2011a. Assessing chlorinated ethene degradation in a large scale contaminant plume by dual carbon-chlorine isotope analysis and quantitative PCR. *J. Contam. Hydrol.* 119, 69–79. doi:10.1016/j.jconhyd.2010.09.009
- Hunkeler, D., Aravena, R., 2000. Determination of compound-specific carbon isotope ratios of chlorinated methanes, ethanes, and ethenes in aqueous samples. *Environ. Sci. Technol.* 34, 2839–2844. doi:10.1021/es991178s
- Hunkeler, D., Aravena, R., Butler, B.J., 1999. Monitoring microbial dechlorination of tetrachloroethene (PCE) in groundwater using compound-specific stable carbon isotope ratios: Microcosm and field studies. *Environ. Sci. Technol.* 33, 2733–2738. doi:10.1021/es981282u
- Hunkeler, D., Aravena, R., Cox, E., 2002. Carbon isotopes as a tool to evaluate the origin and fate of vinyl chloride: Laboratory experiments and modeling of isotope evolution. *Environ. Sci. Technol.* 36, 3378–3384. doi:10.1021/es011479d
- Hunkeler, D., Aravena, R., Shouakar-Stash, O., Weisbrod, N., Nasser, A., Netzer, L., Ronen, D., 2011b. Carbon and chlorine isotope ratios of chlorinated ethenes migrating through a thick unsaturated zone of a sandy aquifer. *Environ. Sci. Technol.* 45, 8247–8253. doi:10.1021/es201415k

- Hunkeler, D., Chollet, N., Pittet, X., Aravena, R., Cherry, J. a., Parker, B.L., 2004. Effect of source variability and transport processes on carbon isotope ratios of TCE and PCE in two sandy aquifers. *J. Contam. Hydrol.* 74, 265–282. doi:10.1016/j.jconhyd.2004.03.003
- Hunkeler, D., Meckenstock, R.U., Lollar, B.S., Schmidt, T.C., Wilson, J.T., 2008. A guide for assessing biodegradation and source identification of organic ground water contaminants using compound specific isotope analysis (CSIA), US EPA Publication. doi:EPA/600/R-08/148
- Hunkeler, D., van Breukelen, B.M., Elsner, M., 2009. Modeling chlorine isotope trends during sequential transformation of chlorinated ethenes. *Environ. Sci. Technol.* 43, 6750–6756. doi:10.1021/es900579z
- Hwang, H.T., Park, Y.J., Sudicky, E.A., Unger, A.J.A., Illman, W.A., Frappe, S.K., Shouakar-Stash, O., 2013. A multiphase flow and multispecies reactive transport model for DNAPL-involved Compound Specific Isotope Analysis. *Adv. Water Resour.* 59, 111–122. doi:10.1016/j.advwatres.2013.05.009
- IAEA/WMO, 2014. Global networks of isotopes in precipitation and rivers (GNIP, GNIR) [WWW Document]. URL <https://nucleus.iaea.org/Pages/GNIPR.aspx>
- IARC, 2008. 1,3-butadiene, ethylene oxide and vinyl halides (vinyl fluoride, vinyl chloride and vinyl bromide). Lyon.
- Imfeld, G., Kopinke, F.D., Fischer, a., Richnow, H.H., 2014. Carbon and hydrogen isotope fractionation of benzene and toluene during hydrophobic sorption in multistep batch experiments. *Chemosphere* 107, 454–461. doi:10.1016/j.chemosphere.2014.01.063
- Jang, E., He, W., Savoy, H., Dietrich, P., Kolditz, O., Rubin, Y., Schiøth, C., Kalbacher, T., 2017. Identifying the influential aquifer heterogeneity factor on nitrate reduction processes by numerical simulation. *Adv. Water Resour.* 99, 38–52. doi:10.1016/j.advwatres.2016.11.007
- Janot, N., Pacheco, J.S.L., Pham, D.Q., Brien, T.M.O., Hausladen, D., Noe, V., Lallier, F., Maher, K., Fendorf, S., Williams, K.H., Long, P.E., Bargar, J.R., 2015. Physico-Chemical Heterogeneity of Organic-Rich Sediments in the Rifle Aquifer, CO: Impact on Uranium Biogeochemistry. *Environ. Sci. Technol.* doi:10.1021/acs.est.5b03208
- Jeannotat, S., Hunkeler, D., 2013. Can soil gas VOCs be related to groundwater plumes based on their isotope signature? *Environ. Sci. Technol.* 47, 12115–12122. doi:10.1021/es4010703
- Jeannotat, S., Hunkeler, D., 2012. Chlorine and carbon isotopes fractionation during volatilization and diffusive transport of trichloroethene in the unsaturated zone. *Environ. Sci. Technol.* 46, 3169–3176. doi:10.1021/es203547p
- Jennings, L.K., Chartrand, M.M.G., Lacrampe-Couloume, G., Lollar, B.S., Spain, J.C., Gossett, J.M., 2009. Proteomic and transcriptomic analyses reveal genes upregulated by cis-Dichloroethene in *Polaromonas* sp. strain JS666. *Appl. Environ. Microbiol.* 75, 3733–3744. doi:10.1128/AEM.00031-09

- Jeong, H.Y., Kim, H., 2007. Reductive dechlorination pathways of tetrachloroethylene and subsequent transformation of their mackinawite (FeS) in the presence of metals. *Environ. Sci. Technol.* 41, 7736–7743.
- Jesus, J., Frascari, D., Pozdniakova, T., Danko, A.S., 2016. Kinetics of aerobic cometabolic biodegradation of chlorinated and brominated aliphatic hydrocarbons: A review. *J. Hazard. Mater.* 309, 37–52. doi:10.1016/j.jhazmat.2016.01.065
- Jin, B., Rolle, M., 2014. Mechanistic approach to multi-element isotope modeling of organic contaminant degradation. *Chemosphere* 95, 131–139. doi:10.1016/j.chemosphere.2013.08.050
- Jin, B., Rolle, M., Li, T., Haderlein, S.B., 2014. Diffusive fractionation of BTEX and chlorinated ethenes in aqueous solution: Quantification of spatial isotope gradients. *Environ. Sci. Technol.* 48, 6141–6150. doi:10.1021/es4046956
- Johnson, R.L., Pankow, J.F., 1992. Dissolution of dense chlorinated solvents into groundwater. 2. source functions for pools of solvent. *Environ. Sci. Technol.* 26, 896–901. doi:10.1021/es00029a004
- Kaown, D., Kim, S.J.R., Woosik, S., 2016. Characterization of a site contaminated by chlorinated ethenes and ethanes using multi-analysis. *Environ. Earth Sci.* 75, 1–13. doi:10.1007/s12665-016-5536-2
- Kaown, D., Shouakar-Stash, O., Yang, J., Hyun, Y., Lee, K.K., 2014. Identification of multiple sources of groundwater contamination by dual isotopes. *Groundwater* 52, 875–885. doi:10.1111/gwat.12130
- Khan, F.I., Husain, T., Hejazi, R., 2004. An overview and analysis of site remediation technologies. *J. Environ. Manage.* 71, 95–122. doi:10.1016/j.jenvman.2004.02.003
- Kittelmann, S., Friedrich, M.W., 2008. Novel uncultured Chloroflexi dechlorinate perchloroethene to trans-dichloroethene in tidal flat sediments. *Environ. Microbiol.* 10, 1557–1570. doi:10.1111/j.1462-2920.2008.01571.x
- Klenk, I.D., Grathwohl, P., 2002. Transverse vertical dispersion in groundwater and the capillary fringe. *J. Contam. Hydrol.* 58, 111–128. doi:10.1016/S0169-7722(02)00011-6
- Kopinke, F.D., Georgi, A., Voskamp, M., Richnow, H.H., 2005. Carbon isotope fractionation of organic contaminants due to retardation on humic substances: Implications for natural attenuation studies in aquifers. *Environ. Sci. Technol.* 39, 6052–6062. doi:10.1021/es040096n
- Kuder, T., Philp, P., 2013. Demonstration of compound-specific isotope analysis of hydrogen isotope ratios in chlorinated ethenes. *Environ. Sci. Technol.* 47, 1461–1467. doi:10.1021/es303476v
- Kuder, T., Philp, P., Allen, J., 2009. Effects of volatilization on carbon and hydrogen isotope ratios of MTBE. *Environ. Sci. Technol.* 43, 1763–1768. doi:10.1021/es802834p
- Kuder, T., Philp, P., van Breukelen, B.M., Thouement, H.A.A., Vanderford, M., 2016. Integrated stable isotope – reactive transport model approach for assessment of

chlorinated solvent degradation.

- Kuder, T., van Breukelen, B.M., Vanderford, M., Philp, P., 2013. 3D-CSIA: Carbon, chlorine, and hydrogen isotope fractionation in transformation of TCE to ethene by a dehalococcoides culture. *Environ. Sci. Technol.* 47, 9668–9677. doi:10.1021/es400463p
- LaBolle, E.M., Fogg, G.E., Eweis, J.B., Gravner, J., Leaist, D.G., 2008. Isotopic fractionation by diffusion in groundwater. *Water Resour. Res.* 44, 1–15. doi:10.1029/2006WR005264
- Lash, L.H., Chiu, W.A., Guyton, K.Z., Rusyn, I., 2014. Trichloroethylene biotransformation and its role in mutagenicity, carcinogenicity and target organ toxicity. *Mutat. Res. Mutat. Res.* 762, 22–36. doi:http://dx.doi.org/10.1016/j.mrrev.2014.04.003
- Lee, P.K.H., Conrad, M.E., Alvarez-Cohen, L., 2007. Stable carbon isotope fractionation of chloroethenes by dehalorespiring isolates. *Environ. Sci. Technol.* 41, 4277–4285. doi:10.1021/es062763d
- Lee, S.S., Kaown, D., Lee, K.K., 2015. Evaluation of the fate and transport of chlorinated ethenes in a complex groundwater system discharging to a stream in Wonju, Korea. *J. Contam. Hydrol.* 182, 231–243. doi:10.1016/j.jconhyd.2015.09.005
- Lee, W., Batchelor, B., 2002. Abiotic, reductive dechlorination of chlorinated ethylenes by iron-bearing soil minerals. 2. Green rust. *Environ. Sci. Technol.* 36, 5348–5354. doi:10.1021/es025836b
- Liang, X., Dong, Y., 2007. Distinguishing abiotic and biotic tetrachloroethylene and trichloroethylene by stable carbon isotope fractionation. *Environ. Sci. Technol.* 41, 7094–7100.
- Liang, X., Paul Philp, R., Butler, E.C., 2009. Kinetic and isotope analyses of tetrachloroethylene and trichloroethylene degradation by model Fe(II)-bearing minerals. *Chemosphere* 75, 63–69. doi:10.1016/j.chemosphere.2008.11.042
- Lihl, C., Douglas, L.M., Franke, S., Perew de Mora, A., Daubmeier, M., Edwards, E.A., Nijenhuis, I., Lollar, B.S., Elsner, M., 2019. Mechanistic Dichotomy in Bacterial Trichloroethene Dechlorination Revealed by Carbon and Chlorine Isotope Effects. doi:10.1021/acs.est.8b06643
- Liu, C., Ball, W.P., 2002. Back diffusion of chlorinated solvent contaminants from a natural aquitard to a remediated aquifer under well-controlled field conditions: predictions and measurements. *Ground Water* 40, 175–184. doi:10.1111/j.1745-6584.2002.tb02502.x
- Lojkasek-Lima, P., Aravena, R., Parker, B.L., Cherry, J.A., 2012. Fingerprinting TCE in a bedrock aquifer using compound-specific isotope analysis. *Ground Water* 50, 754–764. doi:10.1111/j.1745-6584.2011.00897.x
- Lu, C., Bjerg, P.L., Zhang, F., Broholm, M.M., 2011. Sorption of chlorinated solvents and degradation products on natural clayey tills. *Chemosphere* 83, 1467–1474. doi:10.1016/j.chemosphere.2011.03.007

- Lutz, S.R., Meerveld, H.J. Van, Waterloo, M.J., Broers, H.P., van Breukelen, B.M., 2013. A model-based assessment of the potential use of compound-specific stable isotope analysis in river monitoring of diffuse pesticide pollution. *Hydrol. earth Syst. Sci.* 17, 4505–4524. doi:10.5194/hess-17-4505-2013
- Lutz, S.R., van Breukelen, B.M., 2014a. Combined source apportionment and degradation quantification of organic pollutants with CSIA: 2. Model validation and application. *Environ. Sci. Technol.* 48, 6229–6236. doi:10.1021/es4054016
- Lutz, S.R., van Breukelen, B.M., 2014b. A stable isotope model for combined source apportionment and degradation quantification of organic pollutants: 1. Model derivation. *Environ. Sci. Technol.*
- Lutz, S.R., van Der Velde, Y., Elsayed, O.F., Imfeld, G., Lefrancq, M., Payraudeau, S., van Breukelen, B.M., 2017. Pesticide fate on catchment scale: Conceptual modelling of stream CSIA data. *Hydrol. Earth Syst. Sci.* 21, 5243–5261. doi:10.5194/hess-21-5243-2017
- Maghrebi, M., Jankovic, I., Allen-King, R.M., Rabideau, A.J., Kalinovich, I., Weissmann, G.S., 2014. Impacts of transport mechanisms and plume history on tailing of sorbing plumes in heterogeneous porous formations. *Adv. Water Resour.* 73, 123–133. doi:10.1016/j.advwatres.2014.07.007
- Maghrebi, M., Jankovic, I., Weissmann, G.S., Matott, L.S., Allen-King, R.M., Rabideau, A.J., 2015. Contaminant tailing in highly heterogeneous porous formations: Sensitivity on model selection and material properties. *J. Hydrol.* 531, 149–160. doi:10.1016/j.jhydrol.2015.07.015
- Manoli, G., Chambon, J.C., Bjerg, P.L., Scheutz, C., Binning, P.J., Broholm, M.M., 2012. A remediation performance model for enhanced metabolic reductive dechlorination of chloroethenes in fractured clay till. *J. Contam. Hydrol.* 131, 64–78. doi:10.1016/j.jconhyd.2012.01.004
- Marco-Urrea, E., Gabarrell, X., Caminal, G., Vicent, T., Reddy, C.A., 2008. Aerobic degradation by white-rot fungi of trichloroethylene (TCE) and mixtures of TCE and perchloroethylene (PCE). *J. Chem. Technol. Biotechnol.* 83, 1190–1196. doi:10.1002/jctb.1914
- Marco-Urrea, E., Nijenhuis, I., Adrian, L., 2011. Transformation and carbon isotope fractionation of tetra- and trichloroethene to trans-dichloroethene by *Dehalococcoides* sp. strain CBDB1. *Environ. Sci. Technol.* 45, 1555–1562. doi:10.1021/es1023459
- Matthieu, D.E., Brusseau, M.L., Guo, Z., Plaschke, M., Carroll, K.C., Brinker, F., 2014. Persistence of a groundwater contaminant plume after hydraulic source containment at a chlorinated-solvent contaminated site. *Groundw. Monit. Remediat.* 34, 23–32. doi:10.1111/gwmr.12077
- Maymo-Gatell, X., Anguish, T., Zinder, S.H., 1999. Reductive dechlorination of chlorinated ethenes and 1,2-dichloroethane by *Dehalococcoides ethenogenes* 195. *Appl. Environ. Microbiol.* 65, 3108–3113.
- McMahon, P.B., 2001. Aquifer/aquitard interfaces: Mixing zones that enhance biogeochemical reactions. *Hydrogeol. J.* 9, 34–43. doi:10.1007/s100400000109

- McMahon, P.B., Chapelle, F.H., 1991. Microbial production of organic acids in aquitard sediments and its role in aquifer geochemistry. *Lett. To Nat.* 349, 233–235.
- McMillan, L.A., Rivett, M.O., Tellam, J.H., Dumble, P., Sharp, H., 2014. Influence of vertical flows in wells on groundwater sampling. *J. Contam. Hydrol.* 169, 50–61. doi:10.1016/j.jconhyd.2014.05.005
- McNab, W.W., Dooher, B.P., 1998. A critique of a steady-state analytical method for estimating contaminant degradation rates. *Ground Water* 36, 983–987. doi:10.1111/j.1745-6584.1998.tb02105.x
- Miller, G.S., Milliken, C.E., Sowers, K.R., May, H.D., 2005. Reductive dechlorination of tetrachloroethene to trans-dichloroethene and cis-dichloroethene by PCB-dechlorinating bacterium DF-1. *Environ. Sci. Technol.* 39, 2631–2635. doi:10.1021/es048849t
- Mulligan, C.N., Yong, R.N., 2004. Natural attenuation of contaminated soils. *Environ. Int.* 30, 587–601. doi:10.1016/j.envint.2003.11.001
- Mundle, S.O.C., Johnson, T., Lacrampe-Couloume, G., Pérez-De-Mora, A., Duhamel, M., Edwards, E.A., McMaster, M.L., Cox, E., Révész, K., Sherwood Lollar, B., 2012. Monitoring biodegradation of ethene and bioremediation of chlorinated ethenes at a contaminated site using compound-specific isotope analysis (CSIA). *Environ. Sci. Technol.* 46, 1731–1738. doi:10.1021/es202792x
- Nguyen, T.H., Goss, K.-U., Ball, W.P., 2005. Critical review polyparameter linear free energy relationships for estimating the equilibrium partition of organic compounds between water and the natural organic matter in soils and sediments. *Environ. Sci. Technol.* 39, 913–924. doi:10.1021/es048839s
- Nijenhuis, I., Schmidt, M., Pellegatti, E., Paramatti, E., Richnow, H.H., Gargini, A., 2013. A stable isotope approach for source apportionment of chlorinated ethene plumes at a complex multi-contamination events urban site. *J. Contam. Hydrol.* 153, 92–105. doi:10.1016/j.jconhyd.2013.06.004
- Numata, M., Nakamura, N., Koshikawa, H., Terashima, Y., 2002. Chlorine isotope fractionation during reductive dechlorination of chlorinated ethenes by anaerobic bacteria. *Environ. Sci. Technol.* 36, 4389–4394. doi:10.1021/es025547n
- Nzila, A., 2013. Update on the cometabolism of organic pollutants by bacteria. *Environ. Pollut.* 178, 474–482. doi:10.1016/j.envpol.2013.03.042
- Ogata, A., Banks, R.B., 1961. A solution of the differential equation of longitudinal dispersion in porous media. *U.S. Geol. Surv.*
- Ojeda, A.S., Phillips, E., Mancini, S.A., Lollar, B.S., 2019. Sources of Uncertainty in Biotransformation Mechanistic Interpretations and Remediation Studies using CSIA. *Anal. Chem.* 91, 9147–9153. doi:10.1021/acs.analchem.9b01756
- Palau, J., Marchesi, M., Chambon, J.C.C., Aravena, R., Canals, À., Binning, P.J., Bjerg, P.L., Otero, N., Soler, A., 2014. Multi-isotope (carbon and chlorine) analysis for fingerprinting and site characterization at a fractured bedrock aquifer contaminated by chlorinated ethenes. *Sci. Total Environ.* 475, 61–70.

doi:10.1016/j.scitotenv.2013.12.059

- Parker, B.L., Chapman, S.W., Guilbeault, M. a., 2008. Plume persistence caused by back diffusion from thin clay layers in a sand aquifer following TCE source-zone hydraulic isolation. *J. Contam. Hydrol.* 102, 86–104. doi:10.1016/j.jconhyd.2008.07.003
- Parker, B.L., Cherry, J. a., Chapman, S.W., 2004. Field study of TCE diffusion profiles below DNAPL to assess aquitard integrity. *J. Contam. Hydrol.* 74, 197–230. doi:10.1016/j.jconhyd.2004.02.011
- Parkhurst, B.D.L., Appelo, C. a J., 1999. User's Guide To PHREEQC (version 2) — a Computer Program for Speciation, and Inverse Geochemical Calculations, Exchange Organizational Behavior Teaching Journal. Denver, Colorado. doi:Rep. 99-4259
- Petitta, M., Pacioni, E., Sbarbati, C., Corvatta, G., Fanelli, M., Aravena, R., 2013. Hydrodynamic and isotopic characterization of a site contaminated by chlorinated solvents: Chienti River Valley, Central Italy. *Appl. Geochemistry* 32, 164–174. doi:10.1016/j.apgeochem.2012.09.012
- Pooley, K.E., Blessing, M., Schmidt, T.C., Haderlein, S.B., Macquarrie, K.T.B., Prommer, H., 2009. Aerobic biodegradation of chlorinated ethenes in a fractured bedrock aquifer: Quantitative assessment by compound-specific isotope analysis (CSIA) and reactive transport modeling. *Environ. Sci. Technol.* 43, 7458–7464. doi:10.1021/es900658n
- Prommer, H., Barry, D. a, Chiang, W., Zheng, C., 2001. PHT3D – A MODFLOW / MT3DMS-based reactive multi-component transport model. *MODFLOW 2001 Other Model. Odysseys* 477–483. doi:10.1111/j.1745-6584.2003.tb02588.x
- Puigserver, D., Carmona, J.M., Cortés, A., Viladevall, M., Nieto, J.M., Grifoll, M., Vila, J., Parker, B.L., 2013. Subsoil heterogeneities controlling porewater contaminant mass and microbial diversity at a site with a complex pollution history. *J. Contam. Hydrol.* 144, 1–19. doi:10.1016/j.jconhyd.2012.10.009
- Puigserver, D., Herrero, J., Torres, M., Cortés, A., Nijenhuis, I., Kuntze, K., Parker, B.L., Carmona, J.M., 2016. Reductive dechlorination in recalcitrant sources of chloroethenes in the transition zone between aquifers and aquitards. *Environ. Sci. Pollut. Res.* 23, 18724–18741. doi:10.1007/s11356-016-7068-4
- Puls, R.W., Barcelona, M.J., 1995. Low-flow (minimal drawdown) groundwater sampling procedures. Washington DC.
- Qiu, S., Eckert, D., Cirpka, O.A., Huenniger, M., Knappett, P., Maloszewski, P., Meckenstock, R.U., Griebler, C., Elsner, M., 2013. Direct experimental evidence of non- first order degradation kinetics and sorption-induced isotopic fractionation in a mesoscale aquifer: 13 C/ 12 C analysis of a transient toluene pulse. *Environ. Sci. Technol.* 47, 6892–6899.
- Rasa, E., Chapman, S.W., Bekins, B.A., Fogg, G.E., Scow, K.M., MacKay, D.M., 2011. Role of back diffusion and biodegradation reactions in sustaining an MTBE/TBA plume in alluvial media. *J. Contam. Hydrol.* 126, 235–247. doi:10.1016/j.jconhyd.2011.08.006

- Renpenning, J., Keller, S., Cretnik, S., Shouakar-Stash, O., Elsner, M., Schubert, T., Nijenhuis, I., 2014. Combined C and Cl isotope effects indicate differences between corrinoids and enzyme (Sulfurospirillum multivorans PceA) in reductive dehalogenation of tetrachloroethene, but not trichloroethene. *Environ. Sci. Technol.* 48, 11837–11845. doi:10.1021/es503306g
- Rivett, M.O., Dearden, R. a., Wealthall, G.P., 2014. Architecture, persistence and dissolution of a 20 to 45year old trichloroethene DNAPL source zone. *J. Contam. Hydrol.* 170, 95–115. doi:10.1016/j.jconhyd.2014.09.008
- Rolle, M., Chiogna, G., Bauer, R., Griebler, C., Grathwohl, P., 2010. Isotopic fractionation by transverse dispersion: Flow-through microcosms and reactive transport modeling study. *Environ. Sci. Technol.* 44, 6167–6173. doi:10.1021/es101179f
- Ryoo, D., Shim, H., Canada, K., Barbieri, P., Wood, T.K., 2000. Aerobic degradation of tetrachloroethylene by toluene-o-xylene monooxygenase of *Pseudomonas stutzeri* OX1. *Nat. Biotechnol.* 18, 775–778. doi:10.1038/77344
- Sale, T.C., Zimbron, J.A., Dandy, D.S., 2008. Effects of reduced contaminant loading on downgradient water quality in an idealized two-layer granular porous media. *J. Contam. Hydrol.* 102, 72–85. doi:10.1016/j.jconhyd.2008.08.002
- Sanz-Prat, A., Lu, C., Amos, R.T., Finkel, M., Blowes, D.W., Cirpka, O.A., 2016. Exposure-time based modeling of nonlinear reactive transport in porous media subject to physical and geochemical heterogeneity. *J. Contam. Hydrol.* 192, 35–49. doi:10.1016/j.jconhyd.2016.06.002
- Schaefer, C.E., 2016. Naturally occurring dechlorination reactions in rock matrices: Impacts on TCE fate and flux. *Environ. Technol. Innov.* 6, 115–122. doi:10.1016/j.eti.2016.08.003
- Schaefer, C.E., Ho, P., Gurr, C., Berns, E., Werth, C., 2017. Abiotic dechlorination of chlorinated ethenes in natural clayey soils : Impacts of mineralogy and temperature. *J. Contam. Hydrol.* 206, 10–17. doi:10.1016/j.jconhyd.2017.09.007
- Schaefer, C.E., Towne, R.M., Lippincott, D.R., Lazouskaya, V., Fischer, T.B., Bishop, M.E., Dong, H., 2013. Coupled diffusion and abiotic reaction of trichloroethene in minimally disturbed rock matrices. *Environ. Sci. Technol.* 47, 4291–4298. doi:10.1021/es400457s
- Schmidt, K.R., Augenstein, T., Heidinger, M., Ertl, S., Tiehm, A., 2010. Aerobic biodegradation of cis-1,2-dichloroethene as sole carbon source: Stable carbon isotope fractionation and growth characteristics. *Chemosphere* 78, 527–532. doi:10.1016/j.chemosphere.2009.11.033
- Schmidt, K.R., Gaza, S., Voropaev, A., Ertl, S., Tiehm, A., 2014. Aerobic biodegradation of trichloroethene without auxiliary substrates. *Water Res.* 59, 112–118. doi:10.1016/j.watres.2014.04.008
- Semprini, L., 1997. Strategies for the aerobic co-metabolism of chlorinated solvents. *Curr. Opin. Biotechnol.* 8, 296–308. doi:http://dx.doi.org/10.1016/S0958-1669(97)80007-9
- Semprini, L., Kitanidis, P.K., Kampbell, D.H., Wilson, J.T., 1995. Anaerobic

- transformation of chlorinated aliphatic hydrocarbons in a sand aquifer based on spatial chemical distributions. *Water Resour. Res.* 31, 1051–1062.
- Seyedabbasi, M.A., Newell, C.J., Adamson, D.T., Sale, T.C., 2012. Relative contribution of DNAPL dissolution and matrix diffusion to the long-term persistence of chlorinated solvent source zones. *J. Contam. Hydrol.* 134–135, 69–81. doi:10.1016/j.jconhyd.2012.03.010
- Sherwood Lollar, B., Slater, G.F., Ahad, J., Sleep, B., Spivack, J., Brennan, M., MacKenzie, P., 1999. Contrasting carbon isotope fractionation during biodegradation of trichloroethylene and toluene: Implications for intrinsic bioremediation. *Org. Geochem.* 30, 813–820. doi:10.1016/S0146-6380(99)00064-9
- Sherwood Lollar, B., Slater, G.F., Sleep, B., Witt, M., Klecka, G.M., Harkness, M., Spivack, J., 2001. Stable carbon isotope evidence for intrinsic bioremediation of tetrachloroethene and trichloroethene at Area 6, Dover Air Force Base. *Environ. Sci. Technol.* 35, 261–269. doi:10.1021/es001227x
- Shouakar-Stash, O., Drimmie, R.J., Zhang, M., Frape, S.K., 2006. Compound-specific chlorine isotope ratios of TCE, PCE and DCE isomers by direct injection using CF-IRMS. *Appl. Geochemistry* 21, 766–781. doi:10.1016/j.apgeochem.2006.02.006
- Shouakar-Stash, O., Frape, S.K., Drimmie, R.J., 2003. Stable hydrogen, carbon and chlorine isotope measurements of selected chlorinated organic solvents. *J. Contam. Hydrol.* 60, 211–228. doi:10.1016/S0169-7722(02)00085-2
- Slater, G.F., Ahad, J.M.E., Sherwood Lollar, B., Allen-King, R., Sleep, B., 2000. Carbon isotope effects resulting from equilibrium sorption of dissolved VOCs. *Anal. Chem.* 72, 5669–5672. doi:10.1021/ac000691h
- Slater, G.F., Lollar, B.S., Sleep, B.E., Edwards, E.A., 2001. Variability in carbon isotopic fractionation during biodegradation of chlorinated ethenes: Implications for field applications. *Environ. Sci. Technol.* 35, 901–907. doi:10.1021/es001583f
- Slater, G.F., Sherwood Lollar, B., Allen King, R., O'Hannesin, S., 2002. Isotopic fractionation during reductive dechlorination of trichloroethene by zero-valent iron: Influence of surface treatment. *Chemosphere* 49, 587–596. doi:10.1016/S0045-6535(02)00327-2
- Smith, G., Wang, Y., 2015. Treatment optimization through refinement of a conceptual site model using compound specific isotope analysis. *Remediat. J.* 26, 107–116. doi:10.1002/rem.21452
- Song, D.L., Conrad, M.E., Sorenson, K.S., Alvarez-Cohen, L., 2002. Stable carbon isotope fractionation during enhanced in situ bioremediation of trichloroethene. *Environ. Sci. Technol.* 36, 2262–2268. doi:10.1021/es011162d
- Stelzer, N., Imfeld, G., Thullner, M., Lehmann, J., Poser, A., Richnow, H.H., Nijenhuis, I., 2009. Integrative approach to delineate natural attenuation of chlorinated benzenes in anoxic aquifers. *Environ. Pollut.* 157, 1800–1806. doi:10.1016/j.envpol.2009.01.029
- Stenback, G.A., Ong, S.K., Rogers, S.W., Kjartanson, B.H., 2004. Impact of transverse and

- longitudinal dispersion on first-order degradation rate constant estimation. *J. Contam. Hydrol.* 73, 3–14. doi:10.1016/j.jconhyd.2003.11.004
- Stroo, H.F., Leeson, A., Marqusee, J. a., Johnson, P.C., Ward, C.H., Kavanaugh, M.C., Sale, T.C., Newell, C.J., Pennell, K.D., Lebrón, C. a., Unger, M., 2012. Chlorinated ethene source remediation: Lessons learned. *Environ. Sci. Technol.* 46, 6438–6447. doi:10.1021/es204714w
- Suarez, M.P., Rifai, H.S., 1999. Biodegradation Rates for Fuel Hydrocarbons and Chlorinated Solvents in Groundwater. *Bioremediat. J.* 3, 337–362. doi:10.1080/10889869991219433
- Takeuchi, M., Kawabe, Y., Watanabe, E., Oiwa, T., Takahashi, M., Nanba, K., Kamagata, Y., Hanada, S., Ohko, Y., Komai, T., 2011. Comparative study of microbial dechlorination of chlorinated ethenes in an aquifer and a clayey aquitard. *J. Contam. Hydrol.* 124, 14–24. doi:10.1016/j.jconhyd.2011.01.003
- Thouement, H.A.A., Kuder, T., Heimovaara, T.J., van Breukelen, B.M., 2019. Do CSIA data from aquifers inform on natural degradation of chlorinated ethenes in aquitards? *J. Contam. Hydrol.* 226, 103520. doi:10.1016/j.jconhyd.2019.103520
- Tiehm, A., Schmidt, K.R., Pfeifer, B., Heidinger, M., Ertl, S., 2008. Growth kinetics and stable carbon isotope fractionation during aerobic degradation of cis-1,2-dichloroethene and vinyl chloride. *Water Res.* 42, 2431–2438. doi:10.1016/j.watres.2008.01.029
- Uçankuş, T., Ünlü, K., 2008. The effect of aquifer heterogeneity on natural attenuation rate of BTEX. *Environ. Geol.* 54, 759–776. doi:10.1007/s00254-007-0861-0
- van Breukelen, B.M., 2007. Extending the Rayleigh equation to allow competing isotope fractionating pathways to improve quantification of biodegradation. *Environ. Sci. Technol.* 41, 4004–4010. doi:10.1021/es0628452
- van Breukelen, B.M., Hunkeler, D., Volkering, F., 2005. Quantification of sequential chlorinated ethene degradation by use of a reactive transport model incorporating isotope fractionation. *Environ. Sci. Technol.* 39, 4189–4197. doi:10.1021/es048973c
- van Breukelen, B.M., Prommer, H., 2008. Beyond the rayleigh equation: Reactive transport modeling of isotope fractionation effects to improve quantification of biodegradation. *Environ. Sci. Technol.* 42, 2457–2463. doi:10.1021/es071981j
- van Breukelen, B.M., Rolle, M., 2012. Transverse hydrodynamic dispersion effects on isotope signals in groundwater chlorinated solvents plumes. *Environ. Sci. Technol.* 46, 7700–7708. doi:10.1021/es301058z
- van Breukelen, B.M., Thouement, H.A.A., Stack, P.E., Vanderford, M., Philp, P., Kuder, T., 2017a. Modeling 3D-CSIA data: Carbon, chlorine, and hydrogen isotope fractionation during reductive dechlorination of TCE to ethene. *J. Contam. Hydrol.* 204. doi:10.1016/j.jconhyd.2017.07.003
- van Breukelen, B.M., Thouement, H.A.A., Stack, P.E., Vanderford, M., Philp, P., Kuder, T., 2017b. Modeling 3D-CSIA data: Carbon, chlorine, and hydrogen isotope fractionation during reductive dechlorination of TCE to ethene. *J. Contam. Hydrol.*

204, 79–89. doi:10.1016/j.jconhyd.2017.07.003

- Verce, M.F., Madrid, V.M., Gregory, S.D., Demir, Z., Singleton, M.J., Salazar, E.P., Jackson, P.J., Halden, R.U., Verce, A., 2015. A long-term field study of in situ bioremediation in a fractured conglomerate trichloroethene source zone. *Bioremediat. J.* 19, 18–31. doi:10.1080/10889868.2014.978836
- Vogel, T.M., Criddle, C.S., McCarty, P.L., 1987. Transformations of halogenated aliphatic compounds. *Environ. Sci. Technol.* 21, 722–736. doi:10.1021/es00162a001
- Wanner, P., Hunkeler, D., 2015. Carbon and chlorine isotopologue fractionation of chlorinated hydrocarbons during diffusion in water and low permeability sediments. *Geochim. Cosmochim. Acta* 157, 198–212. doi:10.1016/j.gca.2015.02.034
- Wanner, P., Parker, B.L., Chapman, S.W., Aravena, R., Hunkeler, D., 2017. Does sorption influence isotope ratios of chlorinated hydrocarbons under field conditions? *Appl. Geochemistry* 84, 348–359. doi:10.1016/j.apgeochem.2017.07.016
- Wanner, P., Parker, B.L., Chapman, S.W., Aravena, R., Hunkeler, D., 2016. Quantification of degradation of chlorinated hydrocarbons in saturated low permeability sediments using compound-specific isotope analysis. *Environ. Sci. Technol.* 50, 5622–5630. doi:10.1021/acs.est.5b06330
- Wanner, P., Parker, B.L., Chapman, S.W., Lima, G., Gilmore, A., Mack, E.E., Aravena, R., 2018a. Identification of degradation pathways of chlorohydrocarbons in saturated low-permeability sediments using compound-specific isotope analysis. *Environ. Sci. Technol.* 52. doi:10.1021/acs.est.8b01173
- Wanner, P., Parker, B.L., Hunkeler, D., 2018b. Assessing the effect of chlorinated hydrocarbon degradation in aquitards on plume persistence due to back-diffusion. *Sci. Total Environ.* 633, 1602–1612. doi:10.1016/j.scitotenv.2018.03.192
- Weerasooriya, R., Dharmasena, B., 2001. Pyrite-assisted degradation of trichloroethene (TCE). *Chemosphere* 42, 389–396. doi:10.1016/S0045-6535(00)00160-0
- Wehr, R., Saleska, S.R., 2016. The long-solved problem of the best-fit straight line: Application to isotopic mixing lines. *Biogeosciences Discuss.* 0, 1–19. doi:10.5194/bg-2016-315
- West, M.R., Kueper, B.H., 2010. Plume detachment and recession times in fractured rock. *Groundwater* 48, 416–426. doi:10.1111/j.1745-6584.2009.00662.x
- Wiedemeier, T.H., Swanson, M.A., Moutoux, D.E., Gordon, E.K., Wilson, J.T., Wilson, B.H., Kampbell, D.H., Haas, P.E., Miller, R.N., Hansen, E.H., Chapelle, F.H., 1998. Technical protocol for evaluating natural attenuation of chlorinated solvents in ground water. Washington DC.
- Wiegert, C., Aeppli, C., Knowles, T., Holmstrand, H., Evershed, R., Pancost, R.D., Macháčková, J., Gustafsson, Ö., 2012. Dual carbon-chlorine stable isotope investigation of sources and fate of chlorinated ethenes in contaminated groundwater, *Environmental Science and Technology*. doi:10.1021/es3016843
- Wiegert, C., Mandalakis, M., Knowles, T., Polymenakou, P.N., Aeppli, C., Macháčková, J., Holmstrand, H., Evershed, R.P., Pancost, R.D., Gustafsson, O., 2013. Carbon and

- chlorine isotope fractionation during microbial degradation of tetra- and trichloroethene. *Environ. Sci. Technol.* 47, 6449–56. doi:10.1021/es305236y
- Worch, E., 1993. Eine neue Gleichung zur Berechnung von Diffusionskoeffizienten gelöster Stoffe. *Vom Wasser* 81, 289–297.
- Xie, F., Lu, Q., de Toledo, R.A., Shim, H., 2016. Enhanced simultaneous removal of MTBE and TCE mixture by *Paracoccus* sp. immobilized on waste silica gel. *Int. Biodeterior. Biodegrad.* 114, 222–227. doi:10.1016/j.ibiod.2016.07.003
- Xu, S., Sherwood Lollar, B., Sleep, B.E., 2017. Rethinking aqueous phase diffusion related isotope fractionation: Contrasting theoretical effects with observations at the field scale. *Sci. Total Environ.* 607–608, 1085–1095. doi:10.1016/J.SCITOTENV.2017.06.195
- Yan, S., Liu, Y., Liu, C., Shi, L., Shang, J., Shan, H., Zachara, J., Fredrickson, J., Kennedy, D., Resch, C.T., Thompson, C., Fansler, S., 2016. Nitrate bioreduction in redox-variable low permeability sediments. *Sci. Total Environ.* 539, 185–195. doi:10.1016/j.scitotenv.2015.08.122
- Yang, M., Annable, M.D., Jawitz, J.W., 2017. Field-scale forward and back-diffusion through low-permeability zones. *J. Contam. Hydrol.* 202, 47–58. doi:10.1016/j.jconhyd.2017.05.001
- Yang, M., Annable, M.D., Jawitz, J.W., 2015. Back diffusion from thin low permeability zones. *Environ. Sci. Technol.* 49, 415–422. doi:dx.doi.org/10.1021/es5045634
- York, D., Evensen, N.M., Martínez, M.L., De Basabe Delgado, J., 2004. Unified equations for the slope, intercept, and standard errors of the best straight line. *Am. J. Phys.* 72, 367. doi:10.1119/1.1632486
- Zheng, C., Hill, M., Cao, G., Ma, R., 2012. MT3DMS: Model use, calibration, and validation. *Trans. ASABE* 55, 1549–1559.

Acknowledgements

Thank you Boris, your comments and our discussions were always helpful and to the point and helped me greatly through the PhD project. Your knowledge and assistance were invaluable. Timo Heimovaara, thank you for joining this thesis project. I found our conversations motivating and your ideas were welcome. I also would like to thank Tomasz Kuder and Mindy Vanderford for the fruitful collaboration. I am thankful to Stefie, Alice, Guillaume and Sjoerd who also gave some time to this thesis.

I am deeply thankful to my colleagues, my friends and my family, who have been supportive and helpful – or just by my side – through those years.

This page was intentionally left blank

Curriculum Vitae

Héloïse Thouement was born in 1989 in Vitré, France. She received her A-level (baccalauréat) in 2006 from Lycée Lesage in Vannes, France. She graduated in 2012 with a double degree in engineering chemistry (ENSCL, Lille, France) and environmental engineering (DTU, Lyngby, Denmark). She completed her master thesis with subject managed aquifer recharge (project OXIMAR) at the Kompetenzzentrum Wasser Berlin. She worked as an engineering assistant at the DEEP (waste, water, environment, and pollution) laboratory of Insa Lyon in 2018. She now works as a polluted site engineer and R&D engineer at Tauw France.

Part of the Python code employed for this thesis is available on github :

<https://github.com/ThouementH/PhD-Thesis>

List of publications :

Thouement, H.A.A., Kuder, T., Heimovaara, T.J., van Breukelen, B.M., 2019. Do CSIA data from aquifers inform on natural degradation of chlorinated ethenes in aquitards ? J. Contam. Hydrol. 226, 103520. doi:10.1016/j.jconhyd.2019.103520

van Breukelen, B.M., Thouement, H.A.A., Stack, P.E., Vanderford, M., Philp, P., Kuder, T., 2017b. Modeling 3D-CSIA data: Carbon , chlorine , and hydrogen isotope fractionation during reductive dechlorination of TCE to ethene. J. Contam. Hydrol. 204, 79–89. doi:10.1016/j.jconhyd.2017.07.003

M. Staub, H. Thouement, C. Remy, U. Mische, G. Grützmacher, P. Roche, E. Soyeux and B. David, 2015. Aquifer recharge with reclaimed water: life-cycle assessment of hybrid concepts for non-potable reuse. Journal of Water Reuse and Desalination, 5(2): 142-148.